ATTENTION: The Singapore Copyright Act applies to the use of this document. Nanyang Technological University Library

(On the Spine)

COMPUTATIONAL ANALYSIS AND DESIGN OF FAN BLADE CONFIGURATIONS FOR OPTIMAL FAN PERFORMANCE CHARACTERISTICS

NG WAI KEET

2007



NANYANG TECHNOLOGICAL UNIVERSITY

COMPUTATIONAL ANALYSIS AND DESIGN OF FAN BLADE CONFIGURATIONS FOR OPTIMAL FAN PERFORMANCE CHARACTERISTICS

NG WAI KEET

SCHOOL OF MECHANICAL AND AEROSPACE ENGINEERING

2007

ATTENTION: The Singapore Copyright Act applies to the use of this document. Nanyang Technological University Library

Computational Analysis and Design of Fan Blade Configurations for Optimal Fan Performance Characteristics

Ng Wai Keet

School of Mechanical and Aerospace Engineering

A thesis submitted to the Nanyang Technological University
in fulfilment of the requirement for the degree of
Master of Engineering

2007

ATTENTION: The Singapore Copyright Act applies to the use of this document. Nanyang Technological University Library

ABSTRACT

The project is concerned with the computational analysis and design of fan blade configurations to achieve optimal fan performance characteristics such as total efficiency. Developments in computational fluid dynamics offer opportunities to perform optimal design of ventilation fans in a cost-effective manner without redundant fan fabrication in trial and error testing. These computational tools will be integrated to obtain the optimal fan geometry and configuration. Computational analysis using sliding mesh model to obtain flow fields for both single inlet fan and double inlet fan have been done for different design conditions. Fan performance characteristics have been extracted and verified with experimental data provided from industry database. Optimization of total efficiency, constrained optimization and multi objective optimization have been done using genetic algorithm as the optimization method of choice. However, the computational costs of such design optimization problems are huge and hence a technique to reduce the computational cost is developed. A reduced order modeling technique which is proper orthogonal decomposition interpolation method has been used. In this method, the high fidelity solver is used only to generate an ensemble of snapshots of the fluid which are used to create POD modes. These modes are then combined with interpolation methods to estimate the population sample for genetic algorithm optimization.

ATTENTION: The Singapore Copyright Act applies to the use of this document. Nanyang Technological University Library

ACKNOWLEDGEMENT

The author would like to express his utmost appreciation and gratitude to his project supervisor, Associate Professor Murali Damodaran, for the support and most useful guidance he had extended to the author throughout the course of the project. The author is exceptionally thankful to Associate Professor Murali Damodaran and Dr. Shidrati Ali for the various invaluable advices given during crucial phases of the project.

The author would like to express his utmost appreciation and gratitude to his industry sponsor Kruger Ventilation Industries Pte Ltd for partially funding his Master of Engineering degree program. He would also like to thank especially Mr. Kelvin Wong, Mr. Xie Yong Heng and Miss Tin Tin for their invaluable advice and support given during critical phases of the project.

The author acknowledges the use of the computing resources of the Centre for Advanced Numerical Engineering Simulations in Nanyang Technological University of Singapore.

ATTENTION: The Singapore Copyright Act applies to the use of this document. Nanyang Technological University Library

TABLE OF CONTENTS

ABSTRACT			**i**
ACKNOWLEDGEMENT			**ii**
TABLE OF CONTENTS			**iii**
LIST OF FIGURES			**v**
1.	**INTRODUCTION**		**1**
	1.1	Operational Characteristics of Turbomachinery	12
	1.2	Objective and Scope	17
2.	**GRID GENERATION**		**19**
	2.1	Geometry of Fans	19
	2.2	Grid Generation	24
3.	**NUMERICAL FLOW MODELLING IN AN INDUSTRIAL VENTILATION FAN**		**28**
	3.1	Basic Governing Equations	28
	3.2	Finite Volume Method	30
	3.3	Initial and Boundary Conditions	39
	3.4	Turbulence Models	42
	3.5	Results and Discussion	47
4.	**DESIGN OPTIMIZATION OF INDUSTRIAL VENTILATION FAN**		**111**
	4.1	Optimization Problems	111
	4.2	Design Strategies	120
	4.3	Genetic Algorithm	123
	4.4	Reduced Order Modelling	128
	4.5	Results and Discussion	133

ATTENTION: The Singapore Copyright Act applies to the use of this document. Nanyang Technological University Library

5. CONCLUSION & FUTURE WORK **172**

5.1 Conclusion 172

5.2 Future Work 175

REFERENCES **178**

ATTENTION: The Singapore Copyright Act applies to the use of this document. Nanyang Technological University Library

LIST OF FIGURES

	Page No.
Figure 1.1 Comparison between different types of industrial fans such as (a) axial fan, (b) centrifugal fan, (c) cross flow fan and (d) mixed flow fan	2
Figure 1.2 Fan Performance Curve	4
Figure 1.3 Comparison between different types of fan inlet loss such as (a) non-uniform flow into suction of fan, (b) fan inlet swirl, (c) straight inlet duct loss	5
Figure 1.4 Overview of Research Project	11
Figure 1.5 Centrifugal Fan (Cross sectional view)	12
Figure1.6 Fan Surge	14
Figure1.7 Rotating Stall	15
Figure 2.1 Geometry of single inlet fan (a) with outer casing and (b) without outer casing	19
Figure 2.2 Geometry of blade (for both single inlet fan and double inlet fan) in different view such as (a) Front View and (b) Side View	20
Figure 2.3 Geometry of impeller plate with blades in (a) 2-Dimensional View and (b) 3-D dimensional view for single inlet fan	20
Figure 2.4 Geometry of double inlet fan (a) with outer casing and (b) without outer casing	21
Figure 2.5 Geometry of impeller plate with blades in 2-Dimensional View for (a) top plate and (b) bottom plate for double inlet fan	21
Figure 2.6 Geometry of impeller plate with blades in 3-Dimensional View for double inlet fan	22
Figure 2.7 Geometry of airfoil bladed fan (a) with outer casing and (b) without outer casing	22
Figure 2.8 Airfoil blade shape in (a) 3-Dimensional view and (b) top view	23

ATTENTION: The Singapore Copyright Act applies to the use of this document. Nanyang Technological University Library

Figure 2.9 Geometry of impeller plate with blades in 2-Dimensional View for (a) top plate and (b) bottom plate for airfoil bladed fan 23

Figure 2.10 Geometry of impeller without impeller casing in 3-Dimensional View for airfoil bladed fan 23

Figure 2.11 Steps in creating volume mesh for impeller plate which includes (a) Division of impeller plate into 11 sections, (b) Quadrilateral face mesh for one section, (c) Quadrilateral volume mesh for one section and (d) Completed volume mesh for impeller 25

Figure 2.12 Interface between fluid zones looking from top 26

Figure 2.13 Face mesh on (a) impeller with blades, (b) inlet cone and impeller in 2-Dimensional View, (c) inlet cone and impeller casing in 3-Dimensional view and (d) outer casing 26

Figure 2.14 Volume Mesh for (a) single inlet fan and (b) double inlet fan with extended pipe 27

Figure 3.1 Overview of the Segregated Solution Method 31

Figure 3.2 Zones created by Interface Interaction 37

Figure 3.3 Sliding fluid zones attached to impeller wall 37

Figure 3.4 Sliding fluid zones attached to rotating blade wall and shaft wall 38

Figure 3.5 Interface between fluid zones looking from top view 38

Figure 3.6 Comparison between moving fluid zones at different periods of (a) time 1 T and (b) time 1.5 T 39

Figure 3.7 Recommended Setting of Operating Pressure 40

Figure 3.8 Diameter of impeller plate 41

Figure 3.9 Residual Plot for single inlet fan 0.95m^3/s, 2500 rpm 49

Figure 3.10 Plot of gauge total pressure at outlet against different period of revolution 49

Figure 3.11 Contour plot of static pressure at (a) pressure side and (b) suction side of blade for 0.95 m^3/s, 2500 rpm 51

ATTENTION: The Singapore Copyright Act applies to the use of this document. Nanyang Technological University Library

Figure 3.12 Comparison between streamline aft impeller in (a) top view and (b) 3-dimensional view for 0.95 m^3/s, 2500 rpm 52

Figure 3.13 Streamline aft impeller in zoom in 3-dimensional view for 0.95 m^3/s, 2500 rpm 52

Figure 3.14 Streamline aft blades for 0.95 m^3/s, 2500 rpm 53

Figure 3.15 Blade numbering for impeller plate of single inlet fan 54

Figure 3.16 Contour plot of gauge static pressure for blade passages (Top view) for 0.95 m^3/s, 2500 rpm 54

Figure 3.17 Plot of skin friction line on (a) pressure side and (b) suction side of Blade 2 for 0.95 m^3/s, 2500 rpm 55

Figure 3.18 Plot of skin friction line on (a) pressure side and (b) suction side of Blade 10 for 0.95 m^3/s, 2500 rpm 55

Figure 3.19 Plot of skin friction line on (a) pressure side and (b) suction side of Blade 11 for 0.95 m^3/s, 2500 rpm 55

Figure 3.20 Comparison of plots of skin friction line on impeller casing (bottom view), 0.95 m^3/s, 2500 rpm for time (a) after 1 period, (b) after 1.2 period, (c) after 1.4 period, (d) after 1.6 period, (d) after 1.8 period, (e) after 1.8 period and (f) after 2 period 56

Figure 3.21 Plot of skin friction line on impeller casing and blades (3D view), 0.95 m^3/s, 2500 rpm 57

Figure 3.22 Plot of skin friction line on impeller casing and one blade (3D view), 0.95 m^3/s, 2500 rpm 57

Figure 3.23 Residual Plot for single inlet fan (BSB fan) 0.95 m^3/s, 2500 rpm 58

Figure 3.24 Comparison between different number of mesh nodes on blade for (a) mesh nodes on blade face: 320, (b) mesh nodes on blade face: 160, (c) mesh nodes on blade face: 320, (d) mesh nodes on blade face: 640, (e) mesh nodes on blade face: 1280, (f) mesh nodes on blade face: 5120 59

Figure 3.25 Plot of total pressure error against 1/ [No. of mesh nodes of blade] 60

Figure 3.26 Contour plot of (a) gauge static pressure and (b) gauge total pressure at outlet for 0.95 m^3/s, 2500 rpm 61

ATTENTION: The Singapore Copyright Act applies to the use of this document. Nanyang Technological University Library

Figure 3.27 Contour plot of (a) gauge static pressure and (b) gauge total pressure at impeller (top view) for 0.95 m^3/s, 2500 rpm 62

Figure 3.28 Contour plot of gauge dynamic pressure at impeller (a) top view and (b) 3 D view for 0.95 m^3/s, 2500 rpm 62

Figure 3.29 Contour plot of vorticity magnitude at impeller (3 D view) for 0.95 m^3/s, 2500 rpm 63

Figure 3.30 Contour plot of static pressure for impeller (3 D view) for 0.95 m^3/s, 2500 rpm 64

Figure 3.31 Contour plot of static pressure for blade passages (Top view) for 0.95 m^3/s, 2500 rpm 64

Figure 3.32 Comparison between contour plot of (a) 3 dimensional view, (b) gauge static pressure and (c) gauge dynamic pressure at plane X = 0.087m for 0.95 m^3/s, 2500 rpm 65

Figure 3.33 Plot of gauge total pressure at outlet against volume flow rate for single inlet fan running at 2500 rpm for different turbulence models 68

Figure 3.34 Plot of total efficiency for single inlet fan running at 2500 rpm for different turbulence models 68

Figure 3.35 Plot of gauge total pressure at outlet against volume flow rate for single inlet fan running at different rpm with Standard K Epsilon turbulence model 69

Figure 3.36 Plot of flow coefficient against volume flow rate for single inlet fan running at different rpm with Standard K Epsilon turbulence model 69

Figure 3.37 Plot of power coefficient against volume flow rate for single inlet fan running at different rpm with Standard K Epsilon turbulence model 70

Figure 3.38 Comparison between contour plot of gauge static pressure at outlet with volume flow rate 0.95 m^3/s at time (a) 0 second at 2500 rpm, (b) 4.8 second at 2000 rpm, (c) 9.6 second at 1500 rpm, (d) 14.4 second at 1000 rpm, (e) 19.2 second at 500 rpm and (f) 24 second at 0 rpm after the fan is turned off. 72

ATTENTION: The Singapore Copyright Act applies to the use of this document. Nanyang Technological University Library

Figure 3.39 Comparison between contour plot of gauge static pressure at impeller (top view) with volume flow rate 0.95 m^3/s at time (a) 0 second at 2500 rpm, (b) 4.8 second at 2000 rpm, (c) 9.6 second at 1500 rpm, (d) 14.4 second at 1000 rpm, (e) 19.2 second at 500 rpm and (f) 24 second at 0 rpm after the fan is turned off. 73

Figure 3.40 Plot of gauge total pressure at outlet against time for single inlet fan running at reducing rpm 74

Figure 3.41 Plot of gauge total pressure at outlet against rpm for single inlet fan running at reducing rpm 74

Figure 3.42 Contour plot of (a) gauge static pressure and (b) gauge total pressure at outlet for 1.2 m^3/s, 2200 rpm 76

Figure 3.43 Contour plot of gauge static pressure for (a) impeller and (b) impeller with impeller casing and inlet cone in 3 D view for 1.2m^3/s, 2200rpm 76

Figure 3.44 Contour plot of pressure coefficient at (a) pressure side and (b) suction side of blade for 1.2 m^3/s, 2200 rpm 79

Figure 3.45 Spanwise plot of pressure coefficient along lines on (a) pressure side, (b) suction side and (c) both sides of blade surfaces for 1.2 m^3/s, 2200 rpm 79

Figure 3.46 Contour plot of skin friction coefficient at (a) pressure side and suction side of blade for 1.2 m^3/s, 2200 rpm 80

Figure 3.47 Spanwise plot of skin friction coefficient along the lines on (a) pressure side, (b) suction side and (c) both sides of blade surfaces for 1.2 m^3/s, 2200 rpm 80

Figure 3.48 Contour plot of gauge static pressure at (a) top impeller plate and (b) bottom impeller plate for 1.2 m^3/s, 2200 rpm 81

Figure 3.49 Fluid passages midline plot of gauge static pressure along line on (a) top impeller plate and (b) bottom impeller plate for 1.2 m^3/s, 2200 rpm 81

Figure 3.50 Contour plot of skin friction coefficient at top impeller plate for 1.2 m^3/s, 2200 rpm 82

ATTENTION: The Singapore Copyright Act applies to the use of this document. Nanyang Technological University Library

Figure 3.51 Fluid passages midline plot of skin friction coefficient along line on top impeller plate for 1.2 m^3/s, 2200 rpm 82

Figure 3.52 Contour plot of gauge static pressure along the pipe for 1.2 m^3/s, 2200 rpm 82

Figure 3.53 Plot of gauge static pressure along centreline along the pipe for 1.2 m^3/s, 2200 rpm 82

Figure 3.54 Contour plot of gauge static pressure along the pipe at different plane sections for 1.2 m^3/s, 2200 rpm 82

Figure 3.55 Contour plot of vorticity magnitude at (a) pressure side and (b) suction side of blade for 1.2 m^3/s, 2200 rpm 83

Figure 3.56 Plot of vorticity magnitude along the line on blade surfaces for 1.2 m^3/s, 2200 rpm 83

Figure 3.57 Contour plot of vorticity magnitude on impeller for 1.2 m^3/s, 2200 rpm 84

Figure 3.58 Streamlines plot coloured by vorticity magnitude on impeller for 1.2 m^3/s, 2200 rpm 84

Figure 3.59 Blade to blade planes at (a) 3 Dimensional View and (b) 2-dimensional view 87

Figure 3.60 Contour plot of gauge static pressure on blade to blade plane at (a) near to impeller casing, (b) midspan and (c) near to impeller plate for 1.2 m^3/s, 2200 rpm 88

Figure 3.61 Plot of relative velocity vectors on blade to blade plane for 1.2 m^3/s, 2200 rpm 89

Figure 3.62 Plot of relative velocity vectors on blade to blade plane for 2200 rpm under (a) peak efficiency and (b) surge 89

Figure 3.63 Contour plot of relative velocity magnitude on blade to blade plane for 1.2 m^3/s, 2200 rpm 90

Figure 3.64 Contour plots of plane behind blades for 1.2 m^3/s, 2200 rpm 90

ATTENTION: The Singapore Copyright Act applies to the use of this document. Nanyang Technological University Library

Figure 3.65 Comparison on plots along line on plane behind blades for (a) gauge static pressure, (b) absolute velocity profile, (c) relative velocity profile and (d) relative velocity magnitude for 1.2 m^3/s, 2200 rpm 91

Figure 3.66 Contour plot of gauge static pressure on many planes behind blades for relative velocity profile for 1.2 m^3/s, 2200 rpm 92

Figure 3.67 Plot of relative velocity profile along lines on many planes behind blades for 1.2 m^3/s, 2200 rpm 92

Figure 3.68 Comparison between contour plot of gauge static pressure for planes between blades at (a) 3 Dimensional View, (b) 25 % plane between blades, (c) mid-line between blades and (d) 75 % plane between blades 93

Figure 3.69 Plot of gauge static pressure along lines on planes between blades for 1.2 m^3/s, 2200 rpm 93

Figure 3.70 Plot of relative velocity vectors on plane between blades for 1.2 m^3/s, 2200 rpm 93

Figure 3.71 Contour plot of (a) gauge static pressure and (b) gauge total pressure at outlet for 1.2 m^3/s, 2200 rpm with top and bottom impellers rotating in different direction 94

Figure 3.72 Contour plot of (a) gauge static pressure and (b) gauge total pressure at outlet for 1.2 m^3/s, 2200 rpm with top and bottom impellers rotating in same direction 95

Figure 3.73 Comparison between contour plot of gauge static pressure at outlet for 1.2 m^3/s, 2200 rpm for (a) top and bottom impellers before aligned and (b) top and bottom impellers aligned 96

Figure 3.74 Comparison between contour plot of gauge total pressure at outlet for 1.2 m^3/s, 2200 rpm for (a) top and bottom impellers before aligned and (b) top and bottom impellers aligned 96

Figure 3.75 Contour plot of gauge static pressure for (a) impellers and (b) impellers with impeller casing and inlet cone for 1.2 m^3/s, 2200 rpm with top and bottom impellers alignment 97

ATTENTION: The Singapore Copyright Act applies to the use of this document. Nanyang Technological University Library

Figure 3.76 3-Dimensional View of the plane Z = 0 m for 0.95 m^3/s, 2500 rpm (a) top and bottom impellers before alignment and (b) top and bottom impellers aligned 97

Figure 3.77 Comparison between contour plot of gauge static pressure at XY plane for 1.2 m^3/s, 2200 rpm (a) top and bottom impellers before aligned and (b) top and bottom impellers aligned 97

Figure 3.78 Contour plot of gauge static pressure for (a) 11-bladed impeller and (b) 10-bladed impeller, (c) 9-bladed impeller and (d) 8-bladed impeller for double inlet fan (BDB fan), 1600 rpm and 2.5 m^3/s 99

Figure 3.79 Contour plot of gauge total pressure at outlet for (a)11 bladed impeller and (b) 10 bladed impeller, (c) 9 bladed impeller and (d) 8 bladed impeller for BDB fan, 1600 rpm and 2.5 m^3/s 100

Figure 3.80 Plot of gauge total pressure at outlet against volume flow rate for double inlet fan running at 2200 rpm 103

Figure 3.81 Plot of total efficiency for double inlet fan running at 2200 rpm 103

Figure 3.82 Plot of gauge total pressure at outlet against volume flow rate for single inlet fan and double inlet fan running at 2200 rpm 104

Figure 3.83 Plot of total efficiency for single inlet fan and double inlet fan running at 2200 rpm 104

Figure 3.84 Plot of gauge total pressure at outlet against volume flow rate for double inlet fan running at 1600 rpm for different number of blades 105

Figure 3.85 Plot of total efficiency against volume flow rate for double inlet fan running at 1600 rpm for different number of blades 105

Figure 3.86 Comparison of contour plot of gauge total pressure at outlet for (a) double inlet fan and (b) airfoil bladed fan at 1.2m^3/s, 2200rpm 107

Figure 3.87 Comparison of gauge static pressure distribution on impellers for (a) double inlet fan and (b) airfoil bladed fan at 1.2m^3/s, 2200rpm 107

Figure 3.88 Contour plot of gauge static pressure for blade passages (Top view) for 1.2m^3/s, 2200rpm for airfoil bladed fan 108

Figure 3.89 Streamline aft blade arrangement in zoom in 3 dimensional view for 1.2m^3/s, 2200rpm for airfoil blade fan 108

ATTENTION: The Singapore Copyright Act applies to the use of this document. Nanyang Technological University Library

Figure 3.90 Plot of gauge total pressure at outlet against volume flow rate for airfoil blade fan and double inlet fan running at 2200rpm 110

Figure 3.91 Plot of total efficiency for airfoil blade fan and double inlet fan running at 2200rpm 110

Figure 4.1 Comparison between different geometrical constraints for design optimization such as (a) diameter of impeller plate and (b) blade height 112

Figure 4.2 Operating Range of volume flow rate for double inlet fan 112

Figure 4.3 Operating Range of volume flow rate for double inlet fan based on total efficiency 113

Figure 4.4 Comparison between different blade off alignment angle such as (a) 0° and (b) 16.364° 114

Figure 4.5 Comparison between different inlet cone depth such as (a) 0 mm and (b) 20mm 116

Figure 4.6 Comparison between different blade angle such as (a) 36° and (b) 41° 116

Figure 4.7 Comparison between different numbers of blades on impeller such as (a) 8 blades impeller and (b) 11 blades impeller 117

Figure 4.8 Comparison of flow charts of design optimization (a) without reduced order modeling and (b) with reduced order modeling 121

Figure 4.9 Flow chart of model order reduction 122

Figure 4.10 Plot of L_2 Norm of objective function against Blade Off alignment Angle 124

Figure 4.11 Comparing (a) desired pressure profile with (b) inverse design result with initial guess $x_0 = 5$ and (c) inverse design result with initial guess $x_0 = 15$ using least square minimization method for BDB fan, 2200rpm, 1.2 m^3/s and parameter Blade off Alignment Angle 125

Figure 4.12 Flow chart of Genetic Algorithm 126

Figure 4.13 Overview of Reduced Order Modeling 129

Figure 4.14 Plot of Eigenvalue against number of POD modes from 2nd POD mode to 31st POD mode 132

ATTENTION: The Singapore Copyright Act applies to the use of this document. Nanyang Technological University Library

Figure 4.15 POD Snapshot taken at outlet for BDB fan, 2200rpm, 1.2 m^3/s and Blade off Alignment Angle 16.364° 135

Figure 4.16 Design Parameter Blade Off Alignment Angle for (a) 0° and (b) 16.364° 135

Figure 4.17 Comparison between different inlet cone depth such as (a) 0 mm and (b) 20mm 135

Figure 4.18 Contour plot of snapshots taken at outlet for BDB fan, 2200rpm, 1.2 m^3/s with blade off alignment angle (a) 16.364°, (b) 15.818°, (c) 15.273°, (d) 14.727°, (e) 14.182° and (f) 13.636° 136

Figure 4.19 Contour plot of snapshots taken at outlet for BDB fan, 2200rpm, 1.2 m^3/s with blade off alignment angle (a) 13.091°, (b) 12.545°, (c) 12°, (d) 11.455°, (e) 10.909° and (f) 10.364° 137

Figure 4.20 Contour plot of snapshots taken at outlet for BDB fan, 2200rpm, 1.2 m^3/s with blade off alignment angle (a) 9.818°, (b) 9.273°, (c) 8.727°, (d) 8.182°, (e) 7.636° and (f) 7.091° 138

Figure 4.21 Contour plot of snapshots taken at outlet for BDB fan, 2200rpm, 1.2 m^3/s with blade off alignment angle (a) 6.545°, (b) 6°, (c) 5.455°, (d) 4.909°, (e) 4.364° and (f) 3.818° 139

Figure 4.22 Contour plot of snapshots taken at outlet for BDB fan, 2200rpm, 1.2 m^3/s with blade off alignment angle (a) 3.273°, (b) 2.727°, (c) 2.182° and (d) 1.636° 140

Figure 4.23 Contour plot of snapshots taken at outlet for BDB fan, 2200rpm, 1.2 m^3/s with blade off alignment angle (a) 1.091°, (b) 0.545° and (c) 0° 141

Figure 4.24 Comparison of POD results using (a) 1 POD mode and (b) 10 POD modes with (c) FLUENT Flow Simulation Result for BDB fan, 2200rpm, 1.2 m^3/s and Blade off Alignment Angle 16.364° (part of the ensemble of snapshots) 142

Figure 4.25 Comparison of POD interpolation results using (a) 16 POD snapshots and (b) 31 POD snapshots with (c) FLUENT Flow Simulation Result for BDB fan, 2200rpm, 1.2 m^3/s and Blade Off Alignment Angle 8° (not part of the ensemble of snapshots) 143

ATTENTION: The Singapore Copyright Act applies to the use of this document. Nanyang Technological University Library

Figure 4.26 Effect of (a) part or not part of ensemble of snapshots and (b) different number of POD snapshots on the plot of L_2 Relative Error Norm against number of POD Modes 144

Figure 4.27 Comparison of (a) POD interpolation results using 21 POD snapshots and 10 POD modes with (b) FLUENT Flow Simulation Result for BDB fan, 2200rpm, 4.39 m^3/s and Inlet Cone depth 6.3 mm (not part of the ensemble of snapshots) 145

Figure 4.28 Convergence plot of objective function against generations for different population size using design parameter blade off alignment angle 147

Figure 4.29 Convergence plot of objective function for optimization of total efficiency against generations for different volume flow rates using design parameter inlet cone depth 148

Figure 4.30 Convergence plot of objective function for constrained optimization and unconstrained optimization of total efficiency against generations using design parameter inlet cone depth 148

Figure 4.31 Comparison of optimized pressure profile using (a) Fluent flow simulation and (b) 10 POD modes for BDB fan, 2200 rpm, and 1.2 m^3/s using parameter blade off alignment angle 150

Figure 4.32 Comparison of (a) desired pressure profile with (b) inverse design using genetic algorithm for BDB fan, 2200 rpm, and 1.2 m^3/s using parameter blade off alignment angle 151

Figure 4.33 Comparison of (a) desired pressure profile with (b) inverse design using genetic algorithm for BDB fan, 2200 rpm, and 1.2 m^3 /s using parameter inlet cone depth 152

Figure 4.34 Comparison of (a) pressure profile before optimization of total efficiency with (b) pressure profile after optimization of total efficiency for BDB fan, 2200 rpm, and 3.33 m^3/s using parameter inlet cone depth 155

ATTENTION: The Singapore Copyright Act applies to the use of this document. Nanyang Technological University Library

Figure 4.35 Comparison of (a) pressure profile after optimization with FLUENT flow simulation results with (b) pressure profile after optimization with genetic algorithm for BDB fan, 2200 rpm, and 3.33 m^3/s using parameter inlet cone depth 155

Figure 4.36 Section view of vorticity magnitude near inlet cone tip for (a) inlet cone depth 1 mm and (b) inlet cone depth 20 mm for BDB fan, 2200 rpm, and 3.33 m^3/s 156

Figure 4.37 Vorticity magnitudes at inlet cone tip for (a) inlet cone depth 1 mm and (b) inlet cone depth 20 mm for BDB fan, 2200 rpm, and 3.33 m^3/s 156

Figure 4.38 Skin friction lines near inlet cone tip for (a) inlet cone depth 1mm and (b) inlet cone depth 20mm for BDB fan, 2200 rpm, and 3.33 m^3/s 157

Figure 4.39 Plot of total efficiency against inlet cone depth for BDB fan, 2200 rpm, and 3.33 m^3/s 157

Figure 4.40 Comparison of (a) pressure profile before optimization of total efficiency with (b) pressure profile after optimization of total efficiency for BDB fan, 2200 rpm, and 2.8 m^3/s using parameter inlet cone depth 158

Figure 4.41 Comparison of (a) pressure profile after optimization with FLUENT flow simulation results with (b) pressure profile after optimization with genetic algorithm for BDB fan, 2200 rpm, and 2.8 m^3/s using parameter inlet cone depth 158

Figure 4.42 Plot of total efficiency for the double inlet fan running at 2200 rpm within the operating range before and after optimization 159

Figure 4.43 Pressure profile after optimization with genetic algorithm for BDB fan, 2200 rpm at (a) 3.33 m^3/s and (b) 2.8 m^3/s using parameter inlet cone depth 159

Figure 4.44 Comparison of (a) pressure profile before optimization of total efficiency with (b) pressure profile after optimization of total efficiency for 8 Bladed BDB fan, 1600 rpm, and 2.5 m^3/s using parameter Blade Angle 160

Figure 4.45 Plot of Total Efficiency against volume flow rates for different inlet cone depths for double inlet fan, running at 2200 rpm 162

ATTENTION: The Singapore Copyright Act applies to the use of this document. Nanyang Technological University Library

Figure 4.46 Comparison of different optimized inlet cone depths for BDB fan, 2200 rpm with different volume flow rates (a) 2.27m^3/s, (b) 2.80 m^3/s, (c) 3.33m^3/s and (d) 3.86 m^3/s 163

Figure 4.47 Comparison of pressure profile for using (a) parameters of inlet cone depth only and (b) parameters of inlet cone depth and volume flow rates for BDB fan, 2200 rpm, and 3.33 m^3/s 165

Figure 4.48 Comparison of different pressure profiles for using parameters of inlet cone depth and volume flow rates for BDB fan, 2200 rpm 165

Figure 4.49 Comparison of optimized pressure profile for using (a) parameter of inlet cone depth only and (b) parameters of inlet cone depth and volume flow rates for BDB fan, 2200 rpm 166

Figure 4.50 Pressure profile for (a) maximum total efficiency after optimization and (b) multi-objective optimization with a_1 = 0.5 and a_2 =0.5 for BDB fan, 2200 rpm, and 3.33 m^3/s using parameter inlet cone depth 167

Figure 4.51 Pressure profile for multi-objective optimization for (a) a_1 = 0.5 and a_2 =0.5 and (b) a_1 = 0.001 and a_2 =0.999 for BDB fan, 2200 rpm, and 3.33 m^3/s using parameter inlet cone depth 168

Figure 4.52 Plot of Penalty Function Value against Penalty Parameter for BDB fan, 2200 rpm, and 3.33 m^3/s using parameter inlet cone depth 170

Figure 4.53 Pressure profile of (a) unconstrained optimization and (b) constrained optimization with pressure above 1490 Pa for BDB fan, 2200 rpm, and 3.33 m^3/s using parameter inlet cone depth 170

Figure 4.54 Pressure profile of constrained optimization for pressure above 1490 Pa with (a) penalty parameter 0.0000001 and (b) penalty parameter 0.0001 for BDB fan, 2200 rpm, and 3.33 m^3/s using parameter inlet cone depth 171

ATTENTION: The Singapore Copyright Act applies to the use of this document. Nanyang Technological University Library

CHAPTER 1

INTRODUCTION

A fan is a machine with two or more blades or vanes attached to a rotating shaft. Each of these devices, including the impellers, converts rotational mechanical energy, applied to their shafts, to gauge total pressure increases of the moving gas. This conversion is accomplished by changing the momentum of the fluid. Fans produce air flows with high volume and low pressure, as opposed to a gas compressor which produces high pressures at a comparatively low volume. Fans are useful for moving large quantities of air, which is suited for applications such as winnowing grain or blowing a fire, cooling and ventilation purposes, and in conjunction with a heat source for heating and drying. A fan blade rotates when it is exposed to an air stream, and devices that take advantage of this, such as anemometers and wind turbines often have designs similar to that of a fan.

Figure 1 shows the different types of industrial fans such as axial fan, centrifugal fan, cross flow fan and mixed flow fan. An example of axial fan is shown in Figure 1.1(a), which is taken from Continental Fan Manufacturing [1]. The axial-flow fans have blades that force air to move parallel to the shaft about which the blades rotate. Axial fans blow air across the axis of the fan linearly.

An example of centrifugal fan is shown in Figure 1.1(b), which is designed by Kruger Ventilation [2]. The centrifugal fan has an impeller that consists of a central shaft about which a set of blades form a spiral pattern. Centrifugal fans blow air at right angles to the inlet of the fan, and spin centrifugally the air outwards to the outlet. An impeller rotates, causing air to enter the fan near the shaft and move perpendicularly from the shaft to the opening in the scroll-shaped fan casing. Since the ventilation fans used are centrifugal fans, some basic concepts about centrifugal fan are discussed in later section 1.1.1.

An example of cross flow fan is shown in Figure 1.1(c), which is taken from LTG Incorporated [3]. The cross flow fan has a rotor with a hollow centre and axial fan blades along the periphery. Cross flow fans take in air along the periphery of the rotor, and expel it

ATTENTION: The Singapore Copyright Act applies to the use of this document. Nanyang Technological University Library

through the outlet in a similar fashion to the centrifugal fan. Cross flow fans give off an even airflow along the entire width of the fan, and are very quiet in operation. They are comparatively bulky, and the air pressure is low. Cross flow fans are often used for cooling in photocopiers. The action of a fan or blower causes pressures slightly above atmospheric, which are called plenums.

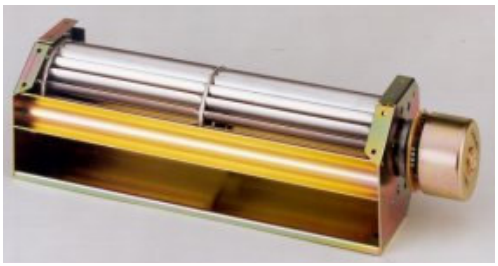
An example of mixed flow fan is shown in Figure 1.1(d), which is developed by Flamgard [4]. This type of fan has an air path through the impeller, which is between that of the axial and centrifugal types. It is capable of being constructed to provide either axial or radial discharge and produces more pressure head than a comparable flow fan. The mixed flow fan is unique because of its non stalling characteristic and is widely used in applications where variations in the system conditions can cause a standard axial or centrifugal fan to enter its stall region causing vibration and premature failure. In addition, the pressures and volume exhausted are comparably larger than other types of fans.



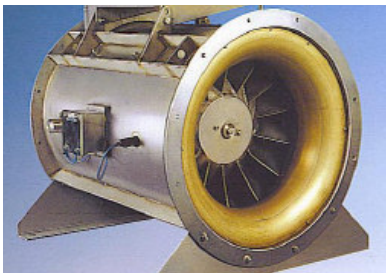
(a) Axial Fan



(b) Centrifugal Fan



(c) Cross Flow Fan



(d) Mixed Flow Fan

Figure 1.1 Comparison between different types of industrial fans such as (a) axial fan, (b) centrifugal fan, (c) cross flow fan and (d) mixed flow fan.

ATTENTION: The Singapore Copyright Act applies to the use of this document. Nanyang Technological University Library

Most experimental results on the fan performance characteristics of ventilation fan have been conducted in laboratory tests according to an appropriate industry test standard Air Movement and Control Association International [5]. CFD technology, which has matured in recent years, has made it possible for one to obtain the fan performance characteristics of ventilation fan without redundant fan fabrication for the initial period of trial testing and design and hence the most efficient fan design can be achieved more economically. This is the main contribution of CFD flow simulation to the turbomachinery industry.

According to Kruger Technical Bulletin [6], a fan performance curve is a graphical presentation of the performance of a fan in which gauge total pressure and total efficiency are plotted against volume flow rate. Total efficiency η_t is defined as $\frac{P_T Q}{W}$ where Q is exhaust volume flow rate in m^3/s, W is the power input in watt and P_T is the gauge total pressure in Pa. Generally, these curves are determined by laboratory tests, conducted according to an appropriate industry test standards. It is important to note that the test setup required by such industry test standards is nearly ideal without taking into account of losses. For this reason, the performance curves for gauge static pressure and brake horsepower versus airflow are those obtained under ideal conditions, which rarely exists in practice.

Figure 1.2 shows a typical fan performance curve obtained from laboratory tests taken from Kruger Technical Bulletin [6] which shows plots of total efficiency against volume flow rate, total pressure against volume flow rate and power required for ventilation fan at different rpm. Flow simulation results for the ventilation fan would be verified with laboratory test results. Results will be used for fan design studies to improve fan performance. A fan is under surge if it has reached a point of instability such that the pressure rise is at the maximum and further reduction in volume flow rate will lead to abrupt change in flow pattern in the compressor. The point of instability is the surge point and locus of these points for different rotational speed is the surge line. Hence, a fan under surge should be avoided as it seriously affects the fan performance.

ATTENTION: The Singapore Copyright Act applies to the use of this document. Nanyang Technological University Library

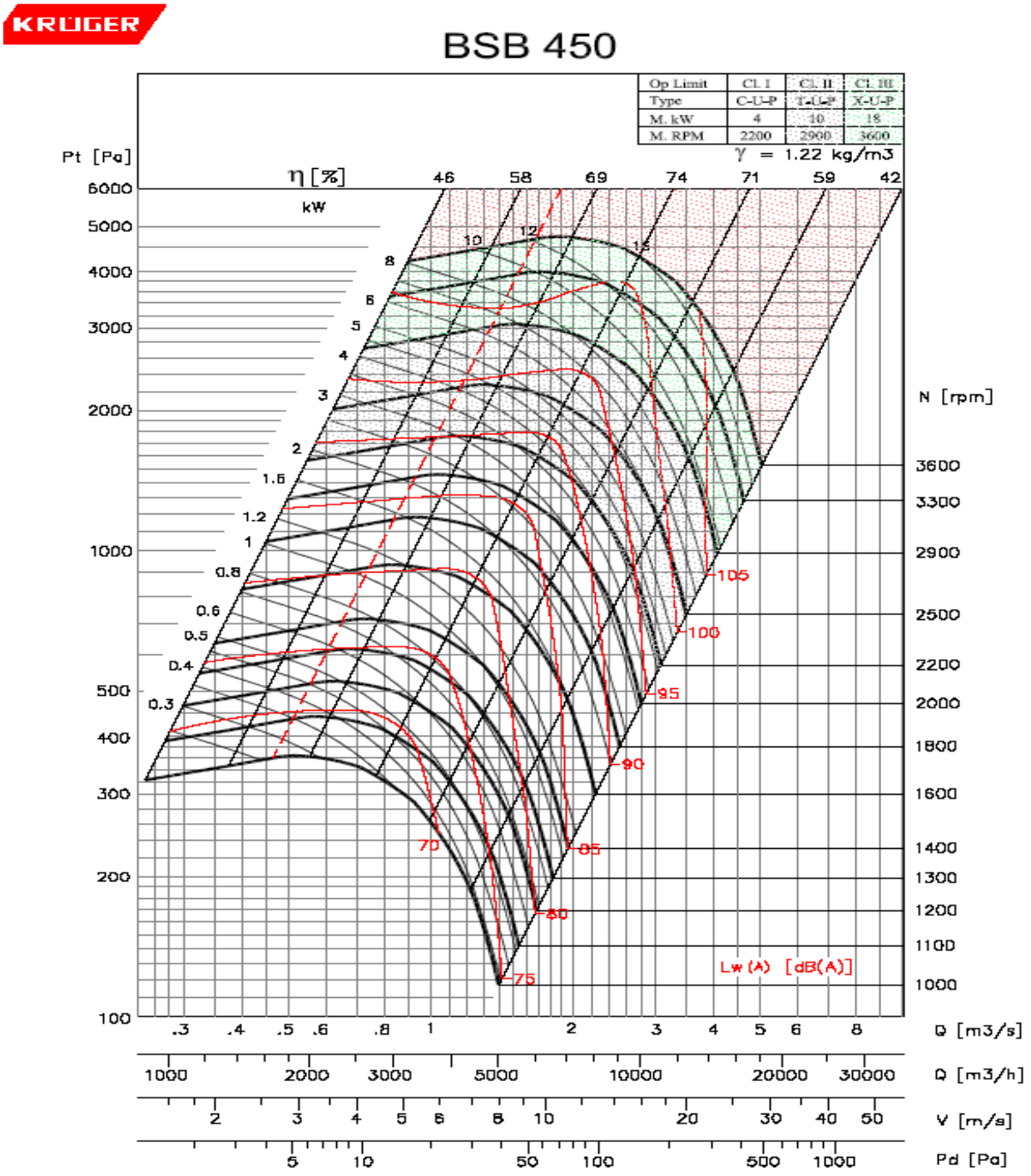
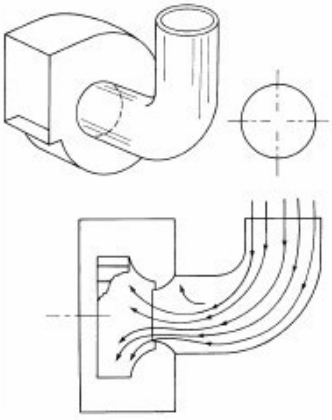


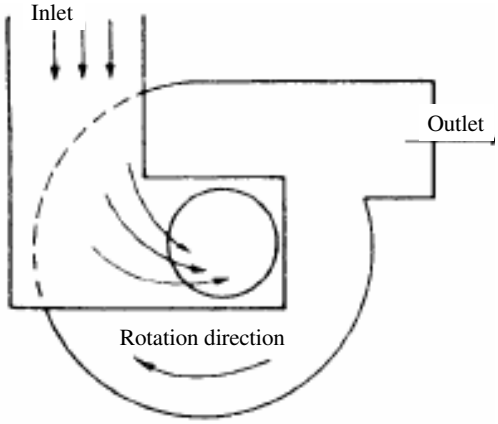
Figure 1.2 Fan Performance Curve

ATTENTION: The Singapore Copyright Act applies to the use of this document. Nanyang Technological University Library

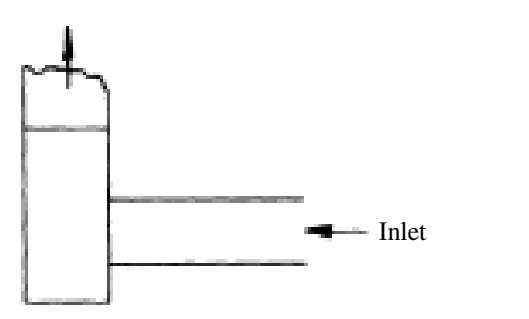
Based on Kruger Technical Bulletin [6], different inlet conditions can affect the difference in inlet loss of the centrifugal fan and is most critical and sensitive for surge. The different inlet conditions shown in Figure 1.3 will result in deviation from the setup of the laboratory test. Figure 1.3(a) shows non-uniform flow into suction of fan, which will cause inlet losses. This non-uniform flow will result in an uneven flow distribution entering the inlet and hence creating an inlet loss. The fan inlet swirl in Figure 1.3(b) will also cause additional inlet loss. This fan inlet swirl is caused by the difference in flow directions of the inlet flow and the rotation. In the case of straight inlet duct in Figure 1.3(c), the straight inlet duct will cause inlet pressure loss, as there is a sudden turn in the flow direction at the corner, which will result in the inlet pressure loss to be equal to 0.9 times of the inlet duct velocity head.



(a) Non-uniform flow into suction of fan



(b) Fan Inlet Swirl



Inlet pressure loss = 0.9x inlet duct velocity head

(c) Straight Inlet Duct Loss

Figure 1.3 Comparison between different types of fan inlet loss such as (a) non-uniform flow into suction of fan, (b) fan inlet swirl, (c) straight inlet duct loss.

ATTENTION: The Singapore Copyright Act applies to the use of this document. Nanyang Technological University Library

Hence, the actual performance of the fan is lower than the laboratory test results. It is possible to use adjustable blade angles to vary the fan performance according to Kruger Technical Bulletin [6]. This might result in an increase in efficiency by reducing the brake horsepower. As outlined in Braembussche [7] for the case for centrifugal compressors maximum gauge static pressure rise is achieved when a limited amount of stall is present. The influence of the overall diffuser gauge static pressure rise on the slope of the compressor performance curve to avoid surge is more important. Diffuser is the pipe extension from the outlet of the inlet fan. The diffuser plays a large role in achieving a static pressure rise. Its purpose is to convert flow kinetic energy leaving the impeller into a maximum rise in static pressure.

As outlined by Greitzer [8], surge occurs when the slope of the overall pressure rise curve exceeds a minimum positive value. Rotating stall or steady stall can proceed to surge, but they influence the surge limit mainly by changing the slope of the pressure rise curve. Hence, rotating stall has to be minimized. For both surge and stall, the flow is no longer axisymmetric but has a circumferentially non-uniform pattern rotating around the annulus. This is called rotating stall. Rotating stall is a mechanism that allows the compressor to adapt to the mass flow rate, which is insufficient. When there is insufficient air to fill in between the blade passages, rotating stall will occur.

According to Dean [9], all impellers, pressure losses are associated with flow separation along the blade surfaces. Boundary layer growth in the presence of decelerating velocities will cause separation and large mixing losses. Hence, to predict loss, it is useful to determine the velocity distributions on the impellers blades using a rapid approximation method developed by Stanitz and Prian [10]. In addition, Dean [9] states that losses within impeller may be subdivided into wall friction of impeller, leakage flow, secondary flow and mixing. However, such losses are found to be relatively small. Based on Hah and Reid [11], flow separation at blades is induced by the shock boundary layer interaction above 60 percent of the span. Below 60 percent of the span, a conventional adverse pressure gradient is the main cause of the flow separation. Baghdadi [12] states that rotor blade wakes do not affect the fan performance significantly because of the rapid mixing of the wakes. Hamrick [13] observes that the efficiency of a radial inlet centrifugal impeller is in general improved

ATTENTION: The Singapore Copyright Act applies to the use of this document. Nanyang Technological University Library

by reduction in tip clearance gap. Bindon [14] states that tip clearance loss is generally associated with the quantity of fluid leaking through the gap between blade and casing. Tip clearance loss varies linearly with gap size. It is suggested that the major part of the gap loss arises when the slow moving separation bubble flow is ejected from the low pressure zone in the gap by the high speed leakage jet which is induced at mid chord.

The scope of the current investigation is divided into two parts. The first part is to do flow simulation using high fidelity flow solver *FLUENT* [15]. Although there are many CFD packages such as the NUMECA and CFX, the *FLUENT* CFD package is chosen because it is widely used for a large number of industrial flow problems. Besides, there is no access to NUMECA and CFX at the Centre for Advanced Numerical Engineering Simulation laboratory in NTU. Many computational works have been done by others in the field of turbomachinery to gain insights for the improvement of fan performance. For example, Abidat et.al [16] has investigated the influence of volute inlet flow conditions on fan performance. Gu and Engeda [17] have discovered that the impeller exit flow pattern depends on the slope of the circumferential variation of the static pressure at the exit. The effect of blade and diffuser vane trimming on the performance characteristics of a single stage centrifugal compressor for a range of flows has been studied by Rodgers [18]. Jahnen et.al [19] has investigated the separate characteristics of the compressor stage, the rotor stage and the diffuser stage so that better understanding of the contribution to instabilities of each stage have been obtained. Kang and Kang [20] have performed study on stall inception in a high speed centrifugal compressor. They have discovered that small amplitude travelling wave is found in high speed centrifugal compressor as stall is approached. Traditionally, the Reynolds Averaged Navier Stokes simulation has been widely used for prediction of transitional flows in turbomachinery. However, Matsuura and Kato [21] have successfully applied large eddy simulation model for compressible transitional flows in a turbine cascade.

Insights gained from flow simulation results such as fan performace characteristics and effect of flow separation on fan performance would prove useful for design optimization. The second part of the project scope is to optimize fan performance. Design optimization problems such as the maximization of total efficiency using different design parameters,

ATTENTION: The Singapore Copyright Act applies to the use of this document. Nanyang Technological University Library

multi objective optimization and constrained optimization would be explored in the later chapters. Those design parameters which would affect flow separations would be chosen for optimization as they would most likely give room for more substantial increase in total efficiency. Some of the suggested design parameters such as inlet cone depth, blade angle, number of blades and blade off alignment angle are explored for design optimization because they have been known to have an impact on flow separation based on feedbacks from the turbomachinery industry. The operating range for the ventilation fan is based on volume flow rates. It is between 30 % and 80 % of the range of volume flow rates tested for the ventilation fan. This operating range is provided by the turbomachinery industry based on their experience on when surge will occur.

There are various optimization methods such as the genetic algorithm method [22] which has been used to optimize rotor blade design by minimizing flow loss manifested via entropy generation. There are also many other algorithms for optimization such as the Levenberg-Marquardt algorithm [23] which is an iterative technique widely used for nonlinear least squares problems. It is more global than the Gauss-Newton algorithm but tends to converge slower than the Gauss-Newton method. Some other optimization design approaches which have been done in research field include using an Euler code designed for computing the unsteady, three-dimensional flow for profanes in transonic flow [24] and using an integrated design system for radial turbine [25]. Hopfield and Tank [26] proposed the idea of using neural networks for optimization. Processing of information by neural networks is characteristically done in parallel rather than in series and hence it can still perform its overall function even if some of the neurons are not functioning. In other words it is less likely to fail. Another optimization method which has been widely used is simulated annealing which is invented by Kirkpatrick et.al [27]. Simulated annealing is a heuristic global optimization routine based on an iterative improvement strategy which allows for trial points to be accepted such that it results in a temporary decrease in goodness of solution. After reviewing the different optimization methods available, the gentic algorithm has been chosen. This is because genetic algorithm is a global optimization method. However, the computational cost of using genetic algorithm for design optimization problems are huge and hence design optimization based on high fidelity flow

ATTENTION: The Singapore Copyright Act applies to the use of this document. Nanyang Technological University Library

solver is not feasible. There are various ways to cut down the computational cost of genetic algorithm optimization. For example, Quagliarella and Vicini [28] have coupled genetic algorithms with gradient based optimization techniques so as to develop a hybrid technique for optimization which is both computational cheap and global. Chung and Alonso [29] have developed a multiobjective design framework by combining genetic algorithms with Kriging method [30]. Another technique to reduce the computational cost of the design optimization process has been developed here. It is reduced order modeling which has made it possible to obtain low dimensional approximations to the state. This allows integration into an overall design and or can be used for optimization purposes.

Many researches have been done in the field of turbomachinery optimization. Chand and Lee [31] created a unique elliptic hyperbolic grid generation method which is coupled to a Navier Stokes flow solver and numerical optimization algorithm to improve the designs of transonic turbine blades. Zangeneh et.al [32] has created a three dimensional inverse design method in turbomachinery blade shape optimization and has successfully applied it on the designs of radial impellers and the vaned diffuser. Kelner et.al [33] have coupled genetic algorithm with a flow parameterization method for multi objective optimization of pressure rise, loss factor and torque for blade shape optimization. Walker and Hesketh [34] have stated that the optimization of turbine blades is a compromise between aerodynamic factor, mechanical constraints and costs. Dennis [35] has successfully optimized the entire airfoil cascade shape by doing an automatic multi objective optimization of pressure loss, aerodynamic loading and the number of airfoils. After reviewing the works done by others in turbomachinery optimization, it can be concluded that this research field is usually focused on fan blade optimization.

According to Lippens et.al [36], all reduced order modeling methods can be classified as projection methods. Proper orthogonal decomposition is a powerful technique for model order reduction of linear and non linear systems and is based on Galerkin type discretization with basis functions created from the systems itself. According to Kahlbacher and Volkwein [37], it has been applied to estimation problems for scalar parameters in elliptic partial differential equations. In addition, proper orthogonal decomposition (POD) analysis can be

ATTENTION: The Singapore Copyright Act applies to the use of this document. Nanyang Technological University Library

used for blade optimization. POD analysis yields a set of empirical eigenfunctions, which describes the dominant behaviour or dynamics of given problem. This technique can be used for a variety of applications, including derivation of reduced-order dynamical models [38], steady analysis and design of inviscid airfoils [39], image processing [40], and pattern recognition [41]. Sirovich [42] introduces the method of snapshots as a way to efficiently determine the POD eigenfunctions for large problems. In particular, the method of snapshots has been widely applied to computational fluid dynamic (CFD) formulations to obtain reduced-order models for unsteady aerodynamic applications. A set of snapshots is obtained from a simulation of the CFD method. The POD process then computes a set of eigenfunctions from these snapshots, which is optimal in the sense that, for any given basis size, the error between the original and reconstructed data is minimized. Reduced-order models are derived by projecting the CFD model onto the reduced space spanned by the POD eigenfunctions. Bui-Thanh et.al [43] states that it is possible to combine the POD approach with a cubic spline interpolation to capture parametric variations or to use gappy POD for data reconstruction. In the optimization stage for this work, inverse design via POD method [43] can be applied on the blade geometry with constraint information provided by the industry. The inverse design shall find the optimized shape of blade geometry which give the highest gauge total pressure at the outlet and hence a higher efficiency. The method of POD snapshots with interpolation is used to reduce the computational cost of the design optimization by estimating the input for the objective functions.

Figure 1.4 shows the project overview. To design complex configurations, time integration of high fidelity models with CFD is prohibitively expensive owing to the large number of degrees of freedom in the problem. Reduced order modeling is particularly feasible in the design process as it allows computational cost to be greatly reduced in orders of magnitude while still maintaining solution accuracy. Proper orthogonal decomposition is the reduced order modeling technique that has been applied in this project. POD interpolation method provides the inputs of total pressure at the outlet for the formulation of the objective function. The objective function is minimized using genetic algorithm as the optimization method of choice because it is able to find the global optimum without gradient information.

ATTENTION: The Singapore Copyright Act applies to the use of this document. Nanyang Technological University Library

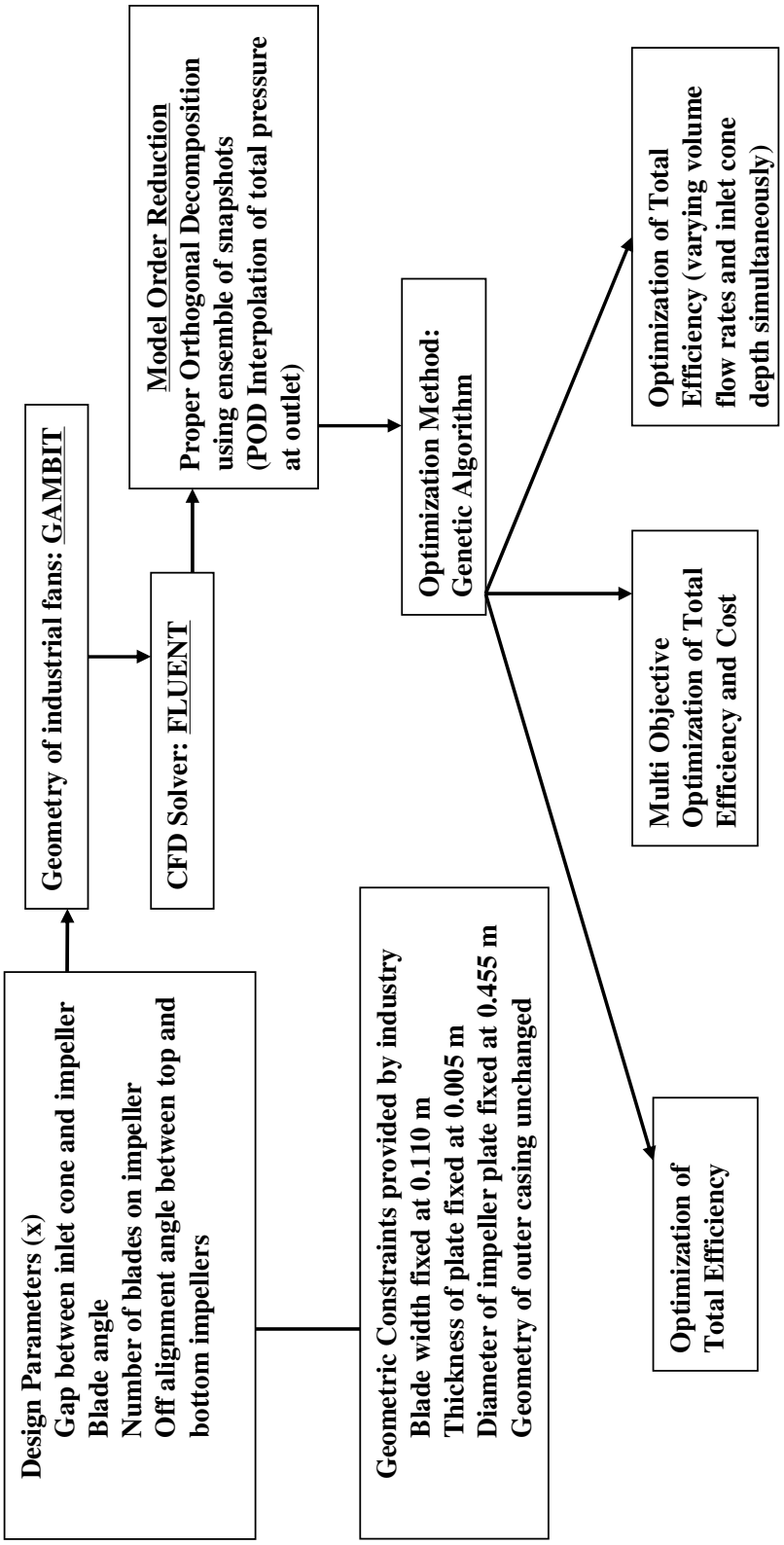


Figure 1.4 Overview of Research Project

ATTENTION: The Singapore Copyright Act applies to the use of this document. Nanyang Technological University Library

1.1 Operational Characteristics of Turbomachinery

1.1.1 Basic Concepts about Centrifugal Fan

Figure 1.5 shows a typical example of a centrifugal fan designed by Dysprosia [44], which has the flow inlet in the direction perpendicular to the figure. The blades are attached to the cylindrical shaft, which is rotated at a certain rpm. The centrifugal fan has an impeller that consists of a central shaft about which a set of blades form a spiral pattern. Centrifugal fans blow air at right angles to the inlet of the fan, and spin centrifugally the air outwards to the outlet. An impeller rotates, causing air to enter the fan near the shaft and move perpendicularly from the shaft to the opening in the scroll-shaped fan casing. Bleier [45] states that a centrifugal fan produces more gauge static pressure than axial-flow fans of the same impeller diameter and the same running speed because of the additional centrifugal force which is missing in axial-flow fans. Since in centrifugal fans the airfoil lift contributes only a small portion of the pressure produced while most of it is produced by centrifugal action, the improvement due to airfoil blades over single-thickness, backward-curved sheet metal blades is not as pronounced in centrifugal fans as it is in axial-flow fans.

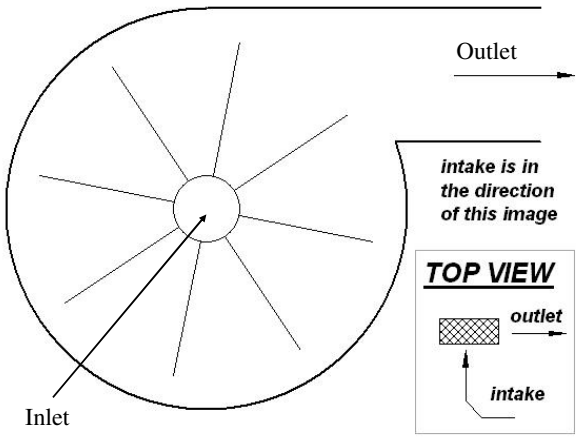


Figure1.5 Centrifugal Fan (Cross sectional view)

ATTENTION: The Singapore Copyright Act applies to the use of this document. Nanyang Technological University Library

For any fan, the minimum pressure occurs at the centre of rotation of the impeller plate and the maximum pressure occurs just at the outlet side of the impeller. This means the rotating plate will have a low-pressure region while the outlet will have a high-pressure region. If the impeller is not rotating and the pressure differential existed, flow will be from high-pressure region to low-pressure region which is opposite from the direction air normally flows inside a centrifugal fan. Hence, the only thing that keeps the air flowing in the proper direction is the rotation of the blades.

Dawes [46] states that the flow in high speed, high performance centrifugal compressor rotors is dominated by the so called jet-wake phenomenon. High rates of diffusion, especially in the nearly radial part of the rotor, lead to enhanced boundary layer growth which in many cases leads to separation of the blade suction surface boundary layers. This separated region is fed by strong secondary flows and a pronounced wake region forms around the suction surface. The wake blockage displaces the bulk flow away from the suction side to form a jet region near the pressure side of the blade passage. The formation of jet-wake phenomenon restricts the pressure rise of the impeller and thus generates losses.

1.1.2 Basic Concepts about Fan Surge and Rotating Stall

When a compressor is running at constant speed, the outlet pressure is increased as the mass flow rate decreased. A point is to be reached eventually such that the pressure rise is the maximum and further reduction in volume flow rate will lead to abrupt change in flow pattern in the compressor. Beyond that point, the compressor will either stall or surge. Figure 1.6 shows the plot of pressure ratio against volume flow rate. The red line represents static instability when the system is under surging. Pressure increases as volume flow rate decreases until it reaches the surge point and after which the pressure drops drastically. The point of instability is the surge point and locus of these points for different rotational speed is the surge line. Toyama et.al [47] define surge as the flow breakdown period during unstable operation. For both surge and stall, the flow is no longer axisymmetric but has a circumferentially non-uniform pattern rotating around the annulus. This is called rotating stall. Kenny [48] proposes two models for the initiation of surge, which are the attainment of a limiting value of static pressure rise from the tip of the impeller to the throat of the inlet

ATTENTION: The Singapore Copyright Act applies to the use of this document. Nanyang Technological University Library

and the attainment of zero skin friction coefficients on the sidewalls of the inlet region. Rotating stall as shown in Figure 1.7 is a mechanism that allows the compressor to adapt to the volume flow rate, which is insufficient. When there is insufficient air to fill in between the blade passages, rotating stall occurs. The flow is shared unequally such that some blade passages have large flow rate and some very little flow rate. Hence, there is circumferentially non-uniform flow. The overall volume flow rate remains constant but the local volume flow rate varies as the rotating cell passes the point. The stall cells always rotate in the direction of the rotor. Blockage caused by the stall cells region leads to a reduction in the blade incidence on one side and an increase in the other. The blade with increased incidence stalls. Stall runs in the direction in which the incidence is increased. For a rotor row, it means that the stall cells moves backward relative to the rotor. The rotation of the stall cells is in the same sense as the rotor but at a greatly reduced speed. Centrifugal compressor operates with axisymmetric stall near the inducer tips. It is not critical to the centrifugal fan to experience rotating stall as it is a common phenomenon. However, fan surge is critical to the centrifugal fan because it would affect the fan performance drastically.

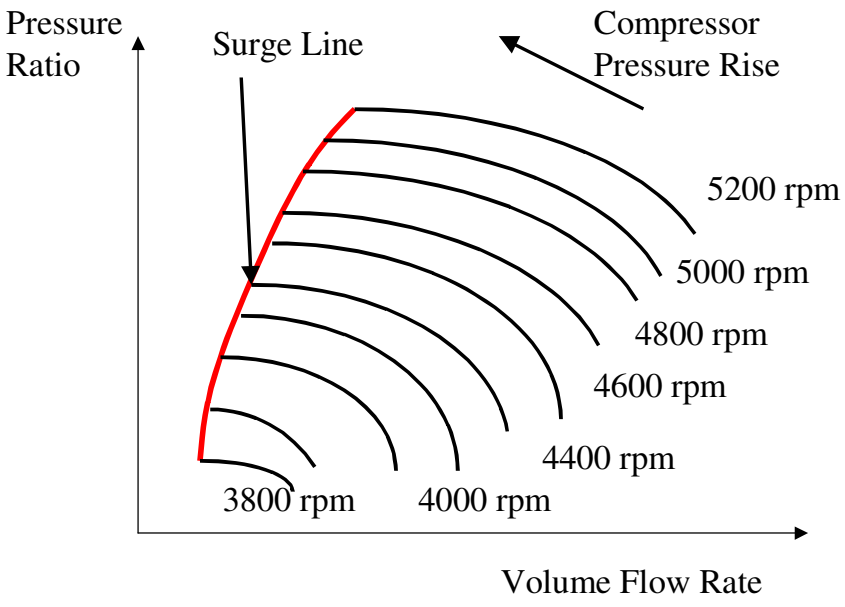


Figure1.6 Fan Surge

ATTENTION: The Singapore Copyright Act applies to the use of this document. Nanyang Technological University Library

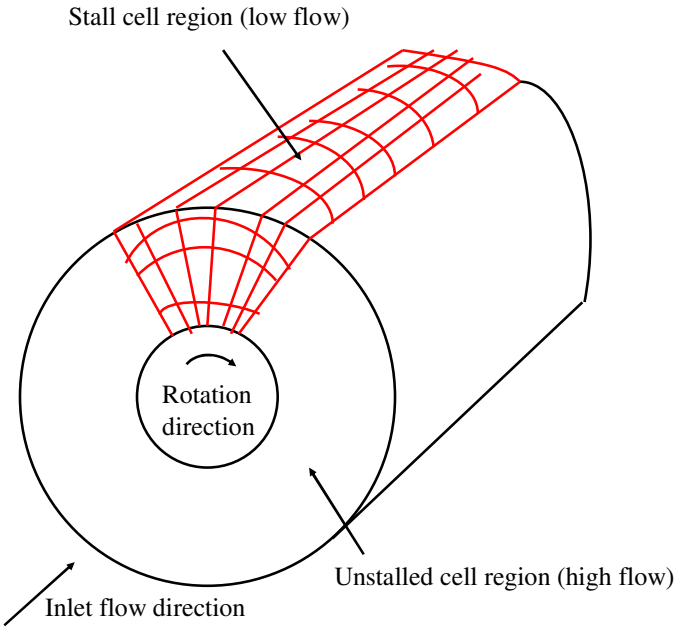


Figure1.7 Rotating Stall

1.1.3 Fan Laws and Dimensionless Coefficients

It is impractical to test the performance of every size of fan in manufacturer's range at all speeds, which it may be applied. It is possible to use fan laws to predict with good accuracy the performance of a fan at other speeds and densities than those in the original rating test. The fan laws [45] as shown in Equation (1.1) are used to calculate change in flow rate, pressure and power of a fan when the size, speed or air density changed. The fan laws are derived assuming that the fan performance is independent of Reynolds number. However, it has been established that fan performance is not independent of Reynolds number due to Reynolds number effect. The Reynolds number effect can only be disregarded when the fan is tested above the threshold Reynolds number and all calculated performance ratings are at or above this threshold Reynolds number.

ATTENTION: The Singapore Copyright Act applies to the use of this document. Nanyang Technological University Library

$$Q_2 = Q_1 \times \left(\frac{N_2}{N_1}\right) \times \left(\frac{D_2}{D_1}\right)^3 \tag{1.1a}$$

$$P_2 = P_1 \times \left(\frac{N_2}{N_1}\right)^2 \times \left(\frac{D_2}{D_1}\right)^2 \times \left(\frac{\rho_2}{\rho_1}\right) \tag{1.1b}$$

$$W_2 = W_1 \times \left(\frac{N_2}{N_1}\right)^3 \times \left(\frac{D_2}{D_1}\right)^5 \times \left(\frac{\rho_2}{\rho_1}\right) \tag{1.1c}$$

where Q is exhaust volume flow rate in m^3/s, P is pressure in Pa, ρ is fluid density in kg/m^3, N is fan speed in rpm, D is impeller diameter in m, W is impeller power in watt. Note that N_1 is fan speed in prototype and N_2 is fan speed in the model.

Equation (1.2) is non-dimensional parameters that characterize fan performance.

$$\text{Power coefficient} = C_W = \frac{W}{\rho\omega^3 D^5} \tag{1.2a}$$

$$\text{Head coefficient} = C_H = \frac{P_d}{\rho\omega^2 D^2} \tag{1.2b}$$

$$\text{Flow rate coefficient} = C_Q = \frac{Q}{\omega D^3} \tag{1.2c}$$

$$\text{Reynolds number} = Re = \frac{\rho\omega D^2}{\mu} \tag{1.2d}$$

$$\text{Total efficiency} = \eta_t = \frac{P_T Q}{W} \tag{1.2e}$$

where Q is exhaust volume flow rate in m^3/s, W is power in watt, ρ is fluid density in kg/m^3, D is impeller diameter in m, ω is rotational speed in rad/s, μ is fluid viscosity, P_d is pressure change in Pa, P_T is gauge total pressure in Pa.

ATTENTION: The Singapore Copyright Act applies to the use of this document. Nanyang Technological University Library

1.2 Objective and Scope

By modifying the fan components such as blade shape design, blade angle and the gap between inlet cone and impeller, a fan of better performance based on higher efficiency can be designed. However, the geometrical component for modification and the degree of adjustment are often unknown and trial and error testing waste too much time and money in the design process. Hence, the objective is to simulate fan performance through the use of computational fluid dynamics software so as to remove redundant fan fabrication during the fan design stage. Thus, it helps to speed up the design cycle, thus saving cost and time. Computational flow analysis using sliding meshes with rotating zonal grids will be used to simulate the internal flow inside both single and double inlet fan for different design and operating conditions specified by the industry. Simulation results will be compared with experimental results provided by the industry. Results will be used for fan design studies to improve fan performance. The design of fan blade configurations for optimizing performance characteristics will be based on Proper orthogonal decomposition (POD) analysis to determine optimal fan blade configurations from bases obtained by flow simulation is the ultimate goal of this project. POD analysis yields a set of empirical eigenfunctions, which describes the dominant behaviour or dynamics of given problem. Optimization of total efficiency, constrained optimization and multi objective optimization will been done using genetic algorithm with inputs from the proper orthogonal decomposition snapshots taken at variation of the design parameters. A two parameters optimization will be done by varying volume flow rates and inlet cone depth simultaneously. The aim is to cut down the computational cost for genetic algorithm optimization by using a reduced order modeling technique known as proper orthogonal decomposition interpolation method. In the POD method, the high fidelity solver is used only to generate an ensemble of snapshots. These snapshots are used to create POD modes which describe the dominant behaviour of a given problem. They are then combined with interpolation methods to estimate the population sample of the genetic algorithm. POD interpolation provides the inputs for the formulation of objective function to be minimized using genetic algorithm optimization method.

ATTENTION: The Singapore Copyright Act applies to the use of this document. Nanyang Technological University Library

The scope is to study the fluid flow characteristics of both the single inlet fan and double inlet fan rotating under steady state condition. Sliding mesh model will be used to find the fluid flow characteristics of the fan. Transient analysis of the fan in which the rotating velocity decreased linearly with time will also be studied. The design optimization method of choice is genetic algorithm. Reduced order modelling will be used to cut down computational cost of design optimization.

The geometry of the single inlet fan and double inlet fan and their surface representation using CAD modelling are outlined in Chapter 2. The grid generation techniques are also described in the same chapter. In Chapter 3, the basic governing equations in the integral form, finite volume method, sliding mesh, initial conditions, boundary conditions and turbulence models are outlined. Results and discussion for flow simulation of single inlet fan and double inlet fan are described in the same chapter. A transient flow analysis has also been done for the single inlet fan. However, transient flow analysis has not been done for the double inlet fan because a transient flow analysis of the single inlet fan is good enough to analyze the effect of reducing rpm with time. Fan performance characteristics and flow fields are described in that chapter. Chapter 4 explains the concept of reduced order modeling, proper orthogonal decomposition, genetic algorithm and the methodology to formulate the objective function for optimization of total efficiency, constrained optimization and multi objective optimization. Results and discussion pertaining to this proper orthogonal decomposition analysis results are described in that chapter. Inverse design of gauge total pressure profile at the fan outlet has been done using proper orthogonal decomposition interpolation as a reduced order modeling technique. Different optimization problems with different objective functions such as multi objective optimization, constrained optimization and optimization using two design parameters are described in that chapter too. Chapter 5 concludes the investigation and outlines possible future wotk that can be done.

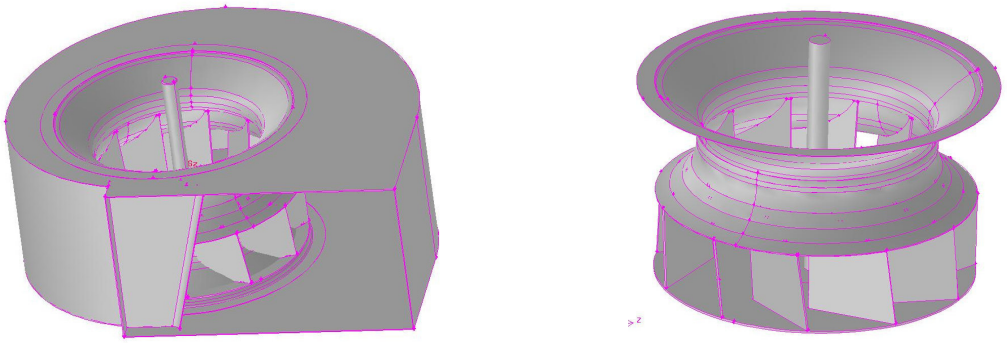
ATTENTION: The Singapore Copyright Act applies to the use of this document. Nanyang Technological University Library

CHAPTER 2
GRID GENERATION

The first step in the numerical simulation of the flow is to generate the mesh for the geometry of the ventilation fans. A typical geometry of a ventilation fan includes inlet cone, impeller, shaft and the outer casing as shown in Figure 2.1(a). It is important to generate a good structured mesh, as it is a major factor in the accuracy of the flow simulation results. This section will describe briefly how hexagonal structured meshes are generated.

2.1 Geometry of Fans

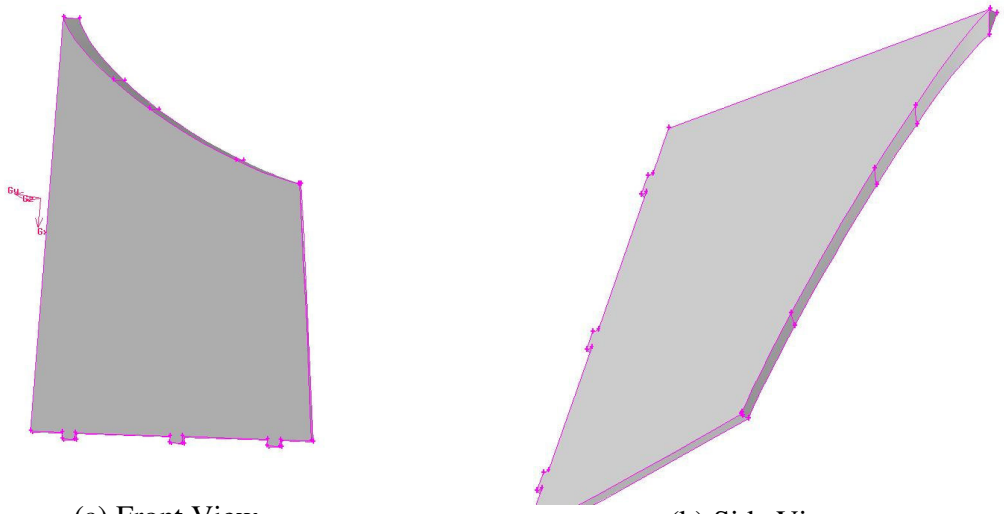
The geometry of the entire single inlet fan is as shown in Figure 2.1(a). Figure 2.1(b) shows the geometry of this single inlet fan without the outer casing. The geometries are given by the industries in parasolid format and imported into Gambit software. The geometry of the blade is an integral part of the ventilation fan as it is a major factor of fan performance characteristics. Figure 2.2 shows the geometrical shape of a blade, which is the same for both single inlet fan and double inlet fan. It is noted that since the blades have single thickness, the geometrical shape of this blade can be improved to minimize flow separation. The single inlet fan has 11 blades on one impeller plate arranged in equal distance. Figure 2.3(a) shows the impeller plate for the single inlet fan with 11 blades as numbered accordingly. Note that the blade numbering in this report follows Figure 2.3(a). Figure 2.3(b) shows the 3 dimensional view of the impeller plate.



(a) With outer casing (b) Without outer casing

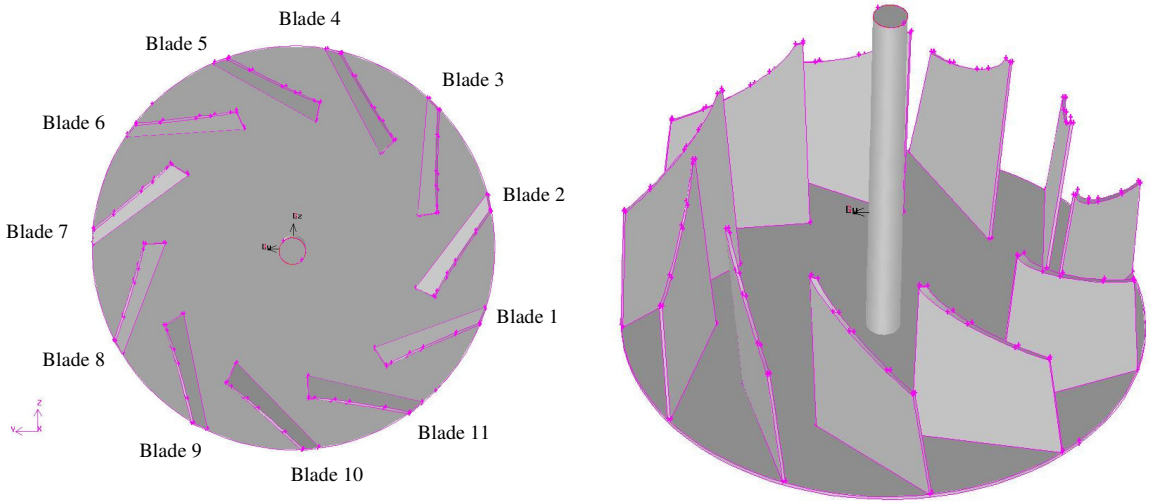
Figure 2.1 Geometry of single inlet fan (a) with outer casing and (b) without outer casing

ATTENTION: The Singapore Copyright Act applies to the use of this document. Nanyang Technological University Library



(a) Front View (b) Side View

Figure 2.2 Geometry of blade (for both single inlet fan and double inlet fan) in different view such as (a) Front View and (b) Side View

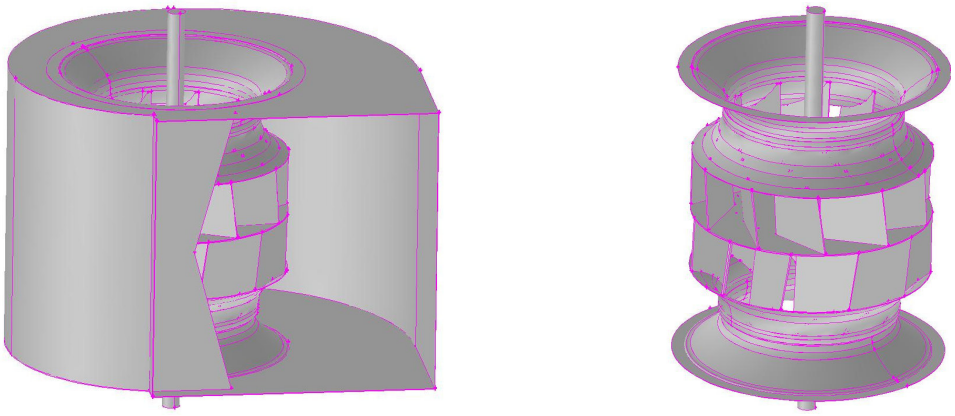


(a) 2-Dimensional View (b) 3-Dimensional View

Figure 2.3 Geometry of impeller plate with blades in (a) 2-Dimensional View and (b) 3-D dimensional view for single inlet fan

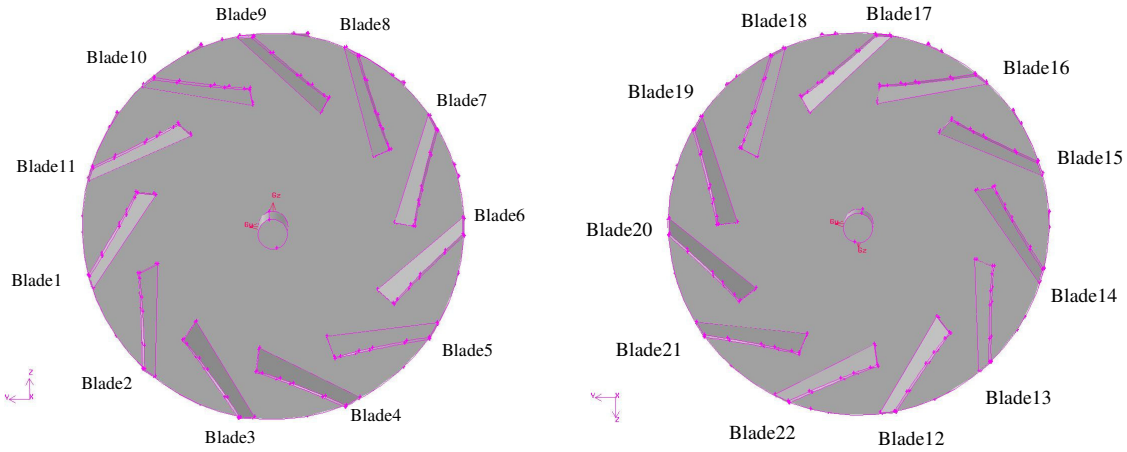
ATTENTION: The Singapore Copyright Act applies to the use of this document. Nanyang Technological University Library

Figure 2.4(a) and Figure 2.4(b) show the geometry of the double inlet fan with and without outer casing respectively. The double inlet fan has 22 blades on two impeller plates. The number of blades has been decided by experimental test done by the industries. Figure 2.5(a) shows the top impeller plate for the double inlet fan with 11 blades as numbered accordingly. Figure 2.5(b) shows the bottom impeller plate for the double inlet fan with another set of 11 blades as numbered accordingly. With such an impeller, it is possible to use structured mesh for grid generation for both the single inlet fan and the double inlet fan. Figure 2.6 shows the 3 dimensional view of the impeller for the double inlet fan.



(a) With outer casing (b) Without outer casing

Figure 2.4 Geometry of double inlet fan (a) with outer casing and (b) without outer casing



(a) Top plate (b) Bottom plate

Figure 2.5 Geometry of impeller plate with blades in 2-Dimensional View for (a) top plate and (b) bottom plate for double inlet fan

ATTENTION: The Singapore Copyright Act applies to the use of this document. Nanyang Technological University Library

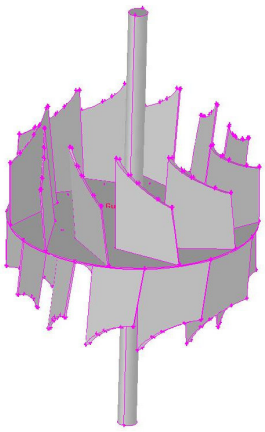
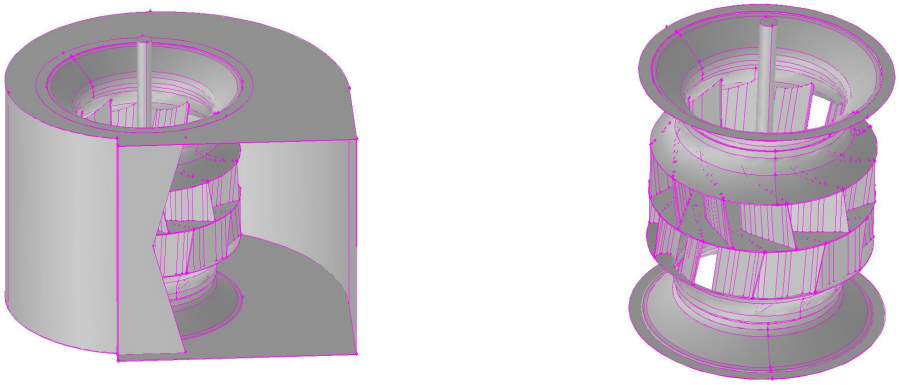


Figure 2.6 Geometry of impeller plate with blades in 3-Dimensional View for double inlet fan

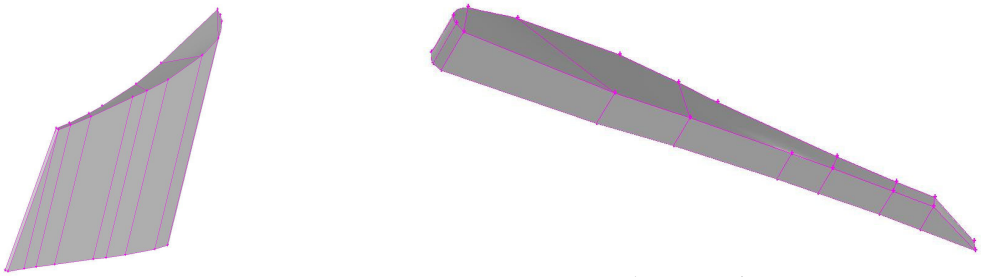
Figure 2.7(a) and Figure 2.7(b) show the geometry of the airfoil bladed fan with and without outer casing respectively. The geometry of the double inlet fan and the airfoil bladed fan is exactly the same except that the airfoil bladed fan has airfoil blades instead of single thickness blades. Figure 2.8 shows the geometrical shape of an airfoil blade for the airfoil bladed fan. The airfoil bladed fan has 22 blades on two impeller plates. Figure 2.9(a) shows the top impeller plate for the airfoil bladed fan with 11 blades as numbered accordingly. Figure 2.9(b) shows the bottom impeller plate for the airfoil bladed fan with another set of 11 blades as numbered accordingly. With such an impeller, it is possible to use structured mesh for grid generation for the airfoil bladed fan. Figure 2.10 shows the 3 dimensional view of the impeller for the airfoil bladed fan.



(a) With outer casing (b) Without outer casing

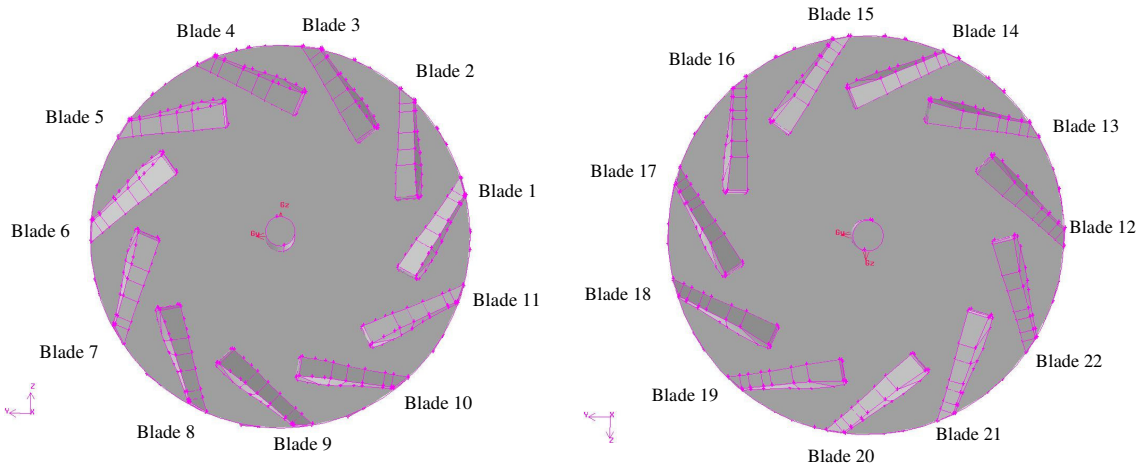
Figure 2.7 Geometry of airfoil bladed fan (a) with outer casing and (b) without outer casing

ATTENTION: The Singapore Copyright Act applies to the use of this document. Nanyang Technological University Library



(a) 3-Dimensional view (b) Top view

Figure 2.8 Airfoil blade shape in (a) 3-Dimensional view and (b) top view



(a) Top plate (b) Bottom plate

Figure 2.9 Geometry of impeller plate with blades in 2-Dimensional View for (a) top plate and (b) bottom plate for airfoil bladed fan

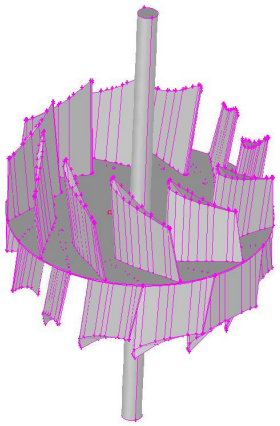


Figure 2.10 Geometry of impeller without impeller casing in 3-Dimensional View for airfoil bladed fan

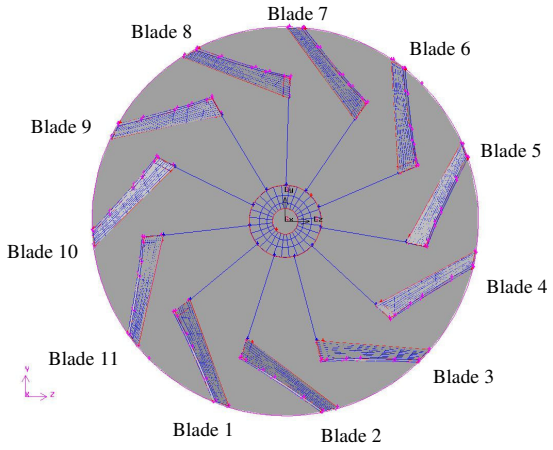
ATTENTION: The Singapore Copyright Act applies to the use of this document. Nanyang Technological University Library

2.2 Grid Generation

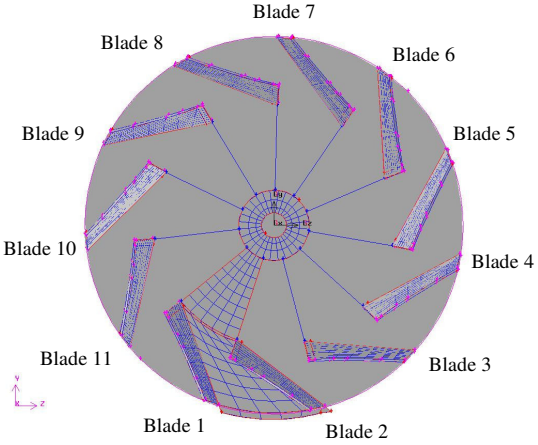
Roth and Peikert [49] state that for turbomachinery problem, structured meshes are advisable. Structured mesh has been used for the grid generation of both the single inlet fan and the double inlet fan. Since each blade are arranged at equal angle 32.7° with adjacent blades, the impeller plate is divided into 11 sections and numbered as shown in Figure 2.11(a). One of the sections is meshed with quadrilateral face mesh as shown in Figure 2.11(b). Using Cooper scheme, the quadrilateral volume mesh for one section as shown in Figure 2.11(c) is created by projecting the quadrilateral face mesh upwards. This volume mesh for one section is copied and rotated about the X-axis to create structured volume mesh for the impeller plate as shown in Figure 2.11(d).

Sliding mesh model which involves cell zones sliding relative to one another along the grid interface will be used for numerical flow simulation. Figure 2.12 shows the volume mesh of ventilation fan from the top view with interface between the blue and grey fluid zones as shown. The purple coloured fluid zone and the blue coloured fluid zones for the impeller are rotating about the X-axis with the rotation velocity. The grey coloured fluid zone is set to be stationary. Casey [50] states that the common best practice advice is to have the computational domain covering the region upstream and downstream of the blade stages as shown in Figure 2.12. Finer mesh at the blade passages and coarser mesh at the stationary zone away from the blade passage are used. According to Casey [50], in order to resolve the turbulence boundary layer accurately using the wall function approach, the near wall mesh need to have a y^+ value below 20 and 200. Figure 2.13(a) shows the structured face meshes on impeller with blades. Figure 2.13(b) and Figure 2.13(c) show the structured face meshes of the inlet cone and impeller in 2 dimensional and 3 dimensional views respectively. Figure 2.13(d) shows the structured face meshes on the outer casing. Structured volume meshes are created for the single inlet fan and double inlet fan as shown in Figure 2.14(a) and Figure 2.14(b) respectively. There are 154589 mesh elements for the single inlet fan. There are 285347 mesh elements for the double inlet fan. The quality of the mesh has been examined. Note that there is a pipe extension from the outlet of the inlet fan which allows the flow to reach fully developed flow.

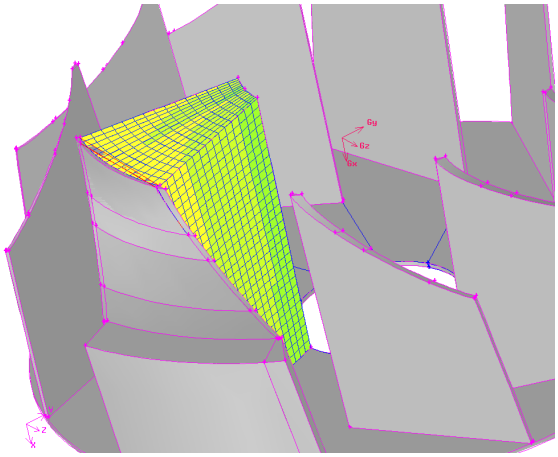
ATTENTION: The Singapore Copyright Act applies to the use of this document. Nanyang Technological University Library



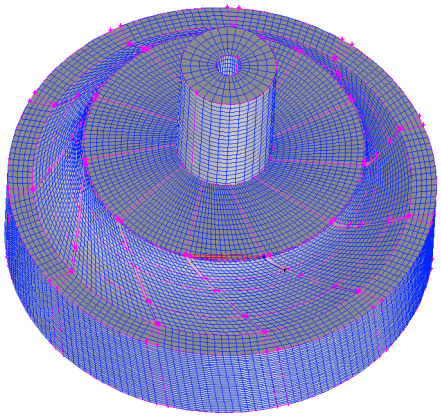
(a) Division of impeller plate into 11 sections



(b) Quadrilateral face mesh for one section



(c) Quadrilateral volume mesh for one section



(d) Completed volume mesh for impeller

Figure 2.11 Steps in creating volume mesh for impeller plate which includes (a) Division of impeller plate into 11 sections, (b) Quadrilateral face mesh for one section, (c) Quadrilateral volume mesh for one section and (d) Completed volume mesh for impeller

ATTENTION: The Singapore Copyright Act applies to the use of this document. Nanyang Technological University Library

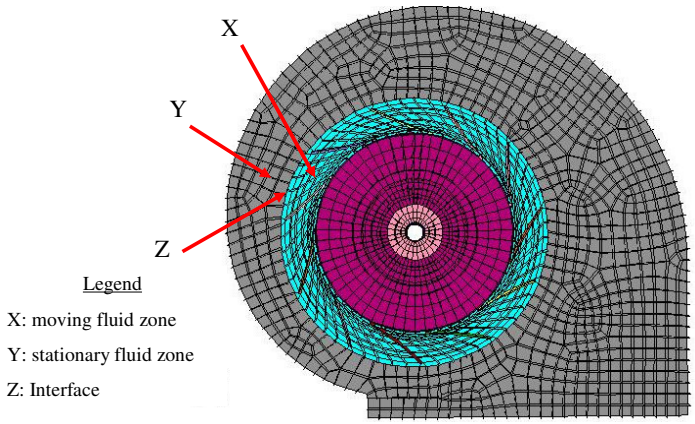
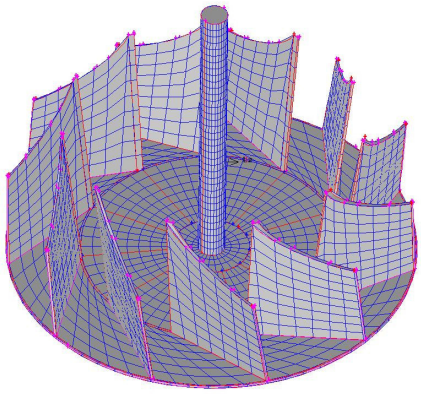
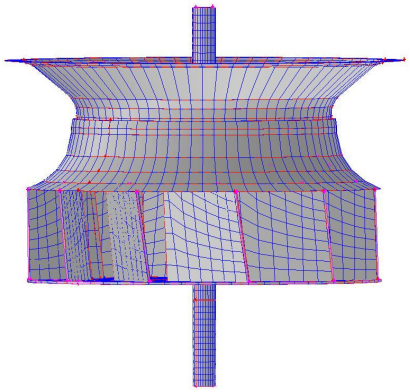


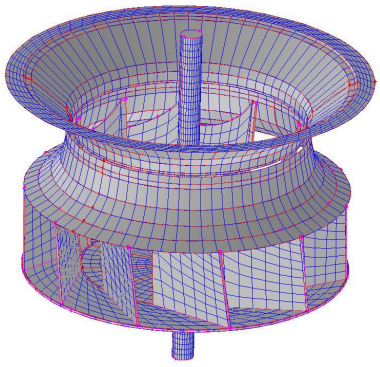
Figure 2.12 Interface between fluid zones looking from top view



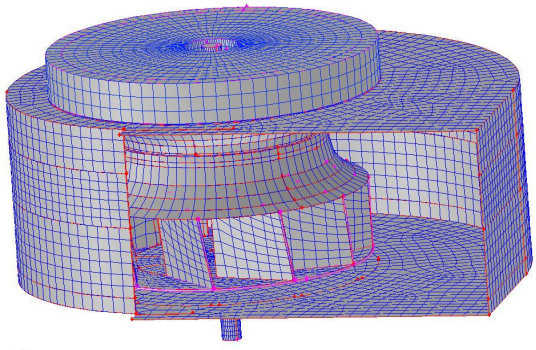
(a) Impeller with blades



(b) Inlet cone and impeller in 2 D view



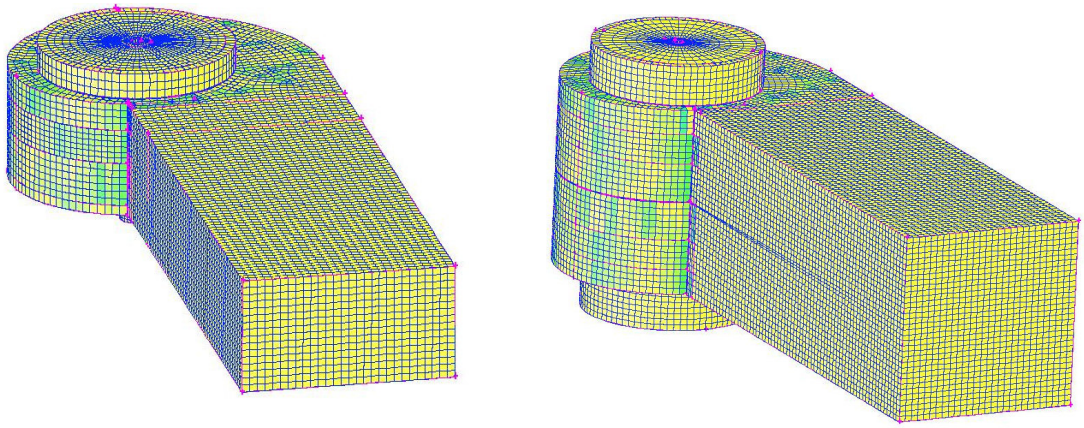
(c) Inlet cone and impeller in 3 D view



(d) Outer casing

Figure 2.13 Face mesh on (a) impeller with blades, (b) inlet cone and impeller in 2-Dimensional View, (c) inlet cone and impeller casing in 3-Dimensional view and (d) outer casing

ATTENTION: The Singapore Copyright Act applies to the use of this document. Nanyang Technological University Library



(a) Volume mesh for single inlet fan (b) Volume mesh for double inlet fan

Figure 2.14 Volume Mesh for (a) single inlet fan and (b) double inlet fan with extended pipe

ATTENTION: The Singapore Copyright Act applies to the use of this document. Nanyang Technological University Library

CHAPTER 3
NUMERICAL FLOW MODELLING IN AN INDUSTRIAL VENTILATION FAN

3.1 Basic Governing Equations

The momentum variables and continuity variables are the outputs from CFD. Principles of conservation of mass, conservation of momentum and conservation of energy are used. CFD used numerical techniques to divide the domain into cells known as "control volumes". Discretised governing partial differential equations are applied on each cell. Large numbers of highly non-linear algebraic equations are obtained. The equations are solved by iterative method. The outputs will be the momentum variables, continuity variables after iteration, satisfying the convergence criterion. The residual plot shows the outputs of CFD.

Initialization means the introduction a guess at the gauge static pressure at the pressure inlet boundary. With this guess, the discretised momentum equation can be solved to yield intermediate velocity field, then the continuity equation in the form of pressure correction equation can be solved, then correct pressure and velocity, then solve all discretised transport equations for scalars variables, and then repeat until all fields converged.

According to Versteeg and Malalasekera [51], for conservation of mass, the rate of increase of mass in fluid element is equal to the net rate of flow of mass into fluid element.

This yields the continuity equation in integral form for rotating reference frame:

$$\frac{\partial}{\partial t}\iiint_{\Omega} \rho d\Omega + \iiint_{\Omega} \nabla \cdot \left(\rho \vec{V}_r\right) d\Omega = 0 \tag{3.1}$$

For incompressible fluid, the density ρ is constant and the continuity equation becomes:

$$\iiint_{\Omega} \nabla \cdot \left(\vec{V}_r\right) d\Omega = 0 \tag{3.2}$$

ATTENTION: The Singapore Copyright Act applies to the use of this document. Nanyang Technological University Library

Newton's second law states that the rate of change of momentum of fluid particle equals the sum of forces of fluid particle. The momentum equation is found by setting the rate of change of momentum of the fluid particle equal to the total force in the direction on the element due to surface stresses plus the rate of increase of momentum due to sources. Source terms $\vec{S}_M$ include contributions due to body forces such as gravitational forces.

The momentum equation for rotating reference frame:

$$\frac{\partial}{\partial t}\iiint_{\Omega}(\rho\vec{V})d\Omega + \oiint_{S}\left[\vec{V}(\rho\vec{V}_r) - \tau\right]\cdot d\vec{S} + \iiint_{\Omega}\rho(\vec{\omega}\times\vec{V}) = \iiint_{\Omega}\vec{S}_M\,d\Omega - \oiint_{S}(p)d\vec{S} \tag{3.3}$$

The stress tensor is $\tau = \begin{bmatrix} \tau_{11} & \tau_{12} & \tau_{13} \\ \tau_{21} & \tau_{22} & \tau_{23} \\ \tau_{31} & \tau_{32} & \tau_{33} \end{bmatrix}$. $\vec{\omega}$ is the angular velocity of the rotating frame. $\vec{V}_r$ is the relative velocity vector. $\vec{V}$ is the absolute velocity vector and they are related by $\vec{V}_r = \vec{V} - (\vec{\omega}\times\vec{V})$. Versteeg and Malalasekera [51] states that the energy equation is derived from the first law of thermodynamics, which states that the rate of change of energy of a fluid particle is equal to the rate of heat addition to the fluid particle plus the rate of work done on the particle. τ_1, τ_2, τ_3, are the first, second and third components of the stress tensor respectively.

The energy equation:

$$\frac{\partial}{\partial t}\iiint_{\Omega}(\rho E)d\Omega + \oiint_{S}\left[\vec{V}(\rho E + p)\right]d\vec{S} = \iiint_{\Omega}\nabla\cdot(K\nabla T)d\Omega + \iiint_{\Omega}\nabla\cdot(u\cdot\tau)d\Omega + \iiint_{\Omega}S_e\,d\Omega \tag{3.4}$$

The energy equation (3.4) is used only when the flows involve compressibility and heat transfer. Since the flow is assumed to be incompressible and does not involve heat transfer, only the momentum equation and continuity equation are required. Hence, the energy equation is not applicable. K is thermal conductivity. The momentum variables and continuity variables are the outputs from CFD. Principles of conservation of mass, conservation of momentum and conservation of energy are used. CFD used numerical techniques to divide the domain into cells known as "control volumes". Discretised

ATTENTION: The Singapore Copyright Act applies to the use of this document. Nanyang Technological University Library

governing partial differential equations are applied on each cell. Large numbers of highly non-linear algebraic equations are obtained. The equations are solved by iterative method. The outputs are the momentum variables, continuity variables after iteration, satisfying the convergence criterion.

3.2 Finite Volume Method

3.2.1 Overview of Numerical Scheme

The governing integral equations for the conservation of mass and momentum, and (when appropriate) for energy and other scalars such as turbulence and chemical species are solved using *FLUENT*. Based on *FLUENT* 6.1 User's Guide [15], in both cases a control-volume-based technique is used that consists of firstly, the division of the domain into discrete control volumes using a computational grid. This is followed by integration of the governing equations on the individual control volumes to construct algebraic equations for the discrete dependent variables such as velocities, pressure, temperature, and conserved scalars. Lastly, there is linearization of the discretized equations and solution of the resultant linear equation system to yield updated values of the dependent variables.

3.2.2 Discretization of Transient Convection-Diffusion Equation

Based on Versteeg and Malalasekera [51], the control volume method is applied and discretization of Equation (3.2) and Equation (3.3) on a given cell yields

$$a_p\varphi_p = a_w\varphi_w + a_E\varphi_E + a_S\varphi_S + a_N\varphi_N + a_B\varphi_B + a_T\varphi_T + \frac{\rho_p^0 \Delta V}{\Delta t}\varphi_p^0 + S_u \tag{3.5}$$

$$\text{where } a_p = a_w + a_E + a_S + a_N + a_B + a_T + \frac{\rho_p^0 \Delta V}{\Delta t} + \Delta F - S_p \tag{3.6}$$

where $S_u + S_P\varphi_p$ is the linearised source.

Note that a_w, a_E, a_S, a_N, a_B and a_T are the neighbouring coefficients in three dimensions for the control volume.

ATTENTION: The Singapore Copyright Act applies to the use of this document. Nanyang Technological University Library

3.2.3 Segregated Solver

As governing equations are non-linear and coupled, several iterations of the solution loop must be performed before a converged solution is obtained. According to user guide of the common solver used here, each iteration steps consists of the steps illustrated in Fig 3.1. Firstly, fluid properties are updated based on the current solution. This will be followed by the solving of *u, v*, and *w* momentum equations in turn using current values for pressure and face mass fluxes, in order to update the velocity field. Since the velocities obtained in Step 2 may not satisfy the continuity equation locally, a Poisson-type equation for the pressure correction is derived from the continuity equation and the linearized momentum equations. This pressure correction equation is then solved to obtain the necessary corrections to the pressure and velocity fields and the face mass fluxes such that continuity is satisfied. Where appropriate, equations for scalars such as turbulence, energy, species, and radiation are solved using the previously updated values of the other variables. When interphase coupling is to be included, the source terms in the appropriate continuous phase equations may be updated with a discrete phase trajectory calculation. A check for convergence of the equation set is made. These steps are continued until the convergence criteria are met.

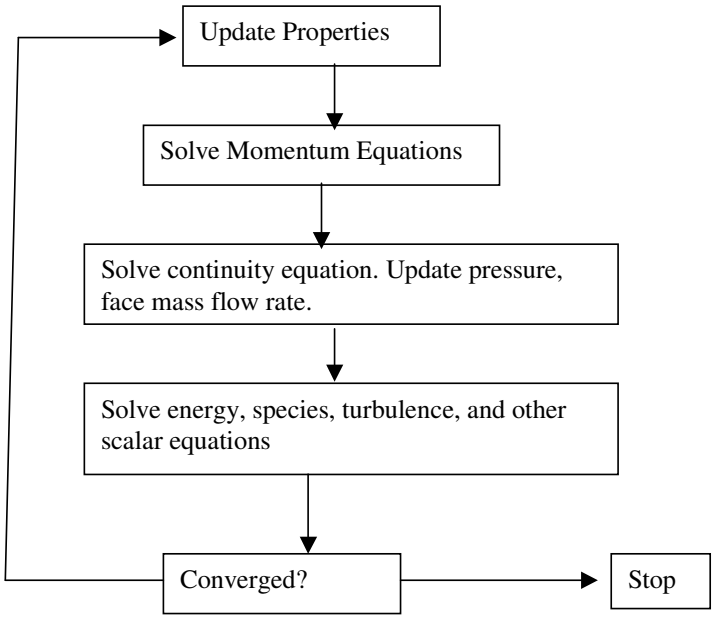


Figure 3.1 Overview of the Segregated Solution Method

ATTENTION: The Singapore Copyright Act applies to the use of this document. Nanyang Technological University Library

3.2.4 Discretization of the Momentum Equation in Segregated Solver

The discretization scheme described in section 3.2.2 for a scalar transport equation is also used to discretize the momentum equations. For example, the x-momentum equation can be obtained by setting $\Phi = u$ according to user guide of the common solver used here:

$$a_p u = \sum a_{nb} u_{nb} + \sum p_f A i + S \tag{3.7}$$

If the pressure field and face mass fluxes are known, the above equation can be solved in the manner outlined in section 3.2.2, and a velocity field obtained. However, the pressure field and face mass fluxes are not known a priori and must be obtained as a part of the solution. There are important issues with respect to the storage of pressure and the discretization of the pressure gradient term; these are addressed next. Since *FLUENT* uses a co-located scheme, whereby pressure and velocity are both stored at cell centres. However, the discretized momentum equation requires the value of the pressure at the face between two cells. Hence, an interpolation scheme is required to compute the face values of pressure from the cell values.

3.2.5 Discretization of the Continuity Equation in Segregated Solver

According to user guide of the common solver used here, Equation (3.5) may be integrated over the control volume to yield the following discrete equation:

$$\sum J_f A_f = 0 \tag{3.8}$$

where J_f is the mass flux through face f.

As described in section 3.2.1 the momentum and continuity equations are solved sequentially. In this sequential procedure, the continuity equation is used as an equation for pressure. However, pressure does not appear explicitly in above equation for incompressible flows, since density is not directly related to pressure.

ATTENTION: The Singapore Copyright Act applies to the use of this document. Nanyang Technological University Library

The upwind scheme is either forward difference or backward difference depending on whether the node is upstream or downstream. In the first order upwind scheme, the node will interpolate from one node upstream or downstream. In 2nd order scheme, the node will interpolate from two nodes upstream or downstream. A smaller numerical viscosity is obtained when the 2nd order scheme is used. With a smaller numerical viscosity, the result is more accurate but it may be unstable. This is especially true for higher order scheme in which the leading error is contributed by dispersion which leads to instability. The central difference scheme is essentially 2nd order. It has a lower dissipation than the 2nd order upwind scheme and the central difference scheme can be applied for large eddy simulation for higher accuracy. However, since it has a very low numerical viscosity, there may be instability problem and in fact there are researches in adding how much artificial viscosity to the central difference scheme to stabilize it without compromising too much accuracy. The QUICK scheme is a weighted average of central difference scheme and 2nd order upwind scheme.

The present scheme uses a 2nd order upwind method to discretize the convective term in the Navier-Stokes equations. This discretization adds implicitly some amount of artificial viscosity and hence artificial viscosity is present by default. It is not practical to estimate the amount of artificial viscosity needed for a general three dimensional flow problem. However, the artificial viscosity generated has stabilized the flow since there are no discontinuities in the fluid. Accuracy is not impaired as flow simulation result obtained with this 2nd order upwind scheme is accurate when compared with experimental result.

3.2.6 Implicit vs. Explicit

In both the segregated and coupled solution methods the discrete, non-linear governing equations are linearized to produce a system of equations for the dependent variables in every computational cell. According to user guide of the common solver used here, the resultant linear system is then solved to yield an updated flow-field solution.

For the case of implicit solver, a given variable, the unknown value in each cell is computed using a relation that includes both existing and unknown values from neighbouring cells.

ATTENTION: The Singapore Copyright Act applies to the use of this document. Nanyang Technological University Library

Each unknown will appear in more than one equation in the system, and these equations must be solved simultaneously to give the unknown quantities.

For the case of explicit solver, a given variable, the unknown value in each cell is computed using a relation that includes only existing values. Each unknown will appear in only one equation in the system and the equations for the unknown value in each cell can be solved one at a time to give the unknown quantities.

In the segregated solution method each discrete governing equation is linearized implicitly with respect to that equation's dependent variable. This will result in a system of linear equations with one equation for each cell in the domain. In summary, the segregated approach solves for a single variable field by considering all cells at the same time. It then solves for the next variable field by again considering all cells at the same time, and so on. There is no explicit option for the segregated solver.

In the coupled solution method there is a choice of using either an implicit or explicit linearization of the governing equations. This choice applies only to the coupled set of governing equations. Governing equations for additional scalars that are solved segregated from the coupled set, such as for turbulence, radiation, etc., are linearized and solved implicitly using the same procedures as in the segregated solution method.

If implicit option of the coupled solver is chosen, each equation in the coupled set of governing equations is linearized implicitly with respect to all dependent variables in the set. This will result in a system of linear equations with N equations for each cell in the domain, where N is the number of coupled equations in the set. Linearization of the coupled continuity, x-, y-, z-momentum, and energy equation set will produce a system of equations in which p, u, v, w, and T are the unknowns. Simultaneous solution of this equation system (using the block AMG solver) yields at once updated pressure, u-, v-, w-velocity, and temperature fields. In summary, the coupled implicit approach solves for all variables (p, u, v, w, T) in all cells at the same time.

When the explicit option of the coupled solver is chosen, then each equation in the coupled set of governing equations is linearized explicitly. As in the implicit option, this too will

ATTENTION: The Singapore Copyright Act applies to the use of this document. Nanyang Technological University Library

result in a system of equations with N equations for each cell in the domain. And likewise, all dependent variables in the set will be updated at once. However, this system of equations is explicit in the unknown dependent variables. The x-momentum equation is written such that the updated x velocity is a function of existing values of the field variables. Hence a linear equation solver is not needed. In summary, the coupled explicit approach solves for all variables (p, u, v, w, T) one cell at a time.

The segregated solver traditionally has been used for incompressible and mildly compressible flows. The coupled approach, on the other hand, is originally designed for high-speed compressible flows.

3.2.7 Sliding Mesh

The sliding mesh model is the most accurate method for simulating flow in rotating reference frames. According to *FLUENT* 6.1 User's Guide [15], the sliding mesh model allows adjacent grids to slide relative to one another. In doing so, the grid faces do not need to be aligned on the grid interface. This situation requires a means of computing the flux across the two non-conformal interface zones of each grid interface. To compute the interface flux, the intersection between the interface zones is determined at each new time step. The resulting intersection produces one interior zone (a zone with fluid cells on both sides) and one or more periodic zones. If the problem is not periodic, the intersection produces one interior zone and a pair of wall zones as shown in Figure 3.2. The resultant interior zone corresponds to where the two interface zones overlap; the resultant periodic zone corresponds to where they do not. The number of faces in these intersection zones will vary as the interface zones move relative to one another. Principally, fluxes across the grid interface are computed using the faces resulting from the intersection of the two interface zones, rather than from the interface zone faces themselves. For flows in rotating domains, the equation for conservation of mass, or continuity equation, can be written as follows for both the absolute and the relative velocity formulations is as shown below where v_r is the relative velocity and v is the absolute velocity and ω is the angular velocity of the rotating frame and r is the position vector in the rotating frame.

ATTENTION: The Singapore Copyright Act applies to the use of this document. Nanyang Technological University Library

$$v_r = v - (\omega r) \tag{3.9}$$

$$\frac{\partial \rho}{\partial t} + div(\rho v_r) = S_M \tag{3.10}$$

Note that since the ventilation fan is rotating in a relatively large domain, the absolute velocity formulation is preferred. The relative velocity formulation is appropriate when most of the fluid in the domain is rotating.

The problem has to be set up with a rotating reference frame for the moving fluid zones first before starting the sliding mesh model. In the rotating reference frame (moving reference frame), the rotational velocity in radian/second has been input. Figure 3.3 and Figure 3.4 show that the blades walls and impeller walls are set as moving walls but the rotating velocity is zero relative to adjacent fluid zone. Figure 3.3 shows that fluid zone 2 is stationary, while fluid zone 1 is sliding with the prescribed rotational velocity. The impeller wall is set as moving wall but its rotation velocity relative to fluid zone 1 is zero. Figure 3.4 shows that the shaft wall and blade wall are set as moving walls but their rotation velocities are zero relative to adjacent fluid zones B and A respectively. Fluid zones A and B are rotating with prescribed rotation velocity. The moving fluid zones which are attached to the blade walls and impeller are set to a certain rotation velocity in radian/second with the rotation axis origin at coordinate point (0,0,0). Figure 3.5 shows the interface between the moving fluid zones and the stationary fluid zones. The rotation axis has been set to be 1 of *X* component. With this rotation axis, the blades walls and impeller will rotate clockwise with respect to the outlet in the direction as shown in Figure 3.6 and expels air towards the outlet.

After the solution has converged for the moving reference frame under steady state flow, the sliding mesh model is started to get a cyclic solution for the ventilation fan until steady state convergence is reached. This is done by changing the moving fluid zones motion types from moving reference frame to moving mesh motion types without changing the rotation velocity magnitude. The unsteady solver is activated and a suitable time step is selected.

ATTENTION: The Singapore Copyright Act applies to the use of this document. Nanyang Technological University Library

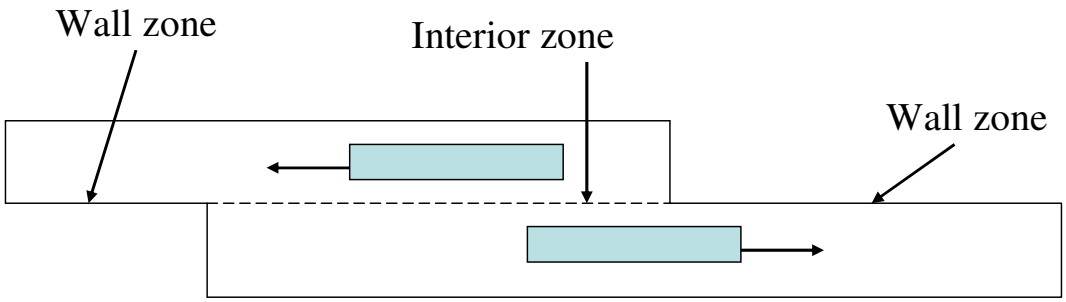


Figure 3.2 Zones created by Interface Interaction

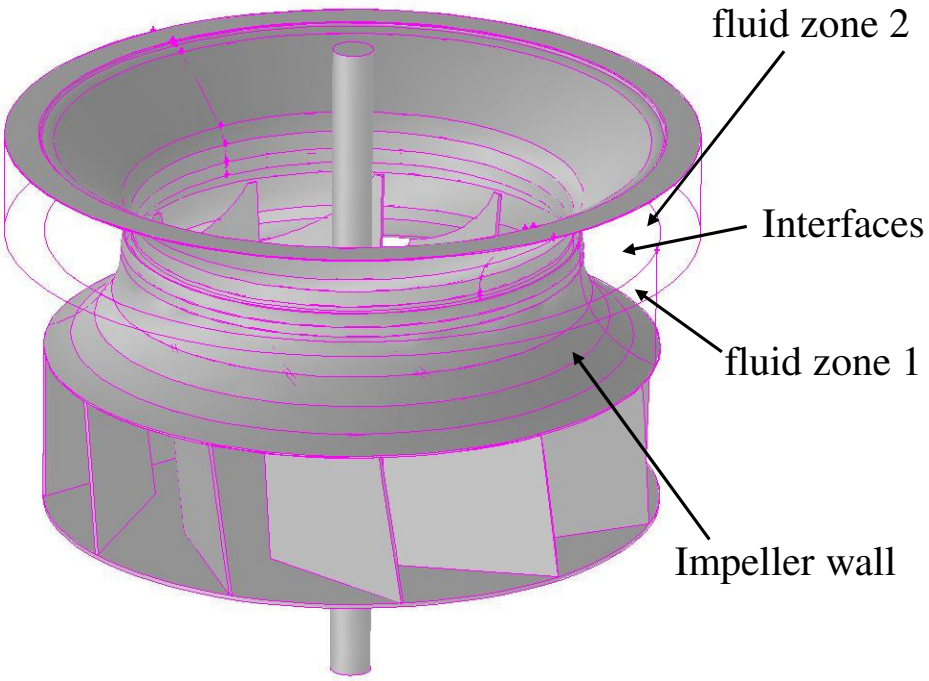


Figure 3.3 Sliding fluid zones attached to impeller wall

ATTENTION: The Singapore Copyright Act applies to the use of this document. Nanyang Technological University Library

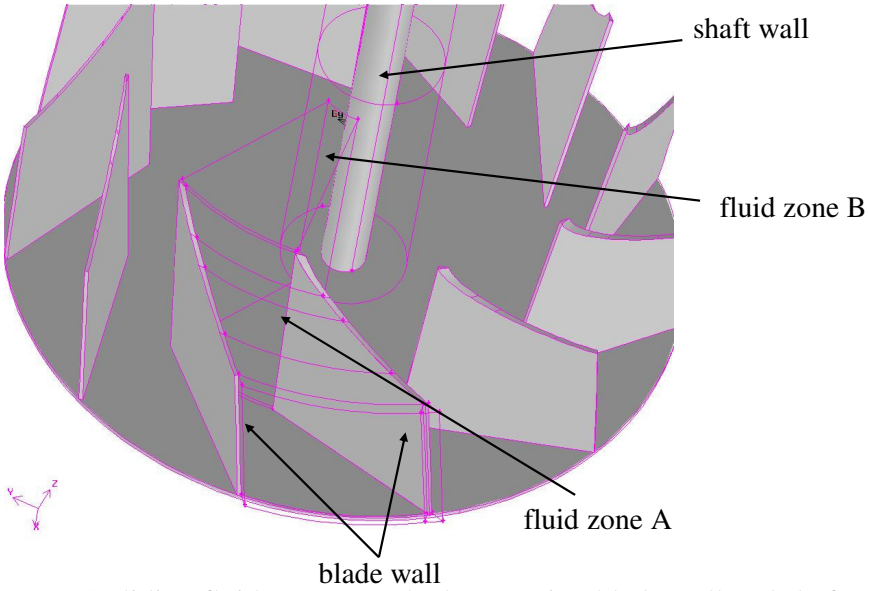


Figure 3.4 Sliding fluid zones attached to rotating blade wall and shaft wall

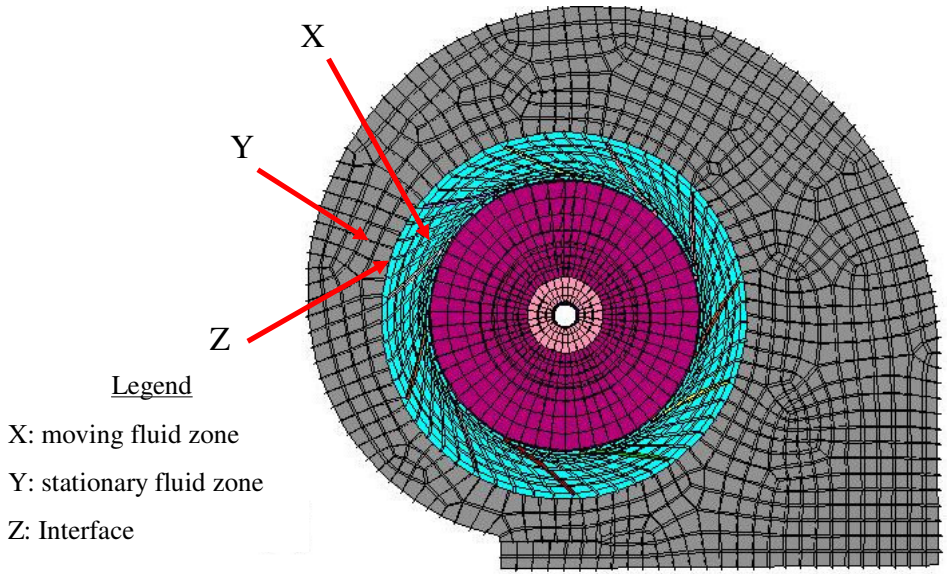
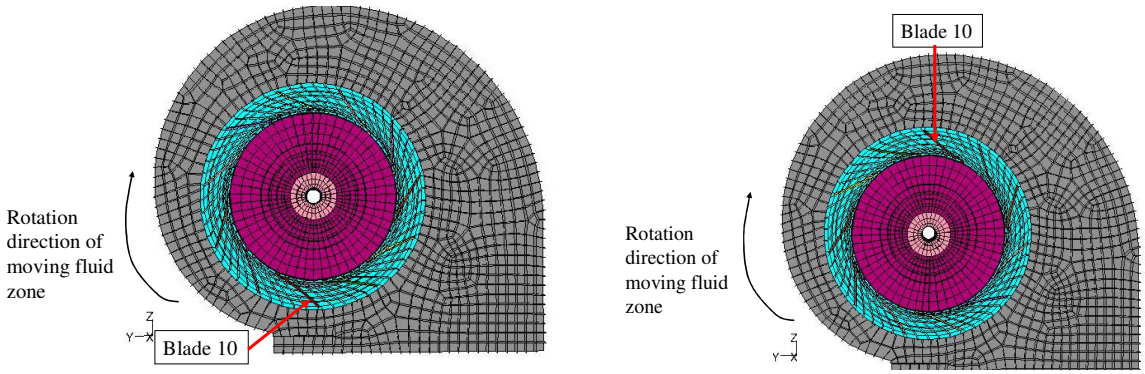


Figure 3.5 Interface between fluid zones looking from top view

ATTENTION: The Singapore Copyright Act applies to the use of this document. Nanyang Technological University Library



(a) Time 1 T (b) Time 1.5 T

Figure 3.6 Comparison between moving fluid zones at different periods of (a) time 1 T and (b) time 1.5 T

3.3 Initial and Boundary Conditions

3.3.1 Pressure Inlet Condition

The area of the outlet of the single inlet fan is 0.172142m^2. The area of the inlet of the single inlet fan is 0.206792m^2. The area of the outlet of the double inlet fan is 0.318886m^2. The area of the inlet of the double inlet fan is 0.2065m^2 for each of the two inlets. The volume flow rate extracted from the fan has been fixed by inputting the gauge static pressure at the pressure inlet boundary. The stagnation pressure at the outlet is an unknown. Since the inlet is exposed to atmospheric air, the inlet has gauge total pressure 0 Pa. Using Bernoulli equation, as shown in Equation (3.11); the gauge static pressure at inlet for a certain volume flow rate is calculated and inputted at the pressure inlet boundary.

$$P = P_T - \frac{\rho v^2}{2} \tag{3.11}$$

where P is the gauge static pressure at inlet in Pa, P_T is the gauge total pressure at inlet in Pa, ρ is the density of air at 1.22kg/m^3, v is the velocity at the inlet in m/s obtained by dividing the volume flow rate by the total inlet area.

ATTENTION: The Singapore Copyright Act applies to the use of this document. Nanyang Technological University Library

3.3.2 Operating Pressure and Gauge Pressure

The absolute pressure is the sum of the gauge pressure and operating pressure. The operating pressure is significant for incompressible ideal gas law and low Mach number compressible flow. To set up a suitable operating pressure, the criteria are based on the Mach-number regime of the flow and the relationship that is used to determine density. A table to illustrate how to set up the operating pressure is shown in Figure 3.7.

Density Relationship	Mach Number Regime	Operating Pressure
Ideal Gas Law	M > 0.1	0 or ≈ Mean flow pressure
	M < 0.1	≈ Mean flow pressure
Profile Function of Temperature	Incompressible	Not used
Constant	Incompressible	Not used
Incompressible Ideal gas Law	Incompressible	≈ Mean flow pressure

Figure 3.7 Recommended Setting of Operating Pressure

For turbomachinery problems, the flow is incompressible and hence the operating pressure is set to be approximate to the mean flow pressure. Note that the operating pressure approximate to mean flow pressure has been specified as atmospheric pressure at a reference location of (-0.222, 0, 0.2318851) which is a point on the face of the pressure inlet layer for the single inlet fan. For the double inlet fan, the operating pressure is specified as atmospheric pressure at a reference location of (-0.4049951, 0.1639675, 0.1639675) which is a point on the face of the pressure inlet layer for the double inlet fan. Note that all static pressures and dynamic pressures are given as gauge pressure.

3.3.3 Selection of Time Step Size

For turbomachinery problems, a suitable time step size is selected such that the cyclic behaviour of the ventilation fan is captured within each time step. The unsteady solution will exhibit a cyclic behaviour after the initial start up phase has passed. It takes several revolutions of the rotor before the solution reaches steady state convergence. A suitable time step size Δt is chosen such that $\frac{60}{N} \times \frac{1}{n}$ where N is the rotation velocity of the fan in

ATTENTION: The Singapore Copyright Act applies to the use of this document. Nanyang Technological University Library

rpm and n is the number of time steps needed to complete one complete revolution of the fan. n is taken as 100 in this case. Since there are 11 blades on each impeller plate, the time step size is sufficient to obtain flow simulation to study the time lapse between the rotations of a blade from one position to another blade position. For a problem of 2500 rpm, the time step sizes for unsteady state iteration and mesh motion are both 2.4×10^{-4} seconds. The corresponding Reynolds numbers has been obtained by $\frac{\rho\omega D^2}{\mu}$ where μ is the viscosity using μ is 1.86×10^{-5} Ns/m^2; D is 0.455m, ω is the rotational velocity in rad/s. ρ is 1.22 kg/m^3. The reference length is the diameter of the impeller plate as shown in Figure 3.8, which is equal to 0.455m. The reference temperature is 304 Kelvin. The reference density is 1.22 kg/m^3. The reference pressure is atmospheric pressure at 0 gauge pressure.

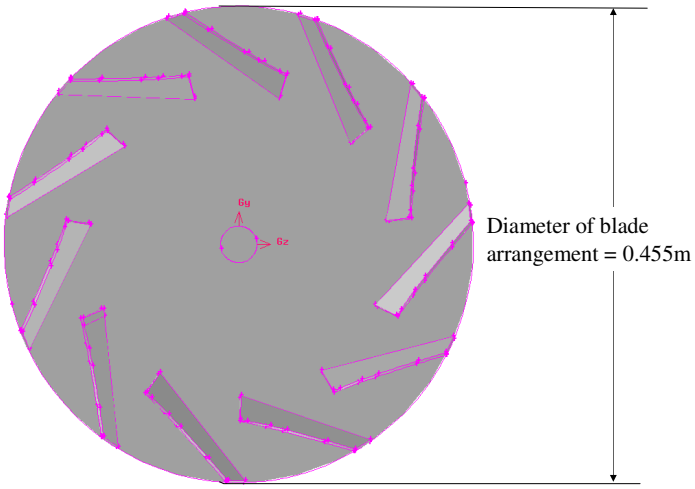


Figure 3.8 Diameter of impeller plate

The flow is incompressible, so the energy equation is not applicable. Since segregated solver traditionally has been used for incompressible and mildly compressible flows, the segregated solver has been selected. Since the realizable k –ε model produces non-physical turbulent viscosities in situations when the computational domain contains both rotating and stationary fluid zones which are sliding meshes, it is not advisable to use realizable k –ε model for sliding mesh model and hence the standard k –ε model has been selected. The inputs for pressure inlet boundaries are computed as in section 3.3.1. The inputs for

ATTENTION: The Singapore Copyright Act applies to the use of this document. Nanyang Technological University Library

operating pressure and gauge pressure have been computed as in section 3.3.2. Rotation velocity of moving fluid zones has been input as in section 3.2.7 for rotating case. The solution has been initialized and solved.

3.4 Turbulence Models

Based on the Reynolds number calculation in section 3.3.3, for a case of 2500 rpm, the Reynolds number is 3.55×10^{6} which is higher than the critical Reynolds number around 1×10^{5} and hence the flow is turbulent. The reference length is the impeller diameter, which is 0.455 m; hence, turbulence model has to be used. Various turbulence models based on the Reynolds Averaged Navier Stokes simulationm have been used to check the effect of different turbulence models on flow simulation results. These turbulence models include the standard $k-\varepsilon$ model, the realizable $k-\varepsilon$ model, the standard $k-\omega$ model and the Reynolds Stress model. Hence, modelled transport equations for the different turbulence models are provided in this section.

3.4.1 The Standard k –ε Model

The two transport equations, one for the turbulent kinetic energy k as in Equation (3.12a) and one for the rate of dissipation of turbulent kinetic energy ε as in Equation (3.12b) are solved. The modelled transport equations for K and ε in the standard $k-\varepsilon$ model are

$$\frac{\partial(\rho k)}{\partial t}+\frac{\partial\left(\rho k u_i\right)}{\partial x_i}=\frac{\partial}{\partial x_j}\left[\left(\mu+\frac{\mu_t}{\sigma_k}\right)\frac{\partial k}{\partial x_j}\right]+G_k+G_b-\rho\varepsilon-Y_M+S_K \tag{3.12a}$$

$$\frac{\partial(\rho\varepsilon)}{\partial t}+\frac{\partial\left(\rho\varepsilon u_i\right)}{\partial x_i}=\frac{\partial}{\partial x_j}\left[\left(\mu+\frac{\mu_t}{\sigma_\varepsilon}\right)\frac{\partial k}{\partial x_j}\right]+C_{1\varepsilon}\left(\frac{\varepsilon}{k}\right)\left[G_k+C_{3\varepsilon}G_b\right]- C_{2\varepsilon}\frac{\rho\varepsilon^2}{k}+S_\varepsilon \tag{3.12b}$$

ATTENTION: The Singapore Copyright Act applies to the use of this document. Nanyang Technological University Library

G_k represents the generation of turbulence kinetic energy due to the mean velocity gradients. G_b is the generation of turbulence kinetic energy due to buoyancy. Y_M represents the contribution of the fluctuating dilatation in compressible turbulence to the overall dissipation rate. $C_{1\varepsilon}$, $C_{2\varepsilon}$ and $C_{3\varepsilon}$ are constants. σ_k and σ_ε are the turbulent Prandtl numbers for k and ε respectively. S_K and S_ε are user-defined source terms.

The eddy viscosity is computed from

$$\mu_t = \rho C_\mu \left(\frac{k^2}{\varepsilon} \right) \tag{3.13}$$

The model constants are $C_{1\varepsilon} = 1.44$, $C_{2\varepsilon} = 1.92$, $C_\mu = 0.09$, $\sigma_k = 1$, $\sigma_\varepsilon = 1.2$. In the derivation of the standard k –ε model transport equations, it was assumed that the flow is fully turbulent, and the effects of molecular viscosity are negligible. Hence, the standard k –ε model is therefore valid only for fully turbulent flows. Since, the turbomachinery flow is expected to be fully turbulent, the standard k –ε model can be applied. It is also robust enough for the turbomachinery problem with desirable accuracy.

3.4.2 The Realizable k –ε Model

The realizable k –ε model is likely to provide superior performance for flows involving rotation, boundary layers under strong adverse pressure gradients, separation, and recirculation according to *FLUENT* [15]. It is especially useful if there are flow features such as strong streamline curvature, vortices, and rotation. The term ``realizable'' means that the model satisfies certain mathematical constraints on the normal stresses, consistent with the physics of turbulent flows. The realizable k –ε model is better than the traditional k –ε model by adopting a new eddy-viscosity formula involving a variable C_μ originally proposed by Reynolds and a new model equation for dissipation ε based on the dynamic equation of the mean-square vorticity fluctuation. The two transport equations, one for the turbulent kinetic energy k as in Equation (3.14a) and one for the rate of dissipation of

ATTENTION: The Singapore Copyright Act applies to the use of this document. Nanyang Technological University Library

turbulent kinetic energy ε as in Equation (3.14b) are solved. The modelled transport equations for K and ε in the realizable k –ε model are

$$\frac{\partial(\rho k)}{\partial t}+\frac{\partial\left(\rho k u_j\right)}{\partial x_i}=G_k+G_b-\rho\varepsilon-Y_M+S_K+\frac{\partial}{\partial x_i}\left[\left(\mu+\frac{\mu_t}{\sigma_k}\right)\frac{\partial k}{\partial x_j}\right] \tag{3.14a}$$

$$\frac{\partial(\rho\varepsilon)}{\partial t}+\frac{\partial\left(\rho\varepsilon u_j\right)}{\partial x_j}=S_\varepsilon+C_{1\varepsilon}\left(\frac{\varepsilon}{k}\right)C_{3\varepsilon}G_b-\rho C_1 S_\varepsilon-\frac{\rho C_2\varepsilon^2}{k+(\upsilon\varepsilon)^{0.5}}+\frac{\partial}{\partial x_j}\left[\left(\mu+\frac{\mu_t}{\sigma_\varepsilon}\right)\frac{\partial k}{\partial x_j}\right] \tag{3.14b}$$

where $C_1=max\left[0.43,\frac{\eta}{\eta+5}\right]$ and $\eta=S\left(\frac{k}{\varepsilon}\right)$

G_k represents the generation of turbulence kinetic energy due to the mean velocity gradients. G_b is the generation of turbulence kinetic energy due to buoyancy. Y_M represents the contribution of the fluctuating dilatation in compressible turbulence to the overall dissipation rate. C_2 and $C_{1\varepsilon}$ are constants. σ_k and σ_ε are the turbulent Prandtl numbers for k and ε respectively. S_K and S_ε are user-defined source terms.

The eddy viscosity is computed from

$$\mu_t=\rho C_\mu\left(\frac{k^2}{\varepsilon}\right) \tag{3.15a}$$

For the realizable k –ε model, C_μ is not constant and is computed from

$$C_\mu=\frac{1}{\left(A_0+A_s\left[\frac{kU^*}{\varepsilon}\right]\right)} \tag{3.15b}$$

ATTENTION: The Singapore Copyright Act applies to the use of this document. Nanyang Technological University Library

$$U^* = [S_{ij}S_{ij} + \tilde{\Omega}_{ij}\,\tilde{\Omega}_{ij}]^{0.5} \tag{3.15c}$$

and $\tilde{\Omega}_{ij} = \Omega_{ij} - 2\varepsilon_{ijk}\omega_k$ and $\Omega_{ij} = \underline{\Omega}_{ij} - \varepsilon_{ijk}\omega_k$ where $\underline{\Omega}_{ij}$ is the mean rate-of-rotation tensor viewed in a rotating reference frame with the angular velocity ω_k.

$$A_0 = 4.04 \tag{3.16a}$$

$$A_s = (6)^{0.5}\cos\Phi \tag{3.16b}$$

$$\Phi = \frac{1}{3}\left[\cos^{-1}\left\{(0.6)^{0.5}\,W\right\}\right] \tag{3.16c}$$

$$W = \frac{\left[S_{ij}\,S_{jk}\,S_{ki}\right]}{\hat{S}} \tag{3.16d}$$

$$\hat{S} = [S_{ij}S_{ij}]^{0.5} \tag{3.16e}$$

$$S_{ij} = \frac{1}{2}\left(\frac{\partial u_j}{\partial x_i} + \frac{\partial u_i}{\partial x_j}\right) \tag{3.16f}$$

C_μ is a function of the mean strain and rotation rates, the angular velocity of the system rotation, and the turbulence fields. The model constants C_2, σ_k and σ_ε have been established to ensure that the model performs well for certain canonical flows. The model constants are $C_{1\varepsilon}$ = 1.44, C_2 = 1.9, σ_k = 1, σ_ε = 1.2 according to *FLUENT* [15]. This model has been extensively validated for a wide range of flows including rotating homogeneous shear flows, free flows including jets and mixing layers, channel and boundary layer flows, and separated flows. For all these cases, the performance of the model has been found to be substantially better than that of the standard k –ε model. However, the realizable k –ε model has an extra rotation terms which is not compatible with the sliding mesh model.

ATTENTION: The Singapore Copyright Act applies to the use of this document. Nanyang Technological University Library

3.4.3 The Standard k –ω Model

The two transport equations, one for the turbulent kinetic energy k as in Equation (3.17a) and one for specific dissipation rate ω as in Equation (3.17b) are solved. The modelled transport equations for K and specific dissipation rate ω in the standard $k-\omega$ model are

$$\frac{\partial(\rho k)}{\partial t}+\frac{\partial\left(\rho k u_i\right)}{\partial x_i}=\frac{\partial}{\partial x_j}\left[\Gamma_K\frac{\partial k}{\partial x_j}\right]+G_k+S_K-Y_K \tag{3.17a}$$

$$\frac{\partial(\rho\omega)}{\partial t}+\frac{\partial\left(\rho\omega u_i\right)}{\partial x_i}=\frac{\partial}{\partial x_j}\left[\Gamma_\omega\frac{\partial \omega}{\partial x_j}\right]+G_\omega+S_\omega-Y_\omega \tag{3.17b}$$

G_k represents the generation of turbulence kinetic energy due to the mean velocity gradients. G_ω represents the generation of ω. Γ_K and Γ_ω represent the effective diffusivity of k and ω, respectively. Y_K and Y_ω represent the dissipation of k and ω due to turbulence. The standard $k-\omega$ model has improved accuracy in shear flow.

3.4.4 The Reynolds Stress Model

The exact transport equation (3.18) for the transport of the Reynolds stress $\rho\overline{u_i' u_j'}$ is:

$$\underbrace{\frac{\partial}{\partial t}\left(\rho\overline{u_i' u_j'}\right)}_{A}+\underbrace{\frac{\partial}{\partial x_K}\left(\rho u_K\overline{u_i' u_j'}\right)}_{B}=\underbrace{-\frac{\partial}{\partial x_K}\left[\rho\overline{u_i' u_j' u_K'}+\overline{P\left(\delta_{kj}u_i'+\delta_{ik}u_j'\right)}\right]}_{C}+\underbrace{\frac{\partial}{\partial x_K}\left[\mu\frac{\partial}{\partial x_K}\left(\overline{u_i' u_j'}\right)\right]}_{D}$$
$$\underbrace{-\rho\left(\overline{u_i' u_K'}\frac{\partial u_j}{\partial x_K}+\overline{u_j' u_K'}\frac{\partial u_i}{\partial x_K}\right)}_{E}\underbrace{-\rho\beta\left(g_i\overline{u_j'\theta}+g_j\overline{u_i'\theta}\right)}_{F}+\underbrace{\overline{P\left(\frac{\partial u_i'}{\partial x_j}+\frac{\partial u_j'}{\partial x_i}\right)}}_{G}\underbrace{-2\mu\overline{\frac{\partial u_i'}{\partial x_K}\frac{\partial u_j'}{\partial x_K}}}_{H} \tag{3.18}$$
$$\underbrace{-2\rho\Omega_K\left(\overline{u_j' u_m'}\varepsilon_{ikm}+\overline{u_i' u_m'}\varepsilon_{jkm}\right)}_{I}+\underbrace{S_{user}}_{J}$$

ATTENTION: The Singapore Copyright Act applies to the use of this document. Nanyang Technological University Library

A term is local time derivative, B term is convection, C term is turbulent diffusion, D term is molecular diffusion, E term is stress production, F term is buoyancy production, G term is pressure strain, H term is dissipation, I term is production by system rotation and J term is user defined source term.

Of the various terms in these exact equations, convection, turbulent diffusion, stress production and production by system rotation do not require any modelling. However, molecular diffusion, buoyancy production, pressure strain and dissipation need to be modelled to close the equations. The Reynolds Stress model should have a very good accuracy for predicting turbomachinery flow. However, the computational cost of such turbulence model is a bit too high for the level of accuracy needed for this project.

3.5 Results and Discussion

The steady state solution for the single inlet fan, double inlet fan and the airfoil bladed fan will be simulated using sliding meshes. The geometry of the single inlet fan and double inlet fan are outlined in the previous section 2.1. After the grid generation stage outlined in section 2.2, the mesh is exported to *FLUENT* software and the boundary conditions are set up as described in section 3.3 with the rotation velocity of the fan and the gauge static pressure at the inlet being specified so that the volume flow rate extracted at the outlet is controlled. Convergence for steady state analysis is outlined in section 3.5.1.1.This is applicable to the single inlet fan, the double inlet fan and the airfoil bladed fan, although only the convergence for the single inlet fan is shown in this chapter. The gauge total pressure at pressure inlet boundary has been input as 0 Pa. The operating temperature has been input as 304 Kelvin. All flow simulation results used the sliding mesh model as described in section 3.2.7. Results and discussions on steady state solution analysis of single inlet fan, the double inlet fan and the airfoil bladed fan will be presented in sections 3.5.1, 3.5.2 and 3.5.3 respectively.

ATTENTION: The Singapore Copyright Act applies to the use of this document. Nanyang Technological University Library

3.5.1 Single Inlet Fan

This section shows the flow simulation results for the single inlet fan and is divided into three smaller sub sections. The first sub section 3.5.1.1 will outline the convergence for steady state analysis. The second sub section 3.5.1.2 will discuss about the computed steady state flow fields of the single inlet fan. The third sub section 3.5.1.3 is about the transient solution analysis of the single inlet fan in which the rotation velocity is reduced to zero within a certain time. A grid dependence test has been done in section 3.5.1.2.3. Since the blade configuration for the double inlet fan is exactly the same with the single inlet fan, it is only necessary to do a grid dependence studies on the single inlet fan. After the appropriate grid size is selected, the double inlet fan, the single inlet fan and the airfoil bladed fan will be meshed accordingly.

3.5.1.1 Convergence for Steady State Analysis

After the solution has converged for the moving reference frame as shown in Figure 3.9, the sliding mesh model is set up according to section 3.2.7 and section 3.3.3 and is run to get a cyclic solution for the ventilation fan until steady state convergence is reached. This is done by changing the moving fluid zones motion types from moving reference frame to moving mesh motion types without changing the rotation velocity magnitude. The unsteady solver is activated and a suitable time step is selected.

Casey [50] states that for all multistage turbomachinery problems, the flow has been modelled as steady flow. The solution has reached steady state convergence if the solution field does not change (such that the change is less than 5 %) from one period to the next. Figure 3.10 shows the plot of gauge total pressure at the outlet against different periods of the revolution. The solution has reached steady state convergence, as the fluctuation is less than 5 % between different periods. It is noted that initially, the gauge total pressure rises rapidly before it stabilized at around the second period. After that, the gauge total pressure at the outlet remains relatively stable and hence steady state convergence is reached.

ATTENTION: The Singapore Copyright Act applies to the use of this document. Nanyang Technological University Library

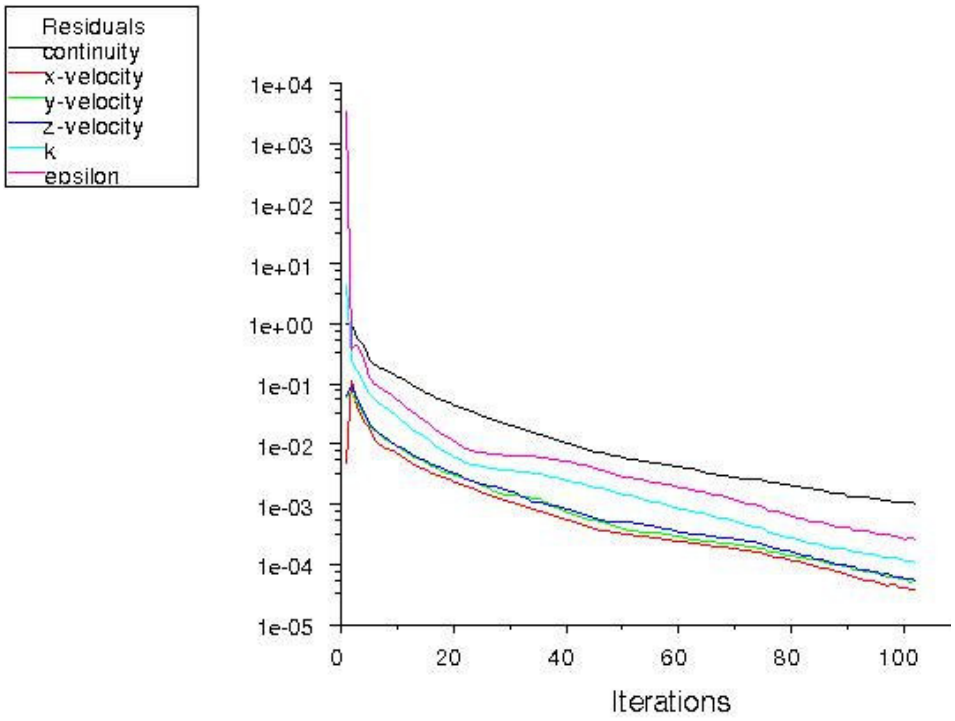


Figure 3.9 Residual Plot for single inlet fan 0.95m^3/s, 2500 rpm

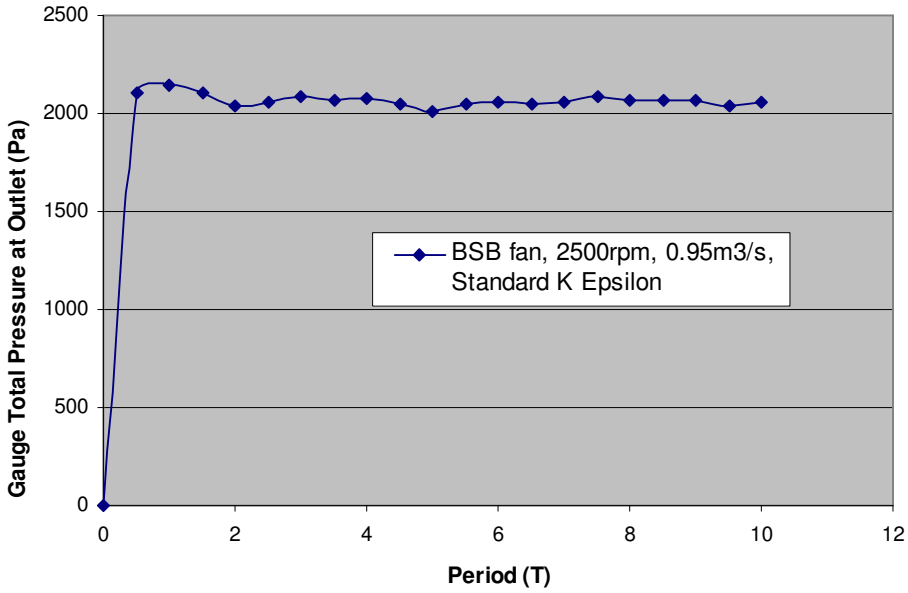


Figure 3.10 Plot of gauge total pressure at outlet against different period of revolution

ATTENTION: The Singapore Copyright Act applies to the use of this document. Nanyang Technological University Library

3.5.1.2 Computed Steady State Flow Fields in Single Inlet Fan

In this section, pressure contour plot at outlet, surface pressure distribution, skin friction lines on blade surfaces and casing, pressure contour plots at plane sections and effect of rotating stall are presented. The case of blades and impeller rotating at 2500 rpm with volume flow rate 0.95 m^3/s at the outlet has been used to study the general fan performance characteristics of single inlet fan. All solutions are in steady state.

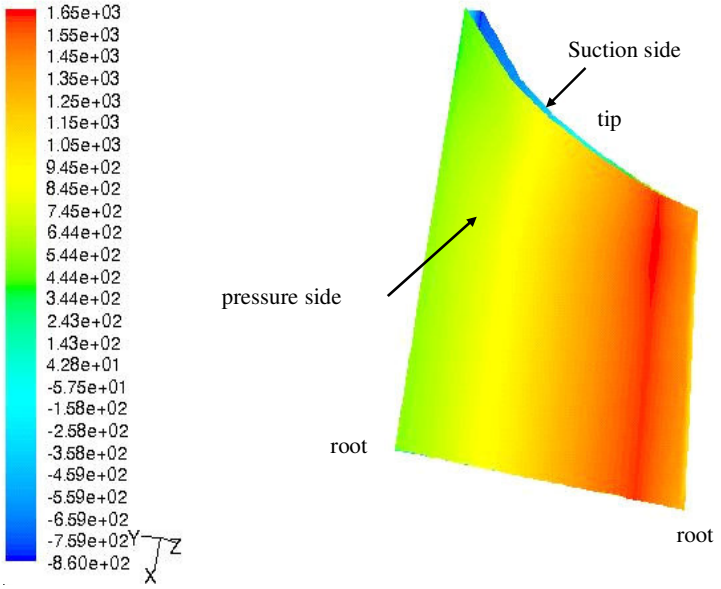
3.5.1.2.1 Surface Pressure Distribution of Blade and Streamlines

It is noted that for each blade, there is a pressure side of the blade and a suction side of the blade. The pressure side of the blade is the side with higher gauge static pressure. Figure 3.11(a) shows that the gauge static pressure increased on the pressure side of the blade in the radial direction. Figure 3.11(b) shows that the gauge static pressure increased on the suction side of the blade in the radial direction.

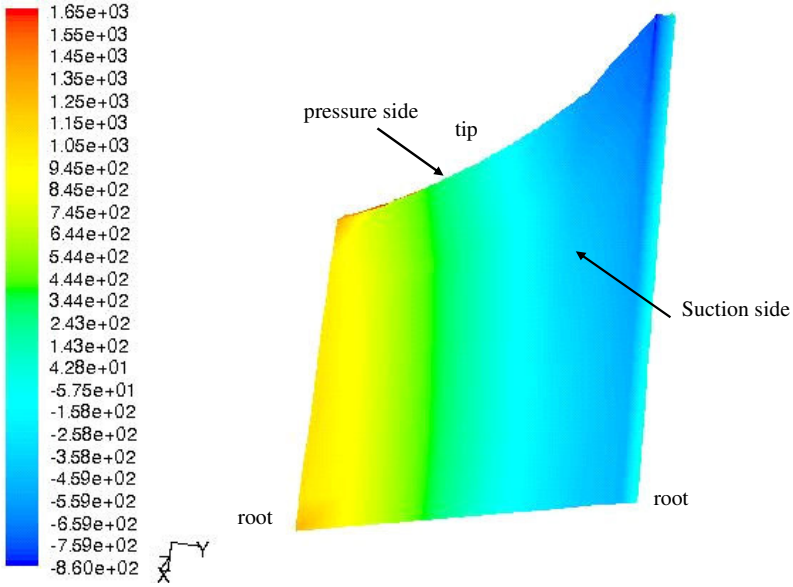
There has been flow visualization for turbomachinery design using computational fluid dynamics. Roth and Peikert [49] emphasize that it is crucial to analyze the flow in its response to small changes of geometry for the design process.

Figure 3.12(a) and Figure 3.12(b) show the streamlines after the impeller in top view and 3-dimensional view respectively. Flow separation with detaching flows at the blades has been noted in Figure 3.12(b) and hence flow simulation results are verified with flow simulation results done by others. Figure 3.12(a) shows the effect of rotation, which creates unsymmetrical streamlines about the Z-axis. Figure 3.12(a) shows the streamline aft the impeller from the top view. Figure 3.13 shows the zoom in 3 dimensional view of the streamline aft the impeller. Vortices are seen clearly. Hence, there is much flow separation at the blades. Figure 3.14 shows the streamlines from the blade to the outlet as the volume extraction flow rate at the outlet affected the streamlines.

ATTENTION: The Singapore Copyright Act applies to the use of this document. Nanyang Technological University Library



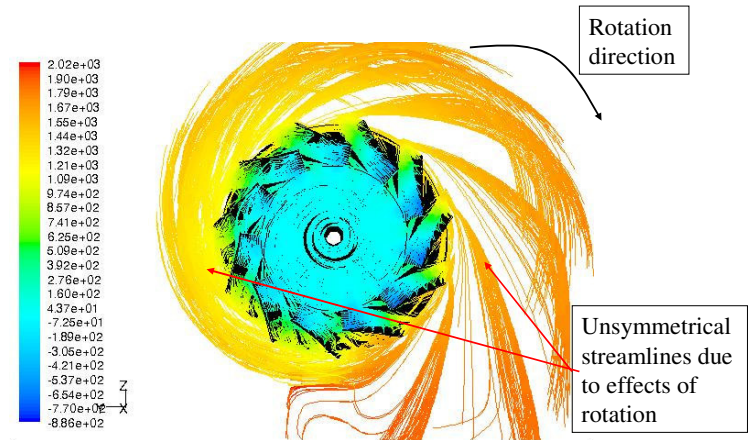
(a) Pressure side of blade



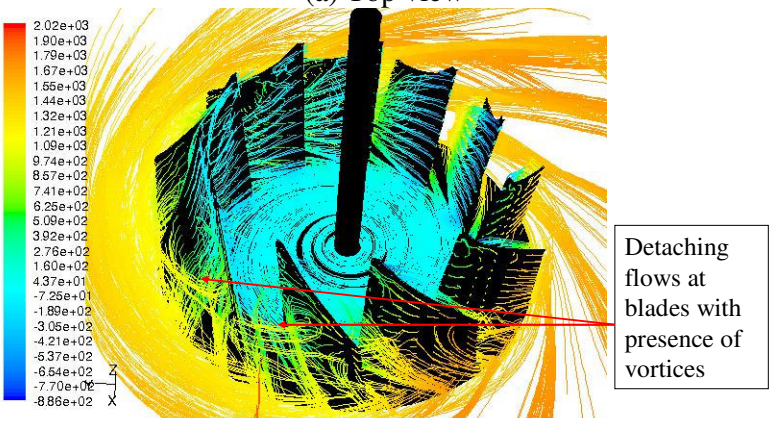
(b) Suction side of blade

Figure 3.11 Contour plot of static pressure at (a) pressure side and (b) suction side of blade for 0.95 m^3/s, 2500 rpm

ATTENTION: The Singapore Copyright Act applies to the use of this document. Nanyang Technological University Library



(a) Top view



(b) 3-dimensional view

Figure 3.12 Comparison between streamline aft impeller in (a) top view and (b) 3-dimensional view for 0.95 m^3/s, 2500 rpm

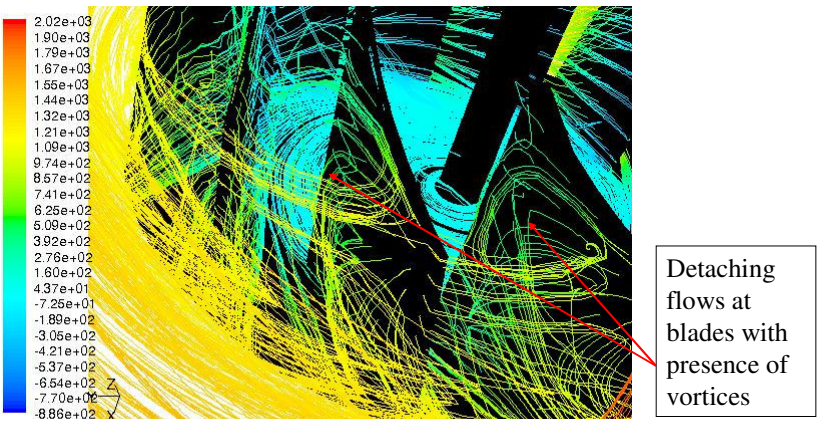


Figure 3.13 Streamline aft impeller in zoom in 3-dimensional view for 0.95 m^3/s, 2500 rpm

ATTENTION: The Singapore Copyright Act applies to the use of this document. Nanyang Technological University Library

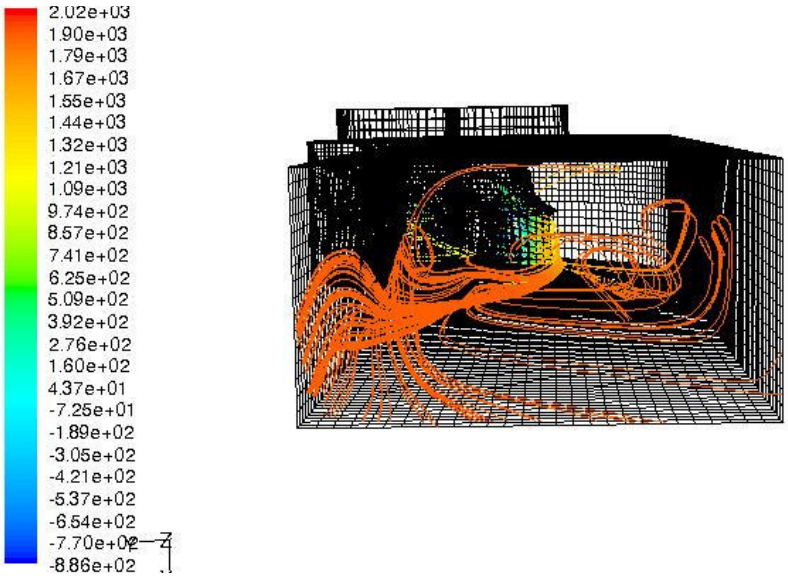


Figure 3.14 Streamline aft blades for 0.95 m^3/s, 2500 rpm

3.5.1.2.2 Skin Friction Lines on Blades and Impeller

Note that the blade numbering in this section follows Figure 3.15. Figure 3.16 shows the presence of rotating stall between blade passages. Stall cell region is the region of high gauge static pressure which is a region of low flow. Tecplot User's Manual [52] states that a streamtrace is dependent on a vector field, and hence vector components must be defined before creating streamtraces in Tecplot. A skin friction line is the flow field on the surfaces of wall. The skin friction line is obtained by setting the wall shear stress $\mu \frac{\partial u}{\partial y}$ at wall surface to be the velocity component in the *XYZ* direction. The skin friction line is plotted using Tecplot software, which allows us to change the velocity variable. Insights gained from plot of skin friction lines tell us the flow separation on surfaces of blade. It is the aim in optimized design to minimize flow separation, which caused losses.

Figures 3.17-19 show the plot of skin friction line on different blades for both pressure side and suction side of blades. It is noted that different blades have different pattern of skin friction lines. This is due to presence of rotating stall as shown in Figure 3.16, which creates

ATTENTION: The Singapore Copyright Act applies to the use of this document. Nanyang Technological University Library

an uneven fluid distribution; the skin friction line on each blade is different. Part span stall cells which exist in a single blade passage are seen in Figure 3.16. It is a part span stall cell because it extends only to part of the annulus span. Blade 2 has a smooth skin friction line pattern as shown in Figure 3.17.

Skin friction lines are plotted on the surface of impeller at different cycle of a period as shown in Figure 3.20. Different sections of impeller casing have different skin friction lines pattern due to effect of rotating stall. Blade 1 which is attached to the impeller acts an indicator of the direction of rotation. At time after 1 period, which is 1 *T*, plot of skin friction lines on the section next to Blade 1 is smooth. However, due to effect of rotating stall, at time after 1.2 *T*, plot of skin friction lines on the section next to Blade 1 are uneven with flow separation. After 1.8 *T*, plot of skin friction lines on the section next to Blade 1 are smooth again. Note that if the skin friction lines on the blades are uneven with flow separation, the sections of the impeller next to the blades have uneven skin friction lines of circular pattern as shown in Figure 3.21. Note that if the skin friction line on the blade is smooth, the section of the impeller next to the blade have smooth skin friction lines as shown in Figure 3.22.

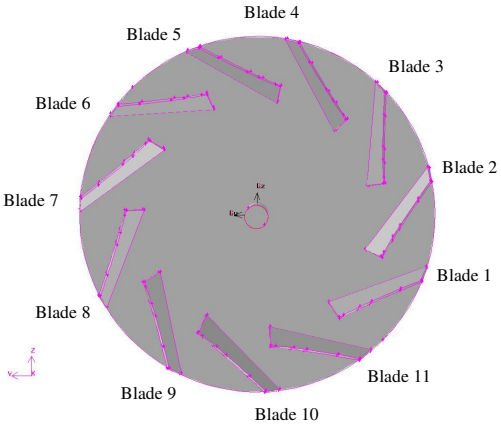


Figure 3.15 Blade numbering for impeller plate of single inlet fan

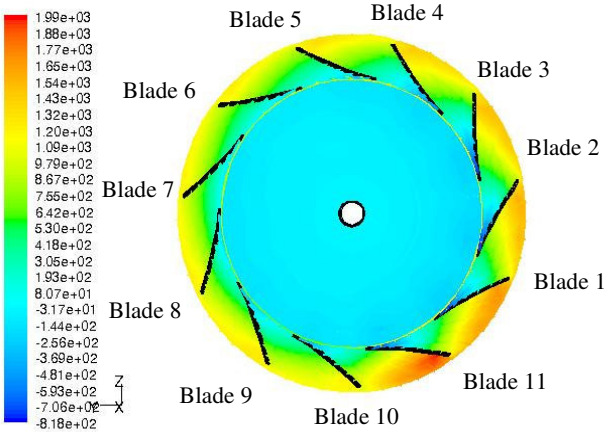
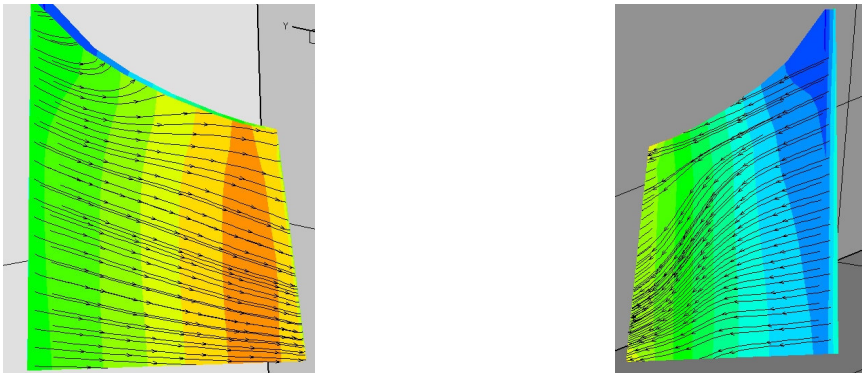


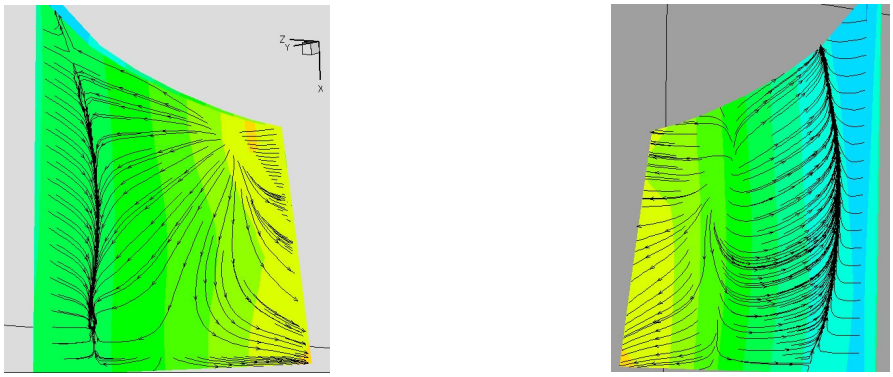
Figure 3.16 Contour plot of gauge static pressure for blade passages (Top view) for 0.95 m^3/s, 2500 rpm

ATTENTION: The Singapore Copyright Act applies to the use of this document. Nanyang Technological University Library



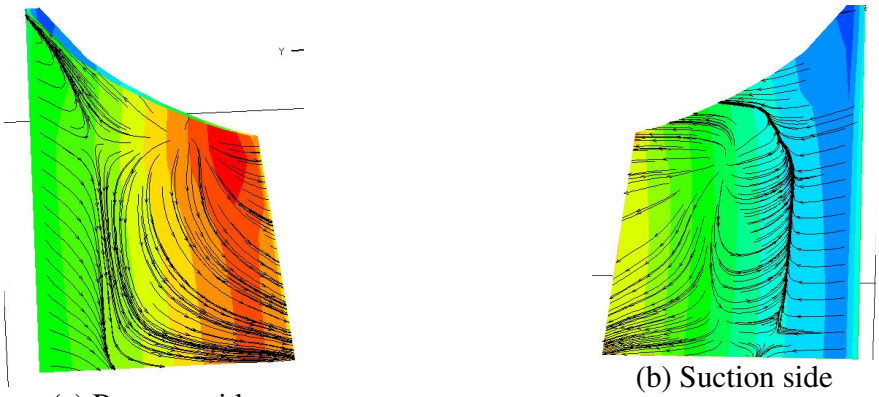
(a) Pressure side (b) Suction side

Figure 3.17 Plot of skin friction line on (a) pressure side and (b) suction side of Blade 2 for 0.95 m^3/s, 2500 rpm



(a) Pressure side (b) Suction side

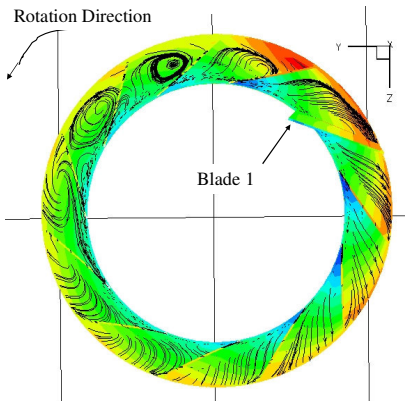
Figure 3.18 Plot of skin friction line on (a) pressure side and (b) suction side of Blade 10 for 0.95 m^3/s, 2500 rpm



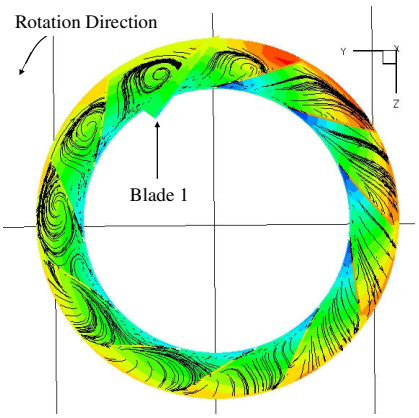
(a) Pressure side (b) Suction side

Figure 3.19 Plot of skin friction line on (a) pressure side and (b) suction side of Blade 11 for 0.95 m^3/s, 2500 rpm

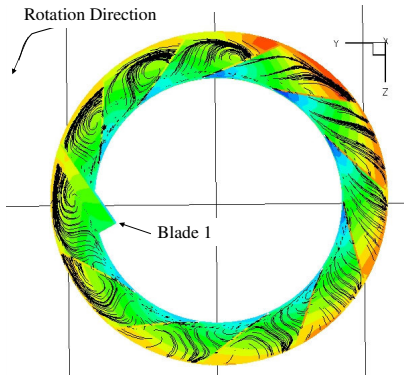
ATTENTION: The Singapore Copyright Act applies to the use of this document. Nanyang Technological University Library



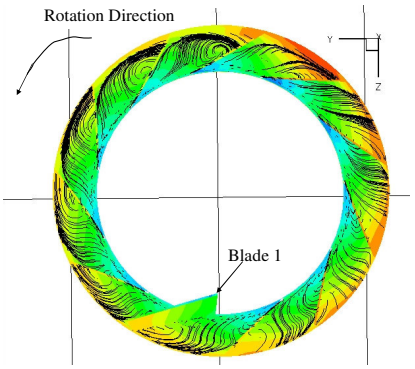
(a) Time = 1 T



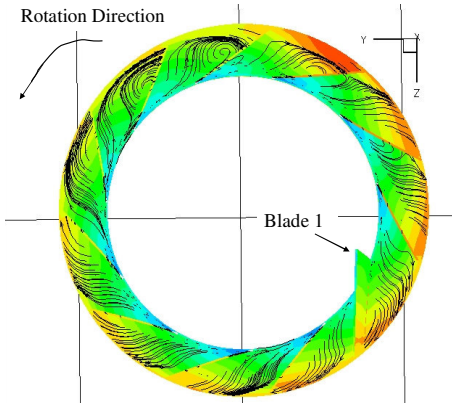
(b) Time = 1.2T



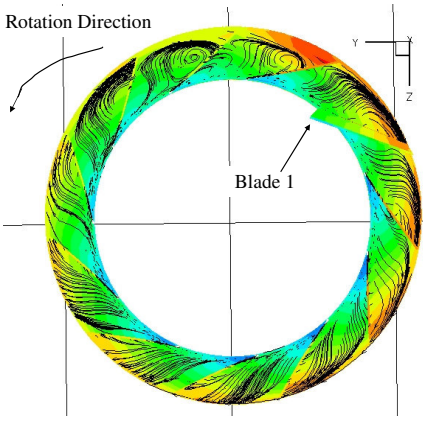
(c) Time = 1.4 T



(d) Time = 1.6 T



(e) Time = 1.8 T



(f) Time = 2 T

Figure 3.20 Comparison of plots of skin friction line on impeller casing (bottom view), 0.95 m^3/s, 2500 rpm for time (a) after 1 period, (b) after 1.2 period, (c) after 1.4 period, (d) after 1.6 period, (d) after 1.8 period, (e) after 1.8 period and (f) after 2 period

ATTENTION: The Singapore Copyright Act applies to the use of this document. Nanyang Technological University Library

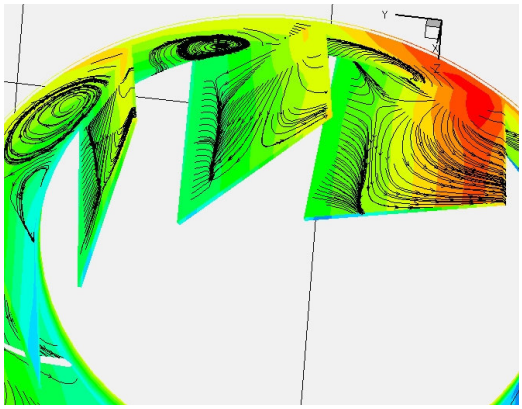


Figure 3.21 Plot of skin friction line on impeller casing and blades (3D view), 0.95 m^3/s, 2500 rpm

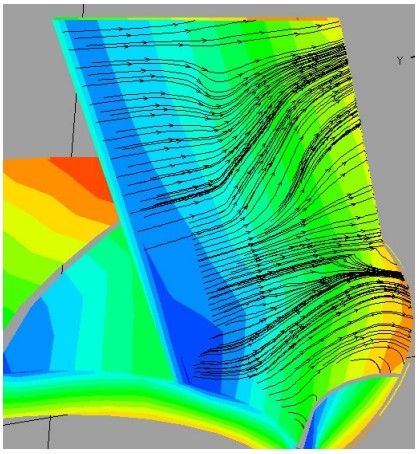


Figure 3.22 Plot of skin friction line on impeller casing and one blade (3D view), 0.95 m^3/s, 2500 rpm

3.5.1.2.3 Grid Dependence Studies for a Single Inlet Fan

It is important to check the effect of grid interval size on flow simulation result so that flow simulation results obtained are accurate. A grid dependence test has been done for the case of blades and impeller plate rotating at 2500 rpm with volume flow rate 0.95 m^3/s at the outlet for the single inlet fan. For all the problems, residual plots have been used to check for convergence. Some basic concepts about convergence, which are applicable to all cases, are briefly described below. Hence, discussion on convergence is not being discussed in other section of this report.

The residual plot is used to monitor on convergence. By setting a convergence criterion, a desired stability for the solution is input. After initializing the solution and running the iterations, convergence has been reached if the convergence criterion is satisfied, which means the solution obtained is consistent and stable to a certain desired level of accuracy. Convergence criterion of 10^{-3} is set for x-velocity, y-velocity, z-velocity, k –ε and continuity. Although, the residuals have reduced by three orders of magnitude, the solution might not have converged. A typical residual plot for convergence has been shown in Figure 3.23.

ATTENTION: The Singapore Copyright Act applies to the use of this document. Nanyang Technological University Library

GAMBIT 2.1 Modelling Guide [53] states that mesh generated for flow simulation must be independent of the mesh interval size. This means that the solution obtained using different number of mesh nodes must not be radically different. Figure 3.24 shows the face meshes on a blade for different number of mesh nodes and different number of volume mesh elements. Different number of mesh nodes on the blade is used to check the effect of increasing number of mesh nodes. As the number of mesh nodes increased, the error is reduced. Figure 3.25 shows that the difference between the experimental results and flow simulation results obtained for different number of meshes nodes reduces till the difference is almost negligent. Note that the total pressure error is the difference between the experimental result and the flow simulation result in term of total pressure at the outlet. Hence, grid dependence studies have been done. The solution has been independent of the mesh interval size. Note that the appropriate number of mesh nodes is also applied to the double inlet fan and hence grid dependence study is only necessarily done for the single inlet fan.

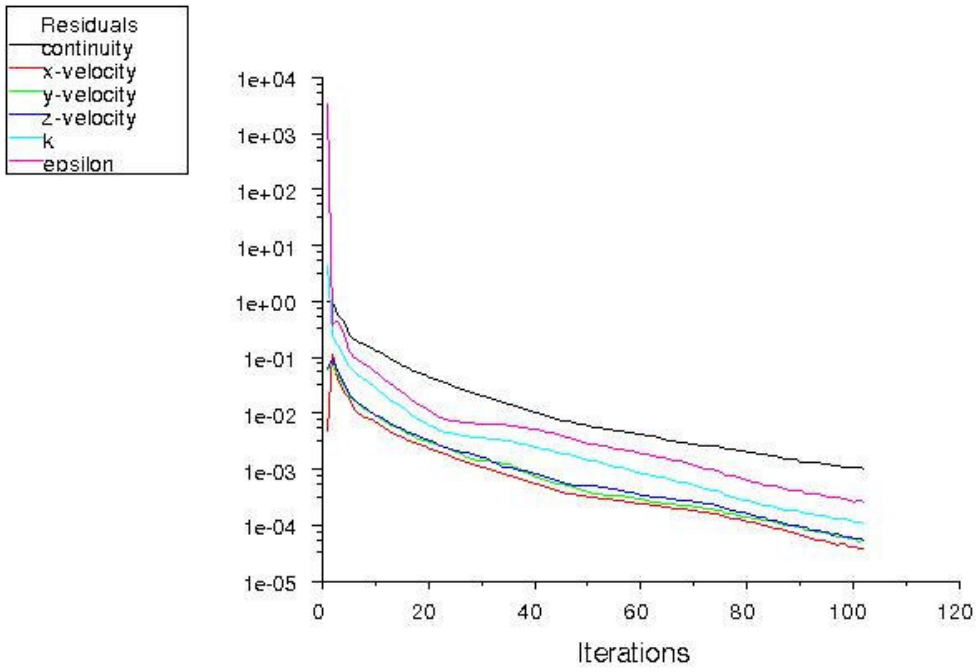
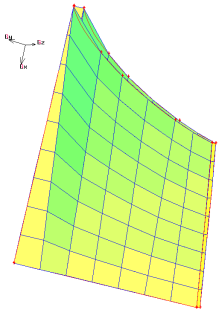
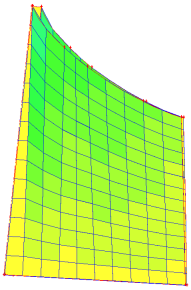


Figure 3.23 Residual Plot for single inlet fan (BSB fan) 0.95 m^3/s, 2500 rpm

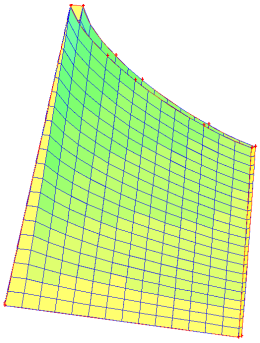
ATTENTION: The Singapore Copyright Act applies to the use of this document. Nanyang Technological University Library



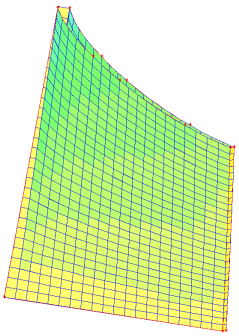
(a) Mesh nodes on blade face: 80
No. of volume mesh elements: 44817



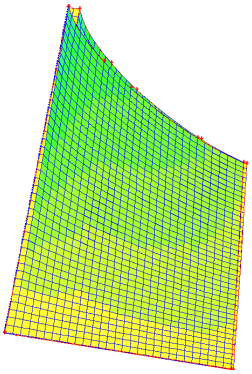
(b) Mesh nodes on blade face: 160
No. of volume mesh elements: 49987



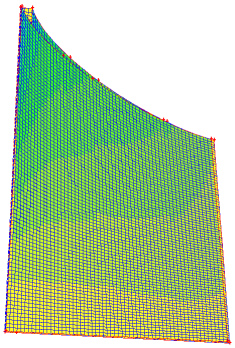
(c) Mesh nodes on blade face: 320
No. of volume mesh elements: 59094



(d) Mesh nodes on blade face: 640
No. of volume mesh elements: 76452



(e) Mesh nodes on blade face: 1280
No. of volume mesh elements: 118587



(f) Mesh nodes on blade face: 5120
No. of volume mesh elements: 154589

Figure 3.24 Comparison between different number of mesh nodes on blade for (a) mesh nodes on blade face: 320, (b) mesh nodes on blade face: 160, (c) mesh nodes on blade face: 320, (d) mesh nodes on blade face: 640, (e) mesh nodes on blade face: 1280, (f) mesh nodes on blade face: 5120

ATTENTION: The Singapore Copyright Act applies to the use of this document. Nanyang Technological University Library

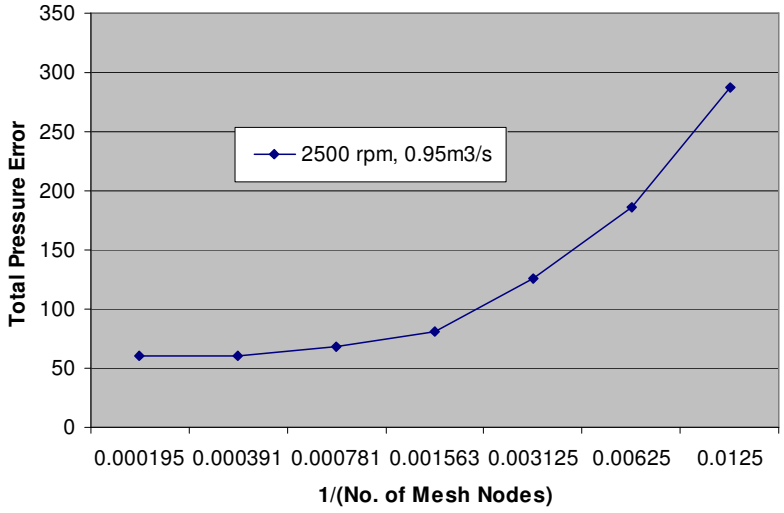


Figure 3.25 Plot of total pressure error against 1/ [No. of mesh nodes of blade]

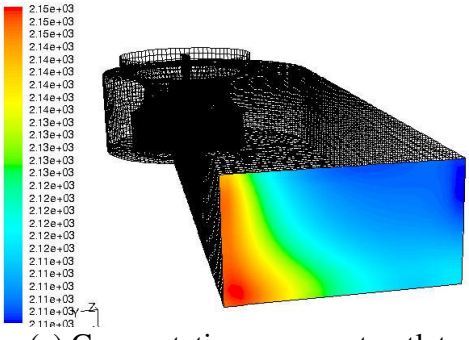
3.5.1.2.4 Pressure Contour Distribution at Outlet and Surface Pressure Distribution

It is important to plot the pressure contour at the outlet as the gauge total pressure is used later to compute the total efficiency of the single inlet fan. Figure 3.26 shows that there is an uneven pressure distribution at the outlet. This is because the geometry of single inlet fan is not symmetrical about the *Y*-axis. Compared with the experimental result, which has a gauge total pressure of 2200 Pa at the outlet for 0.95 m^3/s, 2500 rpm for the single inlet fan, the flow simulation result which gives 2140.107 Pa is a fairly accurate result. The experimental result is obtained by running the ventilation fan at a certain rpm. The fan laws are then applied to calculate the corresponding gauge static pressure at the outlet. The gauge dynamic pressure is calculated by using empirical formulae. This gauge dynamic pressure is then added to the gauge static pressure to obtain the gauge total pressure. Hence, the experimental result is based on the assumption of the applicability of the fan laws and the formula for the calculation of gauge dynamic pressure. However, fan laws may not be applicable due to Reynolds number effect as the fan is tested below the threshold Reynolds number. Moreover, the experimental result is obtained in a wind tunnel test, which is different from the flow simulation setup. This could explain why there is a small difference between experimental and flow simulation result and this matter needs to be addressed in

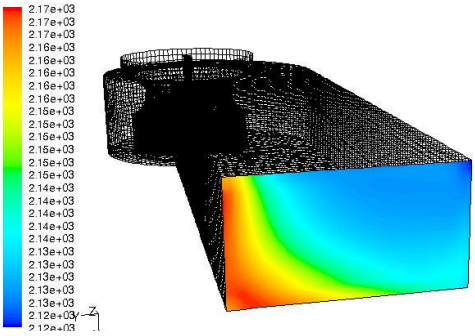
ATTENTION: The Singapore Copyright Act applies to the use of this document. Nanyang Technological University Library

the future. Nevertheless, the total gauge pressure at outlet is larger than the total gauge pressure at the inlet, which satisfied fan performance characteristics predicted in section 1.1.1.

In order to check that the sliding mesh model predict fan performance characteristics correctly as stated in section 1.1.1, the surface pressure distribution on impeller has been plotted in Figure 3.27 showing that the centre of impeller plate is of low-pressure region while the outer edge of impeller plate is of high-pressure region. Hence, low-pressure region is at the centre of rotation. There is a static pressure rise through the flow passages. According to Dean [9], the equation to calculate static pressure rise in centrifugal impeller is $\Delta p = \Delta\left[\rho\left(\frac{r^2\omega^2 - (v_w)^2}{2g_0}\right)\right]$ where Δp is the static pressure rise in centrifugal impeller, r is radius of impeller, ω is angular velocity in rad/s, v_w is relative velocity and g_0 is proportionality constant of Newton's Law. Figure 3.28 shows that surfaces of blades have high dynamic pressure, due to the rotation of blades. The centre of impeller plate has a lower dynamic pressure. Region of high vorticity magnitude implied the presence of vortices, which has to be minimized during design. Vortex is a region of swirling flow. Hence, the presence of high vorticity magnitude at blades tip as shown in Figure 3.29 means that the blades tip has to be redesigned to minimize flow separation such that the fan performance improved.



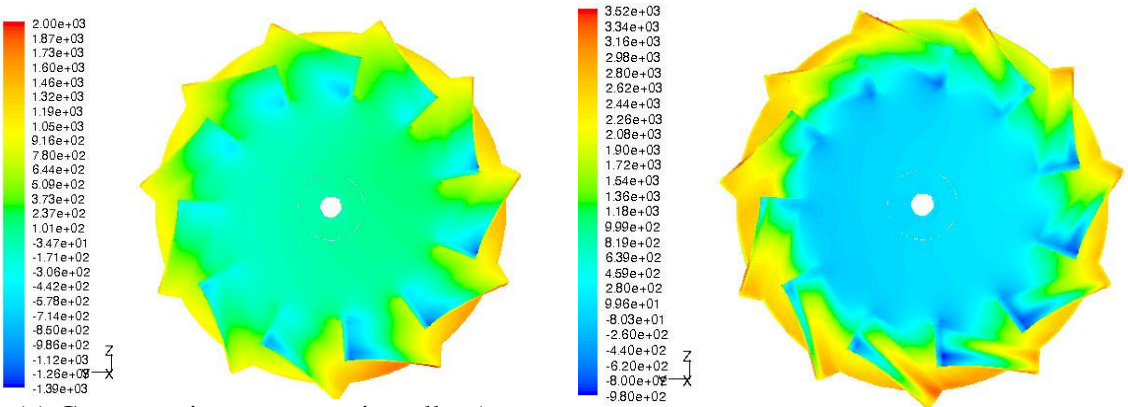
(a) Gauge static pressure at outlet
Average gauge static pressure: 2119.8 Pa



(b) Gauge total pressure at outlet
Average gauge total pressure: 2140.107 Pa

Figure 3.26 Contour plot of (a) gauge static pressure and (b) gauge total pressure at outlet for 0.95 m^3/s, 2500 rpm

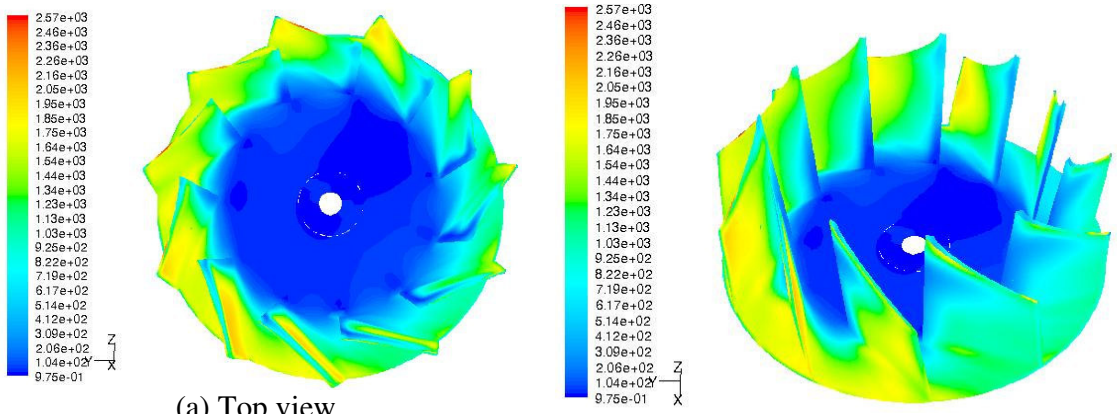
ATTENTION: The Singapore Copyright Act applies to the use of this document. Nanyang Technological University Library



(a) Gauge static pressure at impeller (top view)

(b) Gauge total pressure at impeller (top view)

Figure 3.27 Contour plot of (a) gauge static pressure and (b) gauge total pressure at impeller (top view) for 0.95 m^3/s, 2500 rpm



(a) Top view

(b) 3 D view

Figure 3.28 Contour plot of gauge dynamic pressure at impeller (a) top view and (b) 3 D view for 0.95 m^3/s, 2500 rpm

ATTENTION: The Singapore Copyright Act applies to the use of this document. Nanyang Technological University Library

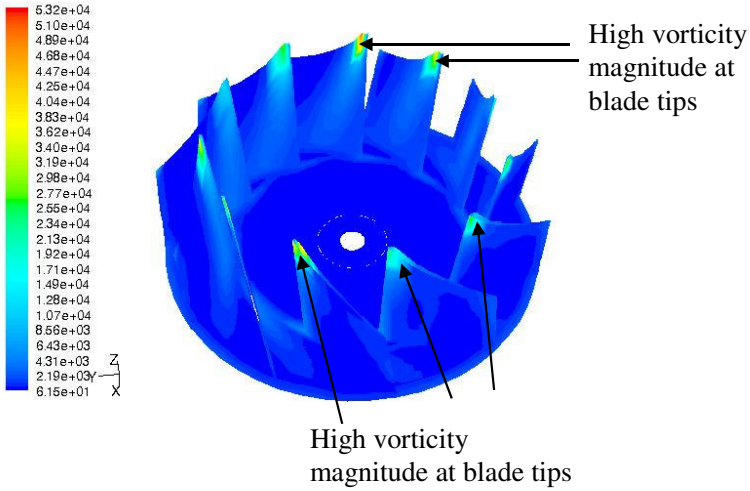


Figure 3.29 Contour plot of vorticity magnitude at impeller (3 D view) for 0.95 m^3/s, 2500 rpm

3.5.1.2.5 Rotating Stall

Flow simulation results obtained using sliding mesh model has fan performance characteristics of turbomachinery problem as stated in section 1.1.2 about rotating stall. Rotating stall is observed when the rotation of the blade passages is animated. This is because there is insufficient air to fill in the space between the blade passages. As a result, the flow is shared unequally such that some blade passages have large flow rate and some very little flow rate. The presence of a stall cell is shown in Figure 3.31, which has a particular blade with higher gauge static pressure.

The stall cells always rotate in the direction of the rotor. Stall runs in the direction in which the incidence is increased. For the rotating blades, it means that the stall cells moves backward relative to the rotating blades. This means that when the rotating blades are rotating clockwise as shown in Figure 3.31, the stall cells are rotating in anti-clockwise direction relative to the blades. The rotation of the stall cells is in the same sense as the rotor but at a greatly reduced speed. These observations prove that the sliding mesh model is a good representation of actual turbomachinery problem.

ATTENTION: The Singapore Copyright Act applies to the use of this document. Nanyang Technological University Library

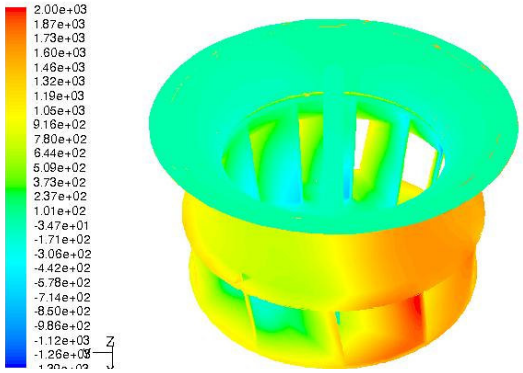


Figure 3.30 Contour plot of static pressure for impeller (3 D view) for 0.95 m^3/s, 2500 rpm

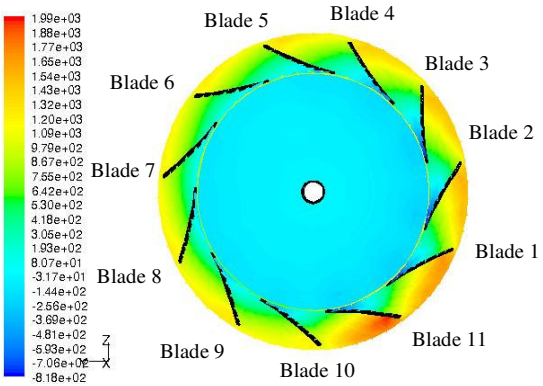
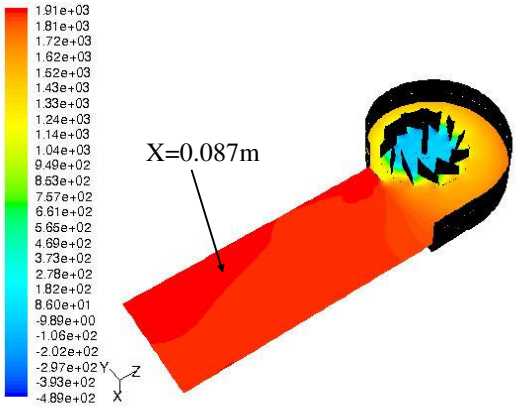


Figure 3.31 Contour plot of static pressure for blade passages (Top view) for 0.95 m^3/s, 2500 rpm

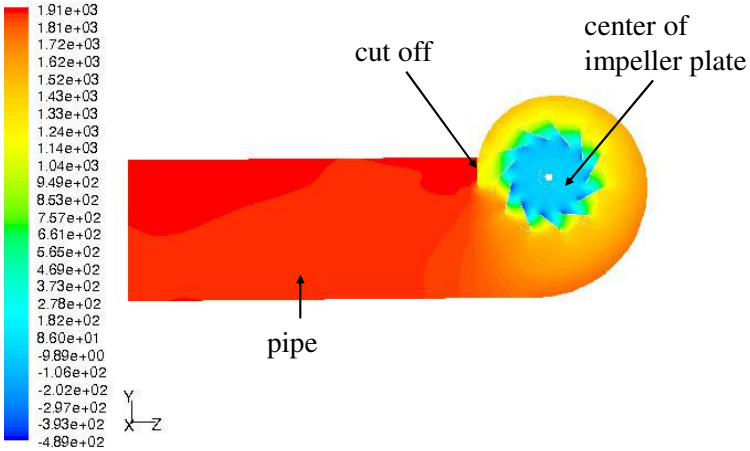
3.5.1.2.6 Pressure Contour Distribution at Plane Sections

Pressure contour plot at *YZ* plane at X = 0.087m as shown in Figure 3.32(a) are plotted to study the effect of the pipe on gauge static pressure and to compare the pressure distribution at sectional view. The single inlet fan has a cut off which has affected pressure distribution. Figure 3.32(b) shows that there is a region of high gauge static pressure region after the cut off. This insight is useful in getting the optimized design of fan geometry. Low-pressure region at the centre of impeller plate is also noted in Figure 3.32(b). There is an increase in gauge static pressure along the pipe. High dynamic pressure is noted at blade passages region as shown in Figure 3.32(c). It is also noted that the pipe is a low dynamic pressure region because it is far away from the rotation of blades and impeller. These fan performance characteristics proved that the fan is rotating to give a large pressure region at the outlet.

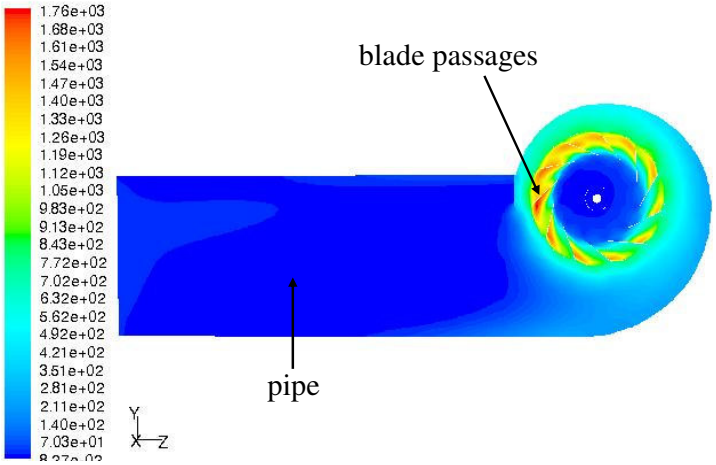
ATTENTION: The Singapore Copyright Act applies to the use of this document. Nanyang Technological University Library



(a) 3-Dimensional View



(b) Gauge static pressure



(c) Gauge dynamic pressure

Figure 3.32 Comparison between contour plot of (a) 3 dimensional view, (b) gauge static pressure and (c) gauge dynamic pressure at plane X = 0.087m for 0.95 m^3/s, 2500 rpm

ATTENTION: The Singapore Copyright Act applies to the use of this document. Nanyang Technological University Library

3.5.1.2.7 Fan Performance Characteristics for Single Inlet Fan

In this section, fan performance characteristics have been plotted for the single inlet fan so that they can be compared with the optimized blade design for single inlet fan. The optimized blade design has to give a higher total efficiency when compared with the original blade design. This is the reason why plots of total efficiency and gauge total pressure are plotted for the original blade design. Plots of gauge total pressure at outlet against volume flow rate for the single inlet fan have been done for different rpm.

Casey [50] states that some of the common best practice advice for turbomachinery problem includes surface pressure distribution, which should be accurately predicted for all turbulence models, and hence different turbulence models have been used to check the consistency of flow simulation result. Plots of total efficiency, power coefficient and flow coefficient have been done for the single inlet fan. This section shows the fan performance plots for original blade design.

Flow simulation results for the single inlet fan have been done using different turbulence models as shown in Figure 3.33. It is shown from Figure 3.33 that the gauge total pressure at the outlet increases as volume flow rate decreases until the surge point is reached. The experimental result is obtained by running the ventilation fan at a certain rpm. Fan laws are then applied to calculate the corresponding gauge static pressure at the outlet. The gauge dynamic pressure is calculated by using empirical formulae. This gauge dynamic pressure is then added to the gauge static pressure to obtain the gauge total pressure. Hence, the experimental result is based on the assumption of the applicability of the Fan Law and the formula for the calculation of gauge dynamic pressure. However, fan laws may not be applicable due to Reynolds number effect as the fan is tested below the threshold Reynolds number. For example, for the backward curved centrifugal fan the threshold Reynolds number is 1×10^{6}. This means that Fan Laws can only be applied if all extrapolated experimental results are obtained above this threshold Reynolds number. Based on feedbacks from the industry, fan is tested at low Reynolds number and extrapolated to very high Reynolds number. In another words, this means that the fan is tested at 50 rpm and extrapolated up to 3000 rpm. Fan is tested at low rpm because the industry lacks the costly

ATTENTION: The Singapore Copyright Act applies to the use of this document. Nanyang Technological University Library

equipment to test the fan at high rpm. At low Reynolds number with the fan running at 50 rpm, the flow may be laminar and any comparison between the turbulent flow at high Reynolds number with low Reynolds number is not justifiable. This means that the experimental result obtained is inaccurate. Moreover, the experimental result is obtained in a wind tunnel test, which is different from the flow simulation setup. This could explain why there is a small difference between experimental and flow simulation result and this matter needs to be addressed in the future. Nevertheless, the flow simulation results are fairly accurate when compared with the experimental results. Figure 3.34 shows the plots of total efficiency against volume flow rate for the experimental results and flow simulation results using different turbulence models. Both the experimental results and flow simulation results showed the maximum total efficiency when the volume flow rate is 1.9 m^3/s. The flow simulation results are fairly accurate when compared with the experimental results.

Flow simulations have been done for different rpm as shown in Figure 3.35. Surge points for different rpm occur when there is adverse pressure drop while reducing the volume flow rate. When the surge points are joined together, the surge line is obtained. Effective fan operation must not cross over the surge line but it has to be near to the surge line to make use of the maximum efficiency. Since specific speed is a term used to describe the geometry shape of a pump impeller, the specific speed for the same centrifugal fan running at different rpm would be the same. As shown in Figure 3.36, a lower rpm has a higher flow coefficient for the same volume flow rate. This is because the flow coefficient as shown in Equation (1.2c) is inversely proportional to the rotational speed in rad/s. Flow coefficient increases linearly with volume flow rate. As shown in Figure 3.37, a lower rpm has a higher power coefficient for the same volume flow rate. This is because the power coefficient as shown in Equation (1.2a) is inversely proportional to the cube of rotational speed in rad/s. Power coefficient increases with volume flow rate non-linearly.

ATTENTION: The Singapore Copyright Act applies to the use of this document. Nanyang Technological University Library

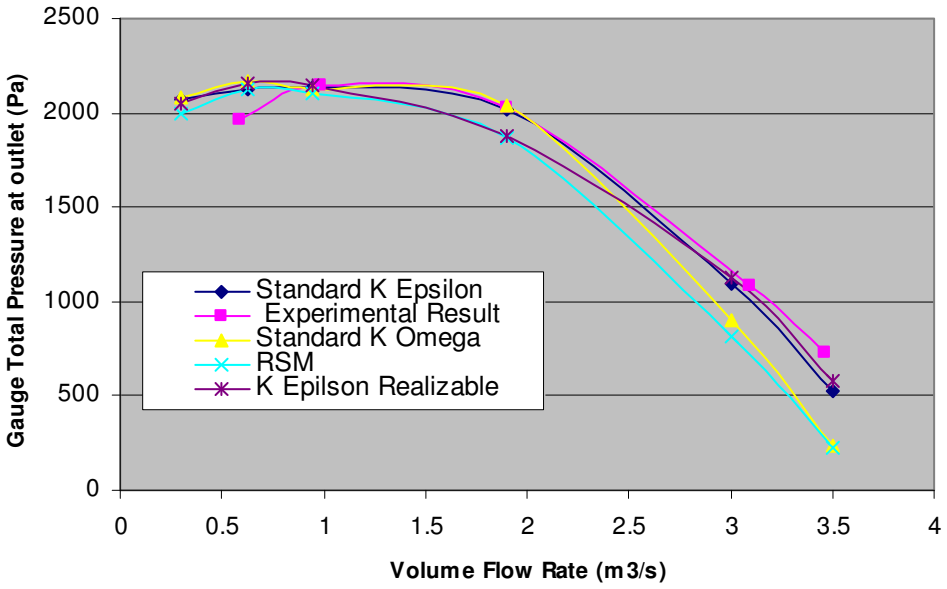


Figure 3.33 Plot of gauge total pressure at outlet against volume flow rate for single inlet fan running at 2500 rpm for different turbulence models

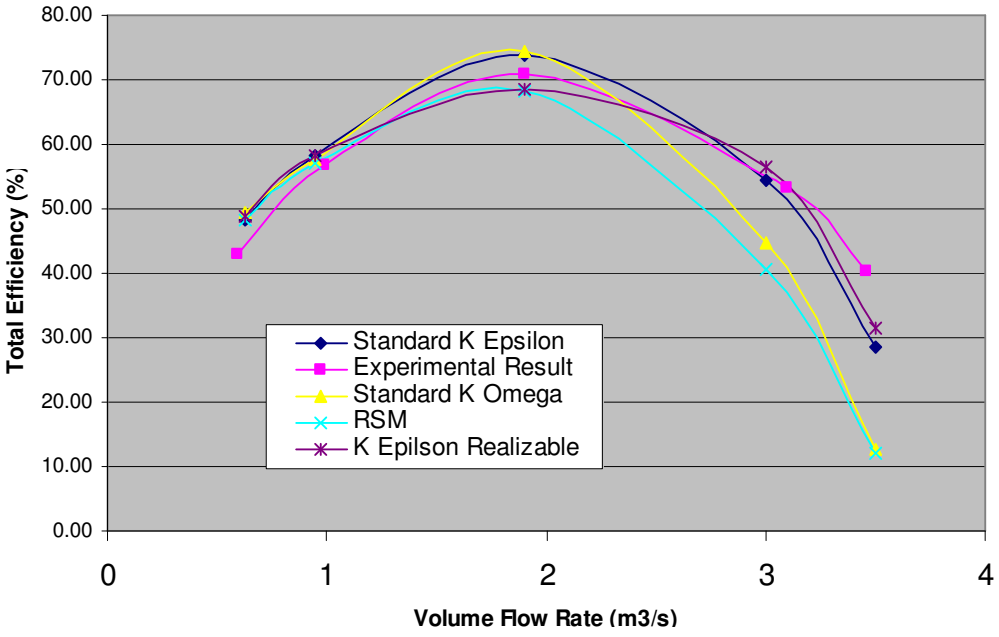


Figure 3.34 Plot of total efficiency for single inlet fan running at 2500 rpm for different turbulence models

ATTENTION: The Singapore Copyright Act applies to the use of this document. Nanyang Technological University Library

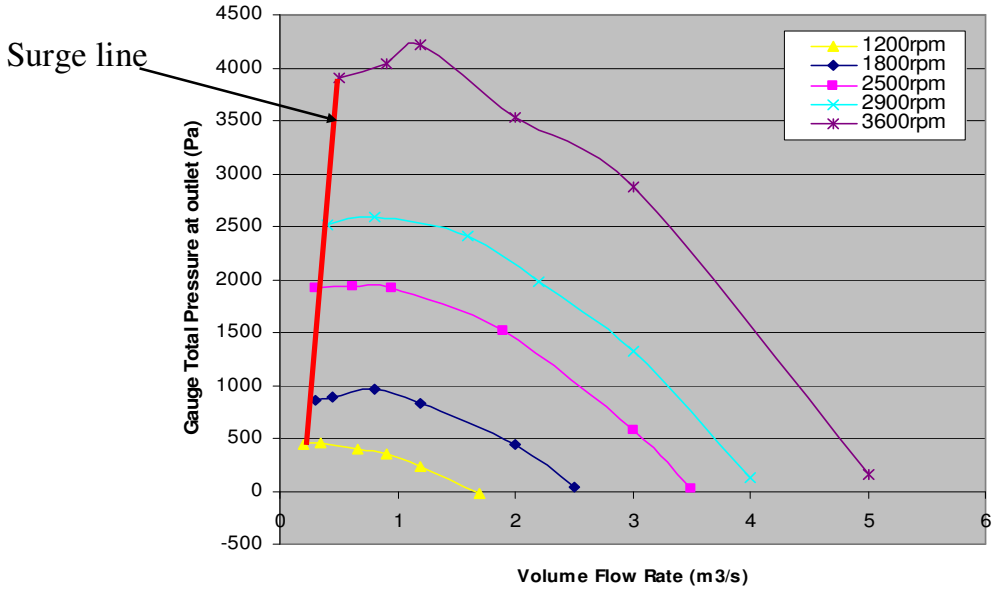


Figure 3.35 Plot of gauge total pressure at outlet against volume flow rate for single inlet fan running at different rpm with Standard K Epsilon turbulence model

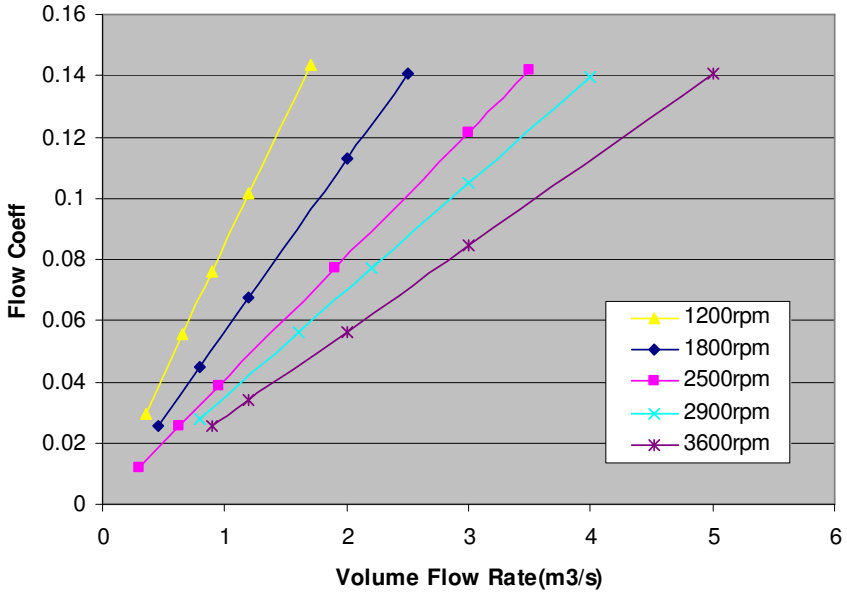


Figure 3.36 Plot of flow coefficient against volume flow rate for single inlet fan running at different rpm with Standard K Epsilon turbulence model

ATTENTION: The Singapore Copyright Act applies to the use of this document. Nanyang Technological University Library

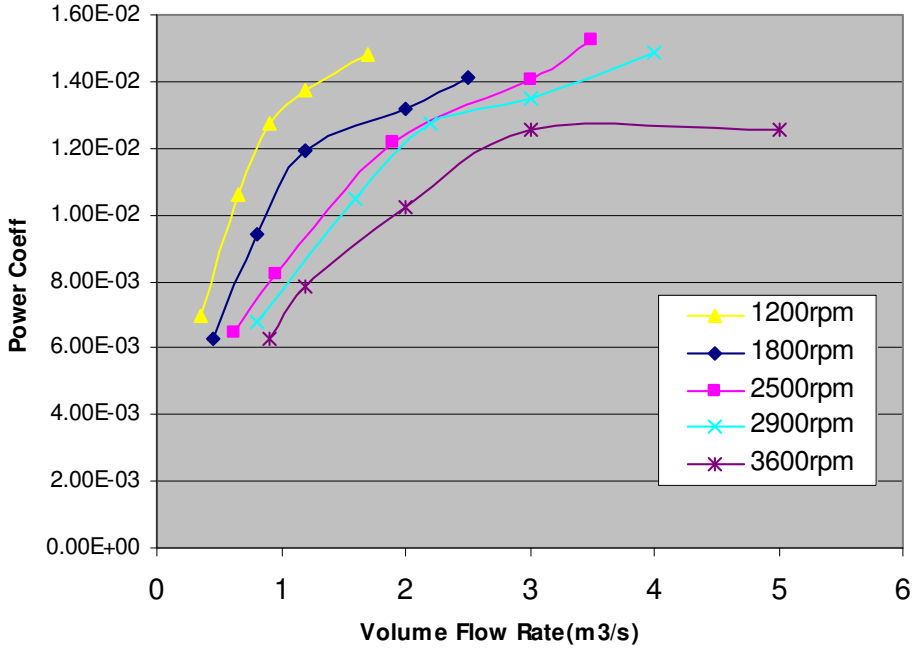


Figure 3.37 Plot of power coefficient against volume flow rate for single inlet fan running at different rpm with Standard K Epsilon turbulence model

3.5.1.3 Transient Solution Analysis for Single Inlet Fan

In this section, pressure contour plot at outlet, surface pressure distribution, pressure contour plots at plane sections and spanwise plot of gauge static pressure on blade surfaces and fluid passages midline plot on surfaces of impeller plate are presented. The case of blades and impeller rotating at 2500 rpm with volume flow rate 0.95 m^3/s extractions at the outlet has been used to study the transient behaviour of single inlet fan. The transient solution started after running under 2500 rpm for 0.24 second. In the transient solution analysis, the single inlet fan takes 24 seconds to have the rpm reduced linearly from 2500 rpm to 0 rpm. Hence, Equation (3.19) is used to show the relationship between time and rotation velocity in rad/s. Note that the equation used 24.24 instead of 24 because 0.24 second has been taken into account as the starting time. A user-defined function has been written to reduce the rpm linearly towards zero.

$$\text{Rotation Velocity in rad/s} = 10.9 \times (24.24 - t) \tag{3.19}$$

ATTENTION: The Singapore Copyright Act applies to the use of this document. Nanyang Technological University Library

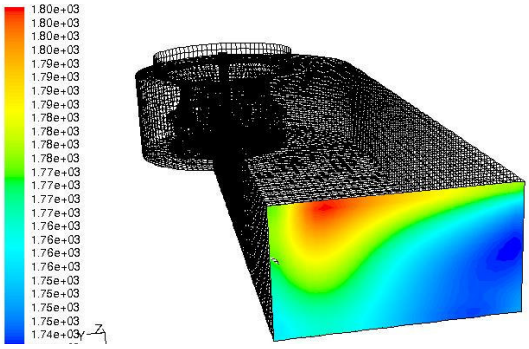
3.5.1.3.1 Pressure Contour Distribution at Outlet and on Surfaces and Planes

In this section, pressure contour plot at outlet, surface pressure distribution and plane pressure distribution have been presented to show the transient behaviour of fan with reducing rpm. According to Dean [9], the equation to calculate static pressure rise in centrifugal impeller is $\Delta p = \Delta\left[\rho\left(\frac{r^2\omega^2 - (v_w)^2}{2g_0}\right)\right]$ where Δp is the static pressure rise in centrifugal impeller, r is radius of impeller, ω is angular velocity in rad/s, v_w is relative velocity and g_0 is proportionality constant of Newton's Law.

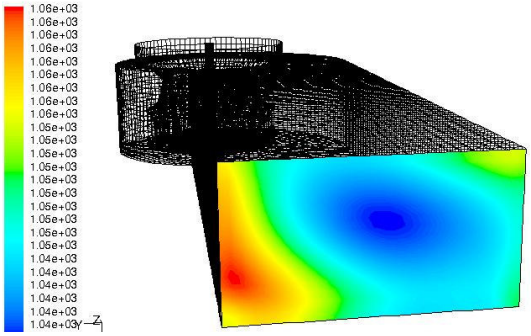
Since, at decreasing rpm, the contribution from the centrifugal term is reduced, the static pressure rise will become negative when the rotation speed is low enough. Hence, the equation of static pressure rise for non-rotating fan is $\Delta p = -\Delta\left[\rho\left(\frac{(v_w)^2}{2g_0}\right)\right]$, which has given a negative static pressure rise.

Figure 3.38 shows the pressure contour plot at outlet under transient behaviour. It is shown that the gauge static pressure at the outlet reduced with decreasing rpm. This showed that the gauge static pressure at the outlet is positive because of the rotation of impeller. At very low rpm such as 500 rpm as shown in Figure 3.38(e), the gauge static pressure is negative, as the fan is not rotating fast enough to give a high pressure region at the outlet. Figure 3.39 shows the surface pressure distribution of the impeller looking from the top view. Initially at higher rpm, the centre of impeller plate is a low-pressure region. Gauge static pressure increases along the radial direction for fan rotating in high rpm. However, as rpm reduced with time, the centre of impeller plate becomes a high-pressure region. At very low rpm as shown in Figure 3.39(e) and Figure 3.39(f), the centre of impeller plate is the high-pressure region. Since the centre of impeller is of low-pressure region only because it is the centre of rotation, it will become a high-pressure region if the fan is not rotating fast enough.

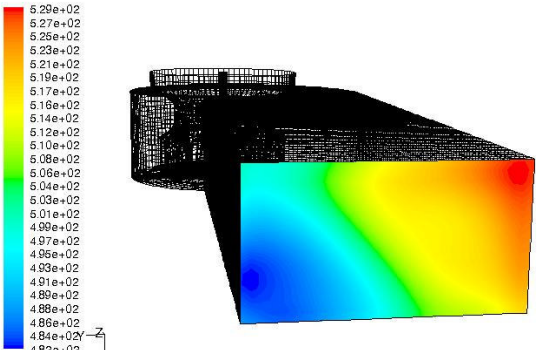
ATTENTION: The Singapore Copyright Act applies to the use of this document. Nanyang Technological University Library



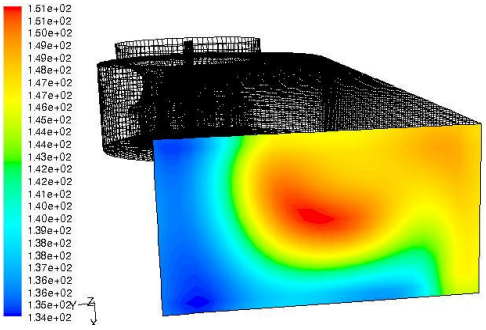
(a) Time: 0 second
Average gauge static pressure: 1764.505 Pa



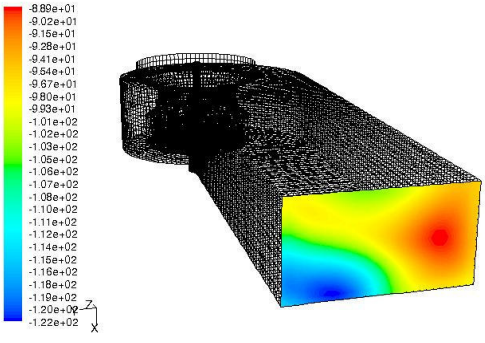
(b) Time: 4.8 second
Average gauge static pressure: 1047.433 Pa



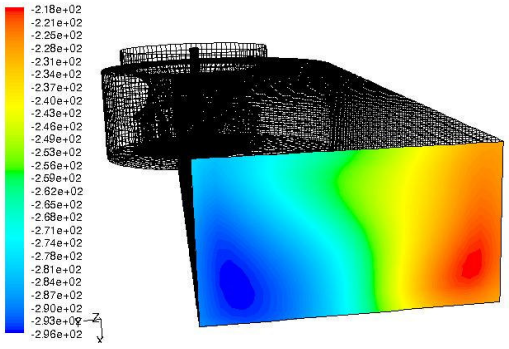
(c) Time: 9.6 second
Average gauge static pressure: 506.3378 Pa



(d) Time: 14.4 second
Average gauge static pressure: 143.3459 Pa



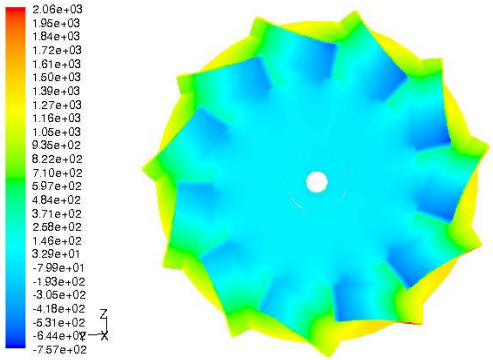
(e)Time: 19.2 second
Average gauge static pressure: -101.2567 Pa



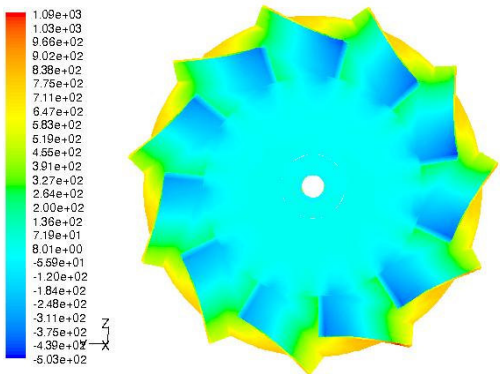
(f) Time: 24 second
Average gauge static pressure: -259.3636 Pa

Figure 3.38 Comparison between contour plot of gauge static pressure at outlet with volume flow rate 0.95 m^3/s at time (a) 0 second at 2500 rpm, (b) 4.8 second at 2000 rpm, (c) 9.6 second at 1500 rpm, (d) 14.4 second at 1000 rpm, (e) 19.2 second at 500 rpm and (f) 24 second at 0 rpm after the fan is turned off.

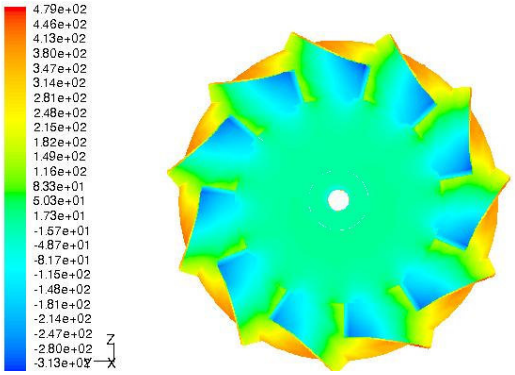
ATTENTION: The Singapore Copyright Act applies to the use of this document. Nanyang Technological University Library



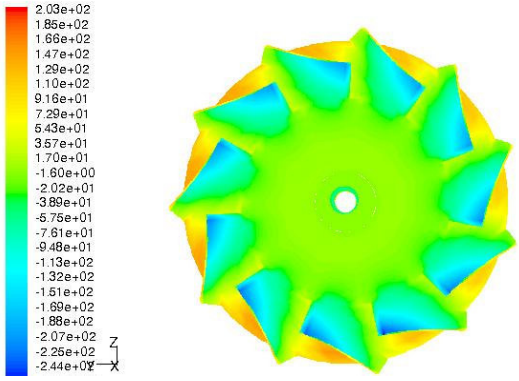
(a) Time: 0 second



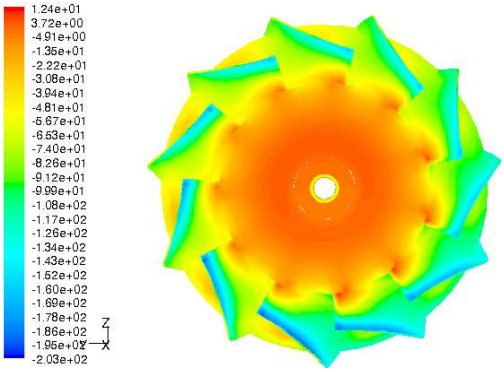
(b) Time: 4.8 second



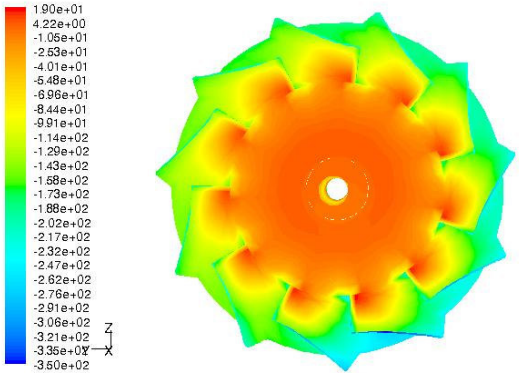
(c) Time: 9.6 second



(d) Time: 14.4 second



(e)Time: 19.2 second



(f) Time: 24 second

Figure 3.39 Comparison between contour plot of gauge static pressure at impeller (top view) with volume flow rate 0.95 m^3/s at time (a) 0 second at 2500 rpm, (b) 4.8 second at 2000 rpm, (c) 9.6 second at 1500 rpm, (d) 14.4 second at 1000 rpm, (e) 19.2 second at 500 rpm and (f) 24 second at 0 rpm after the fan is turned off.

ATTENTION: The Singapore Copyright Act applies to the use of this document. Nanyang Technological University Library

3.5.1.3.2 Fan Performance Characteristics for Transient Analysis

The graph of gauge total pressure at outlet against time is plotted to show the decreasing nature of gauge total pressure at outlet with decreasing rpm. It is shown in Figure 3.40 and Figure 3.41 that the gauge total pressure decreases linearly with time and rpm. This is because the rpm is reduced linearly with time. It is noted that the gauge total pressure at outlet becomes negative at 687.5 rpm and 17.4 second after the fan started to have a reducing rpm. Hence, the minimum rpm for the fan to be in operating condition is 687.5 rpm and below which, the fan is no longer be giving pressure region at the outlet. Since the total efficiency of the fan is dependent on the gauge total pressure at the outlet, fan rotating below 687.5 rpm is of no interest for operating condition.

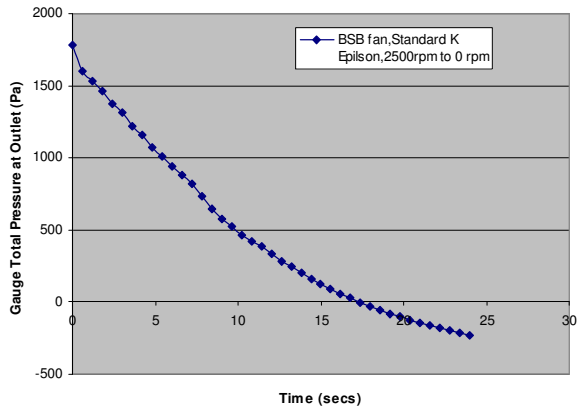


Figure 3.40 Plot of gauge total pressure at outlet against time for single inlet fan running at reducing rpm

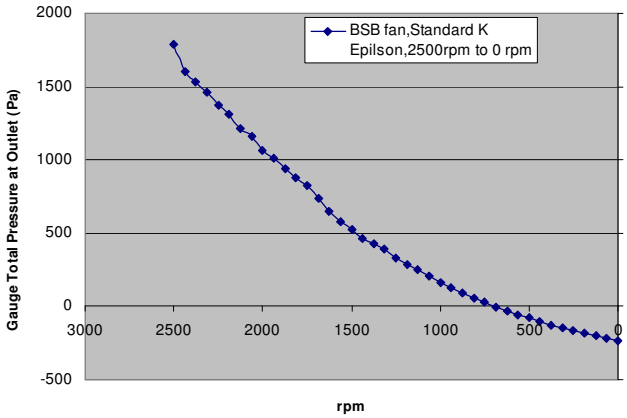


Figure 3.41 Plot of gauge total pressure at outlet against rpm for single inlet fan running at reducing rpm

ATTENTION: The Singapore Copyright Act applies to the use of this document. Nanyang Technological University Library

3.5.2 Double Inlet Fan

This section shows the flow simulation results for the double inlet fan, which discuss about the computed steady state flow fields of the double inlet fan. Effects of top and bottom impeller rotating in opposing directions are presented in section 3.5.2.1.4. Effects of alignment of top and bottom impellers geometry are presented in section 3.5.2.1.5. Effects of the number of blades are presented in section 3.5.2.1.6.

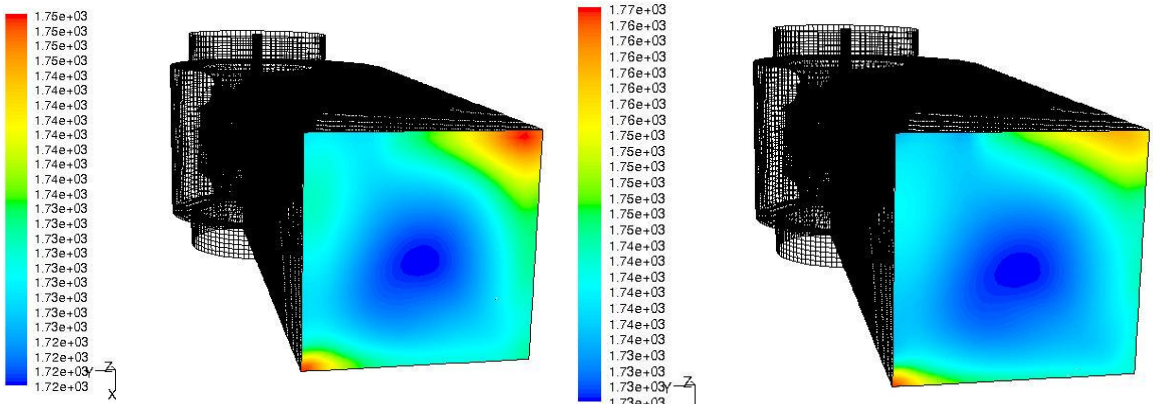
3.5.2.1 Computed Steady State Flow Fields in Double Inlet Fan

In this section, pressure contour plot at outlet, surface pressure distribution, spanwise plot of gauge static pressure and skin friction coefficient on blade surfaces and fluid passages midline plot of gauge static pressure and skin friction coefficient on surfaces of impeller plate are presented. The case of blades and impeller rotating at 2200 rpm with volume flow rate 1.2 m^3/s at the outlet has been used to study the general fan performance characteristics of double inlet fan. All solutions are in steady state.

3.5.2.1.1 Pressure Contour Distribution at Outlet and Surface Pressure Distribution

It is important to plot the pressure contour at the outlet as the gauge total pressure is used later to compute the total efficiency of the double inlet fan. Figure 3.42 shows an uneven pressure distribution at the outlet. This is because the geometry of double inlet fan is not exactly symmetrical about the Y-axis. The double inlet fan is unsymmetrical because the top and bottom impellers are not aligned to one another. The experimental result from industry database gives a gauge total pressure of 1750 Pa at the outlet for 1.2 m^3/s, 2200 rpm for the double inlet fan. The flow simulation result obtained gives a value of gauge total pressure of 1737.845 Pa which is very close to the experimental result. Figure 3.43(a) and Figure 3.43(b) show the gauge static pressure distribution on impeller without impeller casing and with impeller casing and inlet cone respectively. It is shown that both top and bottom impellers have stall cells near to the tips of the blades. The stall cells region is marked by high gauge static pressure region since stall cells region is of low flow and hence higher pressure region.

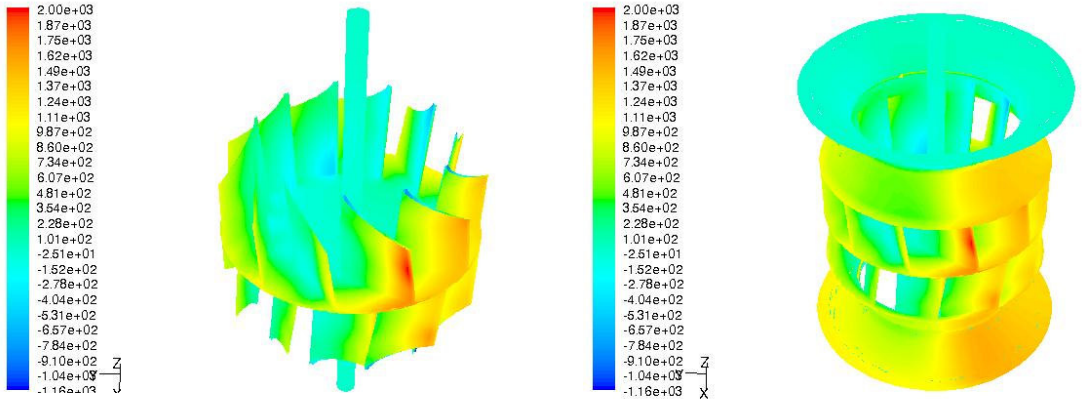
ATTENTION: The Singapore Copyright Act applies to the use of this document. Nanyang Technological University Library



(a) Gauge static pressure at outlet
Average gauge static pressure: 1728.527 Pa

(b) Gauge total pressure at outlet
Average gauge total pressure: 1737.845 Pa

Figure 3.42 Contour plot of (a) gauge static pressure and (b) gauge total pressure at outlet for 1.2 m^3/s, 2200 rpm



(a) Impeller

(b) Impeller with impeller casing and inlet cone

Figure 3.43 Contour plot of gauge static pressure for (a) impeller and (b) impeller with impeller casing and inlet cone in 3 D view for 1.2m^3/s, 2200rpm

ATTENTION: The Singapore Copyright Act applies to the use of this document. Nanyang Technological University Library

3.5.2.1.2 Spanwise Distribution on Blade Surfaces and Fluid Passages Midline Distribution

It is useful to show spanwise pressure distribution on the surfaces of blade and fluid passages midline plot as this information can be used to study the fan performance characteristics of turbomachinery problem. Spanwise plot along lines on blade surfaces have been done to show the increase in pressure coefficient in the radial direction. Figure 3.44(a) and Figure 3.44(b) show the hub lines, midline and tip lines drawn on the pressure side and suction side of the blade respectively. The spanwise plot of pressure coefficient along these lines is shown in Figure 3.45. Figure 3.45(a) and Figure 3.45(b) show that pressure coefficient does not vary much between the tip line, hub line and middle line. However, the pressure coefficient along the tip line is slightly higher near to the edge points B and H. It is shown in Figure 3.45(c) that the pressure side of blade has a higher pressure coefficient than the suction side of blade.

Figure 3.46(a) and Figure 3.46(b) show the hub lines, midline and tip lines drawn on the pressure side and suction side of the blade respectively with contour plot of skin friction coefficient. Contour plot of skin friction coefficient show us that there are regions of high shear stress at blade edges. The spanwise plot of skin friction coefficient along these lines is shown in Figure 3.47. Figure 3.47(a) and Figure 3.47(b) show that the midline edges points such as C, D, I and J have higher skin friction coefficient. Figure 3.47(c) shows that blade edges have high skin friction coefficient. This means that flow separation is concentrated at blade edges. This information tells us that blade edges have to be optimized to gain higher efficiency.

Figure 3.48(a) and Figure 3.48(b) show the lines drawn on the top and bottom impeller plate respectively. These lines are at the midline between one blade passages. The plot of gauge static pressure along these two lines is shown in Figure 3.49(a) and Figure 3.49(b) for the top and bottom impeller respectively. It is noted that both the top and bottom impeller plate show an increase in pressure in the radial direction along the lines. A sharp increase in

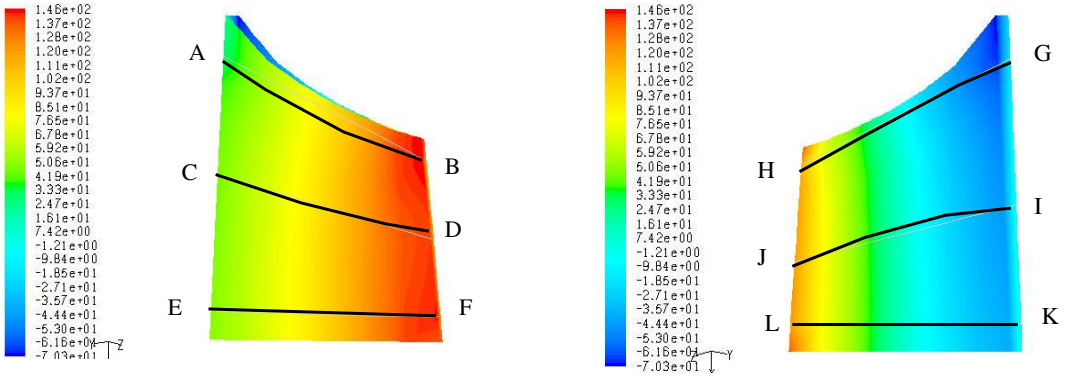
ATTENTION: The Singapore Copyright Act applies to the use of this document. Nanyang Technological University Library

pressure occurs between the blades. This is a result of static pressure rise due to centrifugal effect and the diffusion of relative flow according to Dean [9].

Figure 3.50 shows the line drawn on the top impeller plate with contour plot of skin friction coefficient. The line is at the midline between one blade passages. The plot of skin friction coefficient along this line is shown in Figure 3.51 for the top impeller. It is noted that there is high skin friction coefficient near the entrance of blade passages at point B. Figure 3.52 shows centreline drawn along the pipe for the contour plot of gauge static pressure. It is shown from Figure 3.53 that the gauge static pressure increases along the pipe. It is shown from Figure 3.54 that the gauge static pressure increased at different plane sections along the pipe.

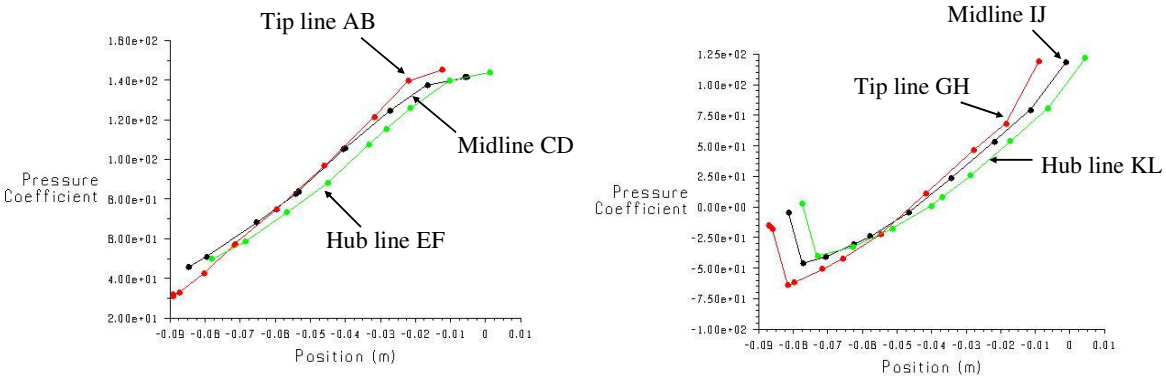
Figure 3.55(a) and Figure 3.55(b) show the lines drawn on the pressure side and suction side of the blade respectively with contour plot of vorticity magnitude. The plot of vorticity magnitude along these two lines is shown in Figure 3.56. It is shown that blade tips have higher vorticity magnitude. This implied the presence of vortices, which has to be minimized during design. Vortex is a region of swirling flow. According to Eckardt [54] the opportunities for possible efficiency increase lie mainly in the flow diffusing elements which means that high performance centrifugal compressors require the highest possible amount of flow diffusion. However, the frequent occurrence in the flow passages is a rapid growth of boundary layers which often initiates flow separation from the suction side of blade with the formation of a wake region. The flow separation impairs the diffusion potential and leads to a highly distorted jet wake velocity pattern at impeller discharge which causes a reduction in efficiency due to mixing losses. Hence, the presence of high vorticity magnitude at blades tip means that the blades tip has to be redesigned to minimize flow separation such that the fan performance improved. Figure 3.57 and Figure 3.58 show that flow separation occurs at high vorticity magnitude region.

ATTENTION: The Singapore Copyright Act applies to the use of this document. Nanyang Technological University Library

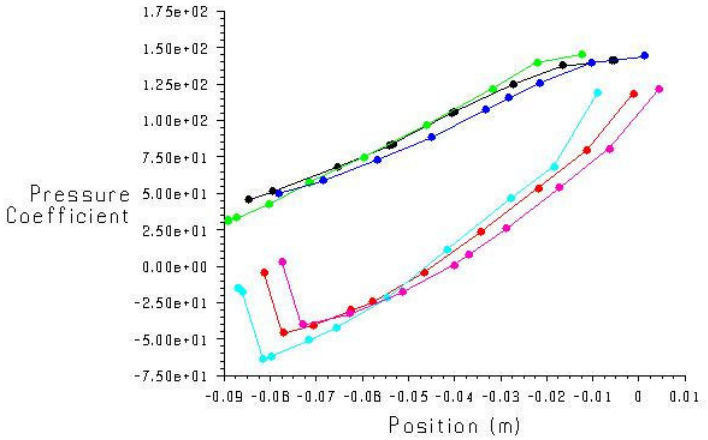


(a) Pressure side (b) Suction side

Figure 3.44 Contour plot of pressure coefficient at (a) pressure side and (b) suction side of blade for 1.2 m^3/s, 2200 rpm



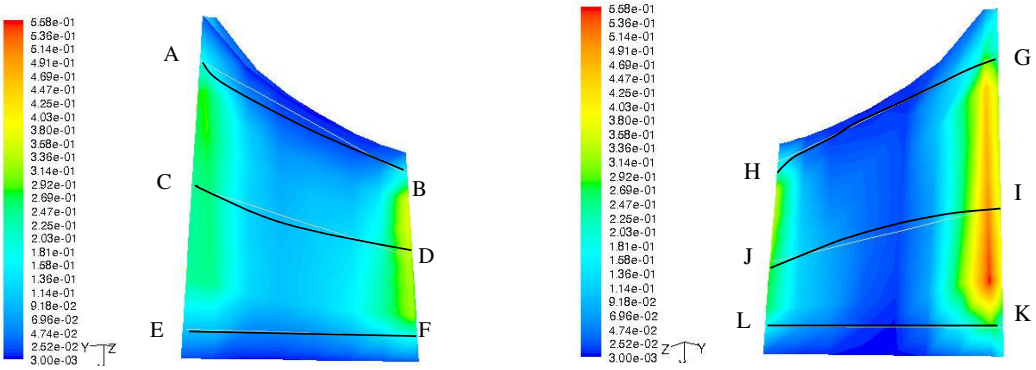
(a) Pressure side (b) Suction side



(c) Both sides

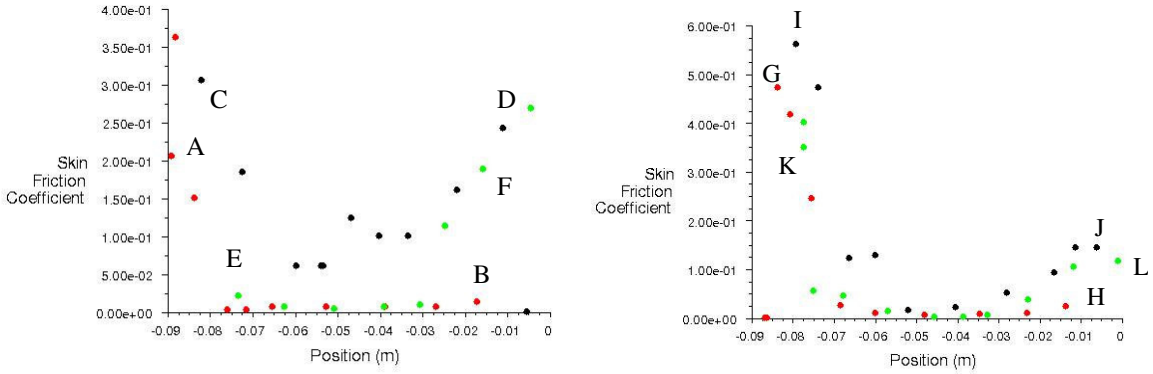
Figure 3.45 Spanwise plot of pressure coefficient along lines on (a) pressure side, (b) suction side and (c) both sides of blade surfaces for 1.2 m^3/s, 2200 rpm

ATTENTION: The Singapore Copyright Act applies to the use of this document. Nanyang Technological University Library

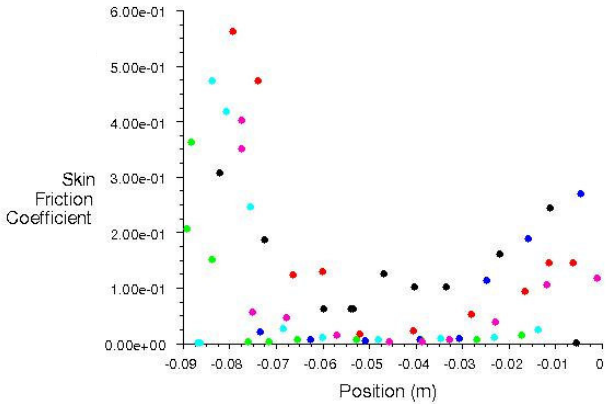


(a) Pressure side (b) Suction side

Figure 3.46 Contour plot of skin friction coefficient at (a) pressure side and suction side of blade for 1.2 m^3/s, 2200 rpm



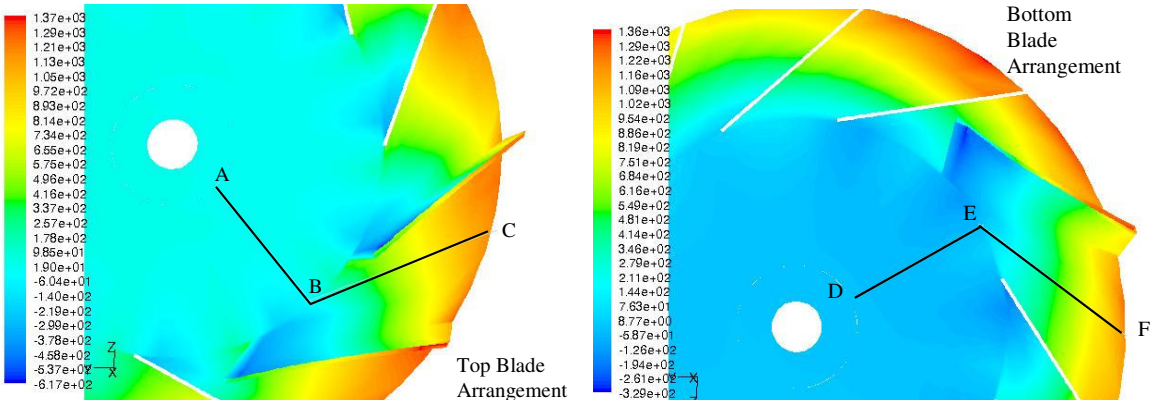
(a) Pressure side (b) Suction side



(c) Both sides

Figure 3.47 Spanwise plot of skin friction coefficient along the lines on (a) pressure side, (b) suction side and (c) both sides of blade surfaces for 1.2 m^3/s, 2200 rpm

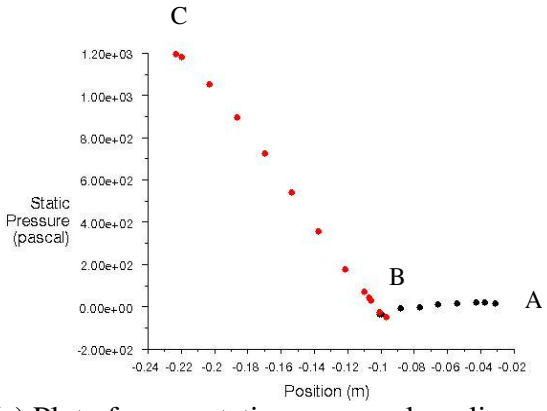
ATTENTION: The Singapore Copyright Act applies to the use of this document. Nanyang Technological University Library



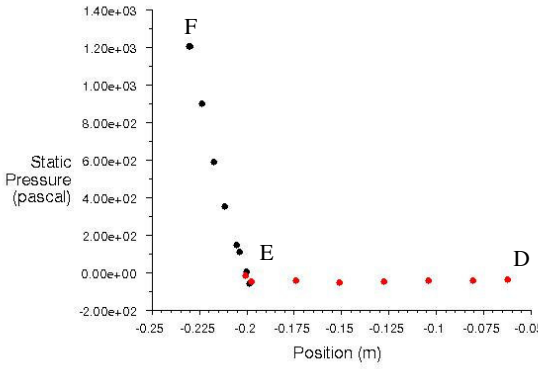
(a) Top impeller plate

(b) Bottom impeller plate

Figure 3.48 Contour plot of gauge static pressure at (a) top impeller plate and (b) bottom impeller plate for 1.2 m^3/s, 2200 rpm



(a) Plot of gauge static pressure along line on top impeller plate



(b) Plot of gauge static pressure along line on bottom impeller plate

Figure 3.49 Fluid passages midline plot of gauge static pressure along line on (a) top impeller plate and (b) bottom impeller plate for 1.2 m^3/s, 2200 rpm

ATTENTION: The Singapore Copyright Act applies to the use of this document. Nanyang Technological University Library

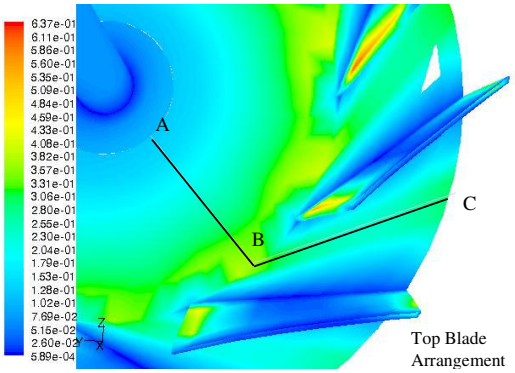


Figure 3.50 Contour plot of skin friction coefficient at top impeller plate for 1.2 m^3/s, 2200 rpm

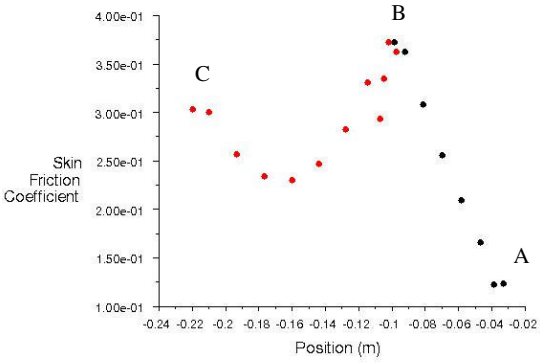


Figure 3.51 Fluid passages midline plot of skin friction coefficient along line on top impeller plate for 1.2 m^3/s, 2200 rpm

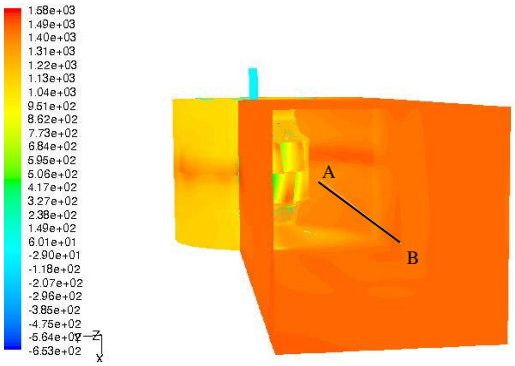


Figure 3.52 Contour plot of gauge static pressure along the pipe for 1.2 m^3/s, 2200 rpm

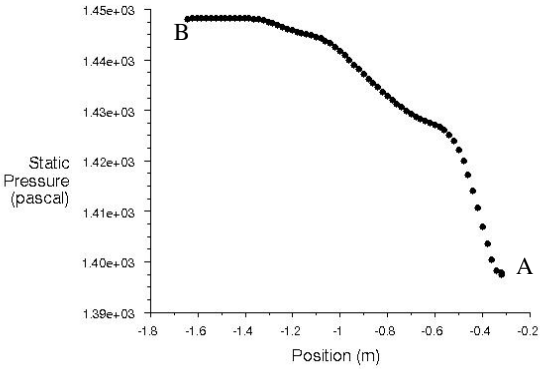


Figure 3.53 Plot of gauge static pressure along centreline along the pipe for 1.2 m^3/s, 2200 rpm

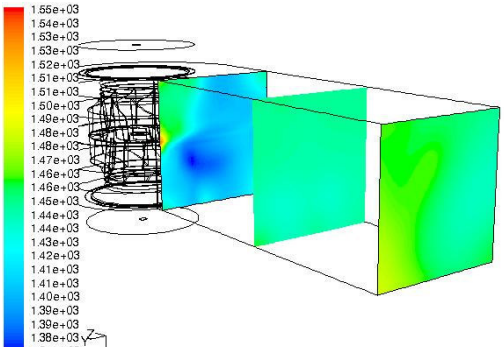
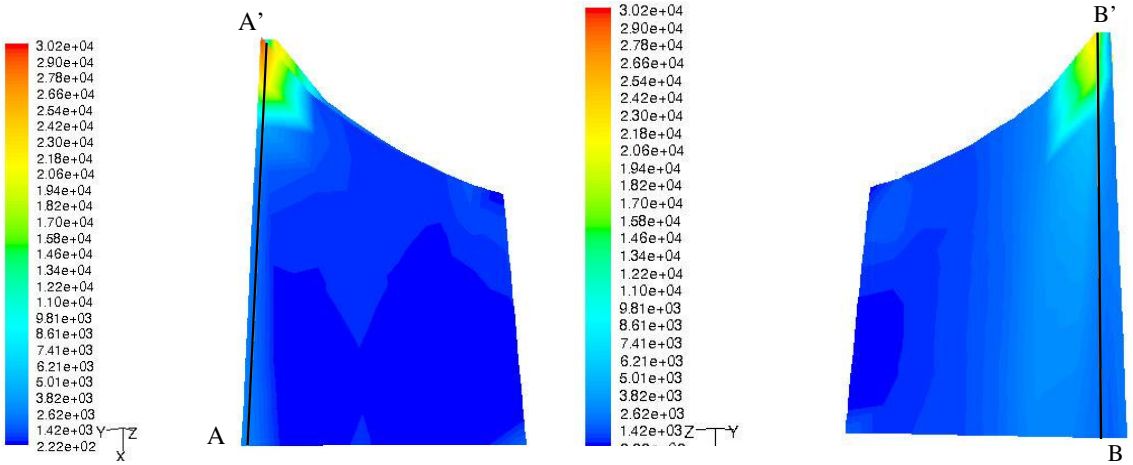


Figure 3.54 Contour plot of gauge static pressure along the pipe at different plane sections for 1.2 m^3/s, 2200 rpm

ATTENTION: The Singapore Copyright Act applies to the use of this document. Nanyang Technological University Library



(a) Pressure side of blade (b) Suction side of blade

Figure 3.55 Contour plot of vorticity magnitude at (a) pressure side and (b) suction side of blade for 1.2 m^3/s, 2200 rpm

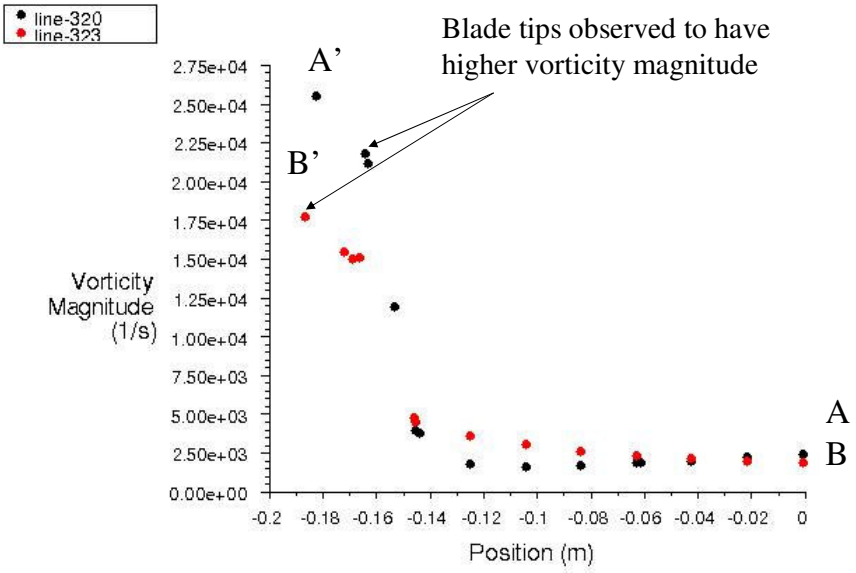


Figure 3.56 Plot of vorticity magnitude along the line on blade surfaces for 1.2 m^3/s, 2200 rpm

ATTENTION: The Singapore Copyright Act applies to the use of this document. Nanyang Technological University Library

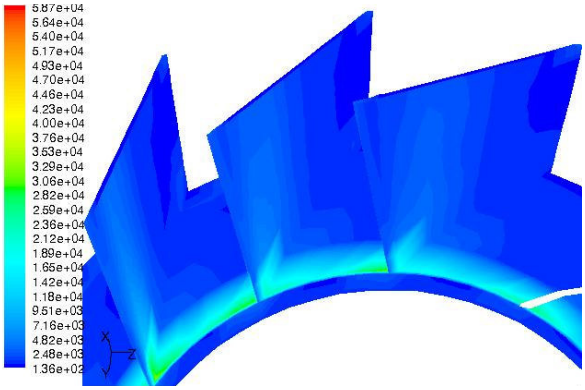


Figure 3.57 Contour plot of vorticity magnitude on impeller for 1.2 m^3/s, 2200 rpm

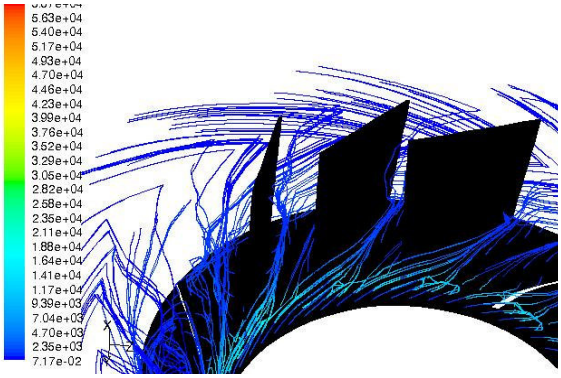


Figure 3.58 Streamlines plot coloured by vorticity magnitude on impeller for 1.2 m^3/s, 2200 rpm

3.5.2.1.3 Analysis on Blade to Blade Plane and Plane behind Blades and Plane between Blades

It is useful to have the blade to blade plane analysis so that the jet wake phenomena can be observed and studied. Yamane et.al [55] state that the wake is generated by an accumulation of low kinetic energy fluid in the suction side of blade. The jet wake pattern causes inlet distortion and hence the flows within the impeller becomes complex. It is important to study the jet wake phenomena so that higher efficiency centrifugal compressor can be designed. Using the blade to blade plane, the flow simulation results can try to verify such findings. The 3-dimensional view of the blade to blade planes is plotted as shown in Figure 3.59(a). Figure 3.59(b) shows the presence of tip leakage near the suction side of the blade. There is a small dip in pressure at the tip of the blades. Such tip leakages are also verified with findings from Zangeneh-Kazemi et.al [56]. The three planes are plotted to study the pressure distribution near to impeller casing, at the midspan between impeller plate and casing and near to impeller plate. Figure 3.60 shows the contour plot of gauge static pressure at three blade to blade planes. The average gauge static pressure on the plane near to impeller casing is 781.5201 Pa. The average gauge static pressure on the plane at midspan is 816.5045 Pa. The average gauge static pressure on the plane near to impeller plate is 842.6779 Pa. Hence, there is a higher gauge static pressure near to the impeller

ATTENTION: The Singapore Copyright Act applies to the use of this document. Nanyang Technological University Library

plate. There is a similar pressure distribution pattern observed from the three planes. At the tip of the blades near to the impeller centre, there is low gauge static pressure. There is a static pressure rise through the flow passages. According to Dean [9], the static pressure rise in the centrifugal impeller consists of centrifugal rise and the diffusion of the relative flow. Dean [9] explains that the centrifugal rise is attributable only to the change in radius of the fluid and the angular velocity of the impeller.

The relative velocity is the difference between the absolute velocity and the grid velocity. For simple rotation, the relative velocity is defined as $\vec{v}_w = \vec{v} - \vec{\omega} \times \vec{r}$ where is $\vec{\omega}$ the angular velocity of a rotating reference frame about the origin, $\vec{v}$ is the absolute velocity vector and $\vec{r}$ is the position vector. The equation to calculate static pressure rise in centrifugal impeller is $\Delta p = \Delta\left[\rho\left(\frac{r^2\omega^2 - (v_w)^2}{2g_0}\right)\right]$ where Δp is the static pressure rise in centrifugal impeller, r is radius of impeller, ω is angular velocity in rad/s, v_w is relative velocity and g_0 is proportionality constant of Newton's Law. Removing the centrifugal term, the additional impeller pressure rise is due to relative velocity diffusion. Hence, the relative velocity diffusion is the only part of the impeller static pressure rise which can be affected by impeller fluid dynamics. A low diffusion ratio not only lowers the impeller discharge pressure but also can cause severe discharge mixing losses.

Dean [9] states that some researchers insert hot wire anemometer at the rim of the centrifugal impeller to study the jet wake phenomena. From these hot wire anemometer results, it is stated that at the discharge of the impeller, it is found out that the relative velocity magnitude of the blade is higher on the pressure side of the blade and lower on the suction side of the blade. Hence, it is important to study the velocity pattern of the jet wake phenomena at a plane which is inserted behind two blades so that the details of jet wake patterns leaving the centrifugal impeller can be studied. It is also useful to study the velocity pattern of the jet wake phenomena at the blade to blade plane such that the wake is clearly visible.

ATTENTION: The Singapore Copyright Act applies to the use of this document. Nanyang Technological University Library

Hah and Reid [11] suggest visualizing flow structure on blade to blade plane by plotting relative velocity vectors on blade to blade plane. Figure 3.61 shows the plot of relative velocity vectors on blade to blade plane. The jet wake pattern is clearly visible from this figure. The wake region has relative velocity vectors pointing in the direction opposite to that of the jet region. Jones et.al [57] states that the term wake implies a net drag in reference to the velocity profile, while the term wake implies a net thrust in reference to the velocity profile. This means that the velocity profile of the jet and wake is in opposite directions to one another. Hence, there is a separation line between the jet and the wake regions. According to Figure 3.61, the wake region is at the suction side of the blade which has a high velocity magnitude. The jet is at the pressure side of the blade which has lower velocity magnitude.

Figure 3.62 shows the comparison of relative velocity vectors on blade to blade plane for a fan under peak efficiency and surge. Figure 3.62 (a) shows that when the fan is under peak efficiency, the separated flow region is smaller. Figure 3.62(b) shows that when the fan is under surge, the separated flow region is much larger and the flow separation line moves ahead of the blade passage. This result is verified by findings from Hah and Reid [11].

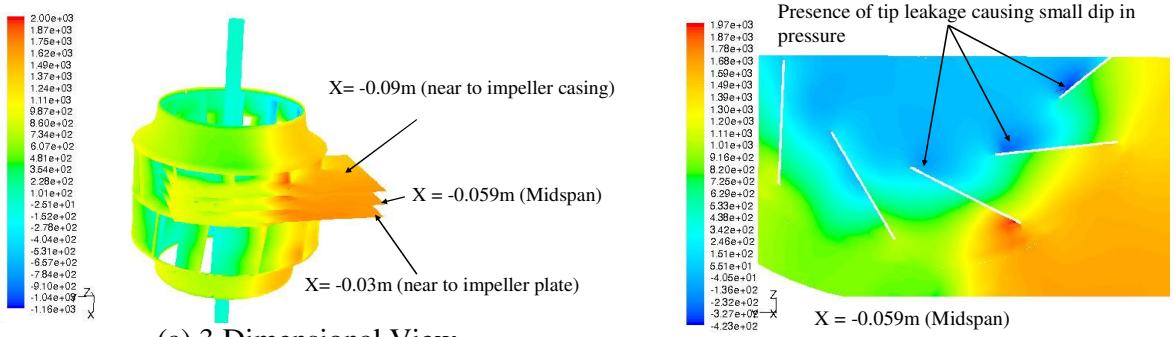
Figure 3.63 shows the contour plot of relative velocity magnitude at blade to blade plane. It is shown that the relative velocity is higher at the pressure side of the blade and is lower at the suction side of the blade. Lapworth and Elder [58] state that the major flow mechanisms which contribute to the formation and development of the wake include the secondary flows induced by the curvature and rotation of the impeller, boundary layer growth on blade surface, flow separation at the suction side of blade, impeller geometry, flow rate and operating speed.

Figure 3.64 shows the contour plot of gauge static pressure on the plane behind the blades. A midline is drawn along that plane so that the jet wake velocity profile can be studied. According to Figure 3.65(a), at the impeller discharge, the region near to the pressure side of the blade has a higher gauge static pressure than the suction side of the blade. The absolute velocity profile at the impeller discharge showing the presence of jet wake phenomena is as shown in Figure 3.65(b). The relative velocity profile at the impeller

ATTENTION: The Singapore Copyright Act applies to the use of this document. Nanyang Technological University Library

discharge showing the presence of jet wake phenomena is as shown in Figure 3.65(c). It is noted that at the jet region near to the pressure side of the blade, the relative velocity profile is positive, while at the wake region near to the suction side of the blade, the relative velocity profile is negative. This means that the relative direction flow vectors at the jet and wake are opposite to one another. Figure 3.65(d) shows that the jet region has a higher relative velocity magnitude than the wake region. It is useful to study the relative velocity profile behind many planes behind the blades as shown in Figure 3.66 so that the relative velocity profile of the jet wake flow can be visualized clearly. Figure 3.67 shows the plot of relative velocity profile of the jet wake flow which has an oscillating profile. These findings are verified by hot wire anemometer at the rim of the centrifugal impeller by Dean [9].

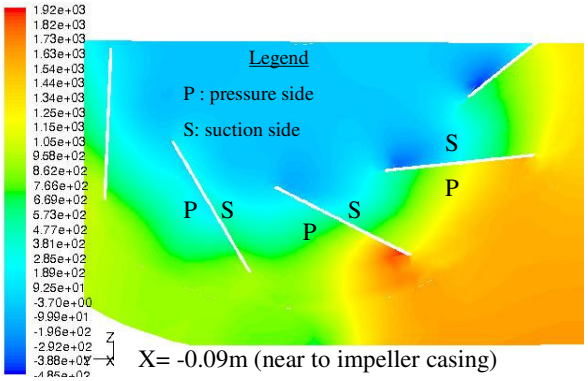
The 3-dimensional view of the planes between two blades is plotted as shown in Figure 3.68(a). The three planes are plotted in Figure 3.68(b), Figure 3.68(c) and Figure 3.68(d) to study the pressure distribution at different sections between the blades. It is shown from Figure 3.69 that there is a static pressure rise along the flow passages. The average gauge static pressure on 25 % plane between the blades is 606.22852 Pa. The average gauge static pressure on mid-plane between the blades is 755.1009 Pa. The average gauge static pressure on the 75 % plane between the blades is 942.9097 Pa. Hence, the gauge static pressure near to the pressure side of the blade is higher. The gradient of static pressure rise along the flow passages is similar along these 3 planes. Figure 3.70 shows the vortex flow structure at a plane between two blades.



(a) 3 Dimensional View (b) 2-Dimensional View

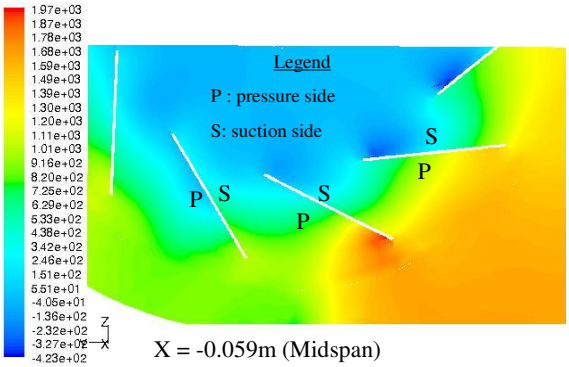
Figure 3.59 Blade to blade planes at (a) 3 Dimensional View and (b) 2-dimensional view

ATTENTION: The Singapore Copyright Act applies to the use of this document. Nanyang Technological University Library



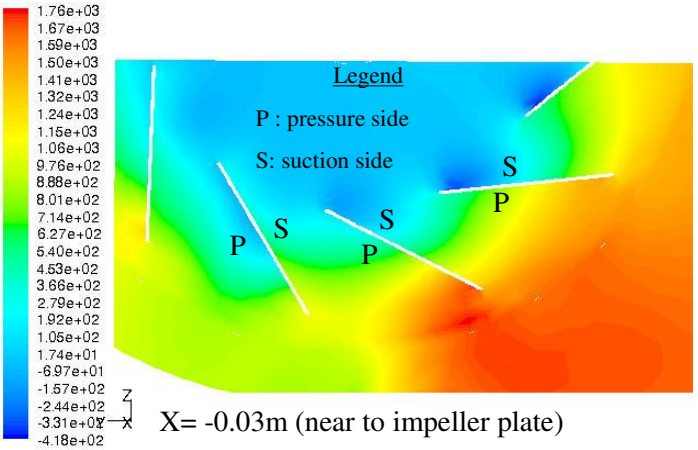
X= -0.09m (near to impeller casing)

(a) Near to impeller casing



X = -0.059m (Midspan)

(b) Midspan



X= -0.03m (near to impeller plate)

(c) Near to impeller plate

Figure 3.60 Contour plot of gauge static pressure on blade to blade plane at (a) near to impeller casing, (b) midspan and (c) near to impeller plate for 1.2 m^3/s, 2200 rpm

ATTENTION: The Singapore Copyright Act applies to the use of this document. Nanyang Technological University Library

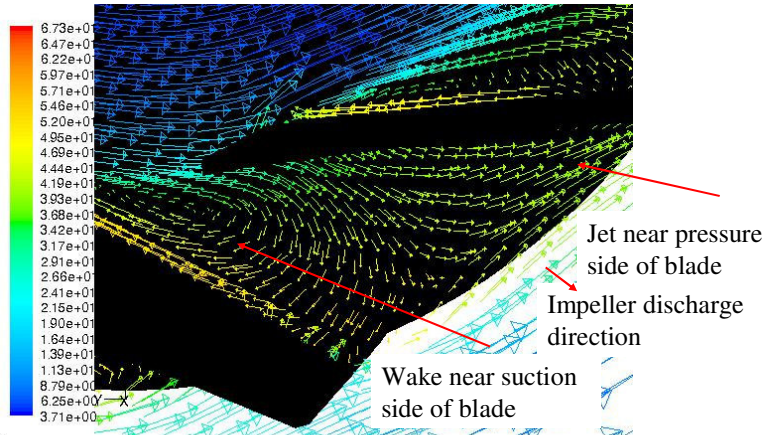
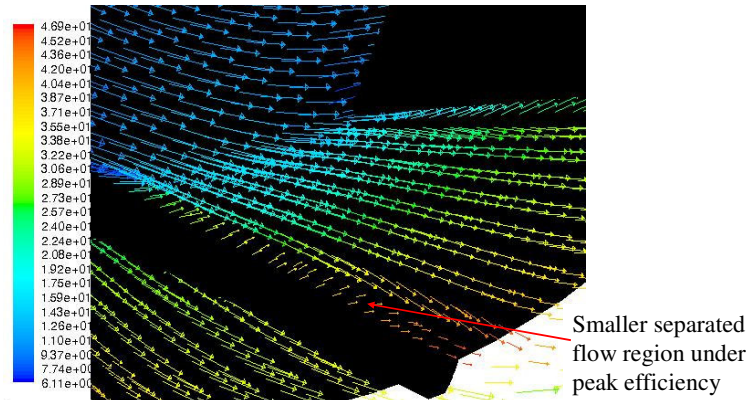
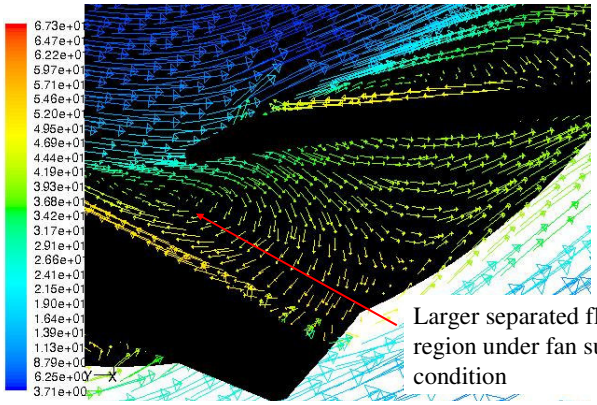


Figure 3.61 Plot of relative velocity vectors on blade to blade plane for 1.2 m^3/s, 2200 rpm



(a) Peak efficiency



(b) Surge

Figure 3.62 Plot of relative velocity vectors on blade to blade plane for 2200 rpm under (a) peak efficiency and (b) surge

ATTENTION: The Singapore Copyright Act applies to the use of this document. Nanyang Technological University Library

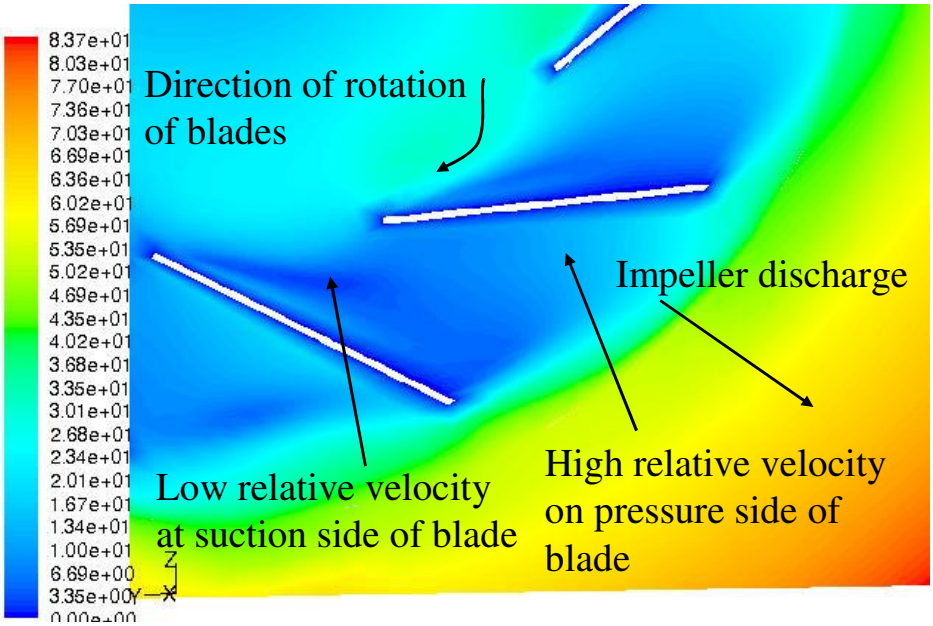


Figure 3.63 Contour plot of relative velocity magnitude on blade to blade plane for 1.2 m^3/s, 2200 rpm

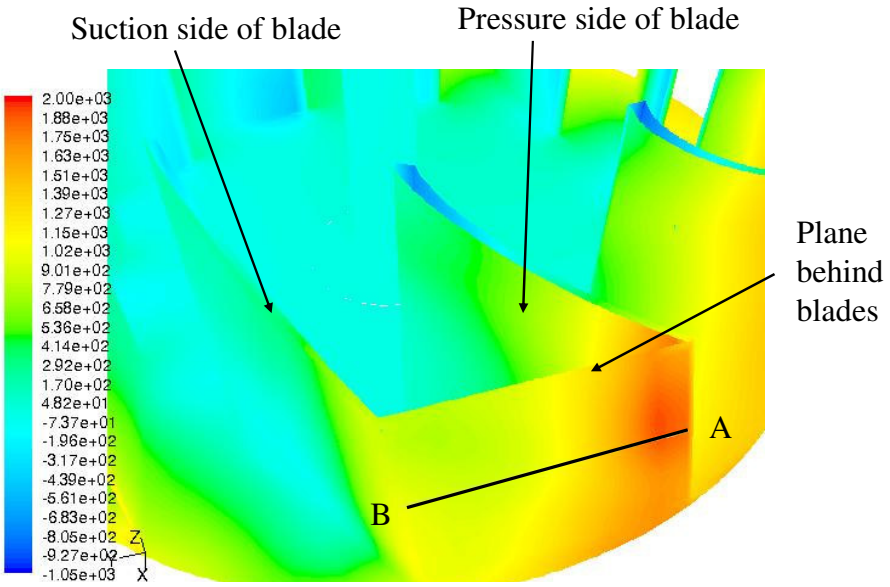
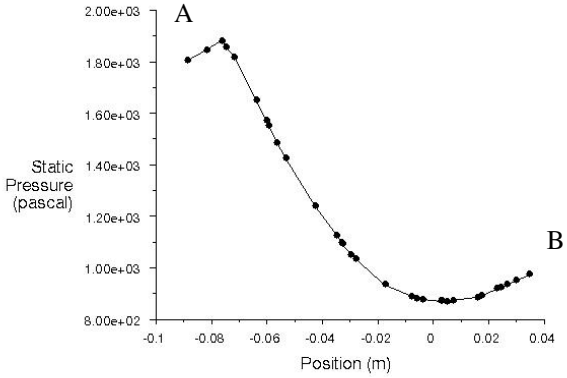
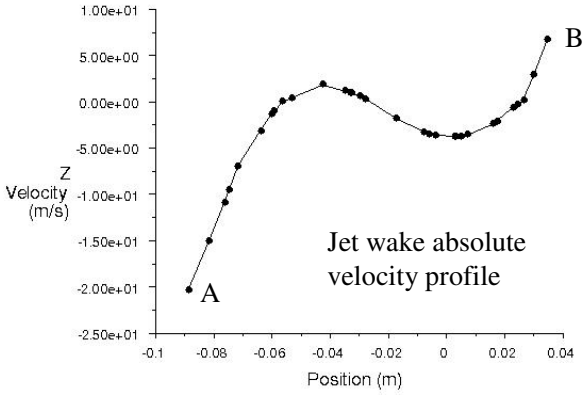


Figure 3.64 Contour plots of plane behind blades for 1.2 m^3/s, 2200 rpm

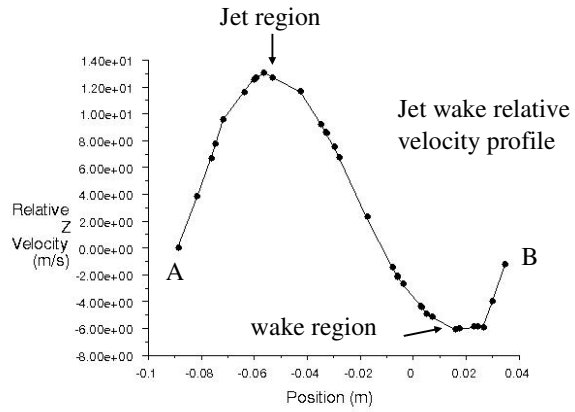
ATTENTION: The Singapore Copyright Act applies to the use of this document. Nanyang Technological University Library



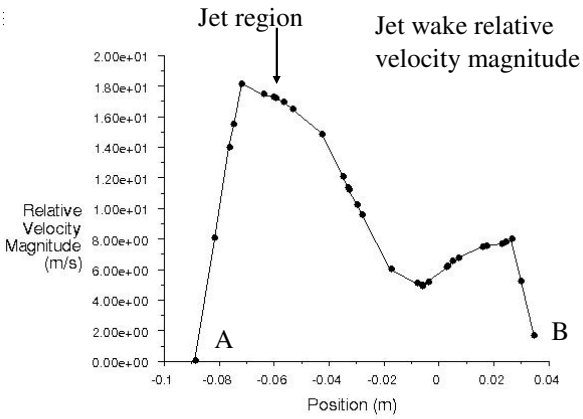
(a) Gauge static pressure



(b) Absolute velocity profile



(c) Relative velocity profile



(d) Relative velocity magnitude

Figure 3.65 Comparison on plots along line on plane behind blades for (a) gauge static pressure, (b) absolute velocity profile, (c) relative velocity profile and (d) relative velocity magnitude for 1.2 m^3/s, 2200 rpm

ATTENTION: The Singapore Copyright Act applies to the use of this document. Nanyang Technological University Library

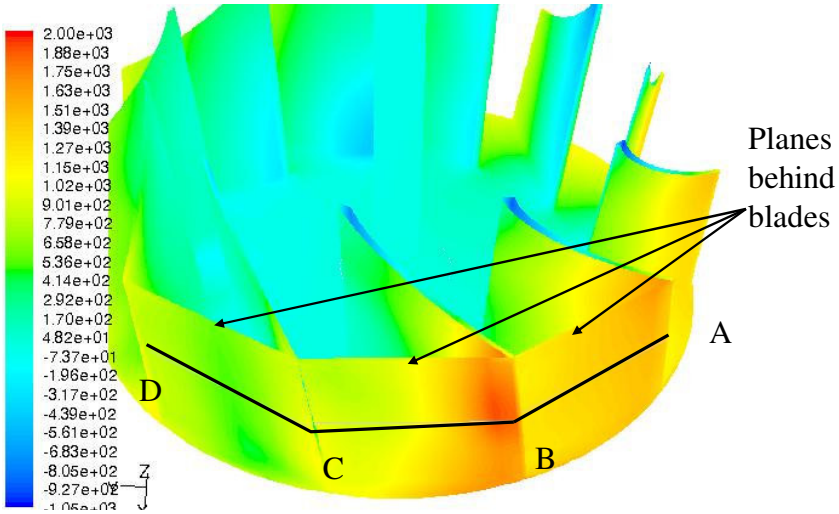


Figure 3.66 Contour plot of gauge static pressure on many planes behind blades for relative velocity profile for 1.2 m^3/s, 2200 rpm

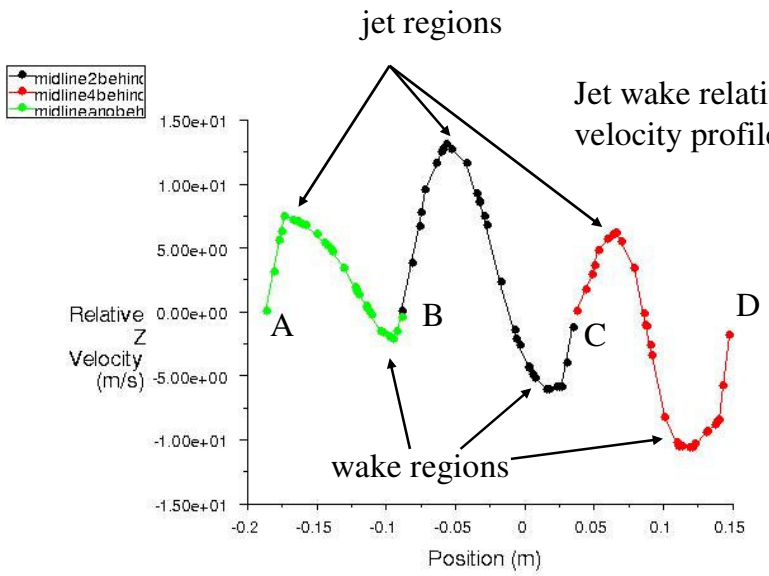


Figure 3.67 Plot of relative velocity profile along lines on many planes behind blades for 1.2 m^3/s, 2200 rpm

ATTENTION: The Singapore Copyright Act applies to the use of this document. Nanyang Technological University Library

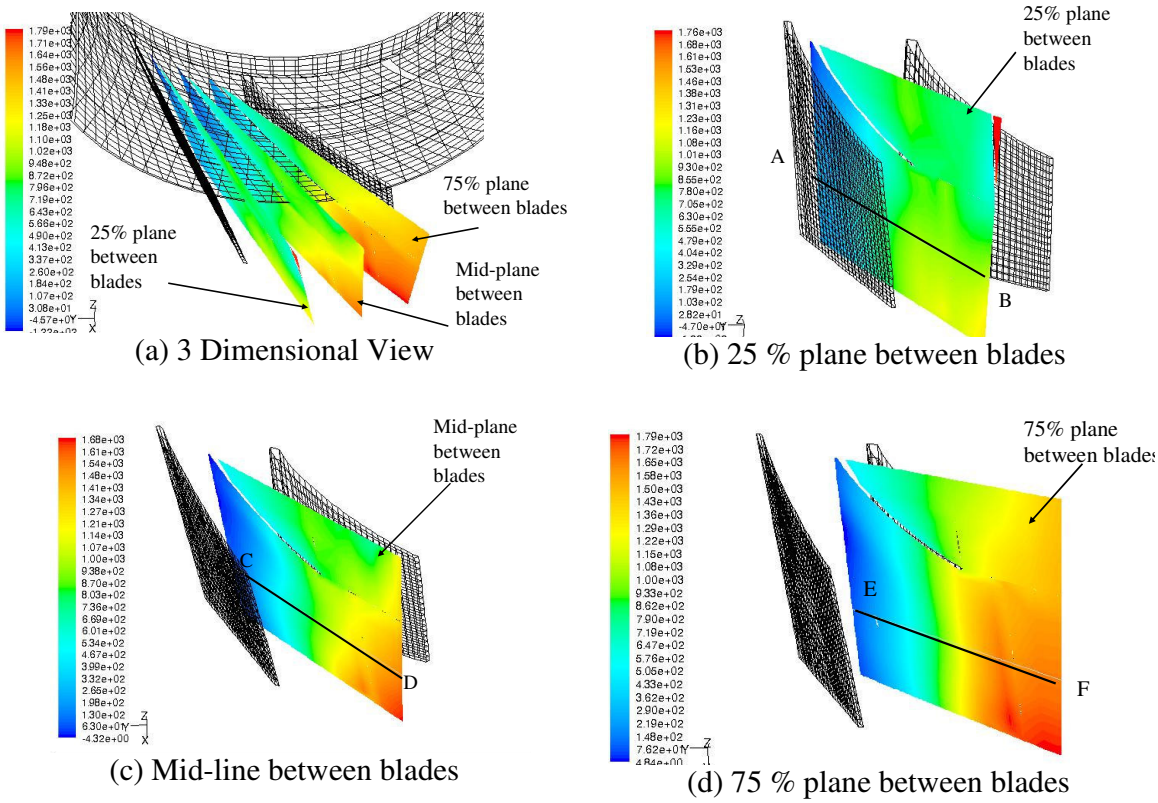


Figure 3.68 Comparison between contour plot of gauge static pressure for planes between blades at (a) 3 Dimensional View, (b) 25 % plane between blades, (c) mid-line between blades and (d) 75 % plane between blades

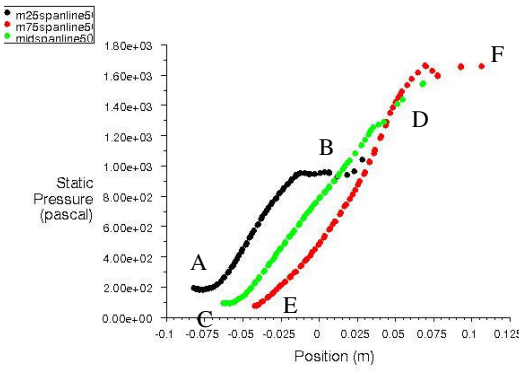


Figure 3.69 Plot of gauge static pressure along lines on planes between blades for 1.2 m^3/s, 2200 rpm

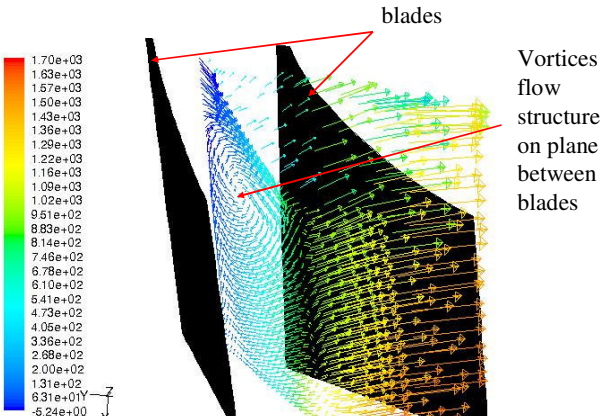


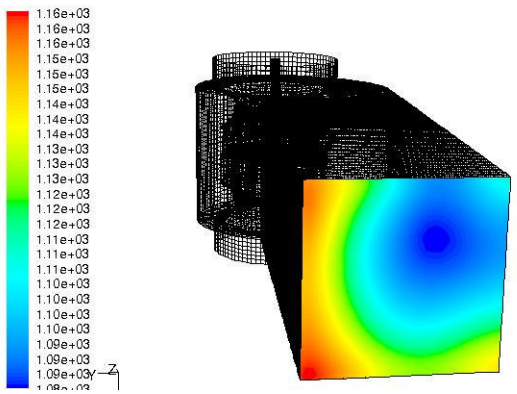
Figure 3.70 Plot of relative velocity vectors on plane between blades for 1.2 m^3/s, 2200 rpm

ATTENTION: The Singapore Copyright Act applies to the use of this document. Nanyang Technological University Library

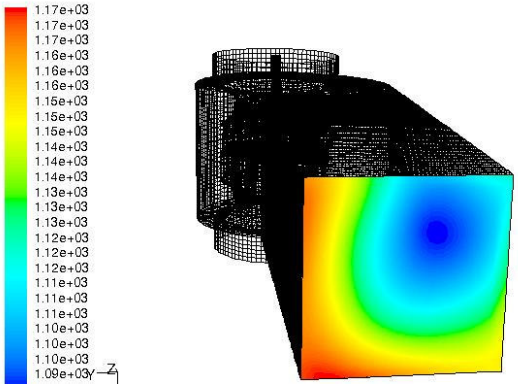
3.5.2.1.4 Comparison between Impellers Rotating in Different Directions

Fan performance characteristics with top and bottom impellers rotating in opposing directions are studied in this section, in which pressure contour plot at the outlet; surface pressure distribution and pressure contour plots at different plane sections are presented. A case of top and bottom impellers rotating in opposing directions have been done to compare with the general case of top and bottom impeller plates with casing and blades rotating in same direction. This is to check the possibility of using top and bottom impellers rotating in opposing directions to generate higher efficiency through a higher gauge total pressure.

Figure 3.71(a) shows the contour plot of gauge static pressure at the outlet for the case of top and bottom impellers rotating in opposing direction. Figure 3.71(b) shows the contour plot of gauge total pressure for the case of top and bottom impellers rotating in opposing direction. When compared with Figure 3.72(a) and Figure 3.72(b), which is the case of top and bottom impellers rotating in same direction, it is noted that rotation in different directions for the top and bottom impellers has created a smaller pressure at the outlet and hence it is undesirable. That is the reason why the double inlet fan has its top and bottom impellers rotating in same direction for the general case. Hence, it is not possible to change the direction of rotation of fan to generate higher efficiency.



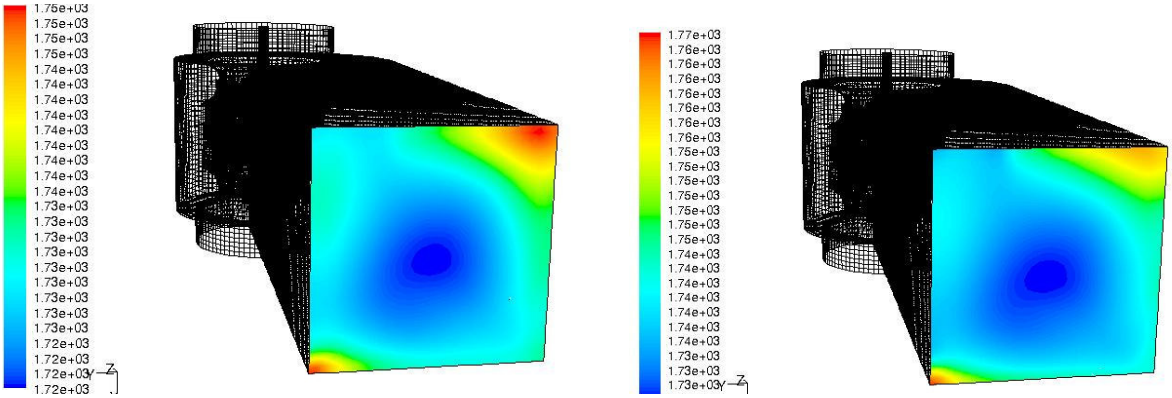
(a) Gauge static pressure at outlet
Average gauge static pressure: 1113.351 Pa



(b) Gauge total pressure at outlet
Average gauge total pressure: 1128.513 Pa

Figure 3.71 Contour plot of (a) gauge static pressure and (b) gauge total pressure at outlet for 1.2 m^3/s, 2200 rpm with top and bottom impellers rotating in different direction

ATTENTION: The Singapore Copyright Act applies to the use of this document. Nanyang Technological University Library



(a) Gauge static pressure at outlet
Average gauge static pressure: 1728.527 Pa

(b) Gauge total pressure at outlet
Average gauge total pressure: 1737.845 Pa

Figure 3.72 Contour plot of (a) gauge static pressure and (b) gauge total pressure at outlet for 1.2 m^3/s, 2200 rpm with top and bottom impellers rotating in same direction

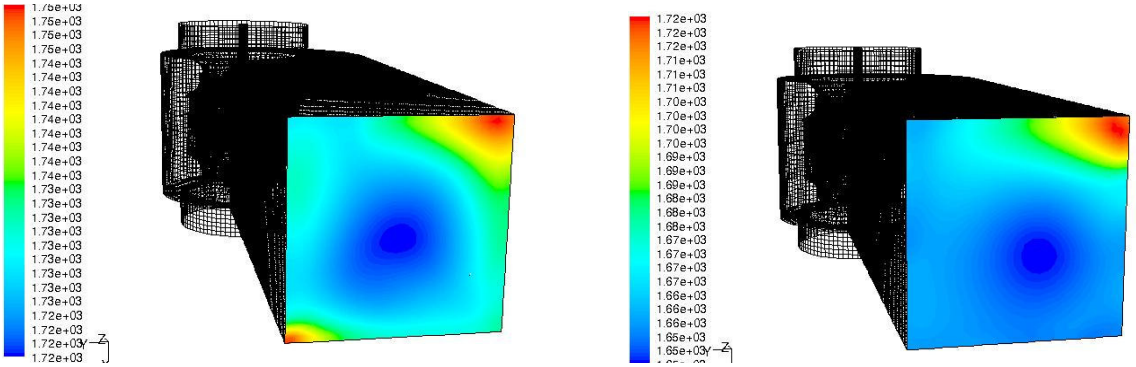
3.5.2.1.5 Alignment of Top and Bottom Impellers Geometry

The case of blades and impellers rotating at 2200 rpm with volume flow rate 1.2 m^3/s at the outlet has been used to study the fan performance characteristics of double inlet fan when the geometry of fan is modified such that the top and bottom impellers are aligned. A case of the geometry of top and bottom impellers aligned have been done to compare with the general case of top and bottom impeller plates with casing and blades rotating in same direction. This is to check the possibility of using a modified geometry with top and bottom impellers aligned to generate higher efficiency through a higher gauge total pressure.

Figure 3.74(b) shows the contour plot of gauge total pressure at the outlet when the geometry of top and bottom impellers is aligned. When compared with Figure 3.74(a), which shows the contour plot of gauge total pressure at outlet before, the geometry is modified, the alignment of top and bottom impellers geometry has given a slightly lower gauge total pressure at the outlet. That is the reason why the geometry of double inlet fan has its top and bottom impellers unaligned for the general case. Hence, it is not possible to use modified geometry of aligned top and bottom impellers to generate higher efficiency. Figure 3.75(a) and Figure 3.75(b) show the gauge static pressure distribution on impeller without impeller casing and with impeller casing and inlet cone respectively for the

ATTENTION: The Singapore Copyright Act applies to the use of this document. Nanyang Technological University Library

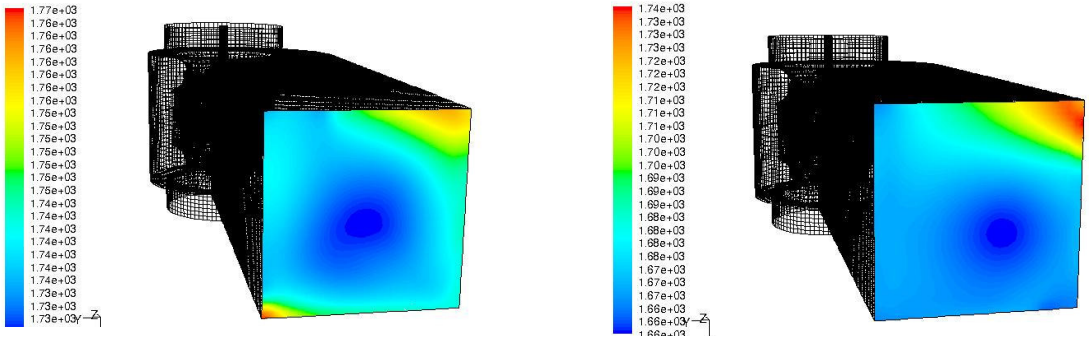
geometry of top and bottom impellers and blades aligned. Pressure contour plot at *XY* plane at Z = 0m as shown in Figure 3.76 are plotted to study the effect of the alignment of impellers geometry on pressure distribution. It is noted from the comparison between Figure 3.77(a) and Figure 3.77(b) that the alignment of top and bottom impellers gave a symmetrical pressure distribution about the Y-axis. This is because of the symmetrical geometry for the aligned impellers.



(a) Top and Bottom Impellers before Aligned
Average gauge static pressure: 1728.527 Pa

(b) Top and Bottom Impellers Aligned
Average gauge static pressure: 1661.725 Pa

Figure 3.73 Comparison between contour plot of gauge static pressure at outlet for 1.2 m^3/s, 2200 rpm for (a) top and bottom impellers before aligned and (b) top and bottom impellers aligned

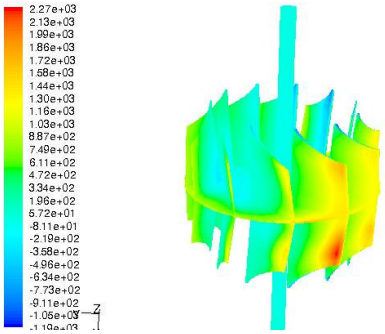


(a) Top and Bottom Impellers before Aligned
Average gauge total pressure: 1737.845 Pa

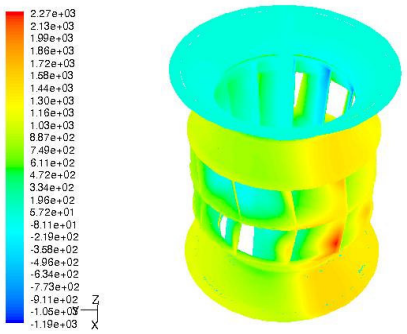
(b) Top and Bottom Impellers Aligned
Average gauge total pressure: 1672.268 Pa

Figure 3.74 Comparison between contour plot of gauge total pressure at outlet for 1.2 m^3/s, 2200 rpm for (a) top and bottom impellers before aligned and (b) top and bottom impellers aligned

ATTENTION: The Singapore Copyright Act applies to the use of this document. Nanyang Technological University Library

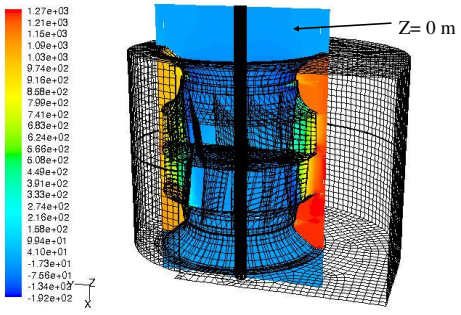


(a) Impellers

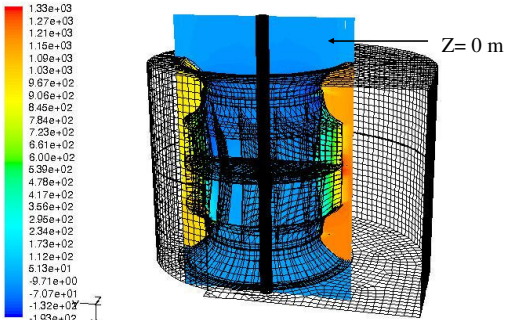


(b) Impellers with impeller casing and inlet cone

Figure 3.75 Contour plot of gauge static pressure for (a) impellers and (b) impellers with impeller casing and inlet cone for 1.2 m^3/s, 2200 rpm with top and bottom impellers alignment

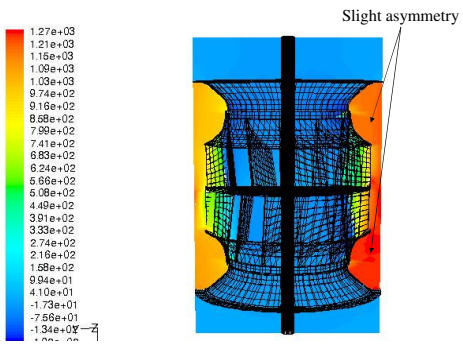


(a) Top and Bottom Impellers before alignment

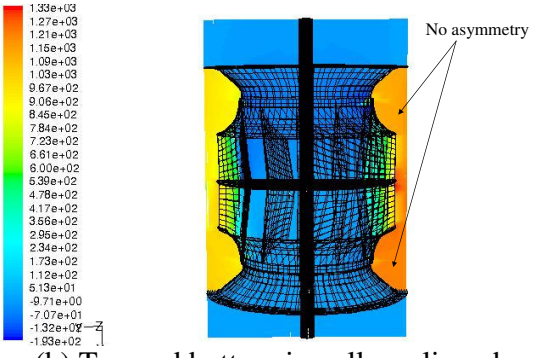


(b) Top and bottom impellers aligned

Figure 3.76 3-Dimensional View of the plane Z = 0 m for 0.95 m^3/s, 2500 rpm (a) top and bottom impellers before alignment and (b) top and bottom impellers aligned



(a) Top and Bottom Impellers before alignment



(b) Top and bottom impellers aligned

Figure 3.77 Comparison between contour plot of gauge static pressure at XY plane for 1.2 m^3/s, 2200 rpm (a) top and bottom impellers before aligned and (b) top and bottom impellers aligned

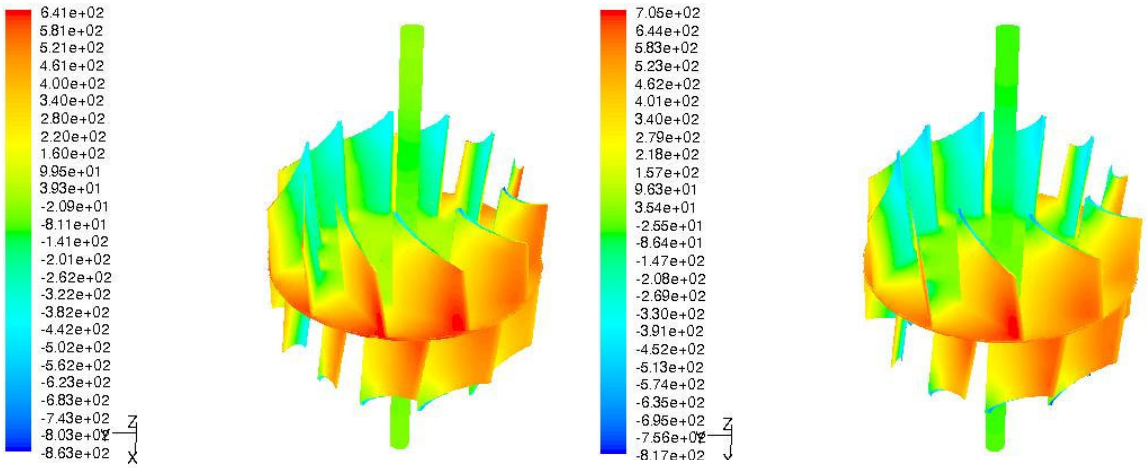
ATTENTION: The Singapore Copyright Act applies to the use of this document. Nanyang Technological University Library

3.5.2.1.6 Effects of number of blades

The effects of the number of blades on the impeller have been studied in this section. The channel between the blades has to be narrow enough for good guidance of the air stream. On the other hand, it has to be wide enough so that the resistance to airflow is not too great. Bleier [45] postulates that between 8 and 12 blades is good selection for most designs. The unoptimzied design geometry of the fan used 11 blades. In this section, flow simulation results of 11-bladed impeller, 10-bladed impeller, 9-bladed impeller and 8-bladed impeller rotating at 1600 rpm with volume flow rate 2.5 m^3/s at the outlet have been obtained. The rest of the fan geometry remains unchanged.

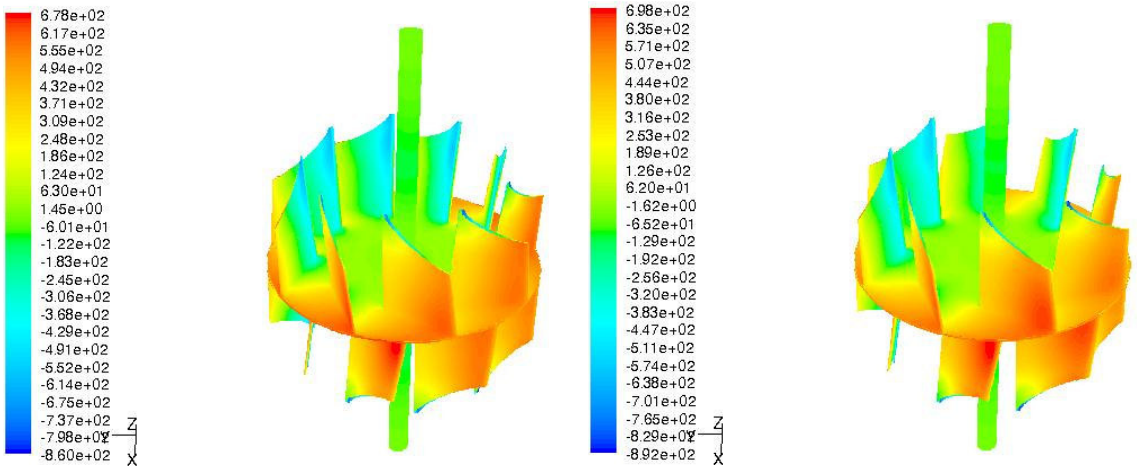
Figure 3.78 shows the gauge static pressure distribution on the impellers with different number of blades. Figure 3.79 shows the contour plot of gauge total pressure at the outlet for 11-bladed impeller, 10-bladed impeller, 9-bladed impeller and 8-bladed impeller rotating at 1600 rpm with volume flow rate 2.5 m^3/s. It is noted that the 11-bladed impeller gives the highest total efficiency. This is probably true because the original fan geometry has 11-bladed impeller because experimental results have already proven that the 11-bladed impeller would give the highest total efficiency. Nevertheless, Figure 3.79(d) shows that the 8-bladed impeller gives a total efficiency which is only 2.289 % lower than the peak efficiency for the 11-bladed impeller. Hence, it is a feasible to try to work on the 8-bladed impeller by improving its total efficiency so that it can match that of the 11-bladed impeller. The advantage of using the 8-bladed impeller is that it is most cost effective as less material is needed to make the fan.

ATTENTION: The Singapore Copyright Act applies to the use of this document. Nanyang Technological University Library



(a) 11-Bladed Impeller

(b) 10-Bladed Impeller

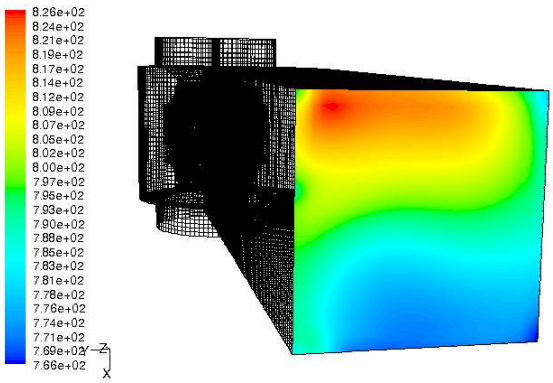


(c) 9-Bladed Impeller

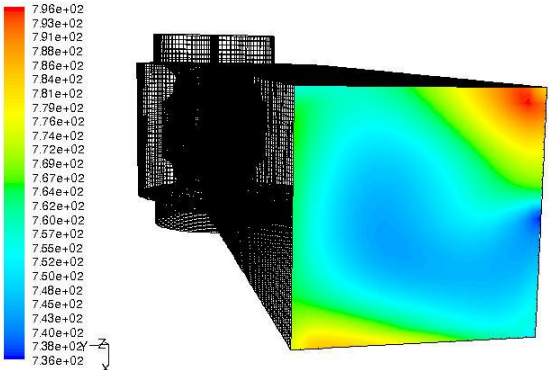
(d) 8-Bladed Impeller

Figure 3.78 Contour plot of gauge static pressure for (a) 11-bladed impeller and (b) 10-bladed impeller, (c) 9-bladed impeller and (d) 8-bladed impeller for double inlet fan (BDB fan), 1600 rpm and 2.5 m^3/s

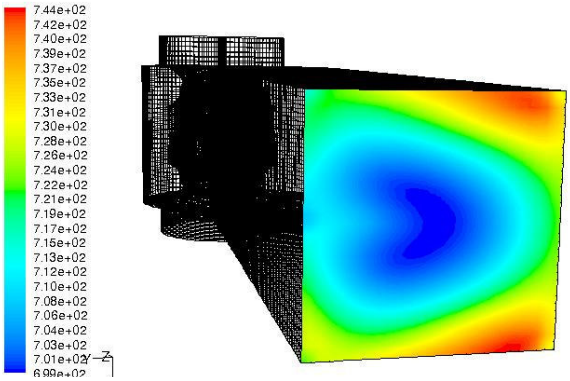
ATTENTION: The Singapore Copyright Act applies to the use of this document. Nanyang Technological University Library



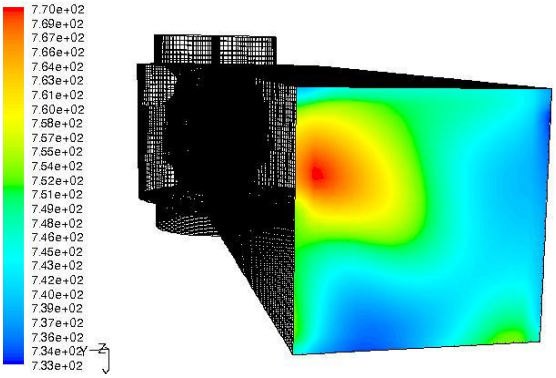
(a) 11-Bladed Impeller
Total Efficiency: 70.532 %



(b) 10-Bladed Impeller
Total Efficiency: 65.261 %



(c) 9-Bladed Impeller
Total Efficiency: 63.995 %



(d) 8-Bladed Impeller
Total Efficiency: 68.243 %

Figure 3.79 Contour plot of gauge total pressure at outlet for (a)11 bladed impeller and (b) 10 bladed impeller, (c) 9 bladed impeller and (d) 8 bladed impeller for BDB fan, 1600 rpm and 2.5 m^3/s

ATTENTION: The Singapore Copyright Act applies to the use of this document. Nanyang Technological University Library

3.5.2.1.7 Fan Performance Characteristics for Double Inlet Fan

In this section, plots of fan performance characteristics for the double inlet fan are shown. There are also some comparisons between the single inlet fan and the double inlet fan. Fan performance plots of double inlet fan have been done so that they can be used to compare with that of the optimized blade design for the double inlet fan. The optimized blade design has to give a higher total efficiency when compared with the original blade design. This is the reason why plots of total efficiency and gauge total pressure are plotted for the original blade design. This section shows the fan performance plots for original blade design.

Flow simulation results for the double inlet fan have been done as shown in Figure 3.80. It is shown from Figure 3.80 that the gauge total pressure at the outlet increases as volume flow rate decreases until the surge point is reached. Figure 3.81 shows the plot of total efficiency against volume flow rate for the experimental results and flow simulation result for double inlet fan. Both the experimental results and flow simulation results showed the maximum total efficiency when the volume flow rate is 3.33m^3/s. Flow simulation result is fairly accurate when compared with the experimental result with the percentage error defined as $\frac{|P_f - P_e|}{P_e} \times 100\%$ where P_f is the gauge total pressure at the fan outlet for flow simulation result and P_e is the gauge total pressure for experimental result. For example, the experimental result from industry database gives a gauge total pressure of 1750 Pa at the outlet for 1.2 m^3/s, 2200 rpm for the double inlet fan. The corresponding flow simulation result gives a value of gauge total pressure of 1737.845 Pa. This means that the percentage error is around 0.69 %. The percentage error between flow simulation result and experimental result is below 5 % for all tested volume flow rates.

Comparison between the single inlet fan and the double inlet fan has been done so as to justify the use of different fans for different purposes. It is shown from Figure 3.82 that the double inlet fan gives a higher gauge total pressure than the single inlet fan rotating in the same rpm and volume flow rate. This is because of the double inlet fan has two impellers instead of one impeller. Hence, the double inlet fan will generate a higher static pressure rise from the rotation of these impellers. The single inlet fan is not suitable for high volume

ATTENTION: The Singapore Copyright Act applies to the use of this document. Nanyang Technological University Library

flow rate as it is shown in Figure 3.82 that the gauge total pressure at the outlet decreases drastically at higher volume flow rate. This is because the single inlet fan has a smaller outlet area when compared with the double inlet fan. By having the same volume flow rate, the flow velocity through the outlet of the single inlet fan has to be higher than that of the double inlet fan, which will cause a drastic drop in gauge total pressure at the outlet. Figure 3.83 shows that the single inlet fan has a higher total efficiency than the double inlet fan despite giving out a lower gauge total pressure at the outlet. This is because the single inlet fan has a much lower power requirement than the double inlet fan. To rotate the impellers in the same rpm, the double inlet fan requires more power as it is turning two impellers instead of one. The higher gauge total pressure at the outlet for the double inlet fan is not enough to compensate for a much higher power requirement. The single inlet fan has a much lower total efficiency at higher volume flow rate due to a sudden reduction of gauge total pressure at the outlet. Hence, to sum up, the single inlet fan has a higher total efficiency than the double inlet fan at low volume flow rate but a lower total efficiency at high volume flow rate. The double inlet fan gives a higher gauge total pressure at the outlet but has a lower total efficiency due to a higher power requirement. Hence, for industrial purposes, the double inlet fan is desirable when a higher gauge total pressure is desired. The single inlet fan is desirable at low volume flow rate as it gives a higher total efficiency.

Comparison between the 11-bladed impeller fan, 10-bladed impeller fan, 9-bladed impeller fan and 8-bladed impeller fan has been done so as to justify the use of number of blades for different purposes. Figure 3.84 shows that the difference in gauge total pressure at the outlet for 11-bladed impeller fan, 10-bladed impeller fan, 9-bladed impeller fan and 8-bladed impeller fan are very marginal. Nevertheless, Figure 3.85 shows that at 2.5 m^3/s, the 8-bladed impeller fan gives a total efficiency which is quite close to that of the 11-bladed impeller fan.

ATTENTION: The Singapore Copyright Act applies to the use of this document. Nanyang Technological University Library

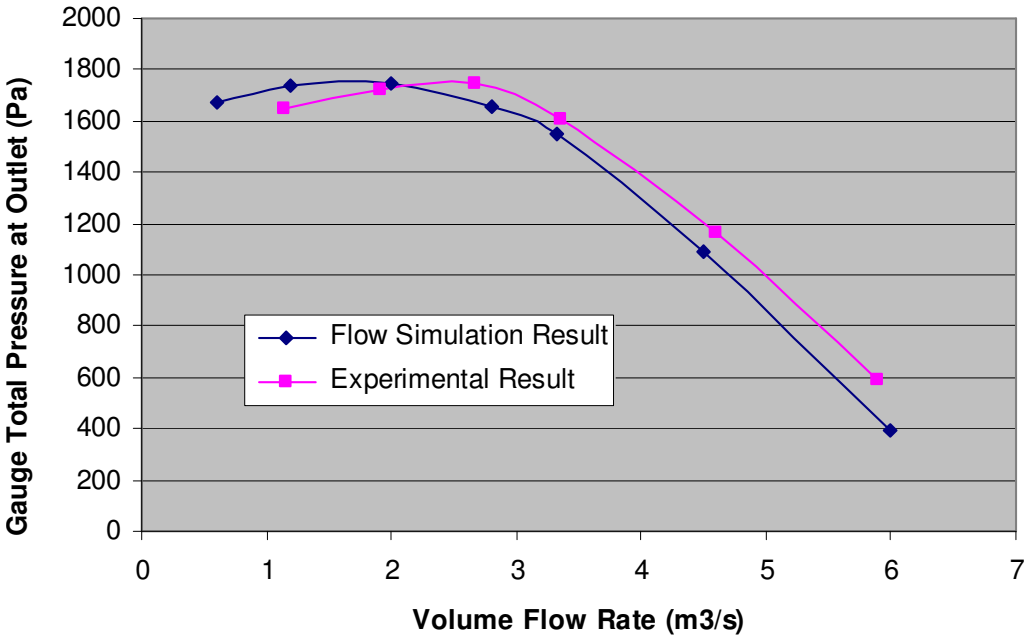


Figure 3.80 Plot of gauge total pressure at outlet against volume flow rate for double inlet fan running at 2200 rpm

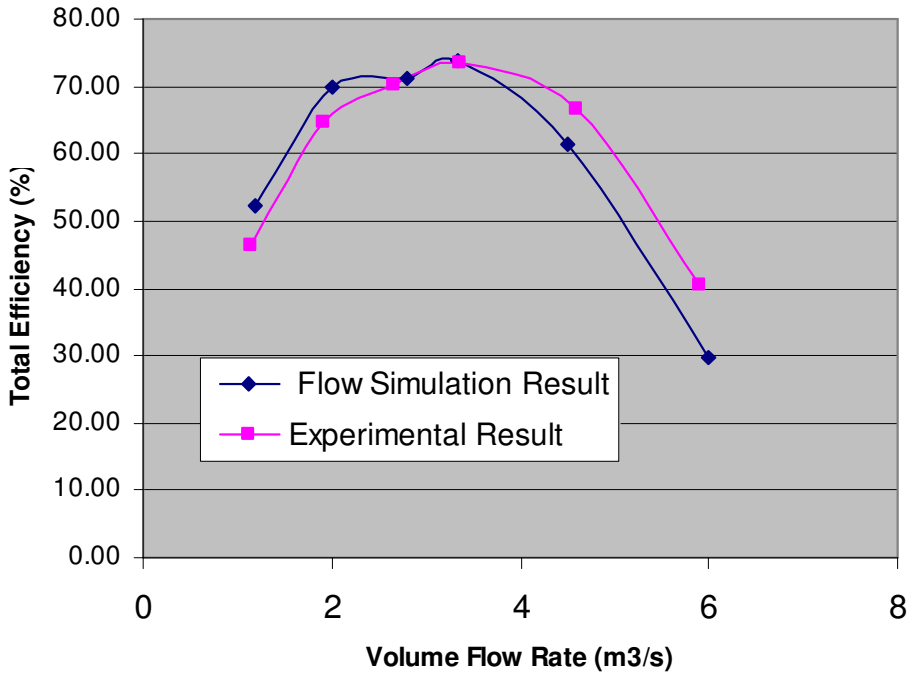


Figure 3.81 Plot of total efficiency for double inlet fan running at 2200 rpm

ATTENTION: The Singapore Copyright Act applies to the use of this document. Nanyang Technological University Library

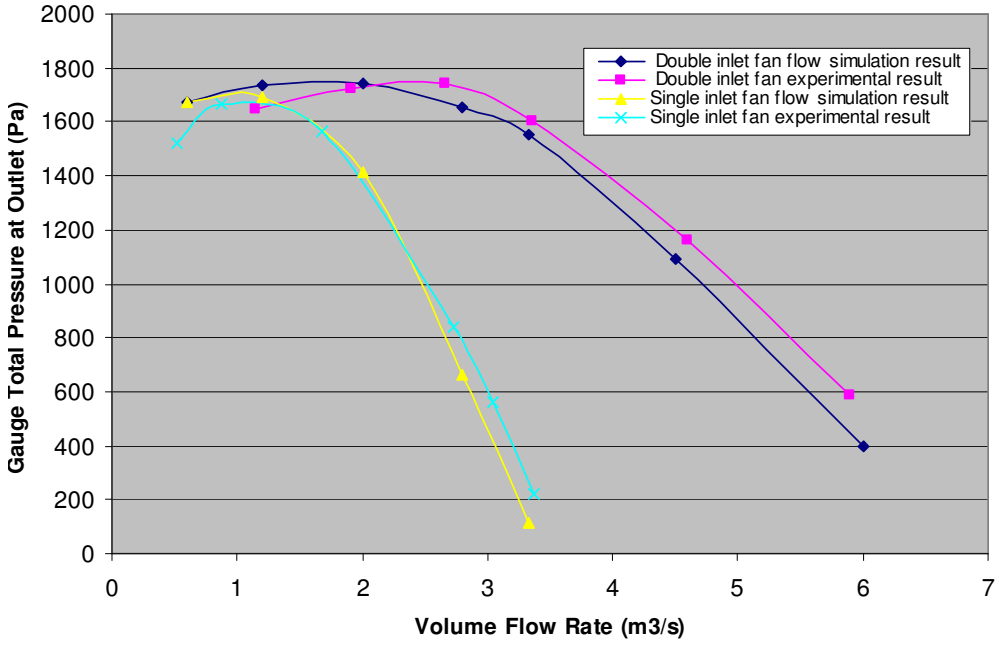


Figure 3.82 Plot of gauge total pressure at outlet against volume flow rate for single inlet fan and double inlet fan running at 2200 rpm

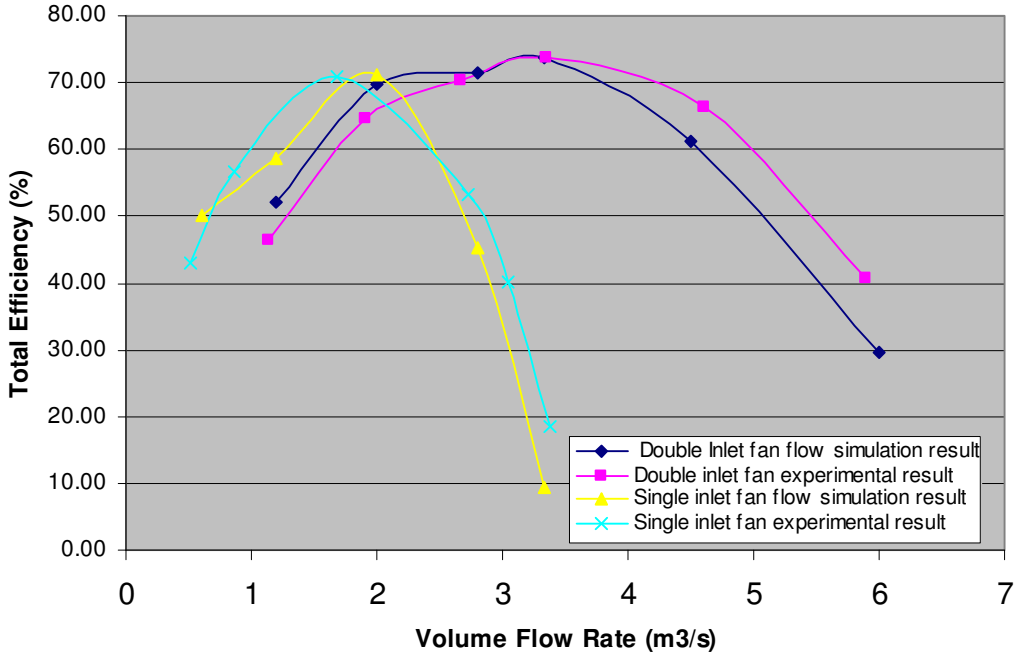


Figure 3.83 Plot of total efficiency for single inlet fan and double inlet fan running at 2200 rpm

ATTENTION: The Singapore Copyright Act applies to the use of this document. Nanyang Technological University Library

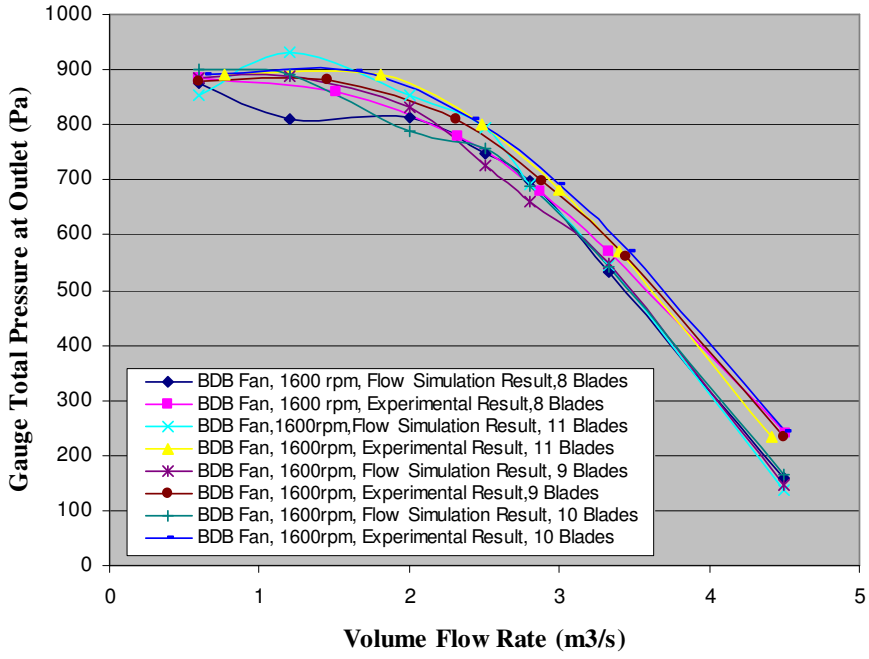


Figure 3.84 Plot of gauge total pressure at outlet against volume flow rate for double inlet fan running at 1600 rpm for different number of blades

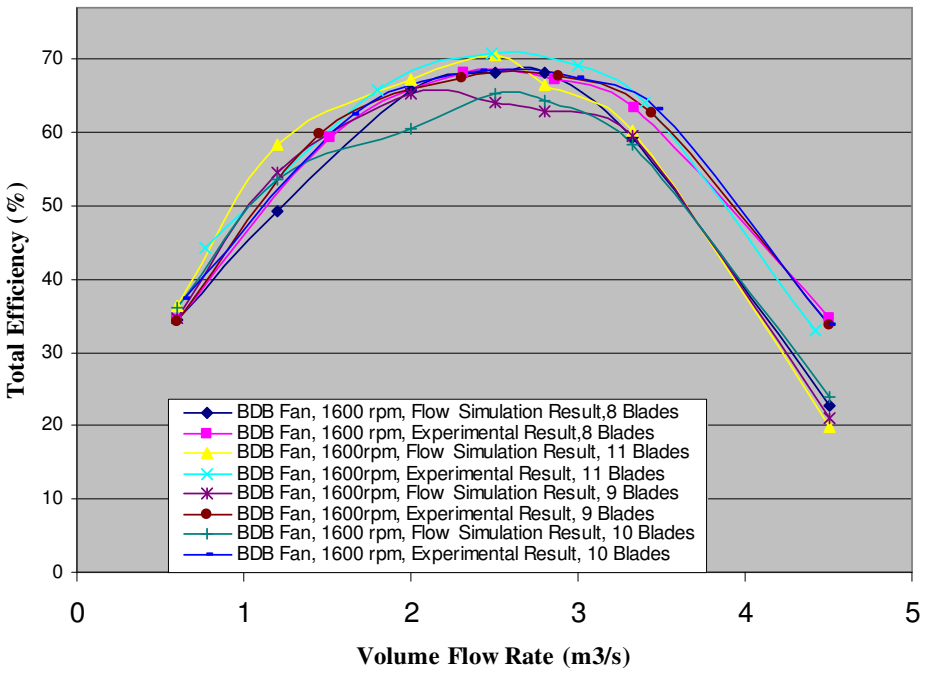


Figure 3.85 Plot of total efficiency against volume flow rate for double inlet fan running at 1600 rpm for different number of blades

ATTENTION: The Singapore Copyright Act applies to the use of this document. Nanyang Technological University Library

3.5.3 Airfoil Bladed Fan

It is suggested in Bleier [45], that centrifugal fans with airfoil blades have the highest efficiencies of all centrifugal fans. It is possible to replace single thickness blades for the unoptimized design with airfoil blades so that higher efficiencies can be obtained. For centrifugal fans with airfoil blades, the passages between adjacent blades are gradually expanding for minimum turbulence. This section shows the flow simulation results for the airfoil bladed fan, which discuss about the computed steady state flow fields of the airfoil bladed fan.

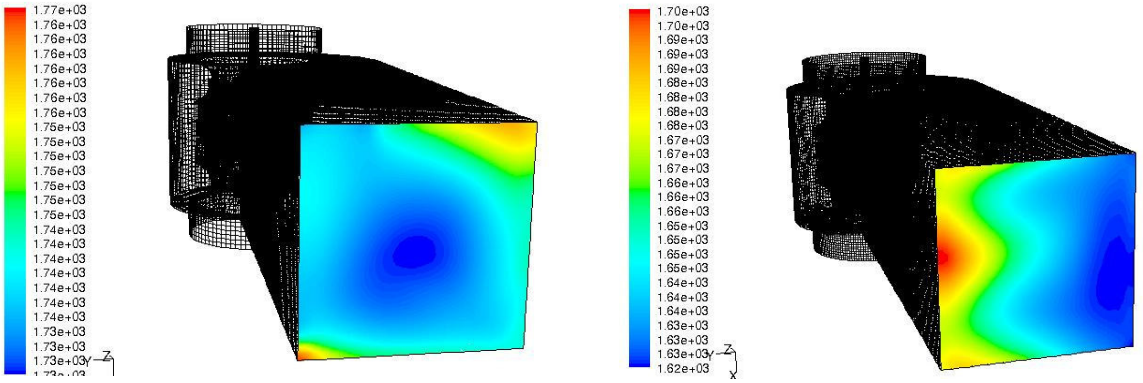
3.5.3.1 Computed Steady State Flow Fields in Airfoil Bladed Fan

In this section, pressure contour plot at outlet, surface pressure distribution for the case of blades and impeller rotating at 2200 rpm with volume flow rate 1.2 m^3/s at the outlet and are presented. The general fan performance characteristics of the airfoil bladed fan have been compared with that of the double inlet fan.

3.5.3.1.1 Pressure Contour Distribution at Outlet and Surface Pressure Distribution

The computed total pressure contours at the outlet of the fan using blades with airfoil sections is shown in Figure 3.86(b). The double inlet centrifugal fan using single thickness edge blades has a gauge total pressure of 1737.845 Pa which is higher than the gauge total pressure at the outlet for the airfoil bladed fan which is 1647.416 Pa for the same volume flow rate and rpm. The power required for rotation for the airfoil blade fan is lower than that of the single thickness bladed fan. The total efficiency of the airfoil blade fan is 51.1 % which is slightly lower than that of single thickness bladed fan at 52.1 %. This discrepancy is due to the flow simulation result for airfoil bladed fan giving a lower gauge total pressure at the outlet when compared with experimental result. The airfoil blade profile can be seen in Figure 3.87 (b). Figure 3.88 shows that for the fan using airfoil section blades, the flow between the blade passages is shared more equally such that there is an almost equal distribution of gauge static pressure in each blade passages. Figure 3.89 shows the presence of flow separation and vortices between blade passages for the airfoil blade fan.

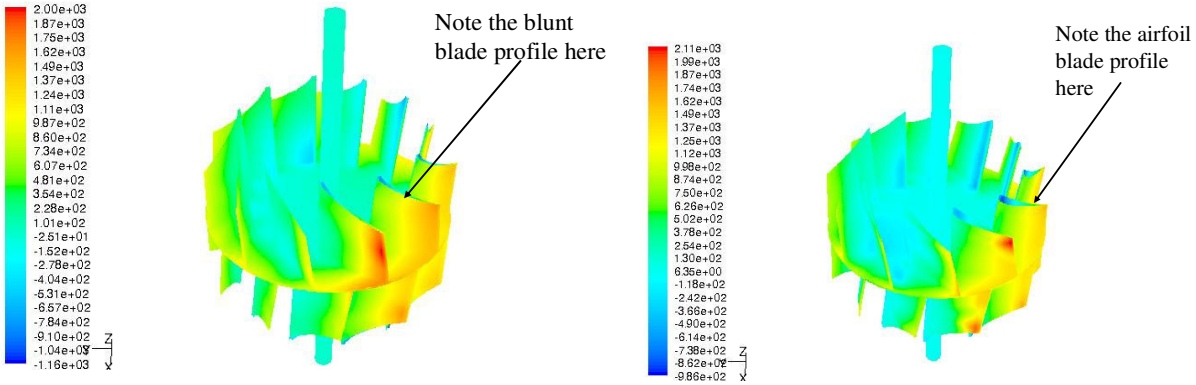
ATTENTION: The Singapore Copyright Act applies to the use of this document. Nanyang Technological University Library



(a) Double inlet fan
Average gauge total pressure: 1737.845 Pa

(b) Airfoil bladed fan
Average gauge total pressure: 1647.416 Pa

Figure 3.86 Comparison of contour plot of gauge total pressure at outlet for (a) double inlet fan and (b) airfoil bladed fan at 1.2m^3/s, 2200rpm



(a) Double inlet fan

(b) Airfoil bladed fan

Figure 3.87 Comparison of gauge static pressure distribution on impellers for (a) double inlet fan and (b) airfoil bladed fan at 1.2m^3/s, 2200rpm

ATTENTION: The Singapore Copyright Act applies to the use of this document. Nanyang Technological University Library

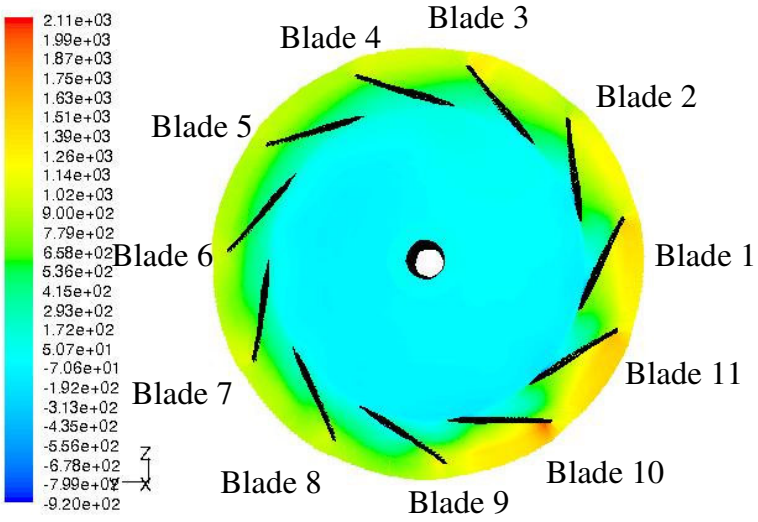


Figure 3.88 Contour plot of gauge static pressure for blade passages (Top view) for 1.2m^3/s, 2200rpm for airfoil bladed fan

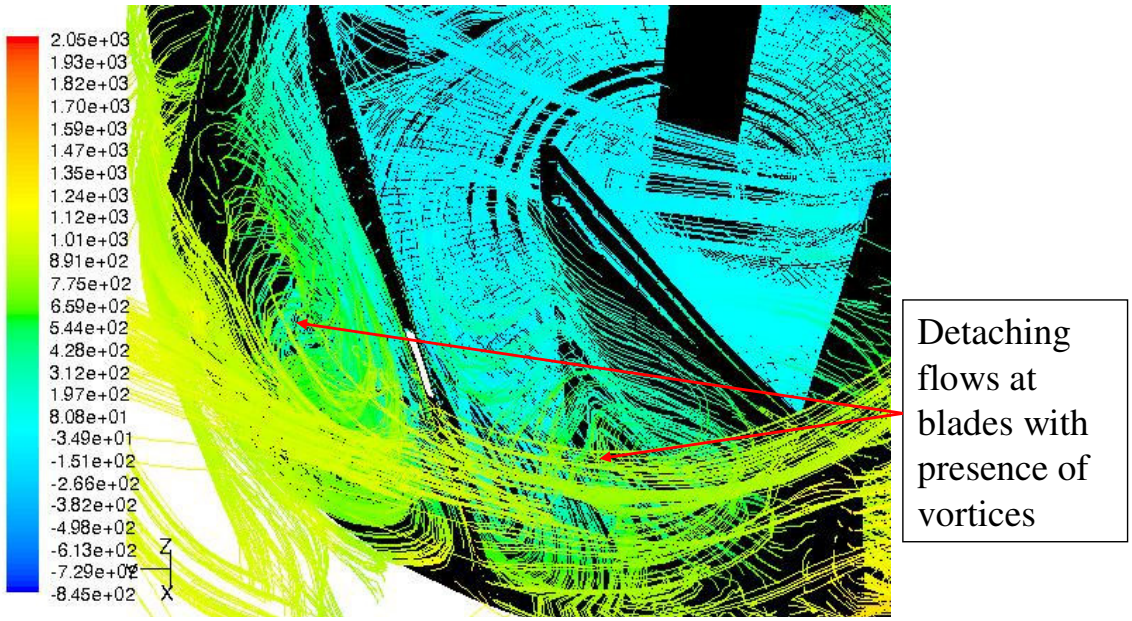


Figure 3.89 Streamline aft blade arrangement in zoom in 3 dimensional view for 1.2m^3/s, 2200rpm for airfoil blade fan

ATTENTION: The Singapore Copyright Act applies to the use of this document. Nanyang Technological University Library

3.5.3.1.2 Fan Performance Characteristics for Airfoil Bladed Fan

In this section, the fan performance characteristics for the airfoil bladed fan have been plotted. There are also some comparisons between the double inlet fan and the airfoil bladed fan. Plot of computed gauge total pressure vs. volume flow rate for airfoil bladed fan is compared with experimental data provided by the vendor. Figure 3.90 shows that the gauge total pressure at the outlet increases with decreasing volume flow rate until the surge point is reached for the airfoil blade fan, while the single thickness bladed fan has a higher gauge total pressure than the airfoil bladed fan for the corresponding volume flow rate.

Figure 3.91 compares the computed total efficiency against volume flow rate curves for the airfoil bladed fan and double inlet fan. Differences between flow simulation result and experimental results can be observed although the trends are very similar. It appears by comparing the experimental results that the total efficiency of the airfoil bladed fan is slightly higher than that of the single thickness bladed fan due to a lower power requirement. There is not much improvement in total efficiency with the airfoil blades because in centrifugal fan, the aerodynamic lift contributed by the airfoil blades does not contribute much to the impeller pressure rise. The airfoil bladed fan has higher total efficiency than the single thickness bladed fan at high volume flow rate. However, the single thickness bladed fan can reach a higher maximum efficiency than the airfoil bladed fan. This is also observed from the experimental results.

The experimental result is obtained by running the ventilation fan at a certain rpm. Fan laws are then applied to calculate the corresponding gauge static pressure at the outlet. The experimental result is based on the assumption of the applicability of the fan laws and the formula for the calculation of gauge dynamic pressure. However, fan laws may not be applicable due to Reynolds number effect as the fan is tested below the threshold Reynolds number. Moreover, the experimental result is obtained in a wind tunnel test, which is different from the flow simulation setup. This could explain why there is a small difference between experimental and flow simulation result and this matter needs to be addressed in the future.

ATTENTION: The Singapore Copyright Act applies to the use of this document. Nanyang Technological University Library

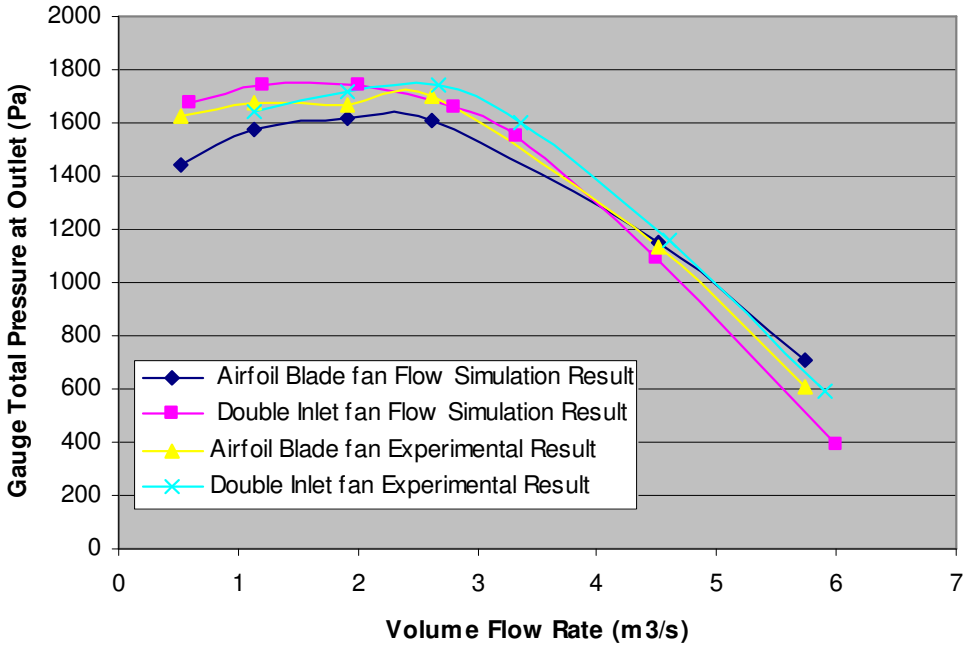


Figure 3.90 Plot of gauge total pressure at outlet against volume flow rate for airfoil blade fan and double inlet fan running at 2200rpm

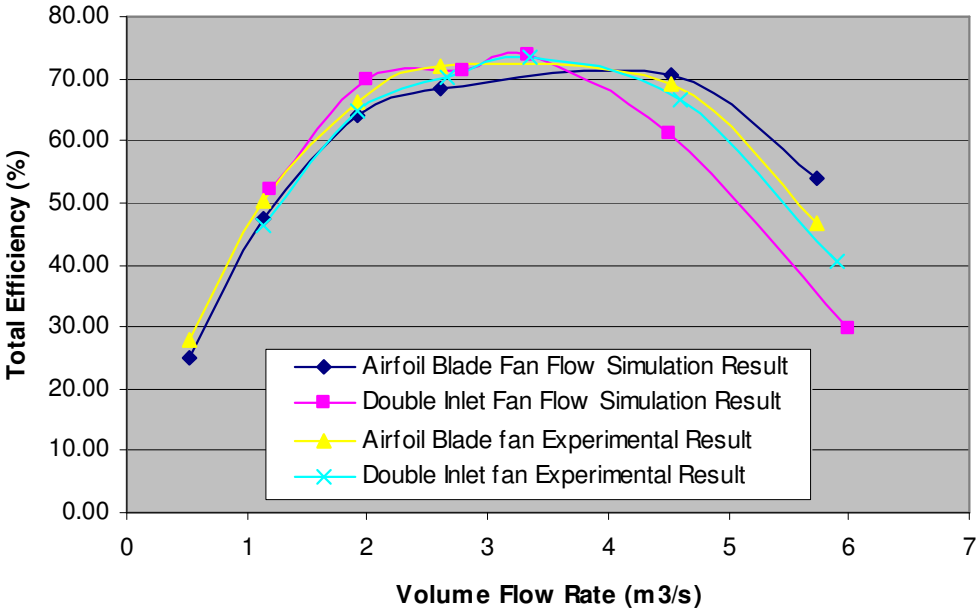


Figure 3.91 Plot of total efficiency for airfoil blade fan and double inlet fan running at 2200rpm

ATTENTION: The Singapore Copyright Act applies to the use of this document. Nanyang Technological University Library

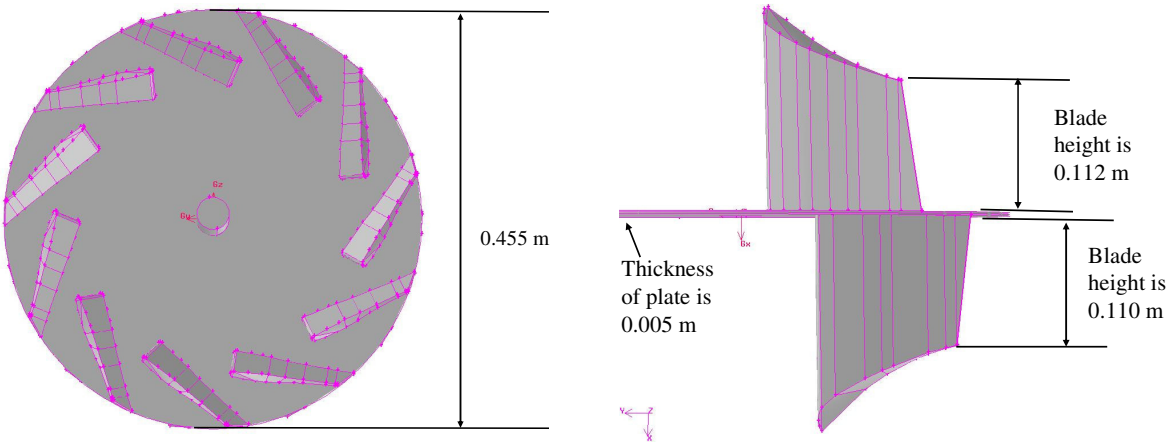
CHAPTER 4

DESIGN OPTIMIZATION OF INDUSTRIAL VENTILATION FAN

Flow simulations of the ventilation fan have provided insight useful for design optimization. It has been noted from such insights that flow separations would impair static pressure rise and hence reduce the fan performance. Hence, there is a need to minimize flow separations by optimizing various design parameters. Those design parameters which would affect flow separations would be chosen for optimization as they would most likely give room for more substantial increase in total efficiency. The aim is to optimize the performance of ventilation fan. Some of the suggested design parameters such as inlet cone depth, blade angle, number of blades and blade off alignment angle are explored for design optimization because they have been known to have an impact on flow separation based on feedbacks from the turbomachinery industry. The physical constraints for the optimization problems are the diameter of the impeller plate as shown in Figure 4.1(a) and the blade height as shown in Figure 4.1(b). These constraints are chosen because based on experimental results provided by the industry, such parameters have little significant effects on the fan performance characteristics. In addition, it is costly to remanufacture those parts each time we change them.

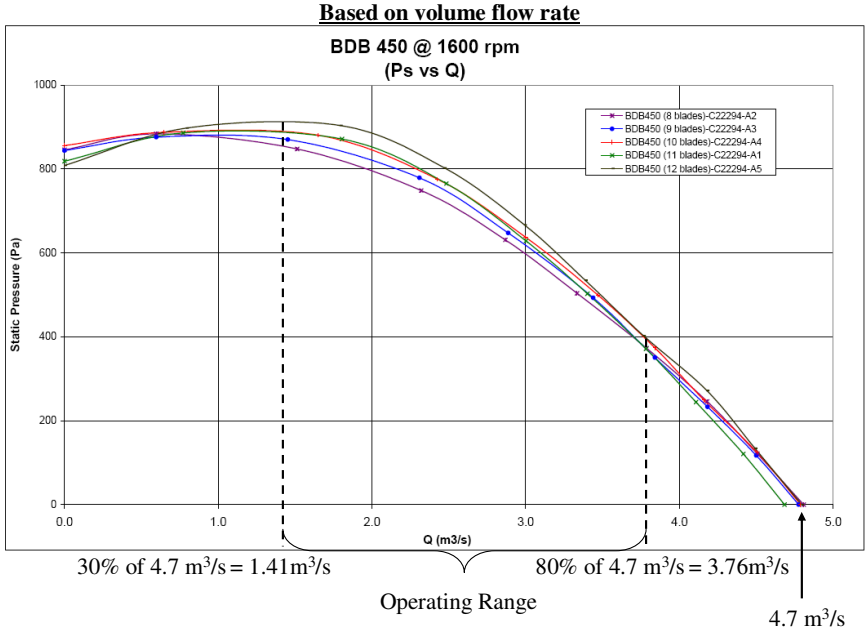
The operating range for the ventilation fan is based on volume flow rates. It is between 30% and 80% of the range of volume flow rates tested for the ventilation fan as shown in Figure 4.2. This is because if the volume flow rate falls below 30 % of the volume flow rate range tested, the fan would most likely enter into surge phenomenon as shown in Figure 1.6. When a fan is under surge, the fan performance will drop drastically. According to Kruger Technical Bulletin [6], if the operating range is beyond 80 % of the tested range, the total efficiency would be too low for operation as shown in Figure 4.3. This information is normally taken as a convention by the turbomachinery industry. All the volume flow rates for optimization are within the operating ranges of 1.96 m^3/s to 5.22 m^3/s for 2200 rpm and 1.41 m^3/s to 3.76 m^3/s for 1600 rpm.

ATTENTION: The Singapore Copyright Act applies to the use of this document. Nanyang Technological University Library



(a) Diameter of impeller plate (b) Blade height

Figure 4.1 Comparison between different geometrical constraints for design optimization such as (a) diameter of impeller plate and (b) blade height



Operating Range for 1600 rpm: 1.41 m^3/s to 3.76 m^3/s

Operating Range for 2200 rpm: 1.96 m^3/s to 5.22 m^3/s

Figure 4.2 Operating Range of volume flow rate for double inlet fan

ATTENTION: The Singapore Copyright Act applies to the use of this document. Nanyang Technological University Library

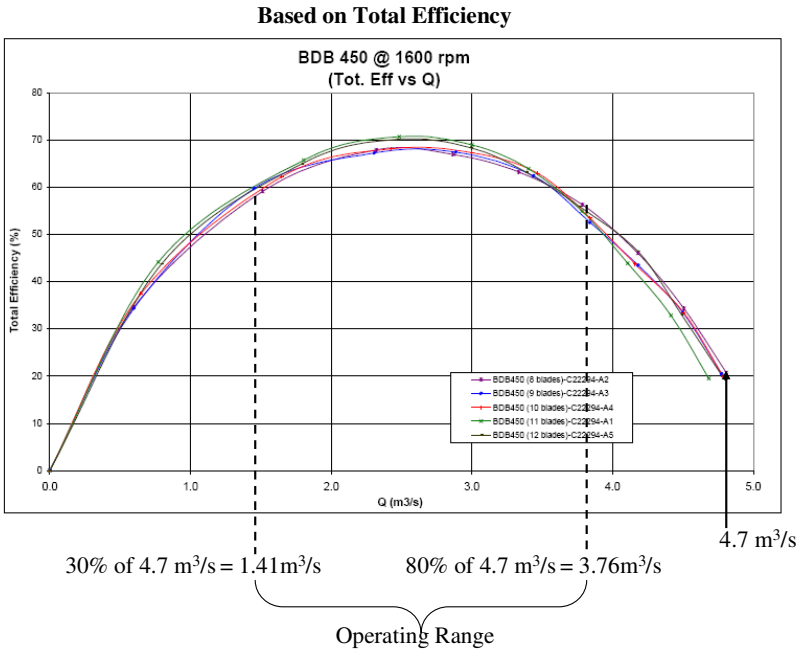


Figure 4.3 Operating Range of volume flow rate for double inlet fan based on total efficiency

4.1 Optimization Problems

In order to satisfy the aim of optimizing fan performance, several design problems are formulated. Some of these are inverse design problem while others are direct problems which use constraints and multi-objective and in which a performance parameter of choice is optimized. Other problems include the maximization of total efficiency, multi objective optimization, and constrained optimization. Genetic algorithm is the optimization method of choice used in this work to find the global optimum of the objective functions in view of the fact that gradient information is not required for such an approach and also because it is quite difficult to estimate gradient information accurately for the problems at hand. The optimization problems considered in this work are described below.

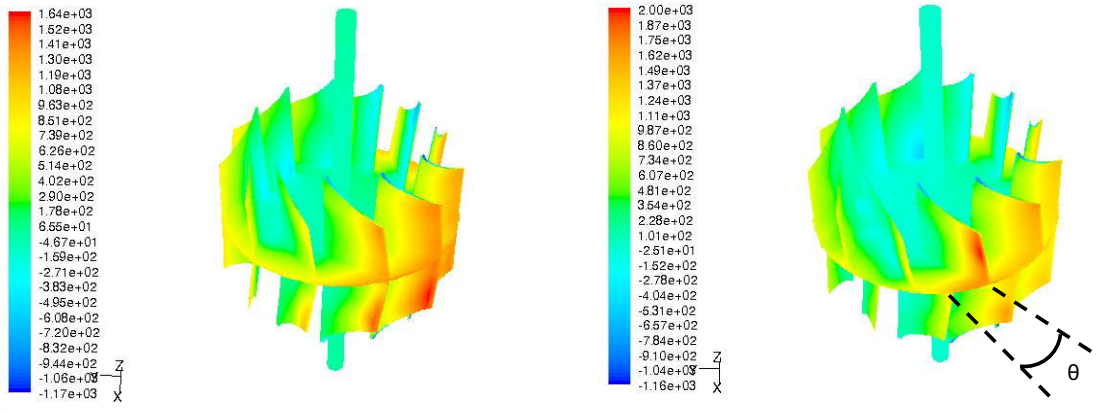
ATTENTION: The Singapore Copyright Act applies to the use of this document. Nanyang Technological University Library

4.1.1 Inverse Design of Pressure Profile at Outlet

In inverse design, the design problem is posed in such a way that we start with some observed data to reach the values of some model parameter. The inverse design problem in this section is to minimize the difference between the desired pressure profile at the fan outlet and estimated pressure profile. The error is calculated in L_2 error norm. The objective function for inverse design is as shown in Equation (4.1).

$$minimize \quad F(\theta) = \left\| P_{desired} - P_T(\theta) \right\|_2 \tag{4.1}$$

where Q is exhaust volume flow rate in m^3/s which is fixed at a particular volume flow rate. $P_{desired}$ is the gauge total pressure of the desired pressure profile. P_T is gauge total pressure in Pa and W is impeller power in watt which varies with blade off alignment angle θ as shown in Figure 4.4. The range of the design parameter blade off alignment angle θ is from 0° to 16.364°. The blade off alignment angle which is the angle between the blades on top and bottom impellers has been used as a design variable for inverse design using POD and the studies of the effects of number of POD modes and POD snapshots and error. This is because it has been known that the alignment of top and bottom impellers has an effect on fan performance characteristics.



(a) θ = 0° (b) θ =16.364°

Figure 4.4 Comparison between different blade off alignment angle such as (a) 0° and (b) 16.364°

ATTENTION: The Singapore Copyright Act applies to the use of this document. Nanyang Technological University Library

4.1.2 Optimization of Total Efficiency in Ventilation Fan

One of the main aims in design optimization is the maximization of total efficiency. The objective function for maximization of total efficiency in percentage has been shown in equation (4.2).

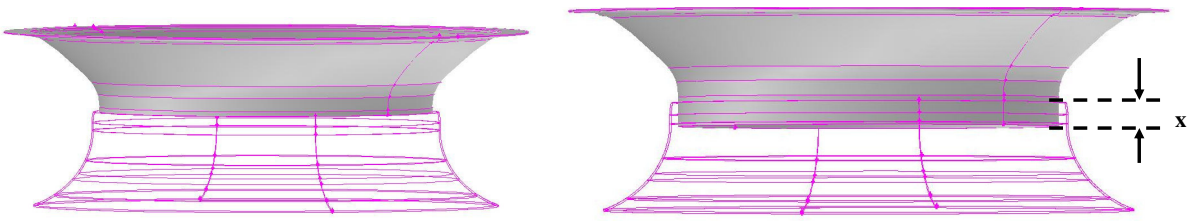
$$minimize \quad F(x) = \frac{W(x)}{P_T(x) \times Q \times 100} \tag{4.2}$$

where Q is exhaust volume flow rate in m^3/s which is fixed at a particular volume flow rate, P_T is gauge total pressure in Pa and W is impeller power in watt which varies with the design parameter x. The objective function is formulated as a reciprocal of the formula for total efficiency in percentage. This is because in genetic algorithm, the objective function would be minimized and hence the reciprocal has to be taken in order to maximize total efficiency.Note that P_T is obtained from POD interpolation using an ensemble of snapshots which varies with design parameter x.

The first design parameter for optimization is the inlet cone depth as shown in Figure 4.5. The inlet cone is shaded in grey. When a fan is under rotation, the impeller cone would rotate and the inlet cone would remain stationary. The inlet cone depth refers to how deep the inlet cone is into the impeller cone as shown in Figure 4.5(b). If the inlet cone is too deep into the impeller cone, there would be good guidance of flow from the inlet into the impeller but at the expense of flow separation due to the interaction between the inlet cone and the impeller cone as the impeller cone rotates. Insight gained from flow simulations from the previous chapter have shown that such flow separations would cause a drop in performance of the fan. Hence, an optimized inlet cone depth should be able to provide good guidance of flow into the impeller cone without creating too much flow separation. The range of inlet cone depth for design optimization is from 0 mm to 20 mm as shown in Figure 4.5.

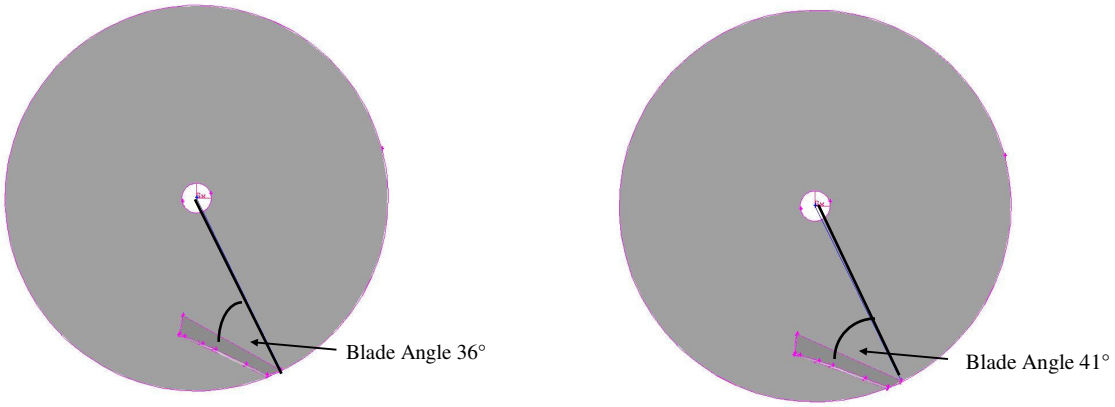
ATTENTION: The Singapore Copyright Act applies to the use of this document. Nanyang Technological University Library

The second parameter for design optimization is the blade angle as shown in Figure 4.6. The blade angle has been chosen as a design parameter because it would affect the guidance of air stream in the channel between the blades. The channel between the blades has to be narrow enough for good guidance of the air stream. On the other hand, it has to be wide enough so that the resistance to airflow is not too great. The original blade angle is about 38.5°. The range of blade angle for design optimization is from 36° to 41°. For the optimization of blade angle, the 8 bladed impeller fan is used. This is because it is economically feasible to try to reduce the number of blades on impeller to 8 blades as shown in Figure 4.7(a) so that material cost is drastically reduced and yet the total efficiency of the fan is only marginally compromised.



(a) x = 0 mm (b) x = 20 mm

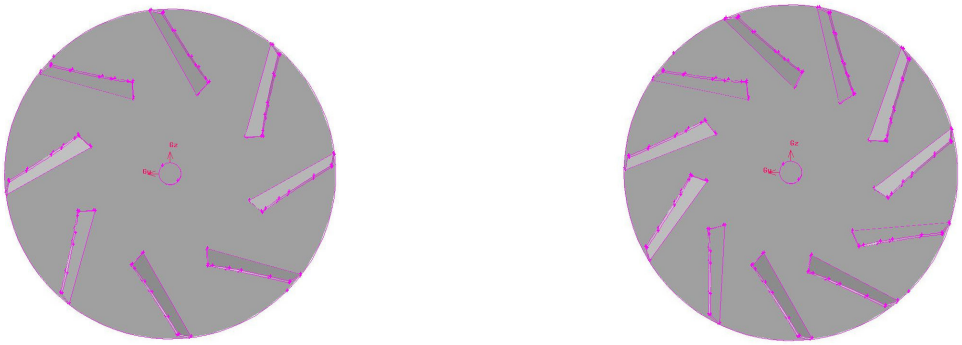
Figure 4.5 Comparison between different inlet cone depth such as (a) 0 mm and (b) 20mm



(a) Blade Angle 36° (b) Blade Angle 41°

Figure 4.6 Comparison between different blade angle such as (a) 36° and (b) 41°

ATTENTION: The Singapore Copyright Act applies to the use of this document. Nanyang Technological University Library



(a) 8 Blades per Impeller (b) 11 Blades per Impeller

Figure 4.7 Comparison between different numbers of blades on impeller such as (a) 8 blades impeller and (b) 11 blades impeller

It has been assumed that 3.33 m^3/s would give the peak efficiency for the double inlet fan running at 2200rpm. However, this might not be true as volume flow rate 3.33 m^3/s gives the peak efficiency only before optimization of inlet cone depth. With a different inlet cone depth, the volume flow rate that gives the peak efficiency might not be 3.33 m^3/s. Hence, there is a need to do optimization using two parameters simultaneously. This means that the inlet cone depths and volume flow rates have to be varied simultaneously. The objective function for two parameters is as shown in Equation (4.3)

$$minimize \quad F(x,Q) = \frac{W(x,Q)}{P_T(x,Q) \times Q \times 100} \tag{4.3}$$

subjects to the following design parameter ranges as shown in Equation (4.4)

$$0 \le x \le 20 \tag{4.4a}$$

$$2.27 \le Q \le 4.39 \tag{4.4b}$$

where Q is exhaust volume flow rate in m^3/s which is another design variable, P_T is gauge total pressure in Pa and W is impeller power in watt which vary with inlet cone depth x (mm) and volume flow rates Q (m^3/s).

ATTENTION: The Singapore Copyright Act applies to the use of this document. Nanyang Technological University Library

4.1.3 Multi Objective Optimization of Cost and Total Efficiency

The new objective function for multi objective optimization is as shown in Equation (4.5).

$$minimize \quad F(x,c) = \frac{a_1}{\left(\frac{P_T(x) \times Q \times 100}{W(x)}\right)} + a_2 \times c \tag{4.5}$$

subjects to the following design parameter ranges as shown in Equation (4.6)

$$0 \le x \le 20 \tag{4.6a}$$

$$70 \le c \le 90 \tag{4.6b}$$

where Q is exhaust volume flow rate in m^3/s which is fixed at a particular volume flow rate, P_T is gauge total pressure in Pa and W is impeller power in watt which vary with inlet cone depth x (mm). The ranges of the design parameters inlet cone depth x (mm) and material cost c ($) are as shown in Equation (4.6). a_1 and a_2 are the weighted coefficients which must add up to 1. This is the weighted sum method which has been used to formulate the new objective function for multi objective optimization. Different combinations of weighted coefficients a_1 and a_2 will give a different gradient. This will affect the importance of each objective function.

4.1.4 Constrained Optimization of Total Efficiency

So far, only linear constrained optimization problems have been discussed. In reality, most optimization problems have non linear constraints. Hence, in the following constrained optimization problem with the inequality constraint $P_T(x) \ge 1490$ Pa, the penalty function is added to the objective function as shown in Equation (4.7).

ATTENTION: The Singapore Copyright Act applies to the use of this document. Nanyang Technological University Library

$$minimize \quad F(x) = \frac{W(x)}{P_T(x) \times Q \times 100} + c(max[0, 1490 - min\{P_T(x)\}]) \tag{4.7}$$

where Q is exhaust volume flow rate in m^3/s which is fixed at a particular volume flow rate, P_T is gauge total pressure in Pa and W is impeller power in watt which vary nonlinearly with inlet cone depth x (mm). Note that c is the penalty parameter used in this exact penalty function method. The basic idea in exact penalty function method is to eliminate the constraints by adding them to the objective function as a penalty term which prescribed a high cost to infeasible solution. As a result of using this penalty function, variables that have caused a violation of this equality constraint would not be chosen as only the solution which gives the smallest fitness function value is chosen as the optimized solution.

In most cases, there is the non-differentiable exact penalty function. According to Bertsekas [59], the disadvantage of the Lagrange Multiplier method is that they require a good starting point in order to converge to an optimal solution. In addition, the constraints are often non-differentiable and hence it is difficult to find the value of Lagrange Multiplier. Hence, the exact penalty function method has been applied for all constrained optimization problems in this project. The range of the design parameter inlet cone depth x is from 0 mm to 20 mm.

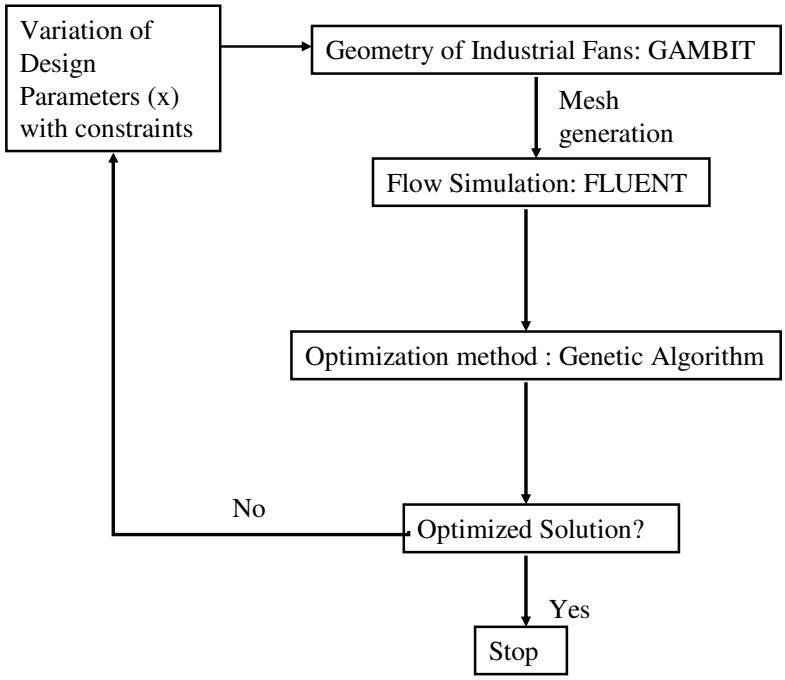
Note that in this penalty function $g(\sigma(x)) = max[0, 1490 - min\{P_T(x)\}]$, either 0 or $1490 - min\{P_T(x)\}$ would be chosen, whichever is greater. Hence, if the pressure profile at the outlet has any pressure point below 1490 Pa, $1490 - min\{P_T(x)\}$ would be greater than zero and hence this would prescribe a high cost to this infeasible solution. As a result of using this penalty function, a variable that cause a violation of this inequality constraint would not be selected as only the solution which has given the minimum fitness function value would be chosen as the optimized solution according to Michalewicz and Janikow [60].

ATTENTION: The Singapore Copyright Act applies to the use of this document. Nanyang Technological University Library

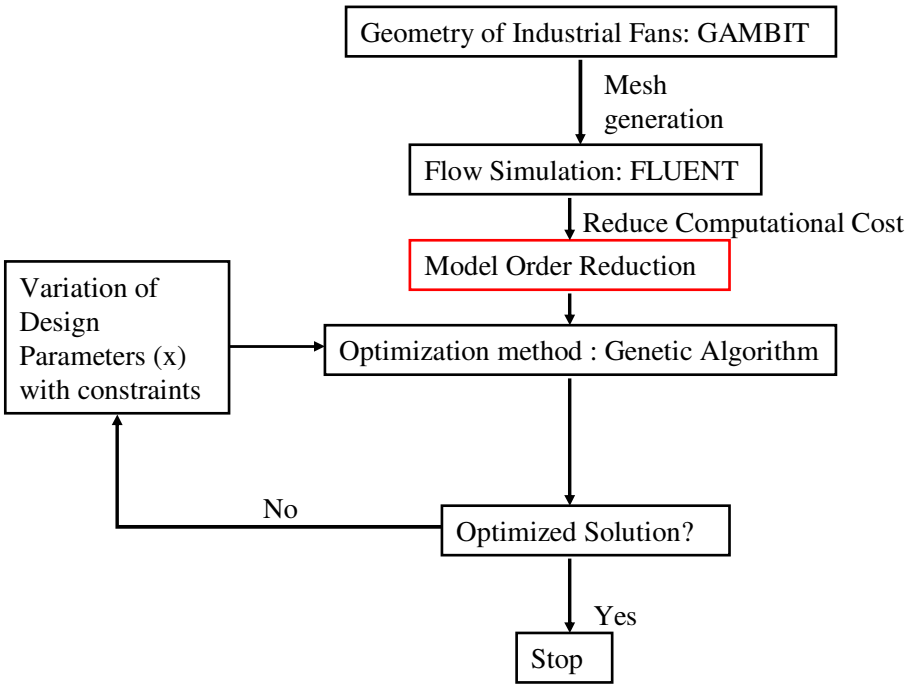
4.2 Design Strategies

Genetic algorithm is the optimization method of choice to solve the above optimization problems as shown in Figure 4.8. This is because it is a global optimization method which can avoid getting stuck in local minima. Moreover, it does not require gradient information which is difficult to estimate for those optimization problems. A high fidelity flow solver *FLUENT* has been used. The flow chart showing the different stages of design optimization is illustrated in Figure 4.8. Genetic algorithm is a heuristic optimization method. The optimization process will stop when the values of objective functions between few successive generations remains constant within a tolerance criteria. This is when the objective function has converged to a value which is an approximation to the optimized solution. Figure 4.8(a) shows the design optimization process if reduced order modeling has not been used. Genetic algorithm begins by creating a random initial population. A large population size is needed for genetic algorithm to be effective. The computational cost of creating this large random initial population is extremely high if only high fidelity flow solver is used as shown in Figure 4.8(a). Given that the population size for genetic algorithm optimization is 500, 500 flow simulations have to be done. Hence, the computational cost for the design optimization process is extremely large. In addition, the computational cost of the large number of iterations in each genetic algorithm generation is high. Hence, design optimization using only high fidelity flow solver is not feasible. As a result, there is a need to develop a technique to cut down the computational cost of the design optimization process. One such technique is the reduced order modeling technique as shown in the red box in Figure 4.8(b). Figure 4.9 shows the flow chart for reduced order modeling. Details of model order reduction as shown in the red box in Figure 4.8(b) are illustrated in the box with dashed red lines in Figure 4.9. Model order reduction has been used to give low dimensional approximations to the state. Proper orthogonal decomposition interpolation has been used to estimate the gauge total pressure at the outlet of the ventilation fan. The estimated gauge total pressure at the outlet is then used as one of the inputs for the formulation of the objective functions.

ATTENTION: The Singapore Copyright Act applies to the use of this document. Nanyang Technological University Library



(a) Without reduced order modeling



(b) With reduced order modeling

Figure 4.8 Comparison of flow charts of design optimization (a) without reduced order modeling and (b) with reduced order modeling

ATTENTION: The Singapore Copyright Act applies to the use of this document. Nanyang Technological University Library

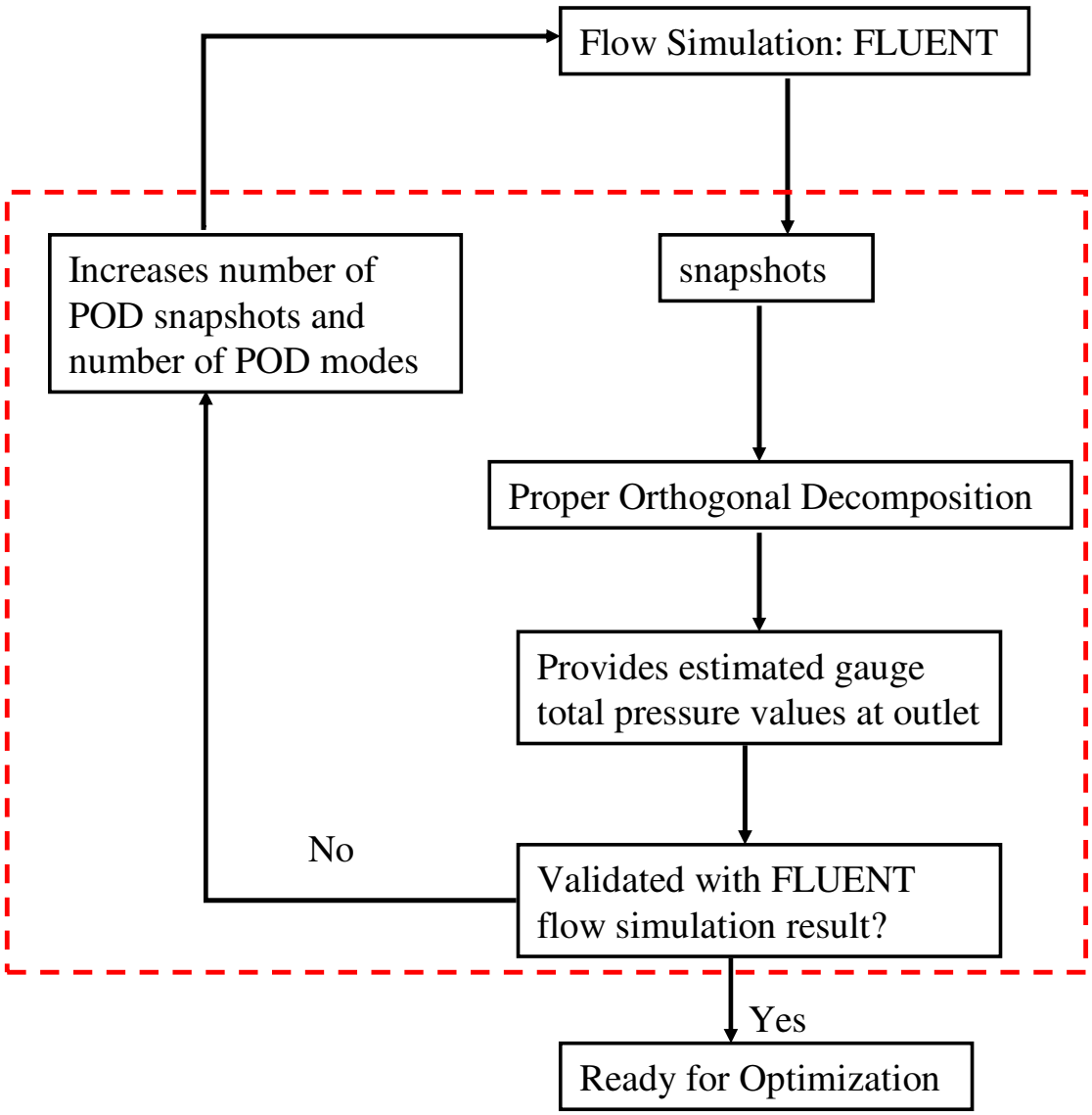


Figure 4.9 Flow chart of model order reduction

ATTENTION: The Singapore Copyright Act applies to the use of this document. Nanyang Technological University Library

4.3 Genetic Algorithm

An appropriate design optimization method has to be selected. Gradient based method requires very low computational cost. However, it is only feasible if the objective function to be optimized does not have local minima or local maxima. This is not true for the design problems as illustrated in Figure 4.10. The L_2 error norm is defined in Equation (4.8)

$$\left\| P_T - P_{desired} \right\|_2 = \sqrt{\sum_{i=1}^{n} \left(P_T - P_{desired} \right)^2} \tag{4.8}$$

such that $P_{desired}$ is the desired pressure profile while P_T is the pressure profile generated from interpolation. It has been noted that there are many local minimum for the L_2 error norm, and the L_2 error norm curve does not follow a convex relationship. Under these circumstances, gradient based method would give a wrong answer as shown in Figure 4.11(c). Depending on the initial guess, the gradient based method gives the wrong solution as shown in Figure 4.11. Hence, the gradient based method has failed. Alternative optimization methods which are able to obtain the global optimum of any objective function have to be explored. One such global optimization method is the genetic alogorithm optimization method. Genetic algorithm is a global optimization method. It does not start with any initial guess but with a population within the parameter range. Genetic algorithm is an optimization method with a long history. It was first proposed by Holland [61]. However, it was Hollstein [62] who first managed to apply genetic algorithms to a pure problem. Genetic algorithm was first applied on multi objective optimization by Schaffer [63]. Baker [64] had investigated the reduction of stochastic errors in selection procedures. De Jong [65] experimented with crossover probabilities and suggested a cross over probability of 0.6 as a reasonable compromise between good on line and off line performance.

Genetic algorithm has been widely used in industrial applications. Alander and Lampinen [66] have applied a shape optimization technique based on genetic algorithm for the optimization of two dimensional boundary shape of a cam cross section. Genetic algorithm

ATTENTION: The Singapore Copyright Act applies to the use of this document. Nanyang Technological University Library

has also been applied for nuclear reactor core reload design by Back et.al [67]. Other industrial applications of genetic algorithm include robot parameter optimization by Floreano [68] and genetic algorithm for dynamic optimization of beer batch fermentation by Andres-Toro [69].

Genetic algorithm has been used as the optimization method to find the global optimum of the objective function. This is because genetic algorithm does not require gradient information. Goldberg [70] explains that genetic algorithm is more global than other optimization methods because the algorithm searches from a population of points instead of from a single point and hence avoids getting stuck in local minima. In addition, genetic algorithm uses probabilistic rules instead of deterministic rules. It has been outlined in section 4.3.1. Some of the factors affecting the performance of the genetic algorithm would be discussed in section 4.3.2.

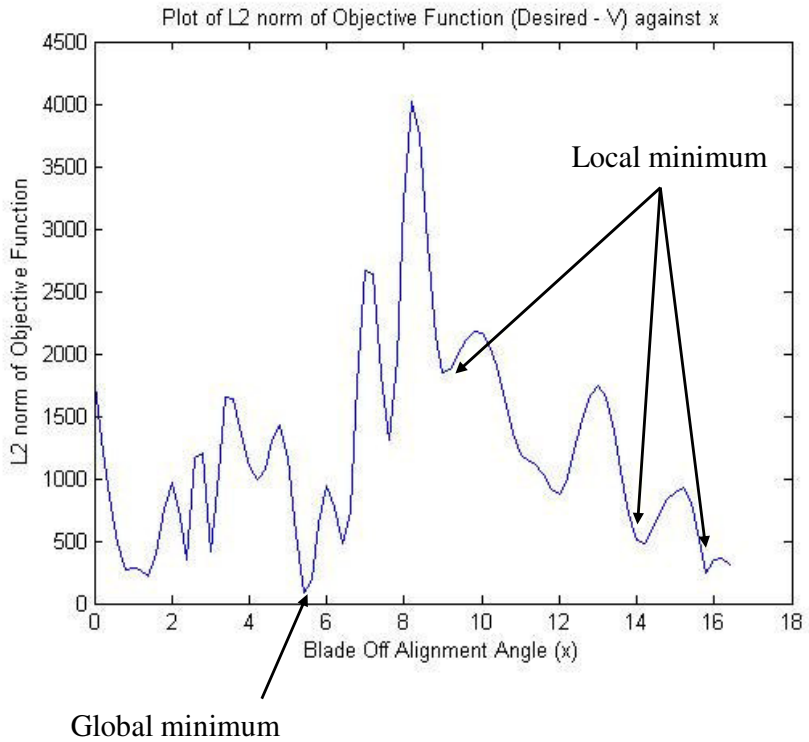
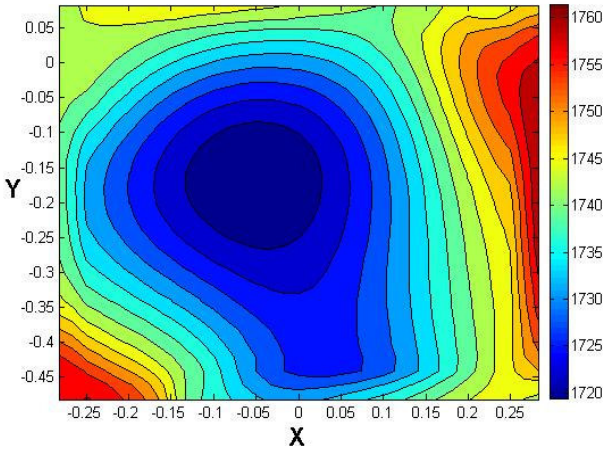
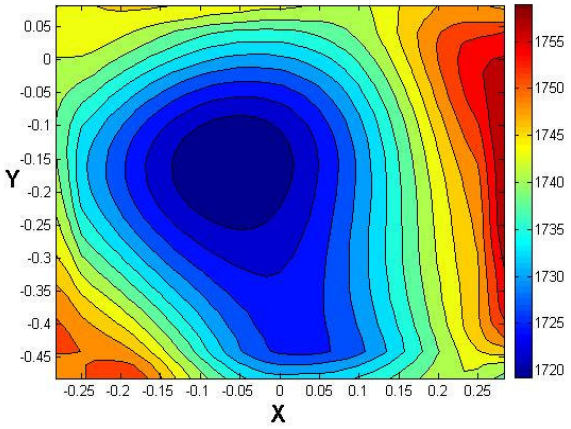


Figure 4.10 Plot of L_2 Norm of objective function against Blade Off alignment Angle

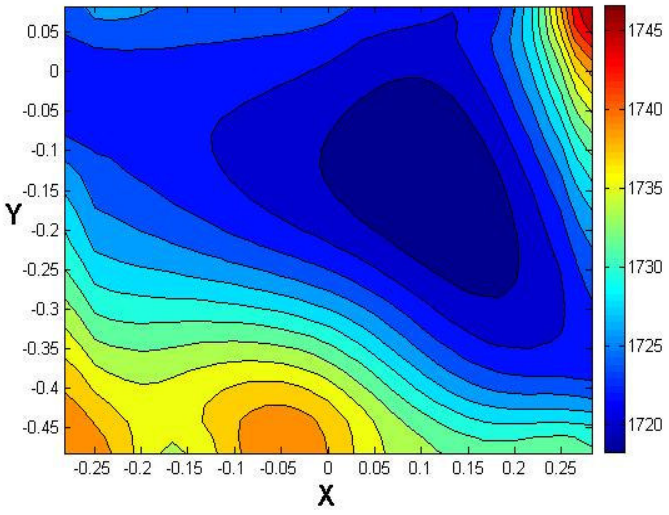
ATTENTION: The Singapore Copyright Act applies to the use of this document. Nanyang Technological University Library



(a) Desired pressure profile
Blade off alignment angle: 5.455



(b) Inverse design with initial guess $x_0 = 5$
Blade off alignment angle: 5.455



(c) Inverse design with initial guess $x_0 = 15$
Blade off alignment angle: 14.112

Figure 4.11 Comparing (a) desired pressure profile with (b) inverse design result with initial guess $x_0 = 5$ and (c) inverse design result with initial guess $x_0 = 15$ using least square minimization method for BDB fan, 2200rpm, 1.2 m^3/s and parameter Blade off Alignment Angle

ATTENTION: The Singapore Copyright Act applies to the use of this document. Nanyang Technological University Library

4.3.1 Outline of Genetic Algorithm

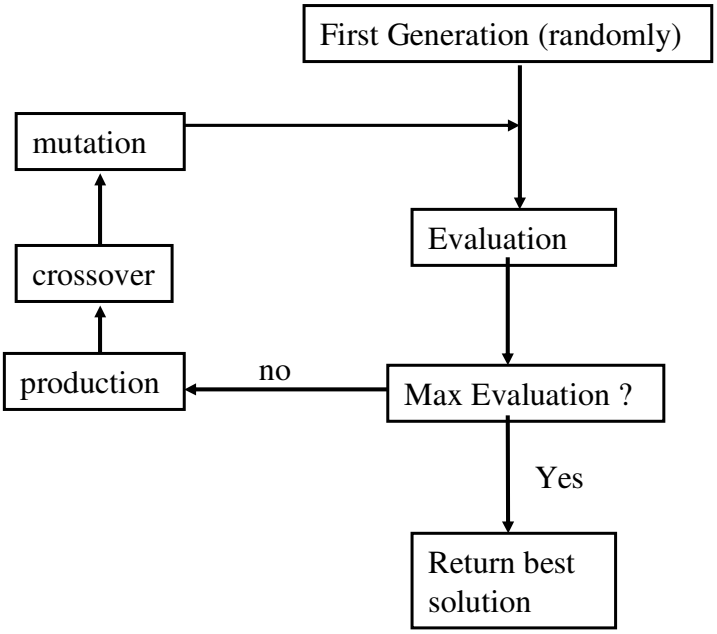


Figure 4.12 Flow Chart of Genetic Algorithm

According to Goldberg [70], the genetic algorithm is a method for solving optimization problems that is based on natural selection, the process that drives biological evolution. A genetic algorithm flow chart is as shown in Figure 4.12. The algorithm begins by creating a random initial population. The algorithm then creates a sequence of new generations. At each step, the algorithm uses the individuals in the current generation to create the next generation. In order to create the new generation, the algorithm performs the following steps. Each member of the current population has been scored by computing its fitness value. The fitness function is the function you want to optimize. For standard optimization algorithms, this is known as the objective function. The raw fitness scores have been scaled to convert them into a more usable range of values. The genetic algorithm creates three types of children for the next generation. The Elite children are the individuals in the current generation with the best fitness values. These individuals automatically survive to the next generation. Crossover children are created by combining the vectors of a pair of parents. The algorithm creates crossover children by combining pairs of parents in the current population. At each coordinate of the child vector, the default crossover function randomly

ATTENTION: The Singapore Copyright Act applies to the use of this document. Nanyang Technological University Library

selects an entry, or gene, at the same coordinate from one of the two parents and assigns it to the child. Crossover enables the algorithm to extract the best genes from different individuals and recombine them into potentially superior children. Mutation children are created by introducing random changes, or mutations, to a single parent. The algorithm creates mutation children by randomly changing the genes of individual parents. By default, the algorithm adds a random vector from a Gaussian distribution to the parent. Mutation adds to the diversity of a population and thereby increases the likelihood that the algorithm will generate individuals with better fitness values. Without mutation, the algorithm could only produce individuals whose genes were a subset of the combined genes in the initial population. The current population has been replaced with the children to form the next generation. The algorithm stops when one of the stopping criteria is met.

4.3.2 Factors Affecting the Performance of Genetic Algorithm

Increasing the population size enables the genetic algorithm to search more points and thereby obtain a better result. However, the larger the population size, the larger is the computational cost of the genetic algorithm optimization taken to compute each generation. In this project, a population size of about 500 has been used. One of the most important factors that determine the performance of the genetic algorithm performance is the diversity of the population. Getting the right amount of diversity is a matter of trial and error. If the diversity is too high or too low, the genetic algorithm might not perform well. The population diversity could be controlled by setting the initial range. The initial range only restricts the range of the points in the initial population. Subsequent generations can contain points whose entries do not lie in the initial range.

In many problems with sufficient complexity, genetic algorithm may have a tendency to converge towards local optima rather than the global optimum of the problem. This means that it does not know how to sacrifice short-term fitness to gain longer-term fitness. The likelihood of this occurring depends on the shape of the fitness landscape. Certain problems may provide an easy ascent towards a global optimum; others may make it easier for the function to find the local optima. This problem may be alleviated by using a different fitness function, increasing the rate of mutation, or by using selection techniques that maintain a

ATTENTION: The Singapore Copyright Act applies to the use of this document. Nanyang Technological University Library

diverse population of solutions. A common technique to maintain diversity is to impose a niche penalty, wherein, any group of individuals of sufficient similarity have a penalty added, which will reduce the representation of that group in subsequent generations, permitting less similar individuals to be maintained in the population.

4.4 Reduced Order Modeling

As explained in the design strategy in section 4.2, reduced order modelling technique has been used to speed up the optimization process by reducing the computational cost. Hence, some basic concepts of reduced order modeling would be explained in this section. Reduced order modeling employs a projection approach, which requires computation of a reduced space basis. There are several methods for constructing the basis functions such as the reduced basis methods proposed by Noor and Peters [71], Krylov subspace methods proposed by Feldmann and Freund [72] and proper orthogonal decomposition method. Proper orthogonal decomposition is also known as the Karhunen Loeve expansion in which the basis functions are derived from an ensemble of data from a high fidelity computational solver. It is proposed independently by Karhunen [73] and Loeve [74]. Sirovich [42] introduces the method of snapshots as a way to efficiently determine the POD eigenfunctions for large problems. In particular, the method of snapshots has been widely applied to computational fluid dynamic formulations to obtain reduced-order models for unsteady aerodynamic applications. The projection method is not used in the design optimization problem. Proper orthogonal decomposition interpolation has been used instead. Figure 4.13 shows the overview of reduced order modeling. Given a certain physical system such as a fan rotating with a certain rpm, the high fidelity flow simulation results have been obtained using the CFD flow solver which provided the snapshots from which the POD basis of the system could be obtained. From the reduced order model, interpolation could be done to obtain reduced order modeling solutions which are an approximate to the solutions obtained from the high fidelity flow simulation solver. Computational cost has been significantly reduced in model order reduction when compared with high fidelity flow simulation. Proper orthogonal decomposition has been used for this project and hence it would be explained in the section 4.4.1.

ATTENTION: The Singapore Copyright Act applies to the use of this document. Nanyang Technological University Library

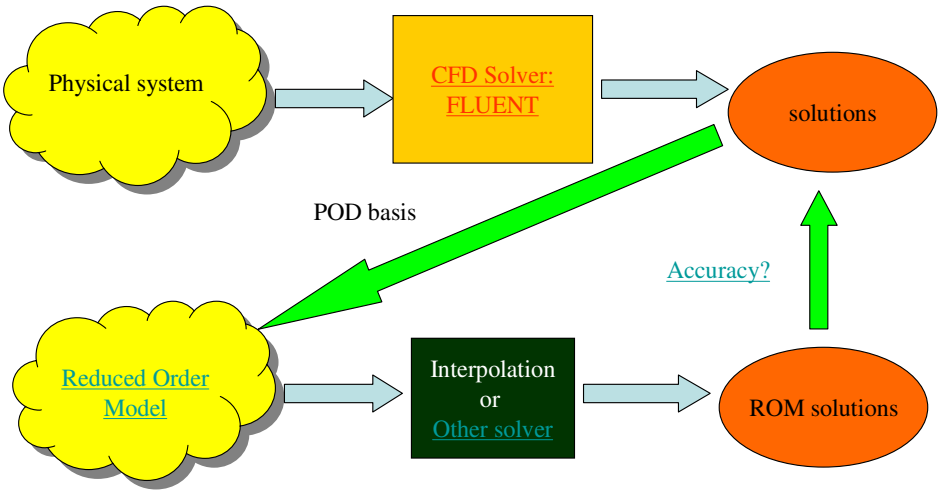


Figure 4.13 Overview of Reduced Order Modeling

4.4.1 Proper Orthogonal Decomposition

Proper orthogonal decomposition is an optimal technique of finding a basis which spans an ensemble of data collected from numerical simulation in the sense that when these basis functions are used in a Galerkin procedure, it will yield a finite dimensional system with the smallest possible degree of freedom. Chatterjee [75] states that Proper Orthogonal Decomposition is a powerful and elegant method of data analysis aimed at obtaining low dimensional approximate descriptions of high fidelity processes. In the following sections, the theory of proper orthogonal decomposition would be explained. Proper Orthogonal Decomposition uses the singular value decomposition proposed by Golub and Van Loan [76] to obtain eigenvalues and eigenvectors for optimal rank approximation. POD interpolation using POD snapshots obtained by varying a design parameter has been explained in section 4.4.1.2.

4.4.1.1 Theory about Proper Orthogonal Decomposition

Proper orthogonal decomposition analysis yields a set of empirical eigenfunctions which describes the dominant behavior or dynamics of a given problem. The optimal POD basis vectors Φ have been chosen such that function of the spatial variable will have the maximum energy content according to Equation (4.9).

ATTENTION: The Singapore Copyright Act applies to the use of this document. Nanyang Technological University Library

$$\max_{\Psi} \frac{\left\langle \left| (U,\Psi)^2 \right| \right\rangle}{(\Psi,\Psi)} = \frac{\left\langle \left| (U,\Phi)^2 \right| \right\rangle}{(\Phi,\Phi)} \tag{4.9}$$

where (U,Φ) is the inner product of the basis vector Φ with the field $U(x)$. x represents the spatial coordinates. The eigenfunctions Φ is linear combinations of the snapshots as shown in Equation (4.10).

$$\Phi = \sum_{i=1}^{m} \beta_i U^i \tag{4.10}$$

where U^i is the solution at a parameter x_i and m is the number of snapshots. β_i is the coefficient which has to satisfy the eigen-problem as shown in Equation (4.11).

$$R\beta = \Lambda\beta \tag{4.11}$$

where R is the correlation matrix as shown in Equation (4.12). Λ is the eigenvalue which is the square of singular values in singular value decomposition.

$$R_{ik} = \frac{1}{m}\left(U^i, U^k\right) \tag{4.12}$$

The relative energy captured by the ith basis vector is given by $\frac{\lambda_i}{\sum_{j=1}^{m} \lambda_j}$. The approximate prediction of the field U is then given by a linear combination of the eigenfunctions as shown in Equation (4.13).

$$U = \sum_{i=1}^{P} \alpha_i \Phi^i \tag{4.13}$$

where P is the number of POD modes chosen to capture the desired level of energy.

ATTENTION: The Singapore Copyright Act applies to the use of this document. Nanyang Technological University Library

According to Anttonen et.al [77], the process of creation of the snapshots comes with a computational cost which is more expensive for a more complete set of snapshots. If the snapshots are not complete, however, the reduced order model would not be able to estimate the changes in parameters that govern the system behavior. As Beran and Silva [78] have noted in their development of POD, the trade-off can be favorable when, after the initial computational investment, a compact reduced order model could be constructed that can be used many times, and is valid over a useful range of system states.

4.4.1.2 POD Interpolation

Ly and Tran [79] have proposed the idea of doing proper orthogonal decomposition with interpolation. In this project, the projection method is not used. Instead, the interpolation method has been used as outlined in this section. Assume that the parameter of interest is denoted by *x*. Let $\{U^{x_i}\}_{i=1}^{m}$ be the snapshots corresponding to the set of parameter values $\{x_i\}_{i=1}^{m}$ where *m* is the number of snapshots. After POD procedure has been performed on $\{U^{x_i}\}_{i=1}^{m}$, the POD basis $\{\Phi^k\}_{k=1}^{m}$ has been obtained. The reconstruction of each snapshot is given by $U^{x_i} = \sum_{j=1}^{P} \alpha_j^{x_i} \Phi^j$ where *P* is the number of eigenfunctions used in the reconstruction. The POD coefficients $\alpha_j^{x_i}$ are given by $\alpha_j^{x_i} = \left(\Phi^j, U^{x_i}\right)$. The prediction of U^x at any values of *x* is given by $U^x = \sum_{j=1}^{P} \alpha_j^x \Phi^j$ where the coefficients α_j^x are found by cubic spline interpolation of the set $\{\alpha_j^{x_i}\}_{i=1}^{m}$. Using method of snapshots with POD interpolation, approximate solution which is not part of the ensemble of snapshots could be obtained.

ATTENTION: The Singapore Copyright Act applies to the use of this document. Nanyang Technological University Library

4.4.1.3 Selection of POD Modes

The number of POD snapshots may be large and hence in practice, fewer modes are chosen than the total number of snapshots. Since the associated eigenvalues are ordered in a descending order $\sigma_1 \geq \sigma_2 \geq \sigma_3 \geq \sigma 4 \geq \ldots \geq \sigma_r \geq 0$ as illustrated from Figure 4.14, one can reasonably expect to achieve a high percentage of the relative energy in a reduced model of order P with P sufficiently smaller than m. The ratio $\frac{\sum_{i=1}^{P} \lambda_i}{\sum_{i=1}^{m} \lambda_i}$ yields the percentage of the total energy in the m POD elements contained in the first P POD elements. Hence, the larger the number of POD modes used for proper orthogonal decomposition, the closer the approximated solution is to the actual solution.

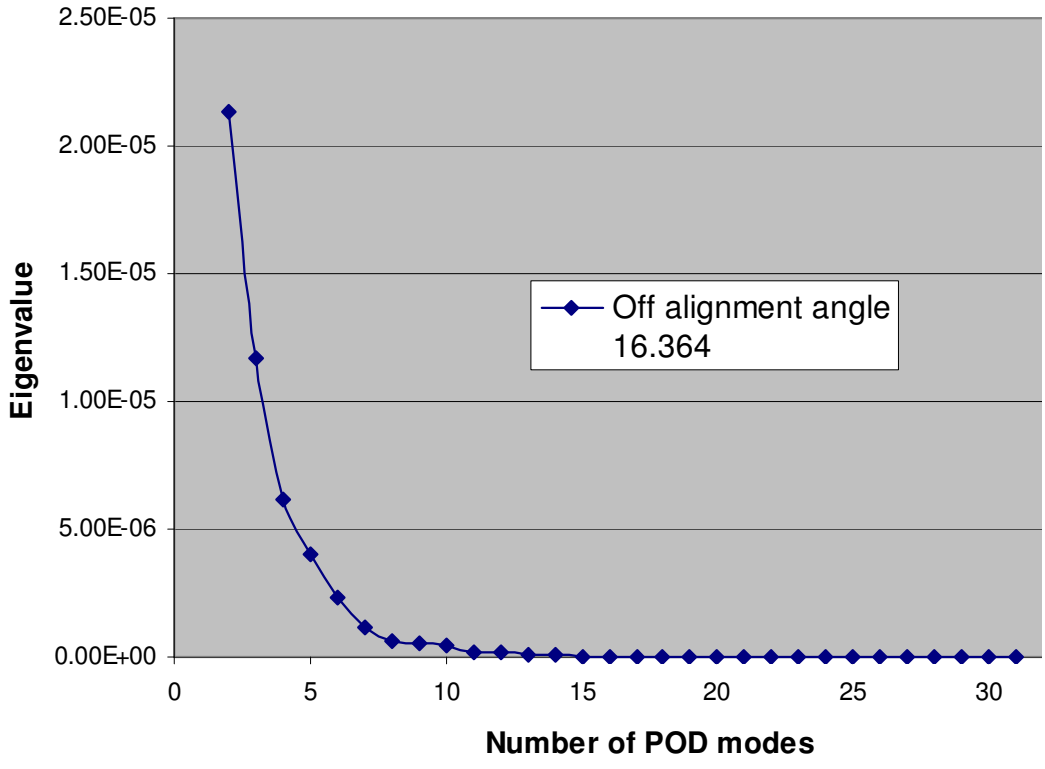


Figure 4.14 Plot of Eigenvalue against number of POD modes from 2nd POD mode to 31st POD mode

ATTENTION: The Singapore Copyright Act applies to the use of this document. Nanyang Technological University Library

4.5 Results and Discussion

4.5.1 POD Analysis

In this section, the proper orthogonal decomposition has been used as a reduced order modeling technique to obtain an approximate solution as it allows computational cost to be greatly reduced in the order of magnitude. In section 4.5.1.1, the effect of number of POD modes and POD snapshots have been studied with design parameters blade off alignment angle and inlet cone depth. The POD results have been verified with high fidelity flow simulation results.

4.5.1.1 Effect of Number of POD modes and Snapshots on POD Interpolation

POD interpolation using the method of snapshots has been used to estimate the gauge total pressure values at the outlet. This section will verify the effect of increasing the number of POD modes on getting more accurate POD results as illustrated in section 4.4.1.3.

Figure 4.15 shows the plane at the outlet where POD snapshots have been taken for variation of design parameters such as blade off alignment angle, inlet cone depth or volume flow rates. It has been taken at the outlet as gauge total pressure is calculated at the outlet and for the calculation of total efficiency as shown in Equation (1.2e). For the case of design parameter blade off alignment angle, 31 snapshots have been taken within the design parameter range of 0° to 16.364° as shown in Figure 4.16. For the case of design parameter inlet cone depth, 21 snapshots have been taken within the range of 0 mm to 20 mm as shown in Figure 4.17.

Figures 4.18-23 show the ensemble of 31 snapshots taken at the outlet for parameter blade off alignment angle of Figure 4.16. Using these snapshots obtained from high fidelity flow simulation solver, proper orthogonal decomposition interpolation has been used as a reduced order modeling technique for an estimation of the gauge total pressure at the outlet of the ventilation fan. Genetic algorithm has been used as the optimization method using inputs of gauge total pressure at the outlet obtained from this method for the objective function.

ATTENTION: The Singapore Copyright Act applies to the use of this document. Nanyang Technological University Library

Figure 4.24 shows that with more POD modes, the error between the POD result and flow simulation result has been greatly reduced. By comparing the values of gauge total pressure in Figure 4.24(c) and Figure 4.24(d), it has been noted that with 10 POD modes, the percentage error is almost negligible. This is because the POD result has been taken at the part of the ensemble of snapshots. Figure 4.25 shows the case when the POD result has been taken at a part not within the ensemble of snapshots. By comparing the values of gauge total pressure in Figure 4.25(b) and Figure 4.25(c), it has been noted that the error between the flow simulation result and POD result is no longer negligible but is rather small at around 1.26 %. Figure 4.25 shows that with more POD snapshots used, the error between the POD interpolation result and flow simulation result is greatly reduced. Error calculation has been based on L_2 relative error norm as shown in equation (4.14).

$$\frac{\left\| P_T - P_{desired} \right\|_2}{\left\| P_{desired} \right\|_2} = \sqrt{\frac{\sum_{i=1}^{n} \left(P_T - P_{desired} \right)^2}{\sum_{i=1}^{n} \left(P_{desired} \right)^2}} \tag{4.14}$$

such that $P_{desired}$ is the desired pressure profile while P_T is the pressure profile generated from POD interpolation.

It is shown in Figure 4.26 that the L_2 relative error norm decreases with more POD modes. When POD interpolation is done on a part not within the ensemble of snapshots, the relative error norm is relatively higher as shown in Figure 4.26(a). In addition, the L_2 relative error norm is smaller when more snapshots are used as shown in Figure 4.26(b). Figure 4.27 shows a case of using design parameter inlet cone depth for POD interpolation at a position not within the ensemble of snapshots. By comparing the values of gauge total pressure in Figure 4.27(a) and Figure 4.27(b), it has been noted that the error is very small at around 0.556 % and hence, proper orthogonal decomposition interpolation method has been verified with flow simulation results.

ATTENTION: The Singapore Copyright Act applies to the use of this document. Nanyang Technological University Library

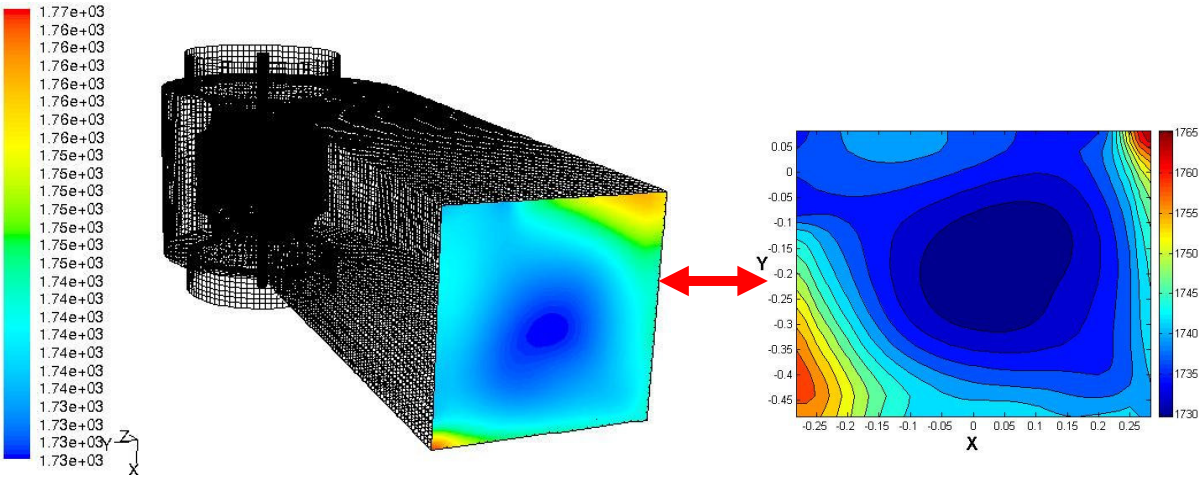
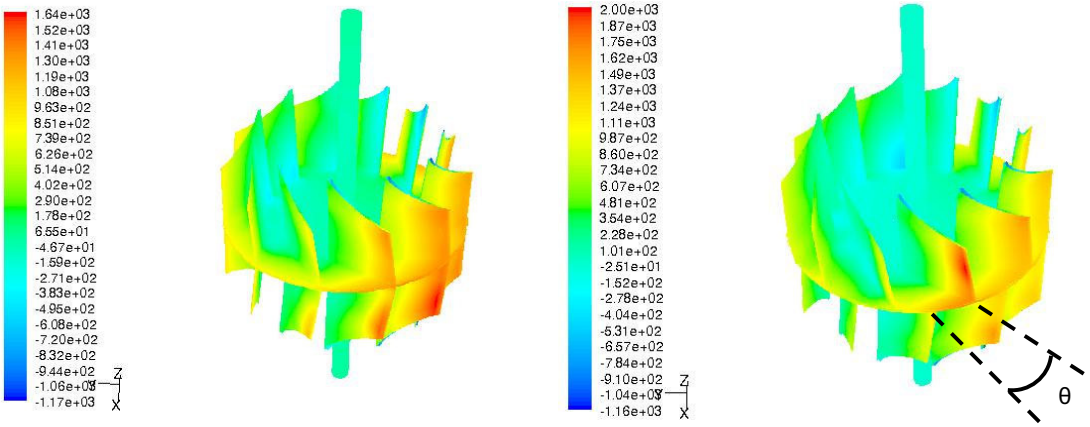
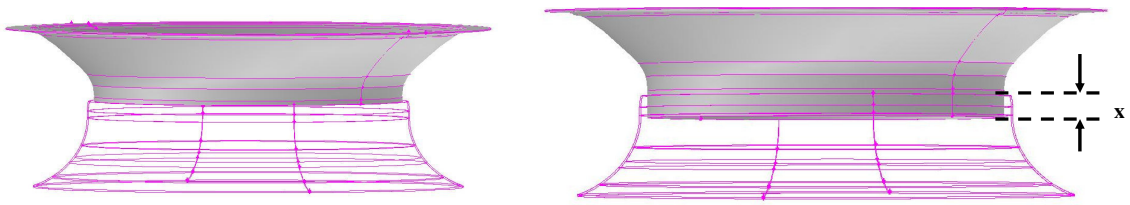


Figure 4.15 POD Snapshot taken at outlet for BDB fan, 2200rpm, 1.2 m^3/s and Blade off Alignment Angle 16.364°



(a) θ = 0° (b) θ =16.364°

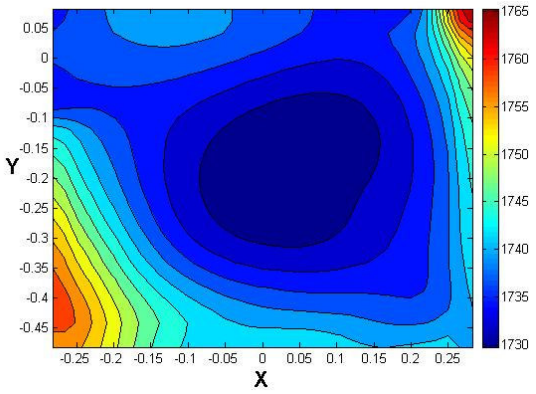
Figure 4.16 Design Parameter Blade Off Alignment Angle for (a) 0° and (b) 16.364°



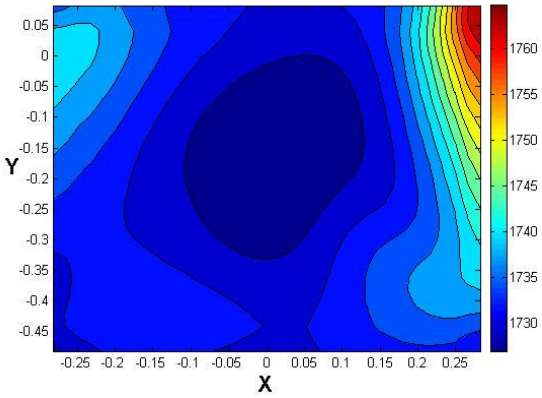
(a) x = 0 mm (b) x = 20 mm

Figure 4.17 Comparison between different inlet cone depth such as (a) 0 mm and (b) 20mm

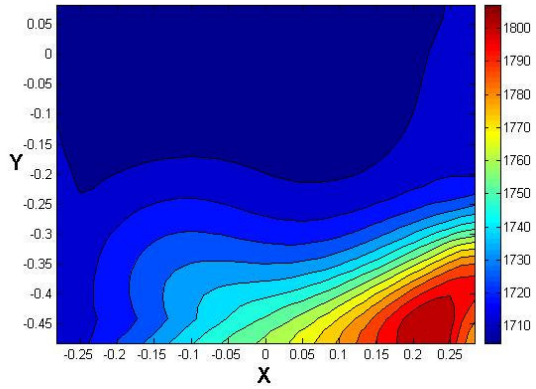
ATTENTION: The Singapore Copyright Act applies to the use of this document. Nanyang Technological University Library



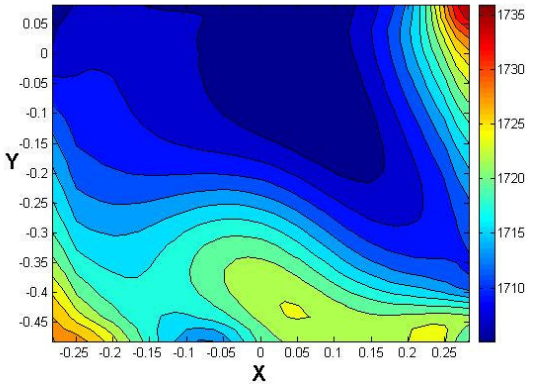
(a) 16.364°



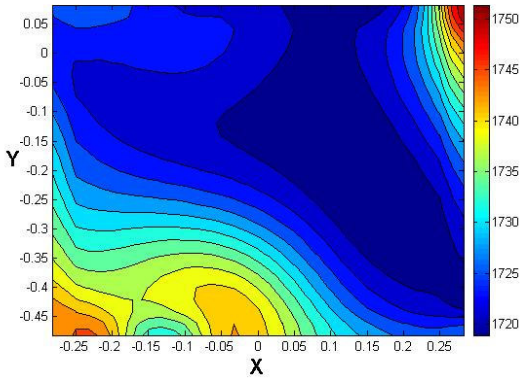
(b) 15.818°



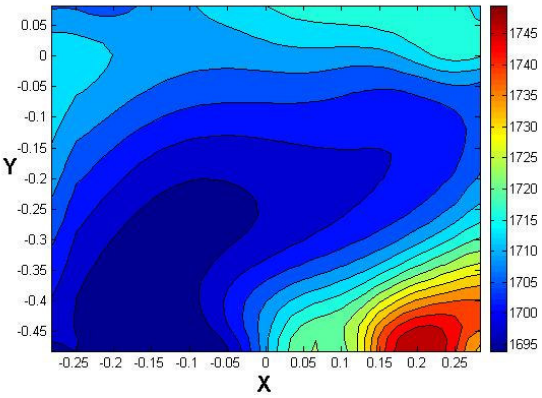
(c) 15.273°



(d) 14.727°



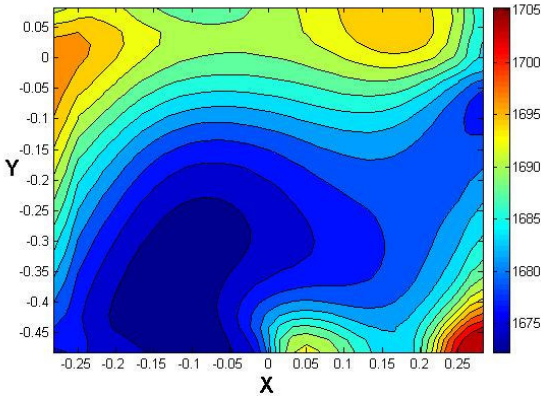
(e) 14.182°



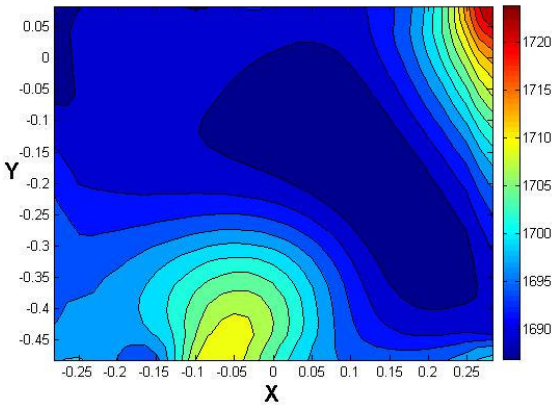
(f) 13.636°

Figure 4.18 Contour plot of snapshots taken at outlet for BDB fan, 2200rpm, 1.2 m^3/s with blade off alignment angle (a) 16.364°, (b) 15.818°, (c) 15.273°, (d) 14.727°, (e) 14.182° and (f) 13.636°

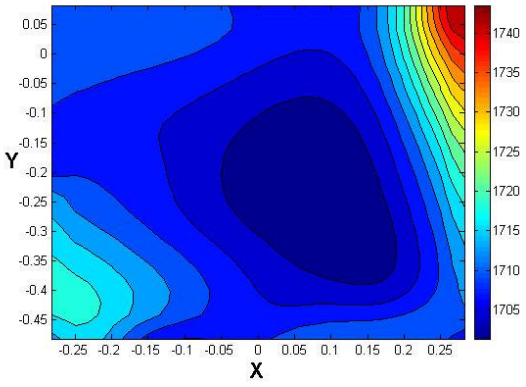
ATTENTION: The Singapore Copyright Act applies to the use of this document. Nanyang Technological University Library



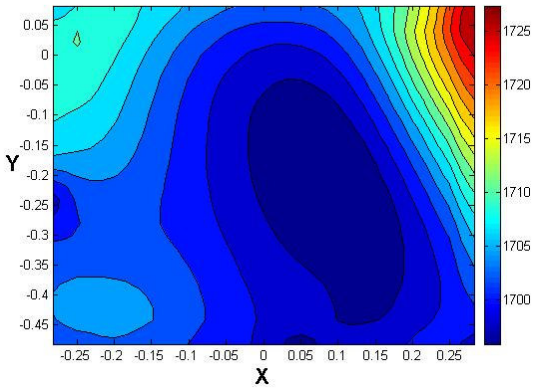
(a) 13.091°



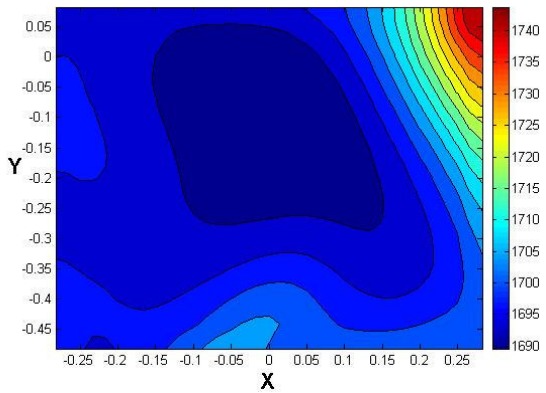
(b) 12.545°



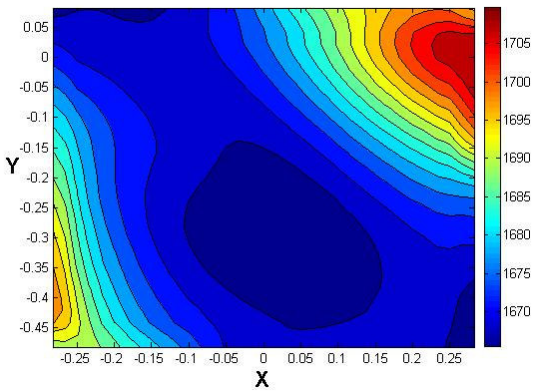
(c) 12°



(d) 11.455°



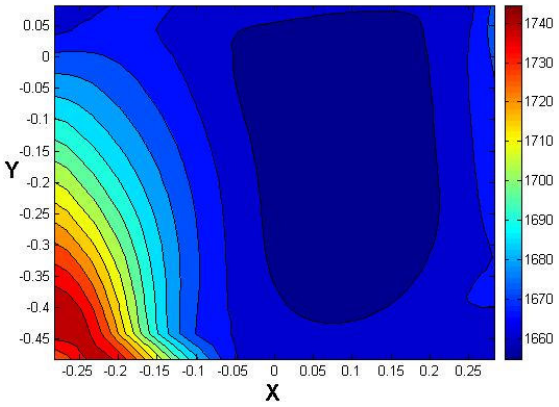
(e) 10.909°



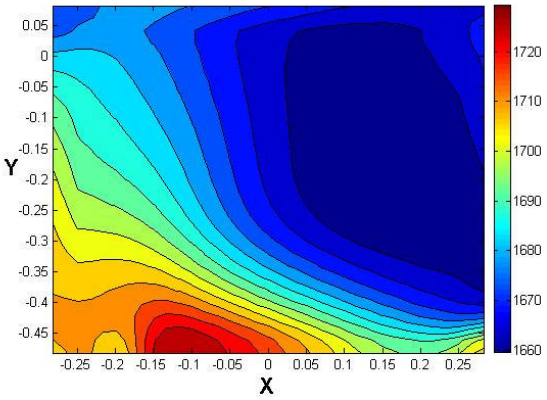
(f) 10.364°

Figure 4.19 Contour plot of snapshots taken at outlet for BDB fan, 2200rpm, 1.2 m^3/s with blade off alignment angle (a) 13.091°, (b) 12.545°, (c) 12°, (d) 11.455°, (e) 10.909° and (f) 10.364°

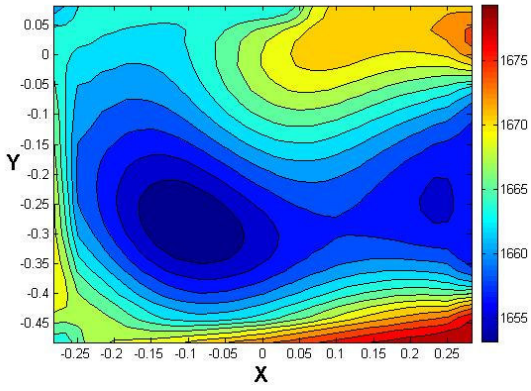
ATTENTION: The Singapore Copyright Act applies to the use of this document. Nanyang Technological University Library



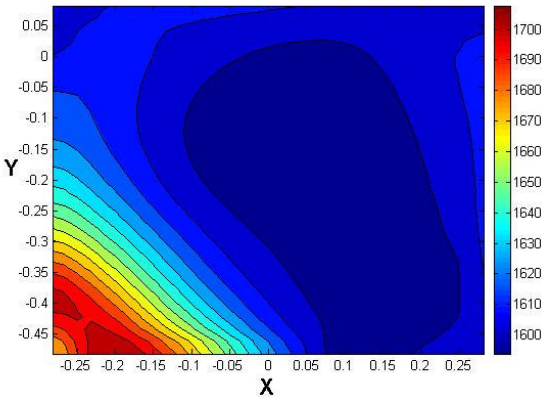
(a) 9.818°



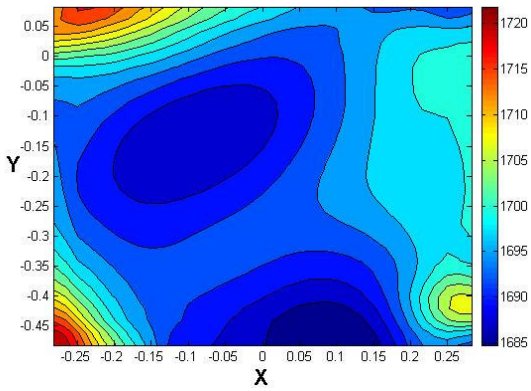
(b) 9.273°



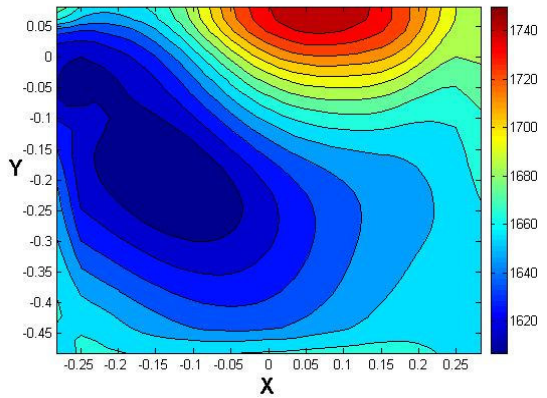
(c) 8.727°



(d) 8.182°



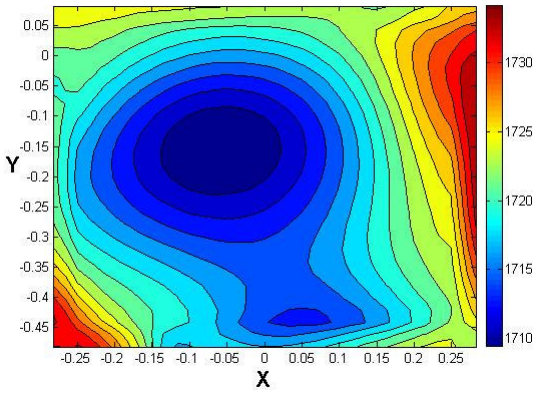
(e) 7.636°



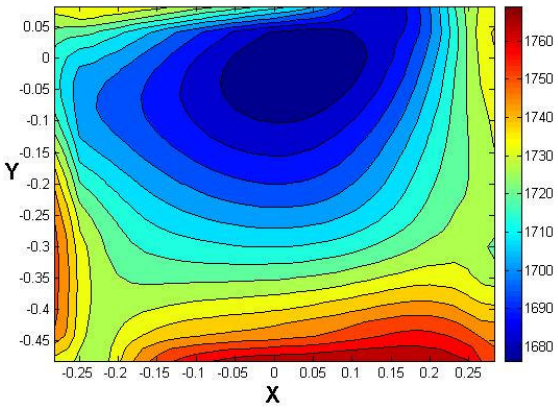
(f) 7.091°

Figure 4.20 Contour plot of snapshots taken at outlet for BDB fan, 2200rpm, 1.2 m^3/s with blade off alignment angle (a) 9.818°, (b) 9.273°, (c) 8.727°, (d) 8.182°, (e) 7.636° and (f) 7.091°

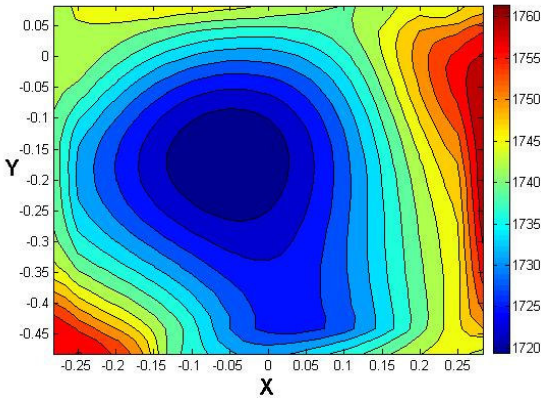
ATTENTION: The Singapore Copyright Act applies to the use of this document. Nanyang Technological University Library



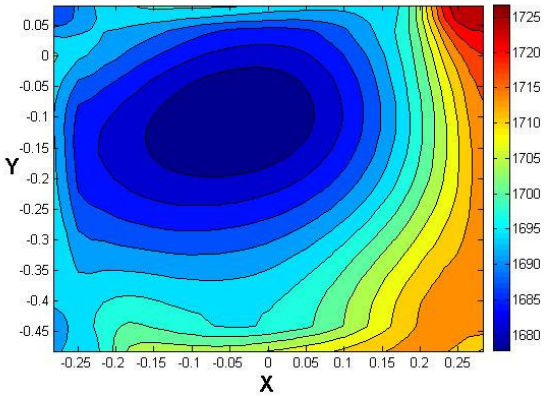
(a) 6.545°



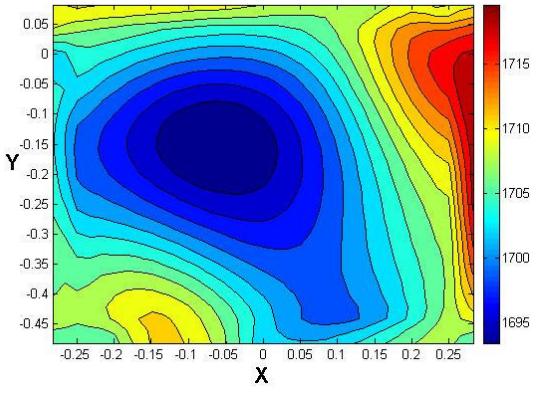
(b) 6°



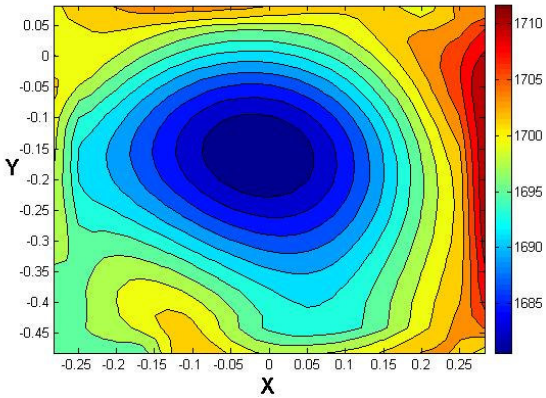
(c) 5.455°



(d) 4.909°



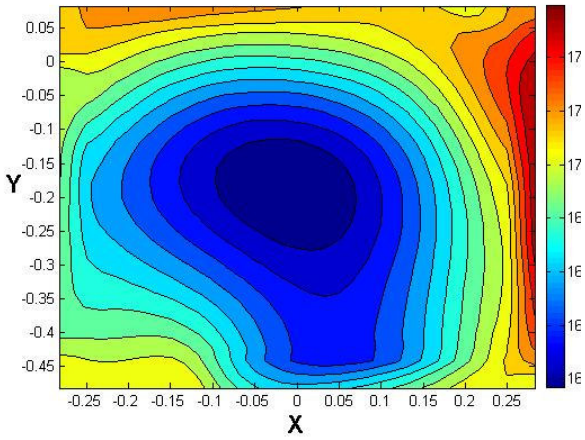
(e) 4.364°



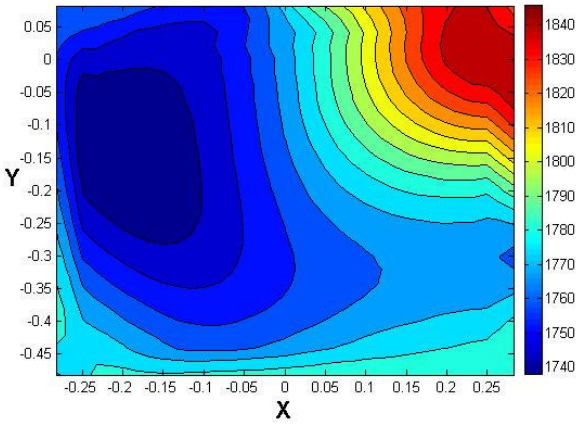
(f) 3.818°

Figure 4.21 Contour plot of snapshots taken at outlet for BDB fan, 2200rpm, 1.2 m^3/s with blade off alignment angle (a) 6.545°, (b) 6°, (c) 5.455°, (d) 4.909°, (e) 4.364° and (f) 3.818°

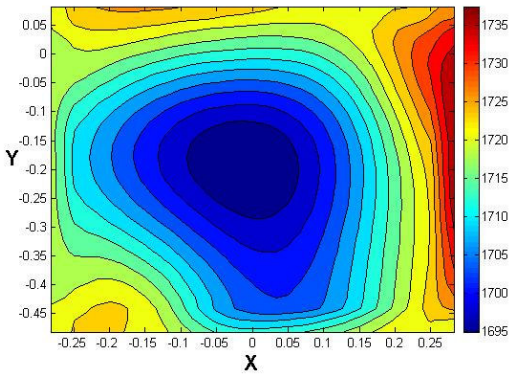
ATTENTION: The Singapore Copyright Act applies to the use of this document. Nanyang Technological University Library



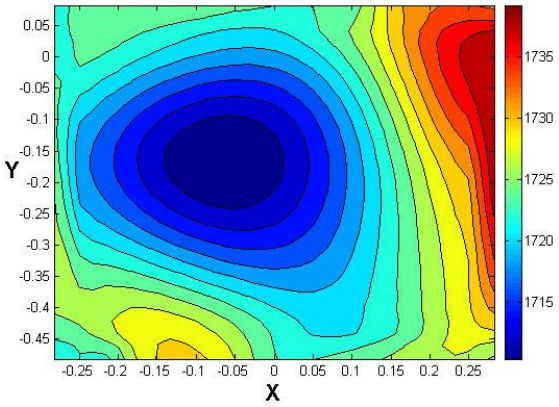
(a) 3.273°



(b) 2.727°



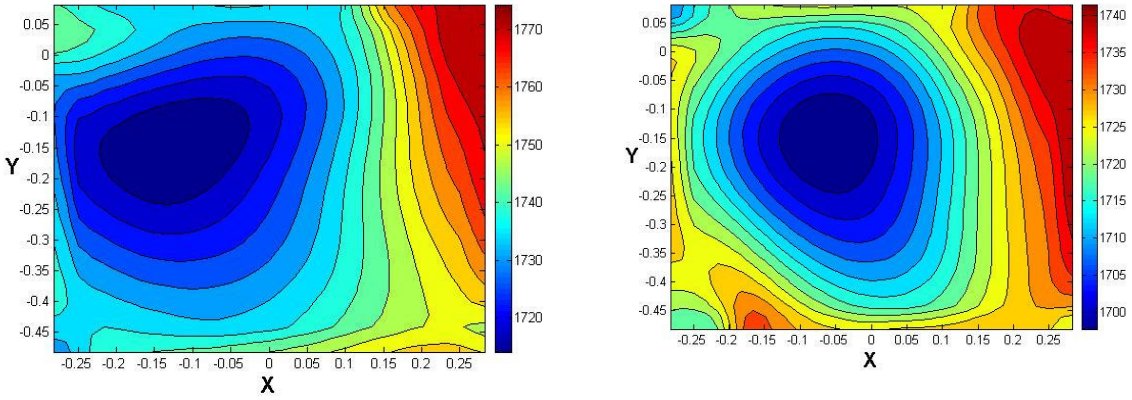
(c) 2.182°



(d) 1.636°

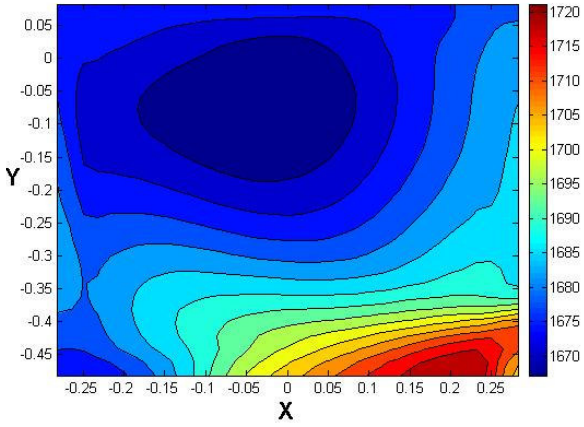
Figure 4.22 Contour plot of snapshots taken at outlet for BDB fan, 2200rpm, 1.2 m^3/s with blade off alignment angle (a) 3.273°, (b) 2.727°, (c) 2.182° and (d) 1.636°

ATTENTION: The Singapore Copyright Act applies to the use of this document. Nanyang Technological University Library



(a) 1.091°

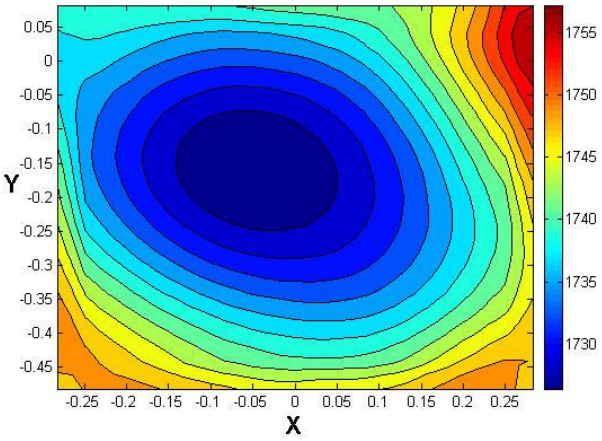
(b) 0.545°



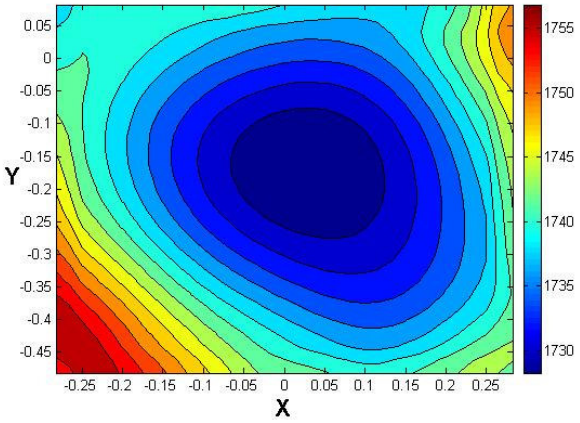
(c) 0°

Figure 4.23 Contour plot of snapshots taken at outlet for BDB fan, 2200rpm, 1.2 m^3/s with blade off alignment angle (a) 1.091°, (b) 0.545° and (c) 0°

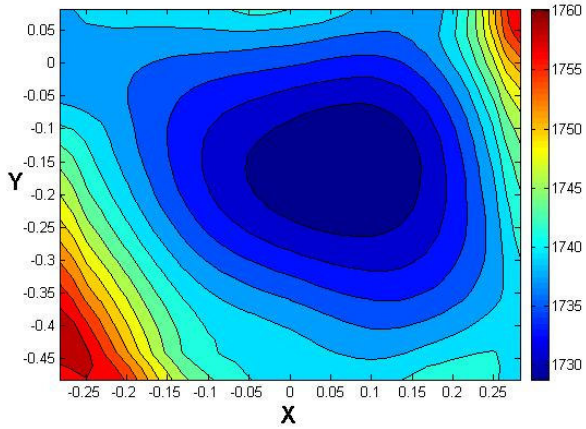
ATTENTION: The Singapore Copyright Act applies to the use of this document. Nanyang Technological University Library



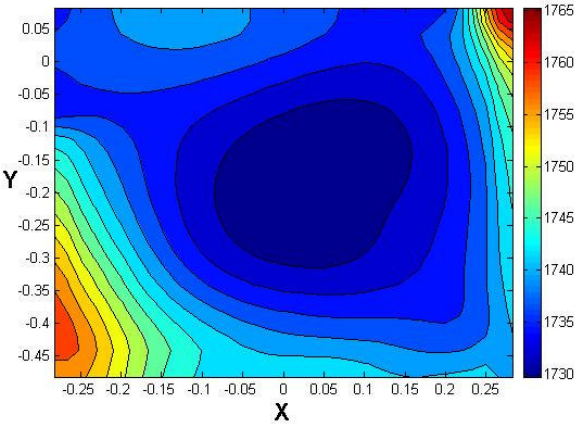
(a) 1 POD mode
Gauge total pressure: 1738.262 Pa



(b) 5 POD modes
Gauge total pressure: 1738.270 Pa



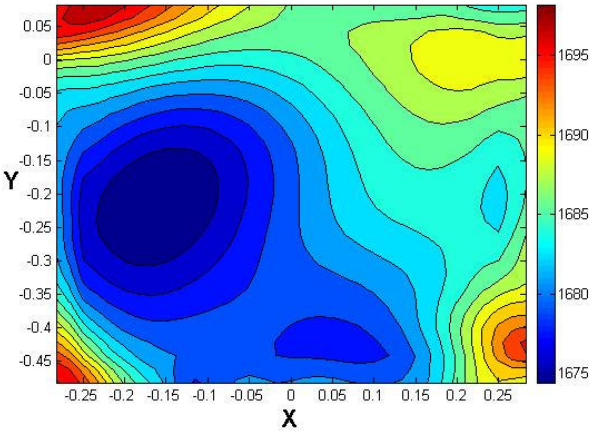
(c) 10 POD modes
Gauge total pressure: 1738.271 Pa



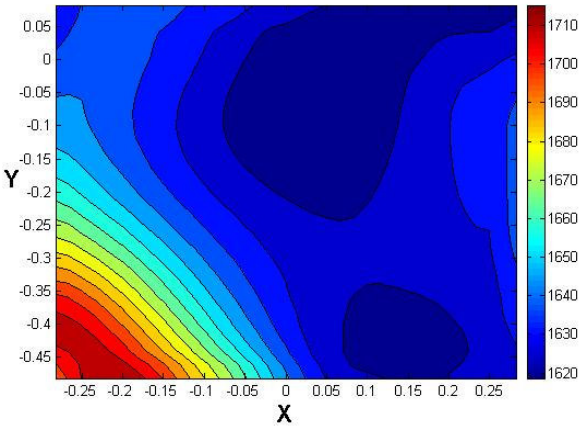
(d) FLUENT Flow Simulation Result
Gauge total pressure: 1738.271 Pa

Figure 4.24 Comparison of POD results using (a) 1 POD mode (b) 5 POD modes, (c) 10 POD modes with (d) FLUENT Flow Simulation Result for BDB fan, 2200rpm, 1.2 m^3/s and Blade off Alignment Angle 16.364° (part of the ensemble of snapshots)

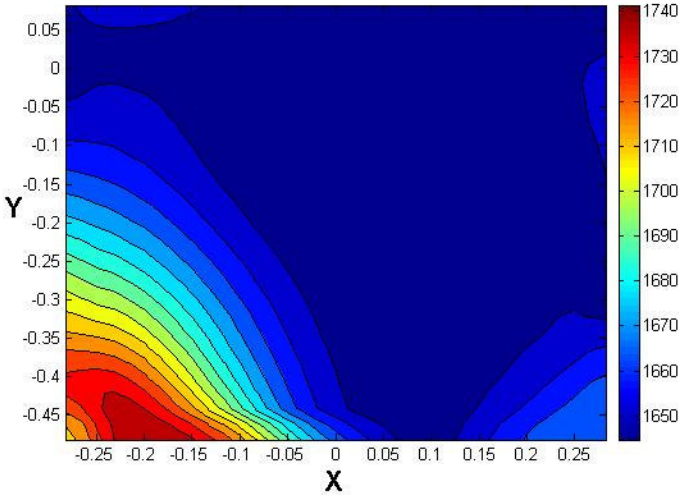
ATTENTION: The Singapore Copyright Act applies to the use of this document. Nanyang Technological University Library



(a) 16 POD snapshots
Gauge total pressure: 1683.187 Pa



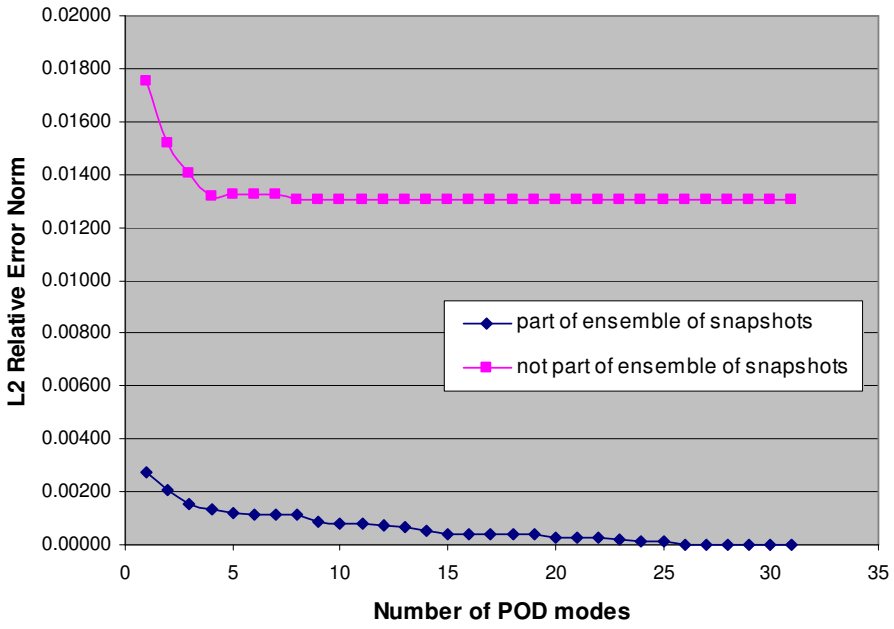
(b) 31 POD snapshots
Gauge total pressure: 1637.992 Pa



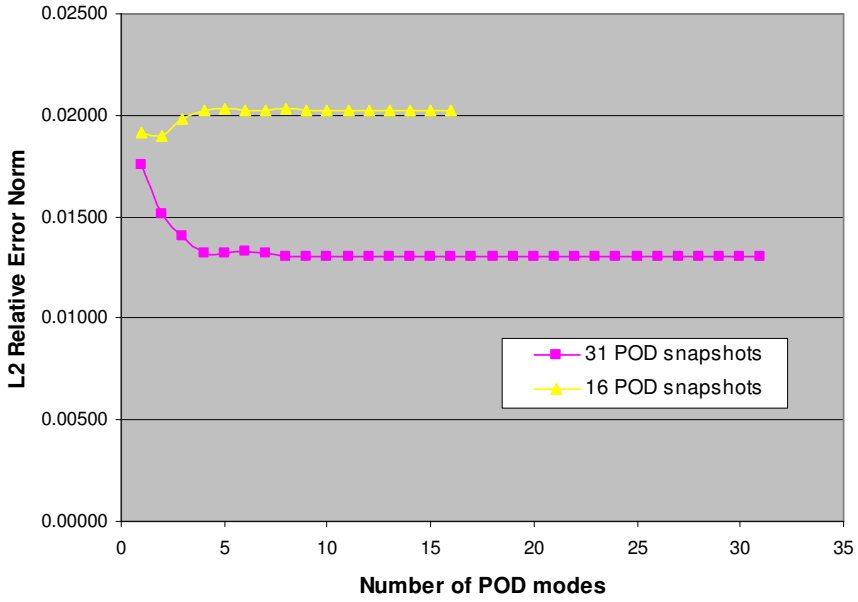
(c) FLUENT Flow Simulation Result
Gauge total pressure: 1658.889 Pa

Figure 4.25 Comparison of POD interpolation results using (a) 16 POD snapshots and (b) 31 POD snapshots with (c) FLUENT Flow Simulation Result for BDB fan, 2200rpm, 1.2 m^3/s and Blade Off Alignment Angle 8° (not part of the ensemble of snapshots)

ATTENTION: The Singapore Copyright Act applies to the use of this document. Nanyang Technological University Library



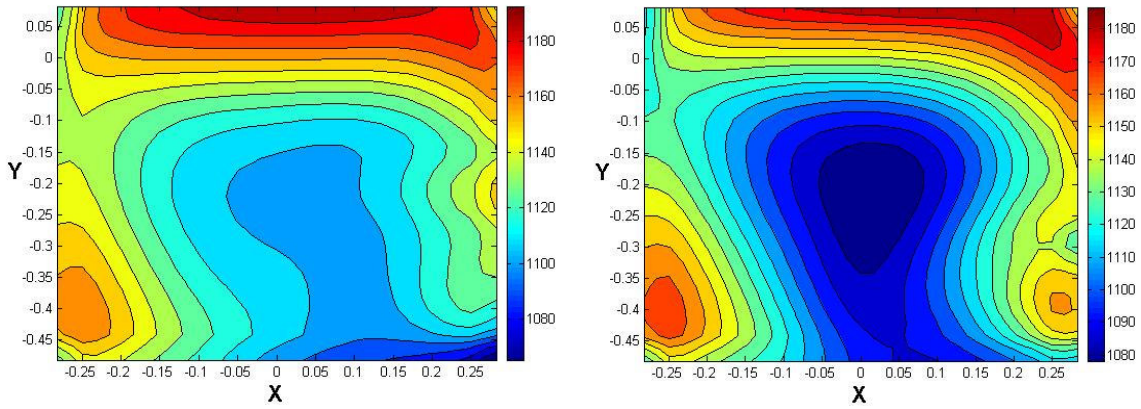
(a) Part or not part of ensemble of snapshots



(b) Different number of POD snapshots

Figure 4.26 Effect of (a) part or not part of ensemble of snapshots and (b) different number of POD snapshots on the plot of L_2 Relative Error Norm against number of POD Modes

ATTENTION: The Singapore Copyright Act applies to the use of this document. Nanyang Technological University Library



(a) POD interpolation with 21 snapshots
Gauge total pressure: 1132.998 Pa

(b) FLUENT Flow Simulation Result
Gauge total pressure: 1126.735 Pa

Figure 4.27 Comparison of (a) POD interpolation results using 21 POD snapshots and 10 POD modes with (b) FLUENT Flow Simulation Result for BDB fan, 2200rpm, 4.39 m^3/s and Inlet Cone depth 6.3 mm (not part of the ensemble of snapshots)

4.5.2 Performance of Genetic Algorithm

In this section, the performance of genetic algorithm as an optimization method would be investigated. Various factors that have affected the performance of genetic algorithm would be discussed. The effect of population size on performance of genetic algorithm would be discussed in section 4.5.2.1. In addition, the improved performance of gentic algorithm when it is coupled with reduced order modelling would be investigated in section 4.5.2.2. Hence, this section would prove that the computational cost of optimization has been reduced via reduced order modelling technique.

4.5.2.1 Effect of Population Size on Performance of Genetic Algorithm

As discussed in section 4.3.2, more points would be searched when the population size is increased and thereby a better result is obtained. However, the larger the population size, the longer the genetic algorithm takes to compute each generation. The algorithm begins by creating a random initial population. The algorithm then creates a sequence of new generations. At each step, the algorithm uses the individuals in the current generation to

ATTENTION: The Singapore Copyright Act applies to the use of this document. Nanyang Technological University Library

create the next generation. The fitness function is the function you want to optimize. It is commonly known as the objective function. Figure 4.28 shows the convergence plot for genetic algorithm for different population sizes. The objective function shown in Figure 4.28 is defined in Equation (4.1). It is illustrated in Figure 4.28 that the objective function for population size 100 decreases faster than that of population size 500. This is because more iteration is needed to generate the sequence of new generations with a larger population size. And hence, more generations are needed before convergence is met. Figure 4.28 also shows that the objective function does not decrease for each successive generation although there is a trend towards convergence. This is because genetic algorithm is not a deterministic optimization method. At each generation, genetic algorithm undergoes selection, cross over and mutuation. It has also been shown that having a bigger population size converges to a smaller objective function. And hence, a better result is obtained with a bigger population size. The time taken to reach convergence for population size 500 is 2150 seconds. The time taken to reach convergence for population size 100 is 1551 seconds.

Figure 4.29 shows the convergence plot for genetic algorithm for different volume flow rates. The objective function is defined in Equation (4.3). It has been noted that the objective function for volume flow rate 3.33 m^3/s converges to the lowest values amongst the various volume flow rates. This is because volume flow rate 3.33 m^3/s has the highest optimized total efficiency of 72.416 %. The objective function in Figure 4.29 is defined as the reciprocal of the total efficiency in percentage. It has also been noted that the objective function of different volume flow rates do not start from the same objective function value in the initial population. This is because the lowest total efficiency in the entire population is different for different volume flow rates. For example, the lowest total efficiency for volume flow rate 2.8 m^3/s is 60.403 % and hence the highest objective function value in the initial population is 0.0166. This means that the highest objective function value in the initial population size for 2.8 m^3/s is 0.0166.

A comparison between the convergence plots for genetic algorithm for constrained optimization and unconstrained optimization has been done in Figure 4.30. The objective function for constrained optimization is defined in Equation (4.7). The objective function for unconstrained optimization is defined in Equation (4.3). It has been noted that the

ATTENTION: The Singapore Copyright Act applies to the use of this document. Nanyang Technological University Library

objective function for constrained optimization starts from a higher value for the initial population. This is because of the addition of penalty function value to the objective function value. This means that in constrained optimization problem, genetic algorithm starts with a random intial population which might violate the constraints. The algorithm then creates a sequence of new generations. At each step, the algorithm uses the individuals in the current generation to create the next generation by mutuation, crossover and selection of elite children. Eventually, genetic algorithm would find a value of the design parameter which does not violate the constraints and hence the penalty function value goes to zero. A variable that cause a violation of the constraint would not be selected as only the solution which has given the minimum fitness function value would be chosen as the optimized solution. This explains why the objective function value of constrained optimization eventually converges to about the same objective function value of that of unconstrained optimization.

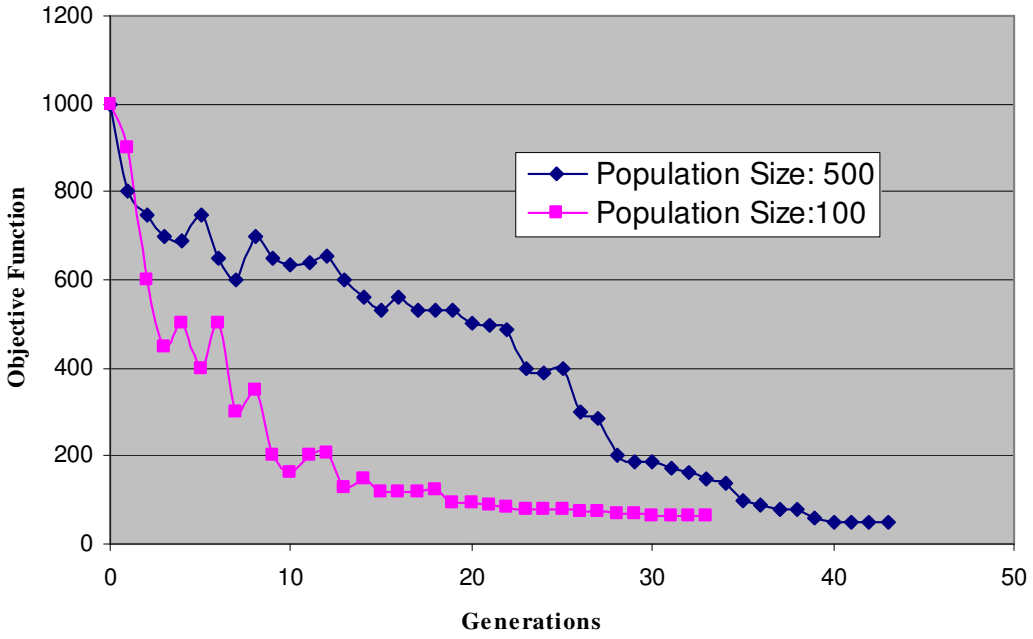


Figure 4.28 Convergence plot of objective function for inverse design against generations for different population size using design parameter blade off alignment angle

ATTENTION: The Singapore Copyright Act applies to the use of this document. Nanyang Technological University Library

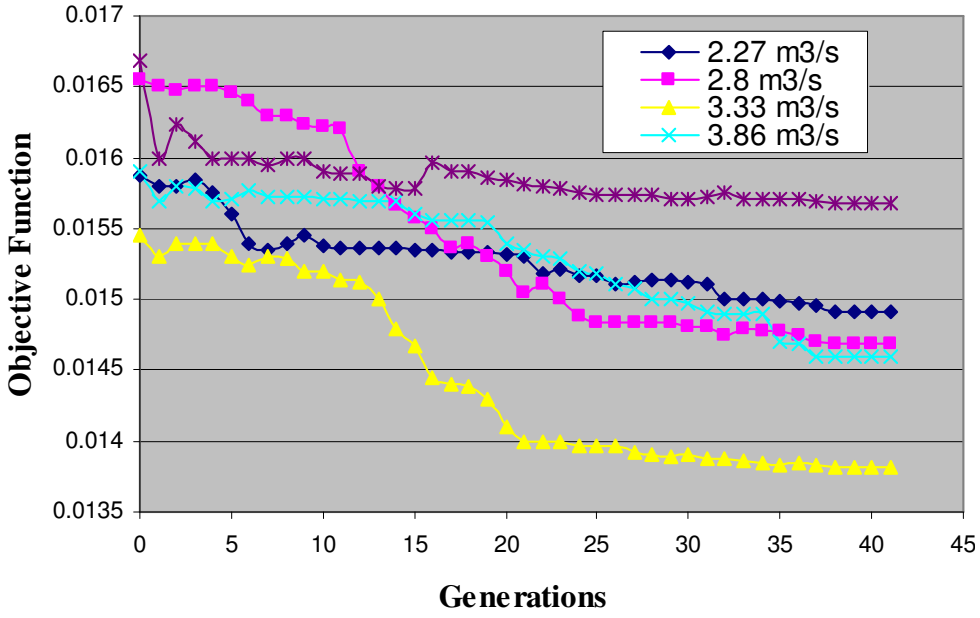


Figure 4.29 Convergence plot of objective function for optimization of total efficiency against generations for different volume flow rates using design parameter inlet cone depth

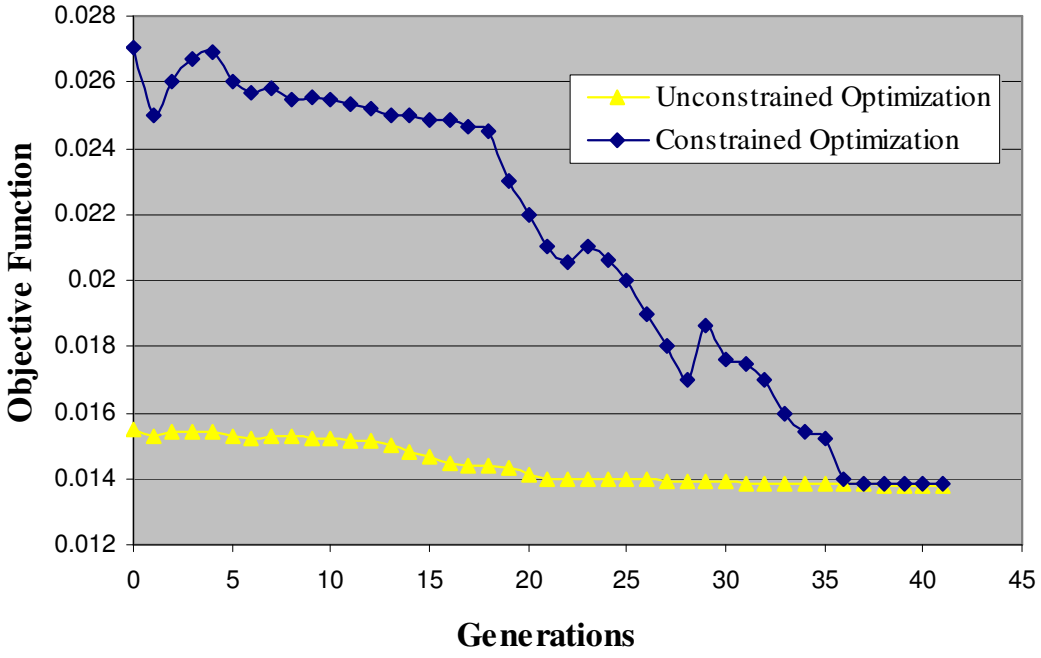


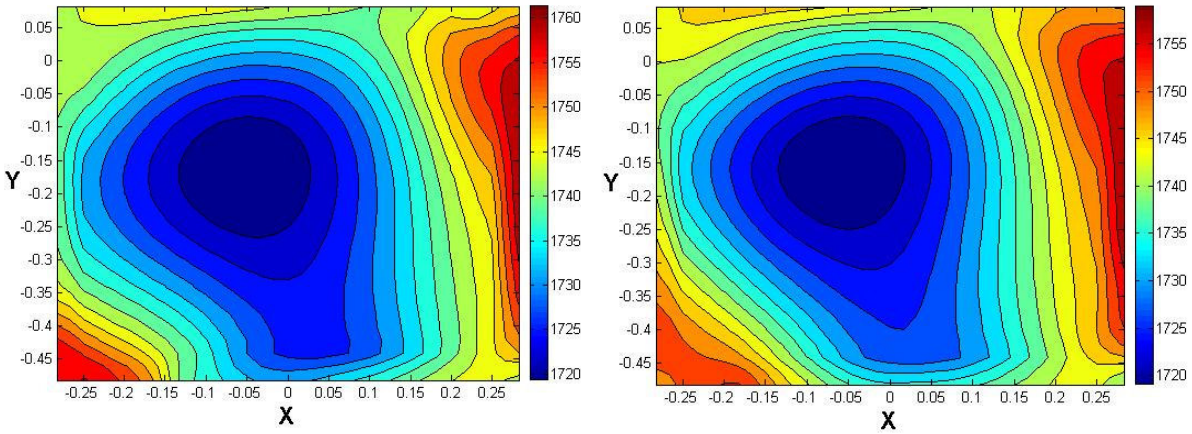
Figure 4.30 Convergence plot of objective function for constrained optimization and unconstrained optimization of total efficiency against generations using design parameter inlet cone depth

ATTENTION: The Singapore Copyright Act applies to the use of this document. Nanyang Technological University Library

4.5.2.2 Effect of Reduced Order Modeling on Performance of Genetic Algorithm

The computational cost of creating the random initial population in genetic algorithm is extremely high if only high fidelity flow solver is used. This is because if the population size is 500, 500 flow simulations have to be done using high fidelity flow solver. In addition, the computational cost of the large number of iterations in each genetic algorithm generation is very high. Hence, design optimization using only high fidelity flow solver is not feasible. Reduced order modelling technique has been used to cut down the computational cost of the design optimization. In this section, the effect of using reduced order modeling on performance of genetic algorithm will be discussed. It has already been proven in section 4.5.1.1 that 10 POD modes would be sufficient for obtaining a good reduced order model. Figure 4.31 shows the comparison between flow simulation result and POD result. It has been illustrated from Figure 4.31(b) that a good approximation of the state has been obtained. The computational cost of genetic algorithm optimization with reduced order modeling is significantly smaller when compared with optimization with only high fidelity flow solver. This is because in reduced order modeling, the proper orthogonal decomposition interpolation method requires only an ensemble of 31 POD snapshots to create the same population size. Hence, only 31 flow simulations have to be done. The computational cost for one flow simulation using high fidelity flow solver is significantly higher than that of POD interpolation result. This is because to solve the full Navier Stokes equations as outlined in Chapter 3, N^3 amount of storage is needed for high fidelity flow solver. This is significantly large when compared with that of POD interpolation result which requires only $m \times N$ amount of storage where m is the number of POD modes and N is the number of mesh nodes. In addition, the number of iterations for each generation during the genetic algorithm optimization process has been reduced. This is because of model order reduction in which less POD modes have been selected than the number of snapshots. Hence, the advantages of using proper orthogonal decomposition with genetic algorithm have been verified by the great reduction in computational time. Computational cost for design optimization has been greatly reduced because there is no longer the need to do many high fidelity flow simulations when proper orthogonal decomposition interpolation has been used.

ATTENTION: The Singapore Copyright Act applies to the use of this document. Nanyang Technological University Library



(a) FLUENT flow simulation
Blade off alignment angle: 5.45454546

(b) 10 POD modes
Blade off alignment angle: 5.47969

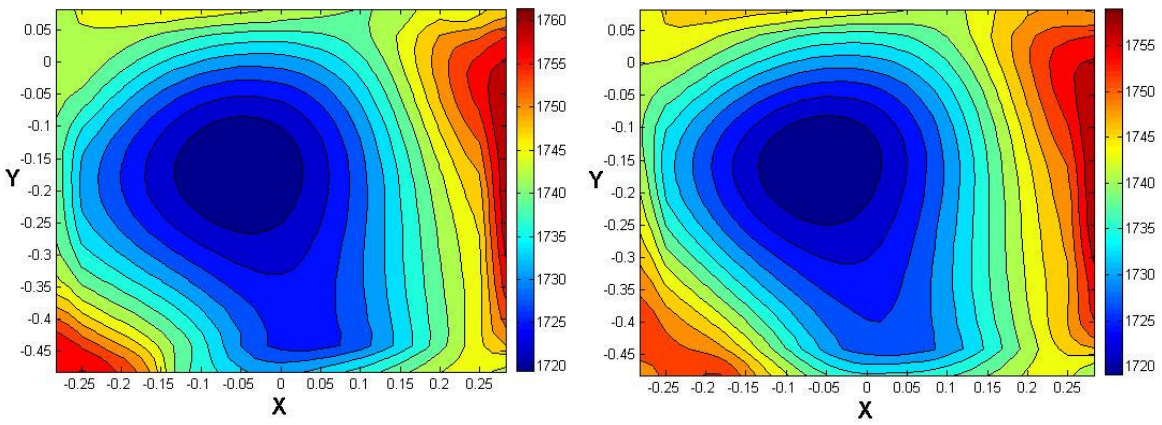
Figure 4.31 Comparison of optimized pressure profile using (a) Fluent flow simulation and (b) 10 POD modes for BDB fan, 2200 rpm, and 1.2 m^3/s using parameter blade off alignment angle

4.5.3 Inverse Design of Pressure Profile at Outlet

In section 4.5.1, proper orthogonal decomposition interpolation has been used as a reduced order modeling techniques to obtain an approximate solution at the part of the ensemble of snapshots and at part which is not provided by the ensemble of snapshots. Given any desired pressure profile, it is possible to use POD interpolation method to do an inverse design. Hence, the parameter which gives the solution of desired pressure profile could be obtained. Section 4.1.1 shows the formulation of the objective function for inverse design using genetic algorithm as outlined in section 4.3.1 to find the global minimum of the objective function within the parameter range. Although gradient based optimization has been known to be fast, they may converge to local minimum depending on the initial design point. Hirsch and Ligout [80] state that despite the fact that genetic algorithm offers the advantage of enhancing the probability of reaching the global optimum; it has such a huge computational cost that it has rarely been applied on industrial design process. The

ATTENTION: The Singapore Copyright Act applies to the use of this document. Nanyang Technological University Library

significance of this project is the success in applying genetic algorithm on the design of an industrial fan. This has been achieved because of using a reduced order modeling technique known as proper orthogonal decomposition interpolation method which helps to cut down computational cost significantly without losing the characteristic features of the system. POD interpolation provides the inputs for the formulation of objective function to be minimized using genetic algorithm optimization method. Given a desired pressure profile as shown in Figure 4.32(a), an approximated pressure profile has been obtained as shown in Figure 4.32(b) using genetic algorithm for inverse design. Note that the blade off alignment angle which has been obtained from inverse design is very close to the desired blade off alignment angle. Inverse design has also been done for the parameter inlet cone depth as shown in Figure 4.33.

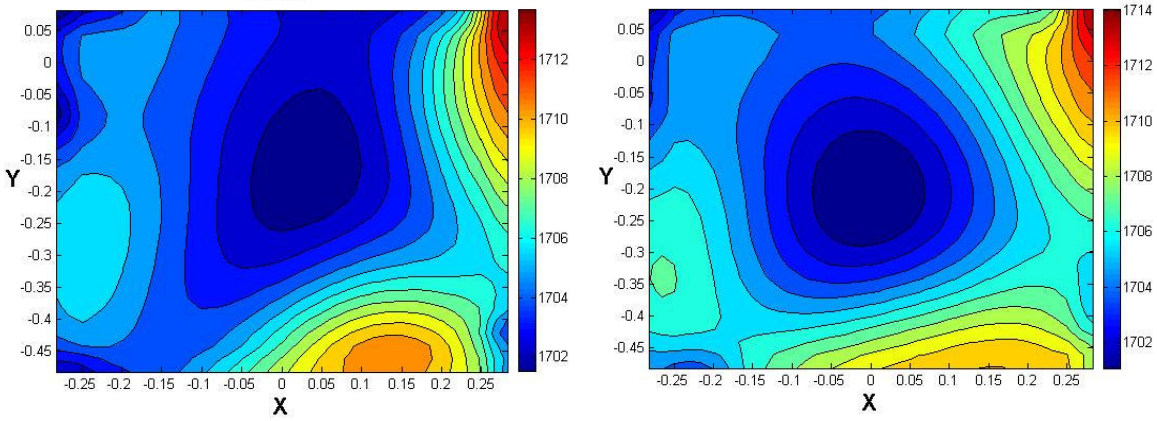


(a) Desired Pressure Profile
Blade off alignment angle: 5.45454546

(b) Inverse design using genetic algorithm
Blade off alignment angle: 5.47969

Figure 4.32 Comparison of (a) desired pressure profile with (b) inverse design using genetic algorithm for BDB fan, 2200 rpm, and 1.2 m^3/s using parameter blade off alignment angle

ATTENTION: The Singapore Copyright Act applies to the use of this document. Nanyang Technological University Library



(a) Desired Pressure Profile
Inlet cone depth: 16 mm

(b) Inverse design using genetic algorithm
Inlet cone depth: 16.0692 mm

Figure 4.33 Comparison of (a) desired pressure profile with (b) inverse design using genetic algorithm for BDB fan, 2200 rpm, and 1.2 m^3 /s using parameter inlet cone depth

4.5.4 Optimization of Total Efficiency

After the application of inverse design using genetic algorithm and POD, the next aim is to optimize the total efficiency using different design parameters such as inlet cone depth and blade angle. The objective functions have been formulated in section 4.1.2. Genetic algorithm has been used as the optimization method to find the global minimum of the objective function within the parameter range. POD interpolation has provided an approximation of the gauge total pressure at the outlet which has then been used for the calculation of total efficiency.

4.5.4.1 Design Parameter Inlet Cone Depth

In this section, the design parameter inlet cone depth 0 mm to 20 mm has been used. It is based on volume flow rate 3.33 m^3/s, which has been assumed to be at the peak efficiency for the 11 bladed impeller double inlet fan running at 2200 rpm. Another case of volume flow rate 2.80 m^3/s has also been done. Both volume flow rates are within the operating range of the fan. The improvement in fan performance for the optimized double inlet fan is also shown.

ATTENTION: The Singapore Copyright Act applies to the use of this document. Nanyang Technological University Library

4.5.4.1.1 POD Results for Optimization of Total Efficiency

Results shown in Figure 4.34-38 are based on volume flow rate 3.33 m^3/s, which has been assumed to be the volume flow rate giving the peak efficiency for 2200 rpm. The inlet cone depth has been optimized to give a higher total efficiency as shown in Figure 4.34 and Figure 4.35. Figure 4.34(b) shows that the optimized pressure profile requires a lower power requirement of 7003 W and hence gives a higher total efficiency of 72.416 %. The total efficiency after optimization has improved by about 1.032 %. Figure 4.35 shows that the optimization method of genetic algorithm is feasible in optimizing the inlet cone depth as the optimized result obtained in Figure 4.35(b) gives a total efficiency of 72.416 % which is a very good approximation of flow simulation result as shown in Figure 4.35(a) with a total efficiency of 72.447 %. Figure 4.36(b) and Figure 4.37(b) show that there is a region of high vorticity magnitude near the inlet cone tip for the 20 mm inlet cone depth. Skin friction lines have been plotted on the surfaces of the inlet cone and impeller cones. It has been shown from the skin friction lines plot in Figure 4.38(b) that there is a region of flow separation near the intersection point between inlet cone and impeller cone and hence this will impair relative velocity diffusion and hence affect the pressure rise in centrifugal impeller according to Eckardt [54] as explained in earlier section 3.5.2.1.2. This has accounted for the low total efficiency for inlet cone depth 20 mm. Figure 4.39 shows that the total efficiency has dropped drastically when the inlet cone depth has been extended to 20 mm. As illustrated in Figure 4.39, different inlet cone depths give different values of total efficiencies. This is because if the inlet cone is too deep into the impeller cone, there would be good guidance of flow from the inlet into the impeller but at the expense of flow separation due to the interaction between the inlet cone and the impeller cone as the impeller cone rotates. As a result, the total efficiency is affected by these two factors. Most total efficiencies for different inlet cone depths are varying between a narrow bandwidth from 70 % to 73 %. This variation is due to the contributions of the two factors. At 0 mm, the total efficiency is 68.710 %, which is very low because there is not enough guidance of flow from the inlet into the impeller. At 20 mm, there is large amount of flow separation and hence a total efficiency of 64.684 % is obtained. Results shown in Figures 4.40 and 4.41 have been based on volume flow rate 2.8 m^3/s, which is still within the operating

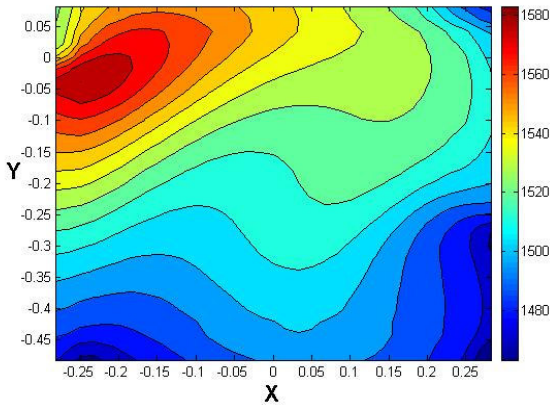
ATTENTION: The Singapore Copyright Act applies to the use of this document. Nanyang Technological University Library

range. Figure 4.40(b) shows that the optimized pressure profile after genetic algorithm requires a lower power requirement of 6677 W and hence it has given a higher total efficiency 68.105 %. Hence, the total efficiency after optimization has improved by about 4.946 %. Figure 4.41 shows that the optimization method of genetic algorithm is feasible in optimizing the inlet cone depth as the optimized result obtained in Figure 4.41(b) gives a total efficiency of 68.105 % which is a very good approximation of flow simulation result as shown in Figure 4.41(a) with a total efficiency of 68.133 %.

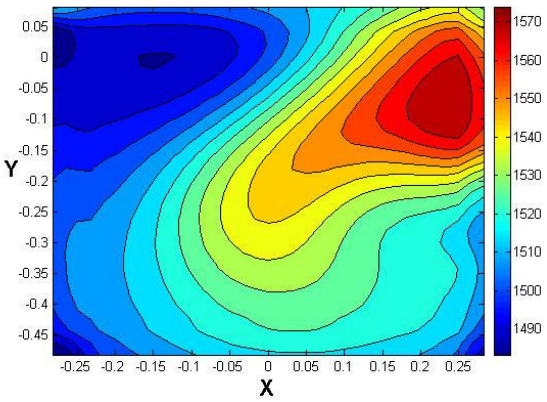
By comparing the POD optimization result with both the experimental result and *FLUENT* flow simulation result in Figure 4.42, it has been shown that the total efficiency of the industrial fan after optimization has improved significantly. At volume flow rate 2.27 m^3/s, the total efficiency after optimization has improved by about 4.929%. Hence, the inlet cone depth has been optimized for different volume flow rates within the operating range. The POD optimization result has also been verified with *FLUENT* optimization result as shown in Figure 4.42.

Hence, the aim of applying genetic algorithm on the design of an industrial fan has been successful by using a reduced order modeling technique known as proper orthogonal decomposition, which helps to cut down computational cost significantly without losing the characteristic features of the system. POD interpolation provides the inputs for the formulation of objective function to be minimized using genetic algorithm optimization method. Figure 4.43 shows that at different volume flow rates, the optimized inlet cone depth has different lengths. Hence, more volume flow rate within the operating range has to be tested to give a set of values of optimized inlet cone depth for different volume flow rates.

ATTENTION: The Singapore Copyright Act applies to the use of this document. Nanyang Technological University Library

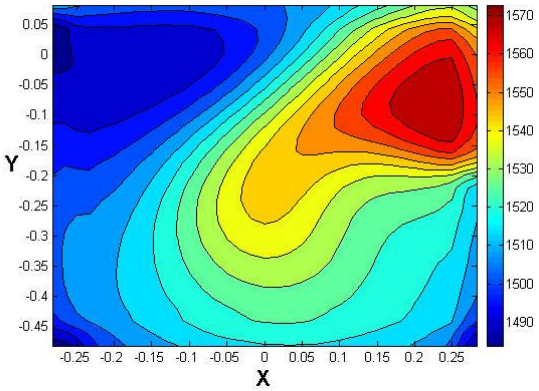


(a) Pressure profile before optimization
Inlet cone depth: 6.3 mm

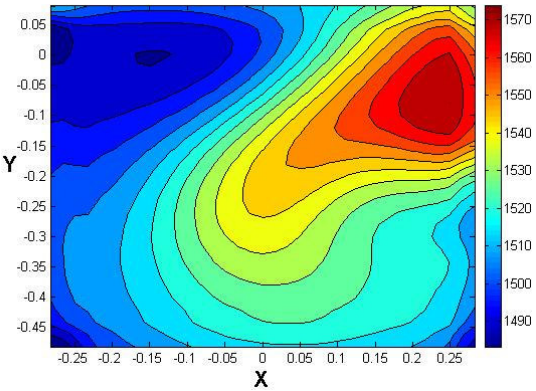


(b) Pressure profile after optimization
Inlet cone depth: 1.02905 mm

Figure 4.34 Comparison of (a) pressure profile before optimization of total efficiency with (b) pressure profile after optimization of total efficiency for BDB fan, 2200 rpm, and 3.33 m^3/s using parameter inlet cone depth



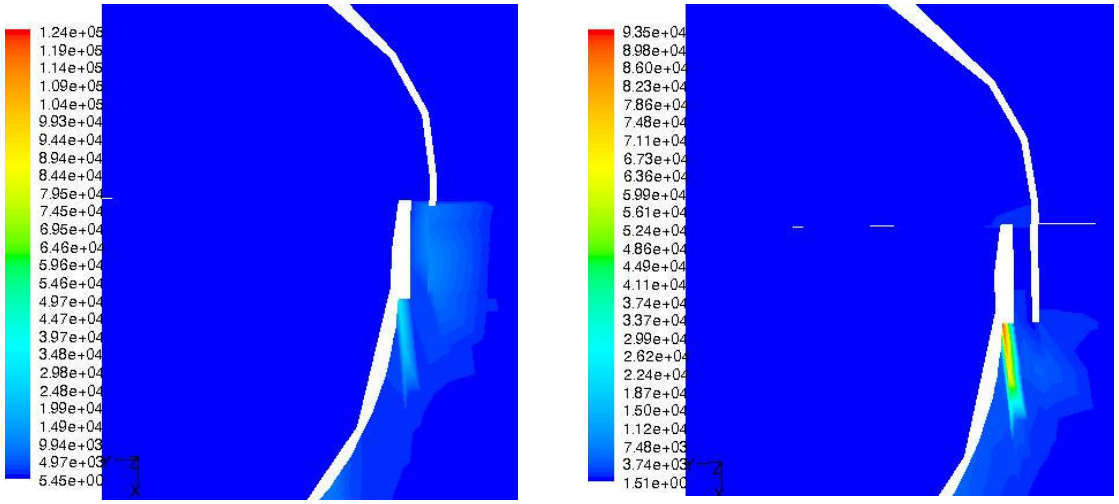
(a) Pressure profile after optimization with FLUENT flow simulation results



(b) Pressure profile after optimization with genetic algorithm

Figure 4.35 Comparison of (a) pressure profile after optimization with FLUENT flow simulation results with (b) pressure profile after optimization with genetic algorithm for BDB fan, 2200 rpm, and 3.33 m^3/s using parameter inlet cone depth

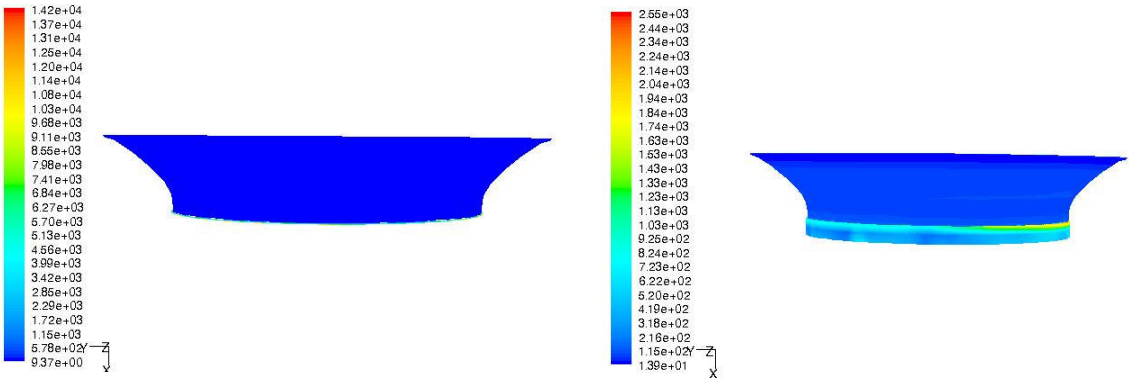
ATTENTION: The Singapore Copyright Act applies to the use of this document. Nanyang Technological University Library



(a) Inlet Cone depth 1 mm

(b) Inlet Cone depth 20 mm

Figure 4.36 Section view of vorticity magnitude near inlet cone tip for (a) inlet cone depth 1 mm and (b) inlet cone depth 20 mm for BDB fan, 2200 rpm, and 3.33 m^3/s

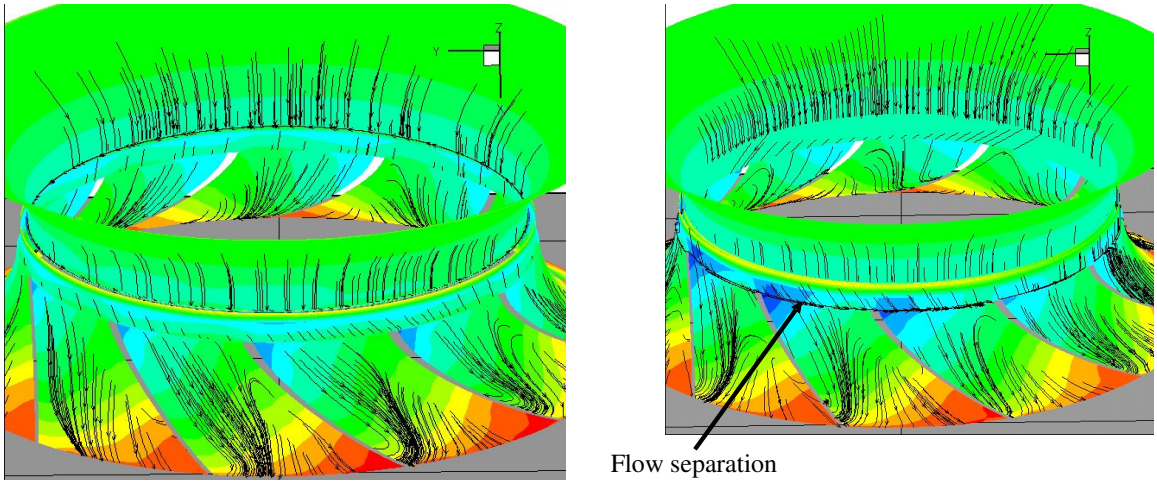


(a) Inlet Cone depth 1 mm

(b) Inlet Cone depth 20 mm

Figure 4.37 Vorticity magnitudes at inlet cone tip for (a) inlet cone depth 1 mm and (b) inlet cone depth 20 mm for BDB fan, 2200 rpm, and 3.33 m^3/s

ATTENTION: The Singapore Copyright Act applies to the use of this document. Nanyang Technological University Library



(a) Inlet Cone depth 1 mm

(b) Inlet Cone depth 20 mm

Figure 4.38 Skin friction lines near inlet cone tip for (a) inlet cone depth 1mm and (b) inlet cone depth 20mm for BDB fan, 2200 rpm, and 3.33 m^3/s

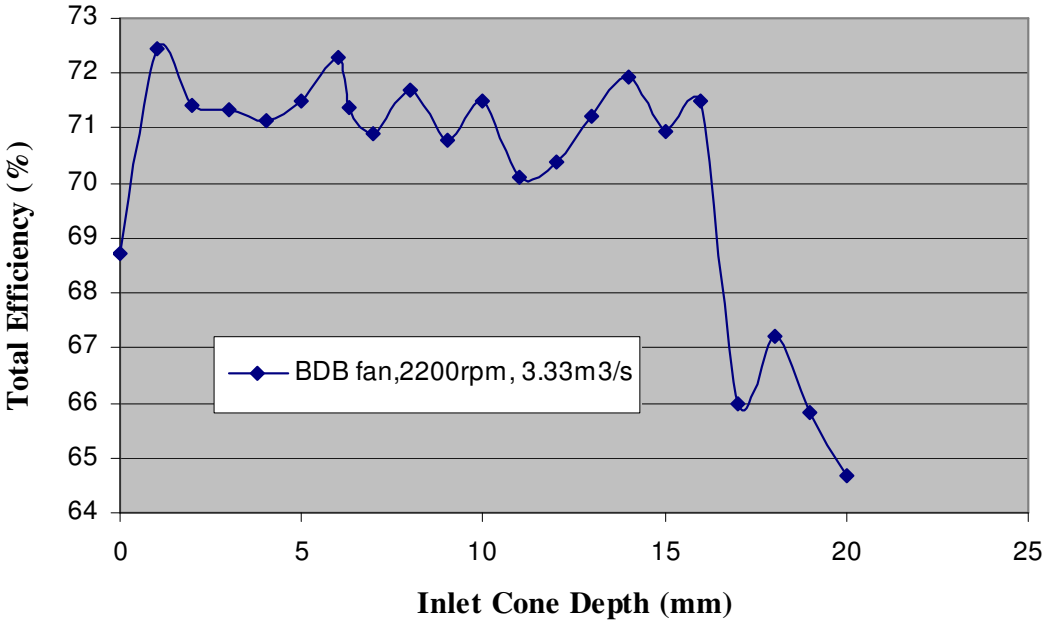
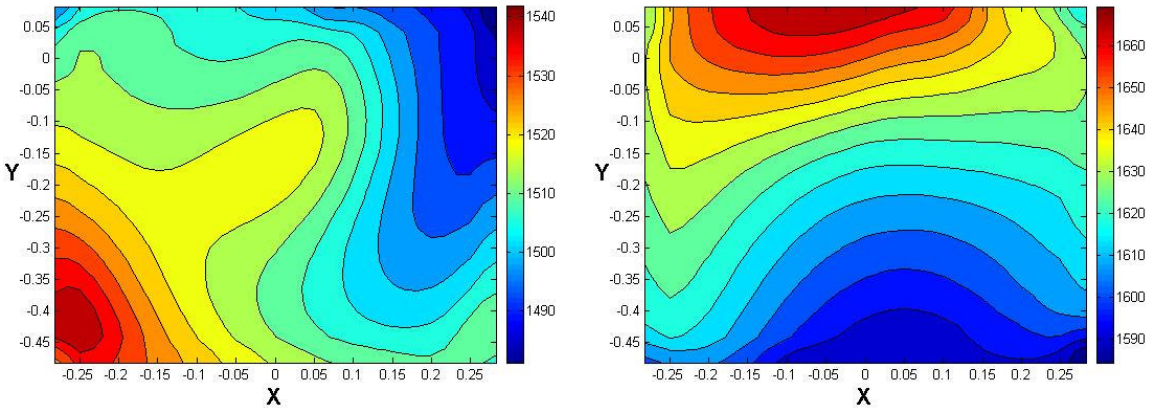


Figure 4.39 Plot of total efficiency against inlet cone depth for BDB fan, 2200 rpm, and 3.33 m^3/s

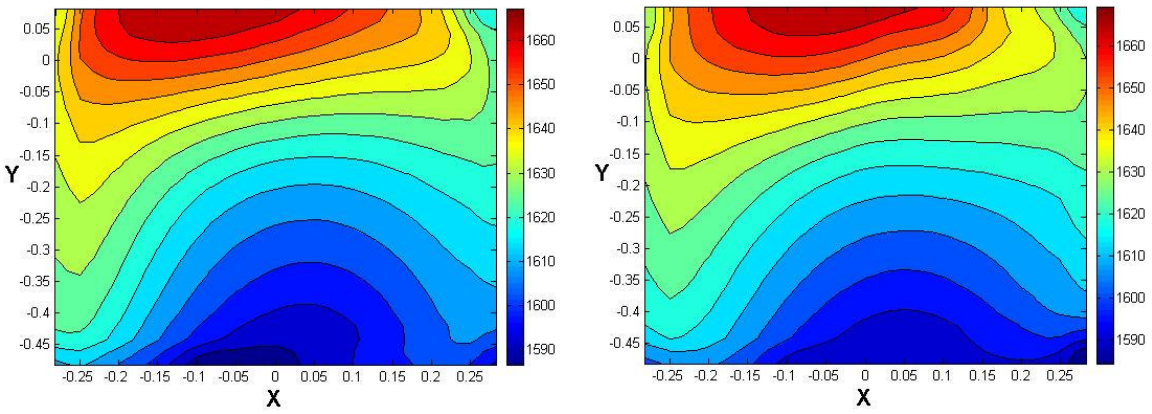
ATTENTION: The Singapore Copyright Act applies to the use of this document. Nanyang Technological University Library



(a) Pressure profile before optimization

(b) Pressure profile after optimization

Figure 4.40 Comparison of (a) pressure profile before optimization of total efficiency with (b) pressure profile after optimization of total efficiency for BDB fan, 2200 rpm, and 2.8 m^3/s using parameter inlet cone depth



(a) Pressure profile after optimization with FLUENT flow simulation results

(b) Pressure profile after optimization with genetic algorithm

Figure 4.41 Comparison of (a) pressure profile after optimization with FLUENT flow simulation results with (b) pressure profile after optimization with genetic algorithm for BDB fan, 2200 rpm, and 2.8 m^3/s using parameter inlet cone depth

ATTENTION: The Singapore Copyright Act applies to the use of this document. Nanyang Technological University Library

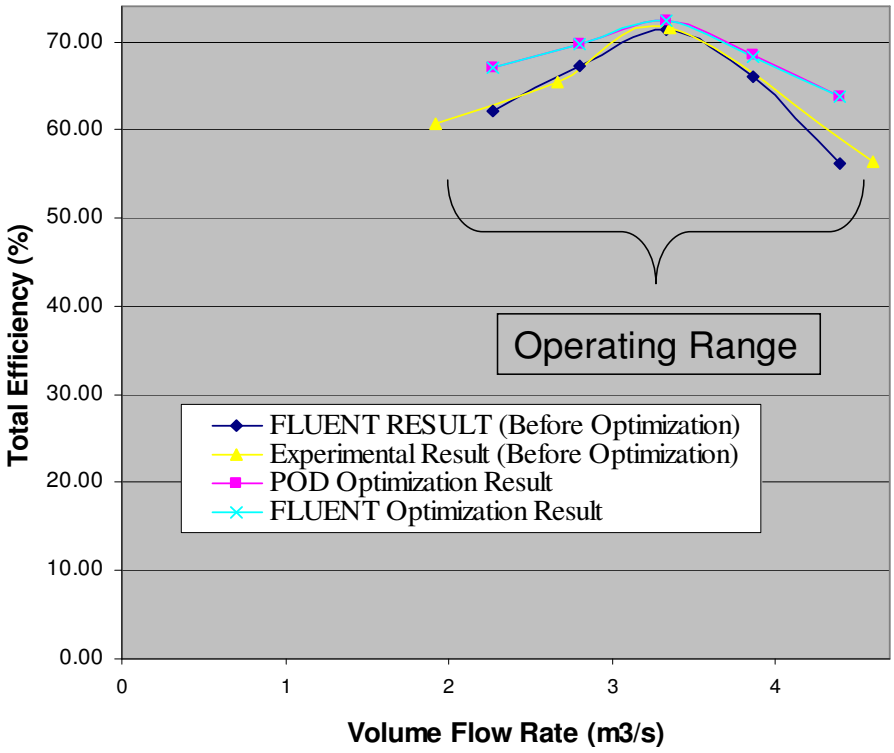
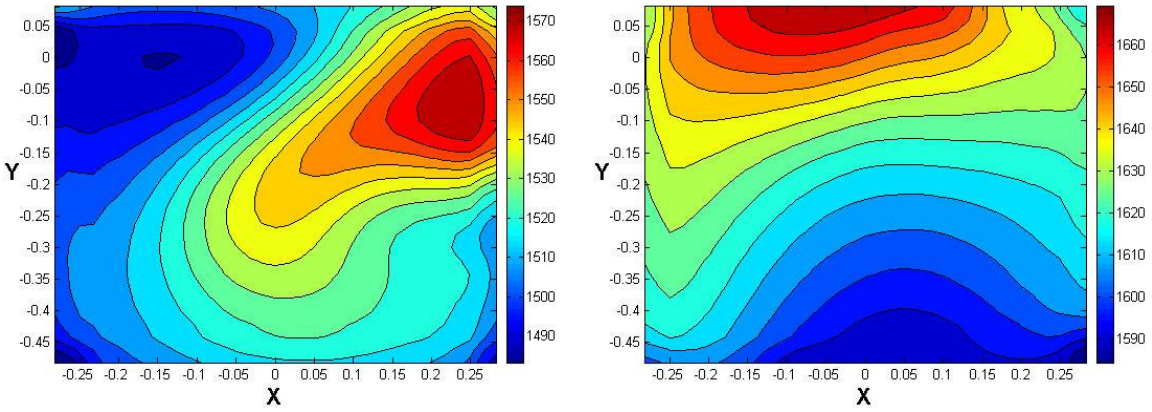


Figure 4.42 Plot of total efficiency for the double inlet fan running at 2200 rpm within the operating range before and after optimization



(a) Volume flow rate 3.33 m^3/s
Inlet cone depth: 1.02905 mm

(b) Volume flow rate 2.8 m^3/s
Inlet cone depth: 19.88591 mm

Figure 4.43 Pressure profile after optimization with genetic algorithm for BDB fan, 2200 rpm at (a) 3.33 m^3/s and (b) 2.8 m^3/s using parameter inlet cone depth

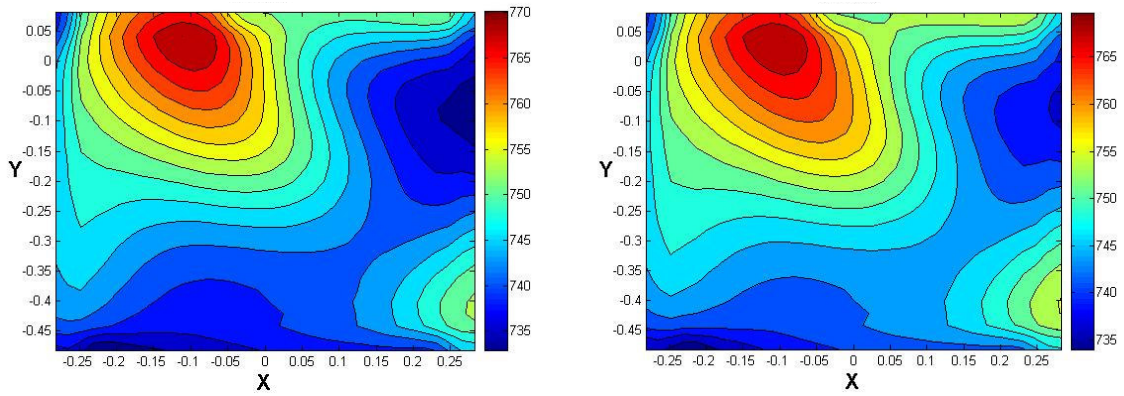
ATTENTION: The Singapore Copyright Act applies to the use of this document. Nanyang Technological University Library

4.5.4.2 Design Parameter Blade Angle

As discussed in earlier section 3.5.2.1.6, the 8-bladed impeller has peak efficiency slightly lower than that of the 11-bladed impeller and hence it is economically feasible to improve the total efficiency of the 8-bladed impeller in this section using design parameter blade angle. This is because both the number of blades and the blade angle affects the channel between the blades which has to be narrow enough for good guidance of the air stream. On the other hand, it has to be wide enough so that the resistance to airflow is not too great according to Bleier [45]. This is the reason why design parameter blade angle 36° to 41° has been used. It is based on volume flow rate 2.5 m^3/s, which is at the peak efficiency for the 8 bladed impeller double inlet fan, running at 1600 rpm.

4.5.4.2.1 POD Results for Optimization of Total Efficiency

Results shown in Figure 4.44 are based on volume flow rate 2.5 m^3/s, which is at the peak efficiency for the 8 bladed impeller double inlet fan running at 1600 rpm. The blade angle has been optimized to give a higher total efficiency of 68.530 % as shown in Figure 4.44(b). The total efficiency after optimization has improved by about 0.287 %. Hence, the aim of optimizing the 8 bladed impeller fan has been achieved.



(a) Pressure profile before optimization
Blade Angle: 38.5°

(b) Pressure profile after optimization
Blade Angle: 38.58337°

Figure 4.44 Comparison of (a) pressure profile before optimization of total efficiency with (b) pressure profile after optimization of total efficiency for 8 Bladed BDB fan, 1600 rpm, and 2.5 m^3/s using parameter Blade Angle

ATTENTION: The Singapore Copyright Act applies to the use of this document. Nanyang Technological University Library

4.5.4.3 Optimization with Two Design Parameters

In the previous sections, optimization of total efficiency has been based on a fixed volume flow rate with the inlet cone depth as the variable. It has been assumed that 3.33 m^3/s would give the peak efficiency for the double inlet fan running at 2200 rpm. However, this might not be true as 3.33 m^3/s gives the peak efficiency only before optimization of inlet cone depth. With a different inlet cone depth, the volume flow rate that gives the peak efficiency might not be 3.33 m^3/s. Hence, there is a need to do optimization using two parameters simultaneously. This means that the inlet cone depths and volume flow rates have to be varied simultaneously. Section 4.5.4.3.1 shows the effect of volume flow rates on optimized inlet cone depth and proves that it is necessary to have two parameters optimization. Equation (4.3) shows the formulation of the objective function for two parameters optimization using genetic algorithm to find the global minimum of the objective function within the parameter range.

4.5.4.3.1 Effect of Volume Flow Rates on Optimized Parameter

Figure 4.45 shows the plot of total efficiency against volume flow rates for different inlet cone depths. The actual optimized inlet cone depth is the one which gives the highest total efficiency amongst all the different volume flow rates in that figure. Figure 4.46 shows the optimized inlet cone depths for different volume flow rates. It is noted that the optimized total efficiencies for each inlet cone depths occur at different volume flow rates and hence there is an illusion that there are many peaks in the total efficieny plot in Figure 4.45. Comparing between Figure 4.46(b) and Figure 4.46(c), it has been shown that the optimized inlet cone depths are different for different volume flow rates. This has proven that different volume flow rates would give different optimized parameters.

ATTENTION: The Singapore Copyright Act applies to the use of this document. Nanyang Technological University Library

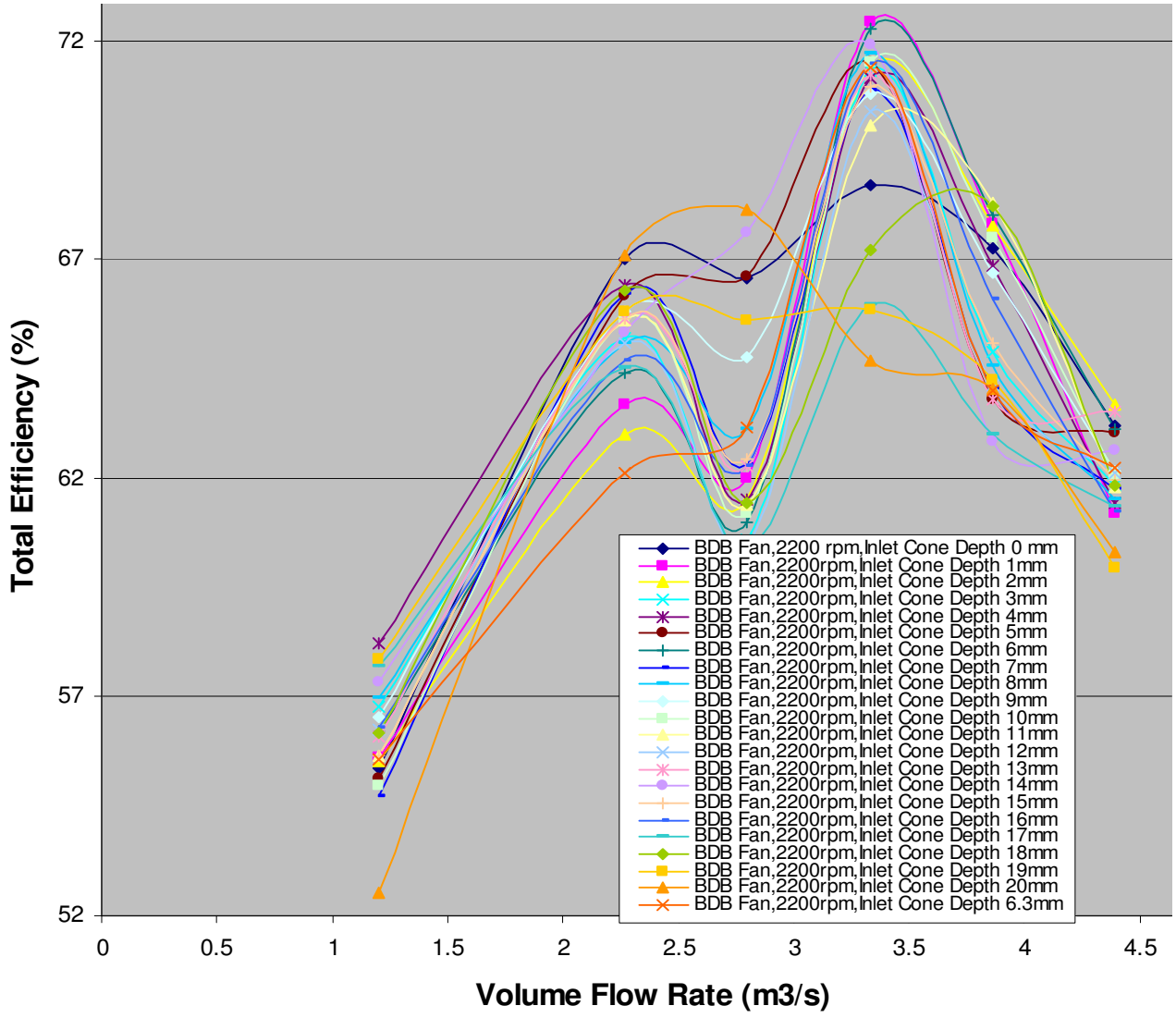
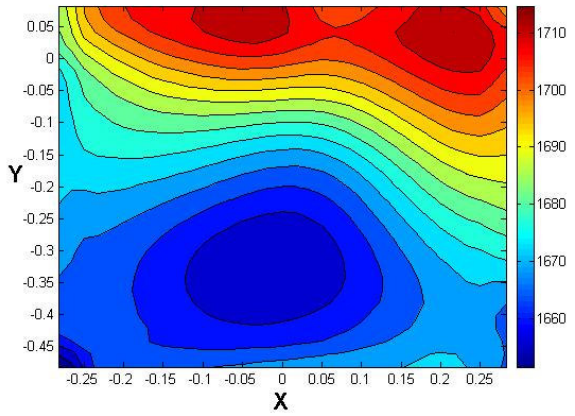
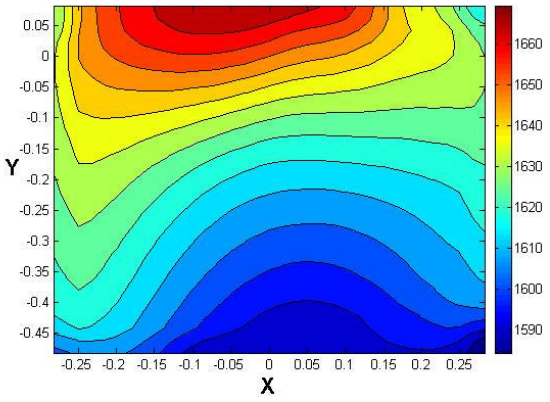


Figure 4.45 Plot of Total Efficiency against volume flow rates for different inlet cone depths for double inlet fan, running at 2200 rpm

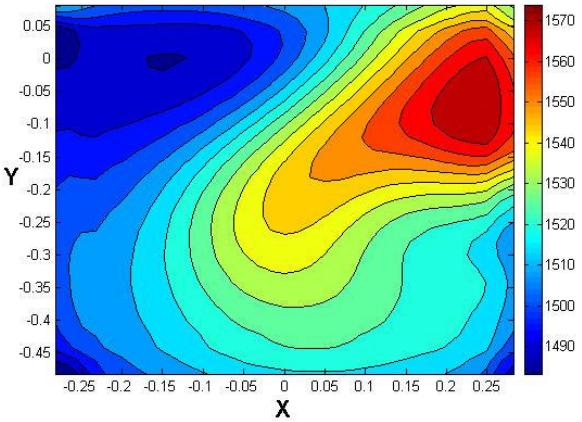
ATTENTION: The Singapore Copyright Act applies to the use of this document. Nanyang Technological University Library



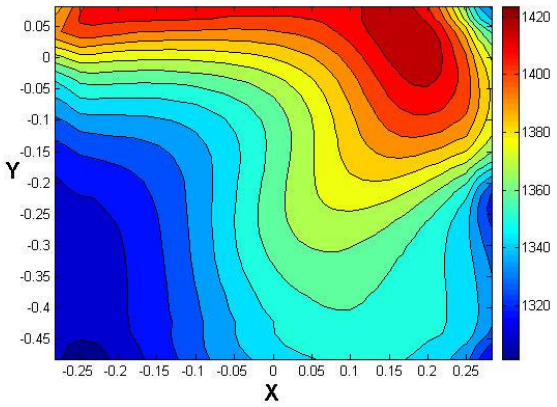
(a) Volume Flow Rate 2.27 m^3/s
Inlet cone depth: 19.98895 mm



(b) Volume Flow Rate 2.80 m^3/s
Inlet cone depth: 19.88591 mm



(c) Volume Flow Rate 3.33 m^3/s
Inlet cone depth: 1.02905 mm



(d) Volume Flow Rate 3.86 m^3/s
Inlet cone depth: 10.83348 mm

Figure 4.46 Comparison of different optimized inlet cone depths for BDB fan, 2200 rpm with different volume flow rates (a) 2.27m^3/s, (b) 2.80 m^3/s, (c) 3.33m^3/s and (d) 3.86 m^3/s

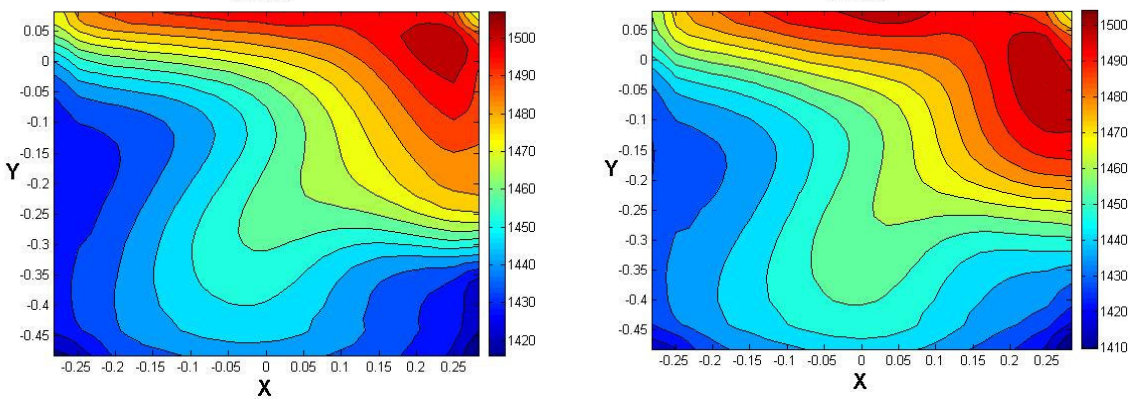
ATTENTION: The Singapore Copyright Act applies to the use of this document. Nanyang Technological University Library

4.5.4.3.2 POD Results Using Two Parameters

It is necessary to verify the POD results obtained from two parameters optimization with that of one parameter optimization under the same volume flow rate and inlet cone depth. Figure 4.47(a) and Figure 4.47(b) have the same total efficiency of 68.708 % and hence POD results with two parameters have been verified. The advantage of two parameter optimization using volume flow rates and inlet cone depth is that POD interpolation could be used to obtain approximation of results at any specified volume flow rate and inlet cone depth as shown in Figure 4.48 as long as it is within the range in Equation (4.4). Previously, POD interpolation results can be obtained only for volume flow rates 2.27 m^3/s, 2.80 m^3/s, 3.33 m^3/s, 3.86 m^3/s and 4.39 m^3/s. With the addition of volume flow rates as a design parameter, a more global optimized inlet cone depth has been obtained as shown in Figure 4.49(b) with total efficiency 72.824 % which gives an additional improvement of 0.408 % in total efficiency. It has been noted that the volume flow rate for the optimized inlet cone depth is not 3.33 m^3/s, as it has been previously assumed. Instead, it is at volume flow rate 3.44 m^3/s as shown in Figure 4.49(b).

In optimization of total efficiency by varying volume flow rate and inlet cone depth, the fluid density effect, viscosity effect and Reynolds number effect are not critical. This is because the flow is incompressible and hence there is no fluid density effect. The viscosity of the fluid is also assumed to be constant. There is no Reynolds number effect as the fan is running at a fixed rpm and hence there is no change in Reynolds number. The Reynolds number effect would only be critical if the result is extrapolated from fan laws.

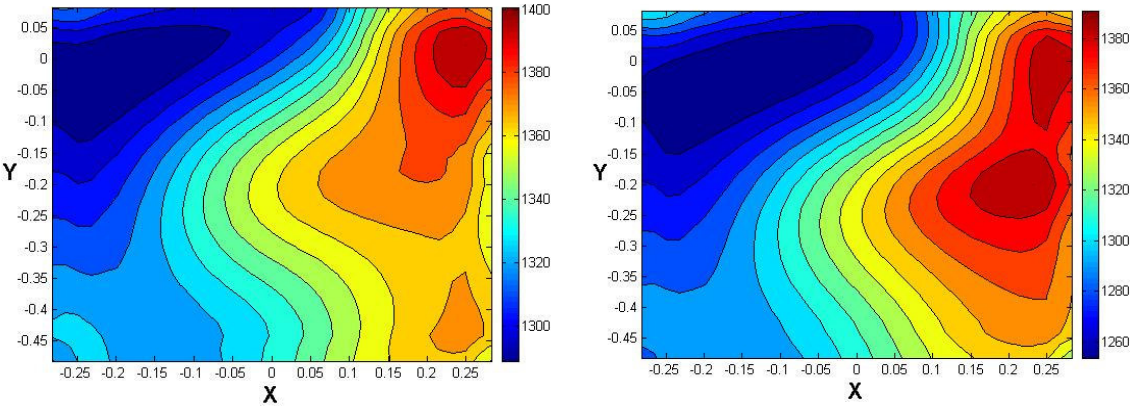
ATTENTION: The Singapore Copyright Act applies to the use of this document. Nanyang Technological University Library



(a) Parameter of Inlet Cone Depth

(b) Parameters of Inlet Cone Depth and Volume Flow Rates

Figure 4.47 Comparison of pressure profile for using (a) parameter of inlet cone depth and (b) parameters of inlet cone depth and volume flow rates for BDB fan, 2200 rpm, inlet cone depth 0 mm and 3.33 m^3/s

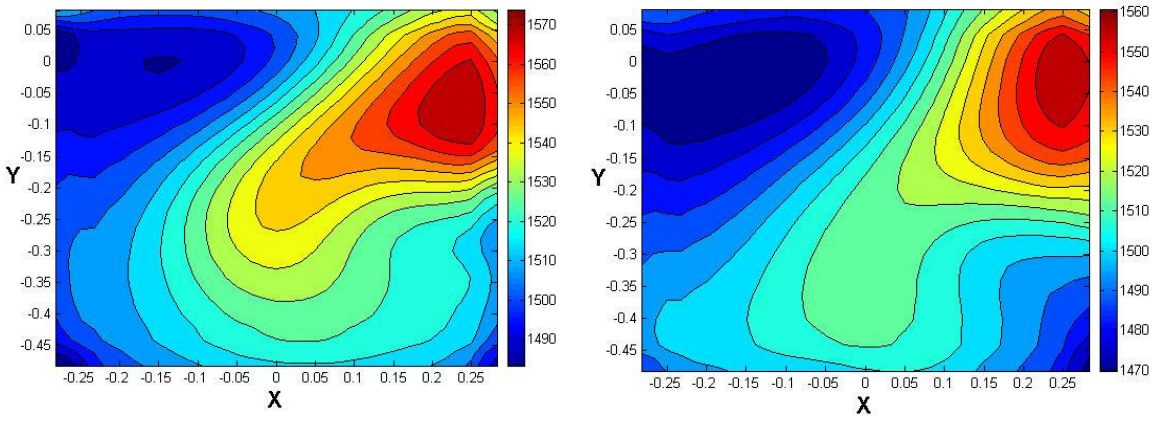


(a) Inlet cone depth: 18.5 mm
Volume Flow Rate: 3.8 m^3/s

(b) Inlet cone depth: 17.89 mm
Volume Flow Rate: 3.93 m^3/s

Figure 4.48 Comparison of different pressure profiles for using parameters of inlet cone depth and volume flow rates for BDB fan, 2200 rpm

ATTENTION: The Singapore Copyright Act applies to the use of this document. Nanyang Technological University Library



(a) Optimized Inlet Cone Depth Only
Inlet cone depth: 1.02905 mm

(b) Optimized Inlet Cone Depth and Volume Flow Rates
Inlet cone depth: 1.19008 mm

Figure 4.49 Comparison of pressure profile for using (a) optimized parameter of inlet cone depth only and (b) optimized parameters of inlet cone depth and volume flow rates for BDB fan, 2200 rpm

4.5.5 Multi Objective Optimization of Cost and Total Efficiency

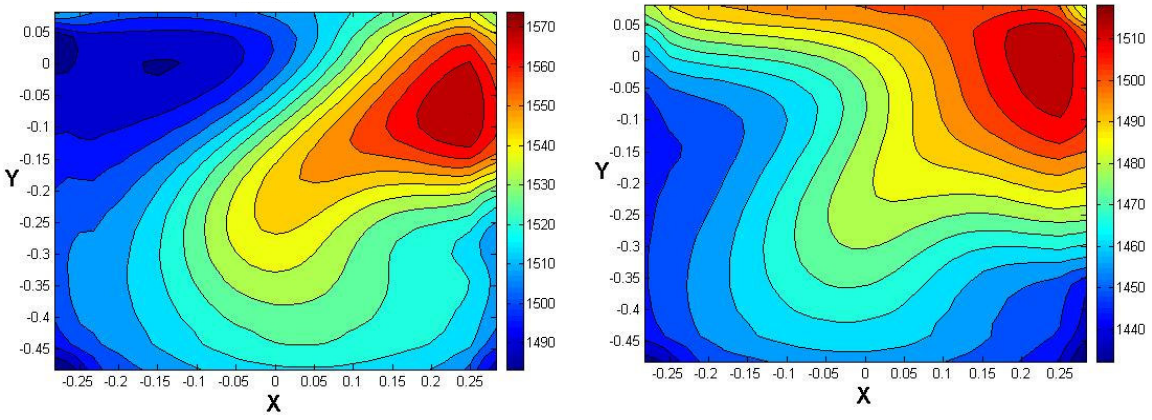
In the previous sections, optimization problems based on a single objective function total efficiency have been done. In this section, cost has been introduced as an additional objective which has to be minimized. At the same time, the total efficiency has to be maximized. Hence, a solution that has to compromise between the two variables has to be obtained using the weighted sum method. Section 4.1.3 shows the formulation of the objective function for multi objective optimization using genetic algorithm to find the global minimum of the new objective function within the parameter range. Obayashi [81] has suggested the use of response surface method as a surrogate model known as Kriging model [30] which predicts the probability density distribution of function values at unknown points instead of the function values themselves and has been applied in multi objective optimization. This is because Obayashi [81] has stated that genetic algorithm being a population based approach required a large number of function evaluations. This

ATTENTION: The Singapore Copyright Act applies to the use of this document. Nanyang Technological University Library

project is different as it evaluates the function values directly for multi objective optimization. This has been achieved because of using a reduced order modeling technique which helps to cut down computational cost significantly without losing the characteristic features of the system. POD interpolation provides the inputs for the formulation of objective function to be minimized using genetic algorithm optimization method.

4.5.5.1 POD Results for Multi Objective Optimization

The effect of varying the weighted coefficient a_1 and a_2 are shown in Figure 4.50 and Figure 4.51. Figure 4.50(b) shows that when equal weight of importance is given to the total efficiency and cost, a solution that compromised both objective functions is obtained. According to Figure 4.50(b), the material cost is \$70.11 and the total efficiency is 69.583 %. This gives a lower material cost but also a lower total efficiency when compared with that of Figure 4.50(a). Hence the multi objective optimization solution has compromised the two objective functions of cost and total efficiency. When the weight coefficient a_2 is set to be 0.999, the importance of having a low cost far outweighs the importance of having a high total efficiency and hence in Figure 4.51(b), a solution with extremely low cost of \$70.05 has been obtained.

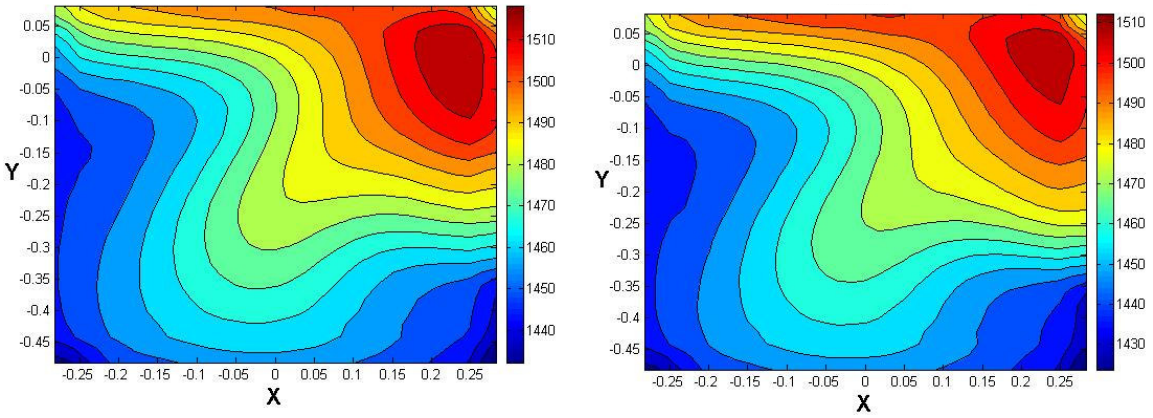


(a) Maximum total efficiency after optimization

(b) Multi-objective optimization: $a_1 = 0.5$, $a_2 = 0.5$

Figure 4.50 Pressure profile for (a) maximum total efficiency after optimization and (b) multi-objective optimization with $a_1 = 0.5$ and $a_2 = 0.5$ for BDB fan, 2200 rpm, and 3.33 m^3/s using parameter inlet cone depth

ATTENTION: The Singapore Copyright Act applies to the use of this document. Nanyang Technological University Library



(a) $a_1 = 0.5$, $a_2 = 0.5$

(b) $a_1 = 0.0001$, $a_2 = 0.999$

Figure 4.51 Pressure profile for multi-objective optimization for (a) $a_1 = 0.5$ and $a_2 = 0.5$ and (b) $a_1 = 0.001$ and $a_2 = 0.999$ for BDB fan, 2200 rpm, and 3.33 m^3/s using parameter inlet cone depth

4.5.6 Constrained Optimization of Total Efficiency

Michalewicz and Janikow [60] have suggested three approaches to the constraints problem in genetic algorithm. They are to transform potential solutions of the problem into a form suitable for a genetic algorithm, penalty function method and lastly modifying the genetic algorithm to suit the problem by using new data structures and new genetic operators. The second approach of using penalty function method has been selected for this project. The exact penalty function method has been applied for the formulation of the objective function in section 4.1.4 of the constrained optimization problem. A possible inequality constraint is the operating range in term of volume flow rate. However, it is unnecessary because only POD snapshots with volume flow rate within the operating range have been taken. The equality constraint for the problem is the fixed diameter of the impeller plate. However, it is also unnecessary to use this equality constraint as all POD snapshots are taken with a fixed impeller diameter and hence, the impeller diameter isn't a parameter. In another words, the equality constraint and inequality constraint are already incorporated into the problem even before the formulation of the objective function.

ATTENTION: The Singapore Copyright Act applies to the use of this document. Nanyang Technological University Library

4.5.6.1 POD Results for Constrained Optimization

The effect of penalty parameter on the penalty function value is as shown in Figure 4.52. The penalty function value will go to zero if no constraint is violated. It is noted that if the penalty parameter chosen is too small, the penalty function value will give a value greater than zero and hence the exact penalty function method will only work for constrained optimization if the penalty parameter is large enough. However Davis [82] has explained that if one gives too large penalty parameter at the start of genetic reproduction, one runs the risk of creating a genetic algorithm that spends most of its time evaluating the violated individuals and when a individuals that do not violate the constraints is found, the population would converge on it without finding better individuals since the likely paths to other legal individuals require the production of illegal individuals as intermediate structures and the penalty for violating the constraint makes production of intermediate structure not possible. Hence, the penalty parameter has been increased marginally from a very small value to a larger value as shown in Figure 4.52 to avoid ill conditioning.

Figure 4.53(b) shows the total pressure profile at outlet with constraint above 1490 Pa. Note that none of the pressure nodes are below 1490 Pa and hence the constraint has worked. When the penalty function value goes to zero, this means that the constraint is not violated. Figure 4.54(a) shows the pressure profile when there is a non-zero penalty function value and hence the inequality constraint is violated. There are pressure nodes below 1490 Pa for Figure 4.54(a) because of the bad choice of penalty parameter c as 0.0000001 which is too small to affect the objective function.

ATTENTION: The Singapore Copyright Act applies to the use of this document. Nanyang Technological University Library

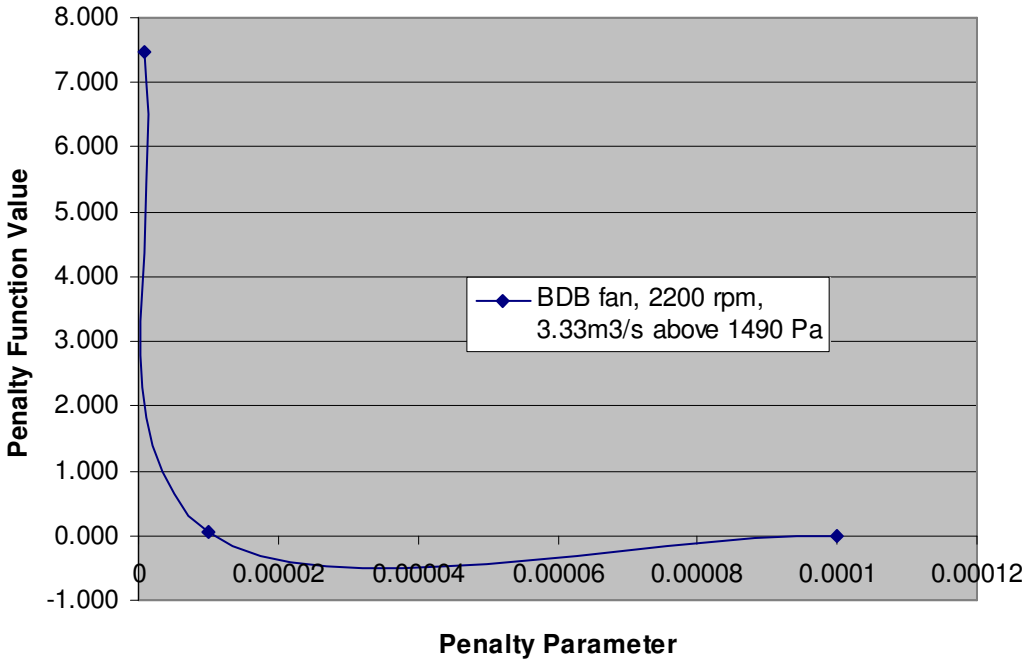
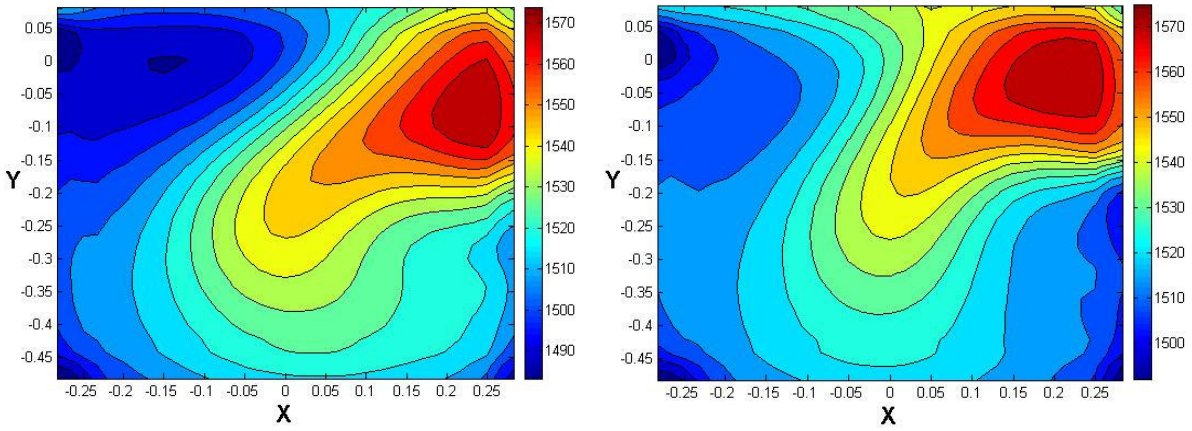


Figure 4.52 Plot of Penalty Function Value against Penalty Parameter for BDB fan, 2200 rpm, and 3.33 m^3/s using parameter inlet cone depth

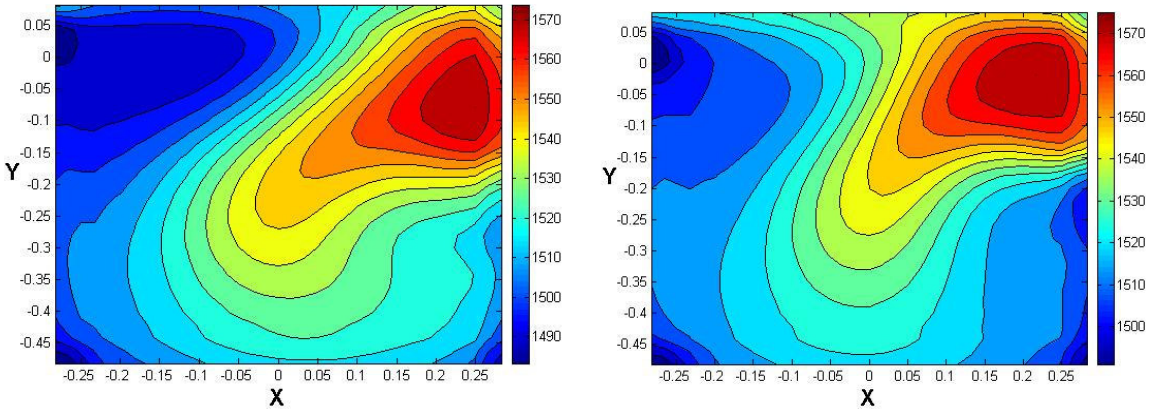


(a) Unconstrained optimization

(b) Constrained optimization with pressure above 1490 Pa

Figure 4.53 Pressure profile of (a) unconstrained optimization and (b) constrained optimization with pressure above 1490 Pa for BDB fan, 2200 rpm, and 3.33 m^3/s using parameter inlet cone depth

ATTENTION: The Singapore Copyright Act applies to the use of this document. Nanyang Technological University Library



(a) Penalty Parameter: 0.0000001
Penalty Function Value: 7.441

(b) Penalty Parameter: 0.0001
Penalty Function Value: 0

Figure 4.54 Pressure profile of constrained optimization for pressure above 1490 Pa with (a) penalty parameter 0.0000001 and (b) penalty parameter 0.0001 for BDB fan, 2200 rpm, and 3.33 m^3/s using parameter inlet cone depth

ATTENTION: The Singapore Copyright Act applies to the use of this document. Nanyang Technological University Library

CHAPTER 5

CONCLUSION & FUTURE WORK

5.1 Conclusion

Fan performance characteristics of single inlet fan and double inlet fan have been investigated using sliding mesh models. Numerical simulation results using sliding mesh models have been verified with experimental results. In addition, different turbulence models have been used to check the consistency of flow simulation results. The standard k epsilon turbulence model is able to obtain accurate flow simulation results for the current turbomachinery problems. Rotating stall occurs because of insufficient air to fill in the spaces between the blade passages. As a result, the flow is shared unequally such that some blade passages have large air flow while others have very little air flow. The rotating stall phenomenon which is commonly found in centrifugal fan has been observed by using the sliding mesh models. Part span stall cells which exist in a single blade passage are seen from animation video. It is a part span stall cell because it extends only to part of the annulus span. This rotating stall phenomenon would eventually result in fan surge. Surge points for different rpm occur when there is adverse pressure drop while reducing the volume flow rate. When the surge points are joined together, the surge line is obtained. This has provided insight about the operating range of the ventilation fan as it is necessary for the ventilation fan to avoid operating near the surge line.

The alignment of top and bottom impellers affects fan performance. A slightly lower gauge total pressure at the outlet is obtained when the top and bottom impellers are aligned. Hence, this explains why the alignment of top and bottom impellers has not been chosen as a design variable for optimization. Fan performance characteristics of ventilation fan rotating in opposing directions for top and bottom impellers have also been investigated. A lower total efficiency has been obtained when the top and bottom impellers are rotating in opposing directions. Hence, it is not a feasible idea to change the direction of rotation of fan to generate a higher total efficiency. The channel between the blades must be narrow

ATTENTION: The Singapore Copyright Act applies to the use of this document. Nanyang Technological University Library

enough for good guidance of the air stream. On the other hand, it has to be wide enough so that the resistance to airflow is not too great. The original design geometry of the fan has 11 blades. The 11-bladed impeller gives the highest total efficiency. However, the 8-bladed impeller has a total efficiency which is only slightly lower than the peak total efficiency of the 11-bladed impeller. Hence, the 8-bladed impeller has been selected for optimization. The advantage of using the 8-bladed impeller is that it is most cost effective as less material is needed to make the fan. The number of blades is a more important design parameter than both the alignment of top and bottom impellers and the directions of rotation of the top and bottom impellers. This is because the number of blades could be changed to improve the total efficiency of the fan significantly unlike the other two design parameters.

Comparing the single inlet fan with the double inlet fan, the single inlet fan has given a higher total efficiency at low volume flow rates but a lower total efficiency at high volume flow rates. The double inlet fan has given a higher gauge total pressure at the outlet but has a lower total efficiency due to a higher power requirement. Hence, for industrial purposes, the double inlet fan is used when a higher gauge total pressure is desired. The single inlet fan is desirable at low volume flow rate as it gives a higher total efficiency. When compared with the double inlet fan with single thickness blades, the airfoil bladed fan has a lower gauge total pressure at the outlet but with a much smaller less power requirement for the same volume flow rate and hence the airfoil bladed fan has a higher total efficiency. This insight provides the possibility of improving the total efficiency of the fan by replacing the single thickness blades with airfoil blades. Hence, blade shape optimization is a feasible way to improve the total efficiency of the fan.

Flow simulations of ventilation fan have provided insights for the design optimization stage. It has been noted that flow separation has affected the impeller static pressure rise and hence would affect fan performance. As such, flow separation must be minimized in design optimization. Those design parameters which would affect flow separations significantly have been chosen for optimization as they would most likely give allowance for a larger increase in total efficiency. These design parameters include inlet cone depth, blade angle and number of blades which have been selected because they have been known to have an impact on flow separation based on feedbacks from the industry. The inlet cone depth is the

ATTENTION: The Singapore Copyright Act applies to the use of this document. Nanyang Technological University Library

most important design parameter for optimization which is followed closely by number of blades and blade angle. This is because the number of blades and blade angle are already been optimized with so many trial and error fan testing. The total efficiency has been optimized for different design parameters such as inlet cone depth and blade angle. The optimization of blade angle for the 8 bladed impeller fan has given a slight improvement in total efficiency. It has noted that at different volume flow rates, the optimized inlet cone depth is different in length. Hence, inlet cone depths and volume flow rates have been varied simultaneously for optimization as two different design parameters. The volume flow rates giving the peak efficiency for different inlet cone depths have been different. There are two advantages of using volume flow rates and inlet cone depth together as design parameters. Firstly, an approximation of results at any specified volume flow rate and inlet cone depth can be obtained as long as it is within the operating range. Secondly, optimized inlet cone depth with a higher total efficiency can be obtained.

The gradient based method has not been used as the optimization method because of the presence of many local minima. Depending on the initial guess, the gradient based method would have converged to a different solution which would be incorrect. Genetic algorithm is the optimization method of choice to solve the above optimization problems. This is because it is a global optimization method which can avoid getting stuck in local minima. Moreover, it does not require gradient information which is difficult to estimate for the optimization problems. Genetic algorithm begins by creating a random initial population. However, one of the most significant disadvantages of genetic algorithm is that a large population size is needed in order for it to be effective. The computational cost of creating this large random initial population is extremely high if only high fidelity flow solver is used. This is because if the population size is 500, 500 flow simulations have to be done using high fidelity flow solver. The computational cost of genetic algorithm optimization with reduced order modeling is significantly smaller when compared with optimization with only high fidelity flow solver. The computational cost for one flow simulation using high fidelity flow solver is significantly higher than that of POD interpolation result. For example, in order to solve the full Navier Stokes equations, N^3 amount of storage is needed for high fidelity flow solver. This is significantly large when compared with that of POD

ATTENTION: The Singapore Copyright Act applies to the use of this document. Nanyang Technological University Library

interpolation result which requires only $m \times N$ amount of storage where m is the number of POD modes and N is the number of mesh nodes. In addition, the proper orthogonal decomposition interpolation method requires only an ensemble of 31 POD snapshots to create the same population size. Hence, only 31 flow simulations have to be done instead of doing all the 500 flow simulations with the high fidelity flow solver.

Although, reduced order modelling has cut down the computational cost of genetic algorithm optimization, the method of snapshots using proper orthogonal decomposition interpolation has some disadvantages. Many POD modes and POD snapshots must be used in order to obtain a good approximation to the flow simulation results. Hence, quite a number of flow simulations have to be done in order to create a complete set of ensemble of snapshots good enough for proper orthogonal decomposition interpolation. Even though, the computational cost of creating these snapshots is significantly smaller when compared with using only high fidelity flow solver, the computational cost can be further reduced by applying writing an automatic mesh generation code for the complex industrial fan geometry so as to speed up the creation of flow simulation snapshots.

5.2 Future Work

There are many areas of future work to be explored. Future work should focus on discovering new optimization method that is computational cheap and global. The Levenberg-Marquardt algorithm could be applied for the design optimization problems. Simulated annealing and neural network could also be tested for the design optimization problems. Comparison of the computational costs of various optimization methods could be done, so that the optimization method which is most global and cheapest in computational cost would be selected. The genetic algorithms could also be coupled with gradient based techniques and reduced order modeling technique to further reduce the computational cost.

There are still many design parameters which have not been explored in this project. This includes the fan blade shape design. Fan blades with airfoil shape could be parameterized for optimization. Three-dimensional inverse design method could then be applied for optimization of fan blade shape. Other design parameters include the blade angle. So far,

ATTENTION: The Singapore Copyright Act applies to the use of this document. Nanyang Technological University Library

only blade angle 36° to 41° for the 8 bladed impeller fan have been explored for design optimization based on feedbacks from the industry. More works could be done by using blade angle as a design parameter for 12 bladed impeller fan, 11 bladed impeller fan, 10 bladed impeller fan and 9 bladed impeller fan. The range of blade angle could be expanded. Multi objective optimization of the material cost and total efficiency could be done by using three design parameters coupled together such as blade angle, inlet cone depth and number of blades. So far, only the double inlet backward curved fan has been optimized. There are many different types of ventilation fans such as forward curved bladed fan which could be optimized. At the present stage of this project, flow simulation has not been done on the forward curved fan and the radial curved fan and hence no comparison could be made. Flow simulation for both the forward curved fan and radial curved fan could be done in the future so that comparison of fan performance characteristics such as total efficiency could be made.

The present technique of using genetic algorithms optimization method coupled with reduced order modeling technqiue to reduce computational cost could be further improved. One area of improvement is the accuracy of the proper orthogonal decomposition interpolation method. This could be done by creating more POD snapshots, although it comes at the expense of higher computational time. However, the idea is that these expensive calculations can be done offline before the optimization of the design parameters is attempted. This means that the ensemble of snapshots needs to be obtainced only once and after which POD interpolation could be used conveniently without additional computational cost. Moreover, the reduced basis could be used for several design settings. So far, reduced order modeling has only been applied at the fan outlet. An approximation of the pressure profile at the fan outlet is then used in the calculation of the objective functions. The use of proper orthogonal decomposition method could be expanded by doing a model order reduction for surface pressure profile of impeller blades and other part of the ventilation fan. This means that reduced order modeling technique is applied to estimate three dimensional pressure profiles. In addition, different population size for genetic algorithm could be used to find the smallest genetic algorithm population sample size

ATTENTION: The Singapore Copyright Act applies to the use of this document. Nanyang Technological University Library

without compromising the accuracy of optimized solution so as to reduce the computational cost for optimization.

Based on experience gained from this project, the most time consuming part of the work is grid generation. Mesh generation using structured hexagonal meshes usually take several weeks and at times even few months. This is undesirable. Automatic mesh generation could be explored. Another way to cut down the computational cost of mesh generation is to use unstructured mesh. However, unstructured mesh is unsuitable for sliding mesh model. Hence, comparison of the accuracy and computational costs of the flow simulation results using sliding mesh model and unstructured meshes could be done. The multi-grid scheme can accelerate the convergence of the solver by computing corrections on a series of coarse grid levels. The use of multi-grid scheme can greatly reduce the number of iterations and the CPU time required to obtain a converged solution, particularly when the model contains a large number of control volumes. Although, the multi-grid has not yet been used in the CFD scheme, it can be used in the future when there is larger number of grid nodes in the model.

ATTENTION: The Singapore Copyright Act applies to the use of this document. Nanyang Technological University Library

REFERENCES

[1] Kent Williams "Continental Fan Manufacturing Product Literature", 2006, USA, URL Source Link: http://www.continentalfan.com/

[2] Kruger Ventilation Industries Official Website, 2006, Singapore, URL Source Link: http://www.krugerfan.com/centri_bdb.php

[3] LTG Incorporated Official Website, 2002, USA, URL Source Link: http://www.ltg-inc.net/auswahl_f.htm

[4] Flamgard, B.O.B. Stevenson Ltd, 2006, United Kingdom, URL Source Link: http://www.bobstevenson.co.uk/flamgard_fans.htm

[5] Air Movement and Control Association International Official Website, USA, URL Source Link: http://cart.amca.org/laboratory/services.asp

[6] Kruger Technical Bulletin, Singapore, 2003

[7] R. Van den Braembussche: "Design and Optimization of Centrifugal Compressors." Von Karman Institute for Fluid Dynamics, Thermodynamics and Fluid Mechanics of Turbomachinery Volume II, Martinus Nijhoff Publishers, the Netherlands, 1985

[8] E.M. Greitzer: "The Stability of Pumping Systems." The 1980 Freeman scholar lecture. ASME Trans., Series I-J. Fluid Engineering, Volume 103, No. 2, June 1981, pp 193-242

[9] R.C. Dean: "On the Unresolved Fluid Dynamics of the Centrifugal Compressor." Creare Incorporated and Darmouth College, Hanover, New Hampshire, Tubomachinery Committee of the ASME Gas Turbine Division, USA, 1967

[10] J.D. Stanitz and V.D. Prian: "A Rapid Approximate Method of Analysis for Determining Velocity Distribution in Impeller Blades of Centrifugal Compressors." NACA TN 2421, July 1951

ATTENTION: The Singapore Copyright Act applies to the use of this document. Nanyang Technological University Library

[11] C. Hah and L. Reid: "A Viscous Flow Study of Shock Boundary Layer Interaction, Radial Transport, and Wake Development in a Transonic Compressor" International Gas Turbine Institute, 36th International Gas Turbine and Aeroengine Congress and Exposition, Orlando, Florida, June 3-6, 1991

[12] S. Baghdadi: "The Effect of Rotor Blade Wakes on Centrifugal Compressor Diffuser Performance" 1976 Joint Gas Turbine and Fluids Engineering Divisions' Conference, New Orleans, Louisiana, the American Society of Mechanical Engineers

[13] Hamrick, J. T. et al, "Study of the three dimensional internal flow distribution based on measurements in a 48-inch inlet centrifugal compressor", NACA TN 3101, February 1954

[14] J. T. Bindon "The Measurement and Formation of Tip Clearance Loss", Presented at the Gas turbine and Aeroengine Congress and Exposition, 1988, The Netherlands, The American Society of Mechanical Engineers.

[15] Fluent Inc, FLUENT 6.1 User's Guide, 2003, Centarra Resource Park, Lebanon, USA.

[16] M. Abidat, M. K. Hamidou, M. Hachemi and M. Hamel, "Design and Flow Analysis of Radial and Mixed Flow Turbine Volutes", European Conference on Computational Fluid Dynamics, ECCOMAS CFD 2006, the Netherlands, 2006

[17] F. Gu and A. Engeda "A Numerical Investigation on the Volute / Impeller Steady State Interaction due to Circumferential Distortion", Michigan State University, Proceedings of ASME Turbo Expo 2001, June 4-7, New Orleans, Louisiana, USA

[18] C. Rodgers "Centrifugal Compressor Blade Trimming for a Range of Flows", Proceedings of ASME Turbo Expo 2001, June 4-7, 2001, New Orleans, Louisiana

ATTENTION: The Singapore Copyright Act applies to the use of this document. Nanyang Technological University Library

[19] W. Jahnen, W. P. Breugem and B. Ribi, "Instability Analysis of a Centrifugal Compressor Stage Near Peak Pressure Rise", Proceedings of ASME Turbo Expo 2001, 2001-GT-318, June 4-7, 2001, New Orleans, Louisiana

[20] J. S. Kang and S. H. Kang, "Stall Inception in a High Speed Centrifugal Compressor", Proceedings of ASME Turbo Expo 2001, 2001-GT-301, June 4-7, 2001, New Orleans, Louisiana

[21] K. Matsuura and C. Kato, "Large-Eddy Simulation of Compressible Transitional Cascade Flows with and without Incoming Free-Stream Turbulence", JSME International Journal Series B, Vol. 49 , No.3 Special Issue on Environmental Flows, page 660-669, 2006

[22] A. Oyama, M.S. Liou and S. Obayashi, "High-Fidelity Swept and Leaned Rotor Blade Design Optimization using Evolutionary Algorithm.", AIAA Paper 2003-4091, 16th AIAA Computational Fluid Dynamics Conference, 23-26 June 2003, Orlando, Florida

[23] K. Levenberg, "A Method for the Solution of Certain Non-Linear Problems in Least Squares", Quarterly of Applied Mathematics, pg 164-168, July 1944

[24] D.L. Whitfield , T.W. Swafford, J.M. Janus, R.A. Mulac and D.M. Belk "Three Dimensional Unsteady Euler Solutions for Propfans and Counter-Rotating Propfans in Transonic Flow." AIAA-87-1197, 19th AIAA Fluid Dynamics, Plasma Dynamics and Lasers Conference, June 8-10, 1987, Hawaii

[25] N. Baines: "Radial Turbines: An Integrated Design Approach." Concepts ETI, Inc., NREC, Chipping Norton, UK, 2005

[26] J. J Hopfield and D.W. Tank, "Neural Computation of Decisions in Optimization Problems", Biological Cybernetics, Springer Berlin, Vol. 52, July, 1985

[27] S. Kirkpatrick, C. D. Gelatt and M. P. Vecchi, "Optimization by Simulated Annealing", Science, Vo1. 220, Number 4598, pg 671-680, May 1983

ATTENTION: The Singapore Copyright Act applies to the use of this document. Nanyang Technological University Library

[28] D. Quagliarella and A. Vicini "Coupling Genetic Algorithms and Gradient Based Optimization Techniques", Genetic Algorithms and Evolution Strategies in Engineering and Computer Science, page 289-309, John Wiley & Sons Ltd, USA, 1998

[29] H. S. Chung and J. J. Alonso, "Multiobjective Optimization Using Approximation Model-Based Genetic Algorithms", 10th AIAA / ISSMO Symposium on Multidisciplinary Analysis and Optimization, Aug 30 – Sept 1, New York, 2004

[30] D. G. Krige, "A Statistical Approach to Some Basic Mine Valuation Problems on the Witwatersrand", Journal of the Chem., Metal and Mining Soc. of South Africa, Vol. 52 (6), Page 119-139, 1951

[31] K. K. Chand and K. D. Lee, "Turbomachinery Blade Optimization Using the Navier Stokes Equations", American Institute of Aeronautics and Astronautics, 36th Aerospace Sciences Meeting and Exhibit, Reno, NV, Jan 12-15, 1998

[32] M. Zangeneh, A. Goto and H. Harada, "On the Role of the Three-Dimesnional Inverse Design methods in Turbomachinery Shape Optimization", Developments in Turbomachinery Design, The Institution of Mechanical Engineers, Professional Engineering Publishing, page 27-42, Bury St Emonds and London, UK, 1999

[33] V. Kelner, G. Grondin, O. Leonard, S. Moreau, "Multi-Objective Optimization of a Fan Blade by Coupling Genetic Algorithm and a Parametric Flow Solver", EUROGEN 2005, Munich, 2005

[34] P. J. Walker and J. A. Hesketh, "Design of low-reaction steam turbine blades", Developments in Turbomachinery Design, The Institution of Mechanical Engineers, Professional Engineering Publishing, Page 153-170, Bury St Emonds and London, UK, 1999

ATTENTION: The Singapore Copyright Act applies to the use of this document. Nanyang Technological University Library

[35] B. H. Dennis, Z. X. Han, I. N. Egorov, G. S. Dulikravich and C. Poloni, "Multi-Objective Optimization of Turbomachinery Cascades for Minimum Loss, Maximum Loading and Maximum Gap to Chord Ratio", 8th AIAA / USAF / ISSMO Symposium on Multidisciplinary Analysis and Optimization, 6-8 Sept 2000, Long Beach, California

[36] G. Lippens, L. Knockaert and D. De Zutter "Reduced Models of Higher Systems Based on Kautz Expansions", ECCOMAS CFD 2006, Ghent University, European Conference on Computational Fluid Dynamics, the Netherlands, 2006

[37] M. Kahlbacher and S. Volkwein "Model Order Reduction by Proper Orthogonal Decomposition for Estimation of Scalar Parameters in Elliptic PDEs", ECCOMAS CFD 2006, University of Graz, European Conference on Computational Fluid Dynamics, the Netherlands, 2006

[38] Holmes P., Lumley J. and Berkooz G, "Turbulence, Coherent Structures, Dynamical Systems and Symmetry", Cambridge University Press, Cambridge, UK, 1996.

[39] LeGresley, P. and Alonso, J., "Investigation of Non-Linear Projection for POD Based Reduced Order Models for Aerodynamics", AIAA Paper 2001-0926, 39th Aerospace Sciences Meeting and Exhibit, Reno, NV, 2001.

[40] Sirovich, L. and Kirby, M., "Low-dimensional procedure for the characterization of human faces." Journal of the Optical Society of America A, 4(3):519-524, 1987.

[41] Fukanaga, K., Introduction to Statistical Pattern Recognition, Academic Press, New York, 1972.

[42] Sirovich, L., "Turbulence and the Dynamics of Coherent Structures. Part 1: Coherent Structures," Quarterly of Applied Mathematics, Vol. 45, No. 3, October 1987, pp. 561–571.

[43] T. Bui-Thanh, M. Damodaran and K. Willcox, "Proper Orthogonal Decomposition Extensions for Parametric Applications in Transonic Aerodynamics", AIAA Paper 2003-4213, 21st AIAA Applied Aerodynamics Conference

ATTENTION: The Singapore Copyright Act applies to the use of this document. Nanyang Technological University Library

[44] Dysprosia: Wikimedia: Centrifugal fan.png ,10 February 2004

[45] F. P. Bleier: "Fan Handbook: Selection, Application, and Design." McGraw-Hill, 1998

[46] W. N. Dawes: "Development of a 3D Navier Stokes Solver for Application to All Types of Turbomachinery." Gas Turbine and Aeroengine Congress, Amsterdam, the Netherlands, June 6-9, 1988.

[47] K. Toyama, P.W. Runstadler and R.C. Dean: "An Experimental Study of surge in Centrifugal Compressors" 1976 Joint Gas Turbine and Fluids Engineering Divisions' Conference, New Orleans, Louisiana, The American Society of Mechanical Engineers

[48] Kenny, D.P., "A Comparison of the Predicted and Measured Performance of High Pressure Ratio Centrifugal Compressors", Lecture Note, von Karman Institute Lecture Note Series 50, Advanced radial compressors, May 1972

[49] M. Roth and R. Peikert, "Flow Visualization for Turbomachinery Design", Swiss Center for Scientific Computing, Switzerland.

[50] M. Casey, "Thematic Area 6: Best Practice Advice for Turbomachinery Internal Flows." QNET-CFD Network Newsletter Volume 2, No.4, Switzerland, July 2004.

[51] H.K. Versteeg and W. Malalasekera,"An Introduction to Computational Fluid Dynamics", Prentice Hall, 1995, England.

[52] Tecplot Inc. TECPLOT User's Manual: Version 10, 2005, Bellevue, Washington

[53] Fluent Inc. GAMBIT 2.1 Modelling Guide, 2003 Centarra Resource Park, Lebanon, USA.

[54] D. Eckardt: "Detailed Flow Investigations within a Higher Speed Centrifugal Compressor Impeller", Fluid Engineering Division of the American Society of Mechanical Engineers, Gas Turbine and Fluids Engineering Conference, 1976

ATTENTION: The Singapore Copyright Act applies to the use of this document. Nanyang Technological University Library

[55] T. Yamane, H. Fujita and T. Nagashima: "Transonic Discharge Flows Around Diffuser Vanes from a Centrifugal Impeller", American Institute of Aeronautics and Astronautics, Inc and the International Symposium on Air Breathing Engines, 1993, University of Tokyo

[56] M. Zangeneh-Kazemi, W. N. Dawes and W. R. Hawthorne "Three Dimensional Flow in Radial-Inflow Turbines" The American Society of Mechanical Engineers, Gas Turbine and Aeroengine Congress, Amsterdam, The Netherlands, 1988, Cambridge University.

[57] K. D. Jones, C. M. Dohring and M. F. Platzer "Experimental and Computational Investigation of the Knoller-Betz Effect" AIAA Journal, Vol. 36, No. 7, July 1998, 34th AIAA Aerospace Sciences Meeting

[58] B. L. Lapworth and R. L. Elder "Computation of the Jet-Wake Flow Structure in a Low Speed Centrifugal Impeller" Presented at the Gas Turbine and Aeroengine Congress, Amsterdam, the Netherlands, 1988

[59] D. P, Bertsekas, "Constrained Optimization and Lagrange Multiplier Methods", Academic Press, Inc, 1982, London

[60] Z. Michalewicz and C. Z. Janikow "Handling Constraints in Genetic Algorithms", University of North Carolina, Proceedings of the Fourth International Conference on Genetic Algorithms, Page 151-157, July 13-16 1991, Morgan Kaufmann Publishers

[61] J. H. Holland "Adaptation in Natural and Artificial Systems", University of Michigan Press, USA, 1975

[62] R. B. Hollstein, "Artificial genetic adaptation in computer control systems", University of Michigan, Dissertation Abstracts International, 32(3), 1510B, University Microfilms No.71-23,773, 1971

[63] J. D. Schaffer, "Multiple objective optimization with vector evaluated genetic algorithms", Proceedings of an International Conference on Genetic Algorithms and Their Applications, 93-100, 1985

ATTENTION: The Singapore Copyright Act applies to the use of this document. Nanyang Technological University Library

[64] J. E. Baker, "Reducing bias and inefficiency in the selection algorithm", Proceedings of the Second International Conference on Genetic Algorithms, 14-21, 1987

[65] K. A. De Jong, "An Analysis of the Behavior of a class of genetic adaptive systems", University of Michigan, Dissertation Abstracts International 36(10), 5140B, Univesrity Microfilms No.76-9381, 1975

[66] J. T. Alander and J. Lampinen "Cam Shape Optimization by Genetic Algorithm", Genetic Algorithms and Evolution Strategies in Engineering and Computer Science, page 153-174, John Wiley & Sons Ltd, USA, 1998

[67] T. Back, U. Hammel, R. Lewandowski, M. Mandischer, B. Naujoks, S. Rolf, M. Schutz, H. Schwefel, J. Sprave, S. Theis "Evolutionary Algorithms: Applications at the Informatik Center Dortmund", Genetic Algorithms and Evolution Strategies in Engineering and Computer Science, page 175-204, John Wiley & Sons Ltd, USA, 1998

[68] D. Floreano, "Evolutionary Mobile Robotics", Genetic Algorithms and Evolution Strategies in Engineering and Computer Science, page 341-365, John Wiley & Sons Ltd, USA, 1998

[69] B. D. Andres-Toro, J. M. Giron-Sierra, J.A. Lopez-Orozco, C. Fernandez-Conde, "Using Genetic Algorithms for Dyanmic Optimization: An Industrial Fermentation Case", Proceedings of the 36th IEEE CDC, San Diego, CA, Dec,1997.

[70] D. E. Goldberg "Genetic Algorithms in Search, Optimization, and machine Learning", "The University of Alabama, Addison-Wesley Publishing Company, INC, USA, 1989

[71] A. K. Noor and J. M. Peters "Reduced basis technique for nonlinear analysis of structures", AIAA Journal, Vol.18, no.4, pp. 455-462, 1980

[72] P. Feldmann and R. W. Freund, "Efficient linear circuit analysis by Pade approximation via the Lanczos process," IEEE Transactions on Computer-Aided Design of Integrated Circuits and Systems, vol.14, no.5, pp.639-649, 1995

ATTENTION: The Singapore Copyright Act applies to the use of this document. Nanyang Technological University Library

[73] K. Karhunen, "Zur Spektraltheorie Stochastischer Prozesse", Ann. Acad. Sci. Fennicae, 1946

[74] M. M. Loeve, "Probability Theory", Princeton, N.J, VanNostrand, 1955

[75] A. Chatterjee, "An Introduction to the Proper Orthogonal Decomposition" Dec 18, 1999, Current Science publication, Penn State University

[76] G. H. Golub and C. F. Van Loan, "Matrix Computations", Oxford: North Oxford Academic, 1983

[77] J. S. R. Anttonen, P.I. King and P.S. Beran "POD-Based Reduced-Order Models with Deforming Grids", Mathematical and Computing Modelling Issue 38, 2003, Page 41-62

[78] P. Beran and W. Silva, "Reduced Order Modelling: New Approaches for computational physics, AIAA 2001-0853, 39th Aerospace Sciences Meeting and Exhibit, Reno, NV, January 2001

[79] H.V. Ly and H. T. Tran, "Proper Orthogonal Decomposition for Flow Calculations and Optimal Control in a Horizontal CVD Reactor," Center for Reasearch in Science Computation, North Carolina State University, USA, March 1998

[80] C. Hirsch and A. Ligout "Integrated Multipoint Optimization System for Turbomachinery Blades", ECCOMAS CFD 2006, European Conference on Computational Fluid Dynamics 2006, the Netherlands, 2006

[81] S. Obayashi "Multi-Objective Design Using Efficient Global Optimization", Tohoku University, ECCOMAS CFD 2006, European Conference on Computational Fluid Dynamics, the Netherlands, 2006

[82] L. Davis, "Genetic Algorithms and Simulated Annealing", Morgan Kaufmann Publishers 1987, San Francisco, CA, USA